

18305

54.1

a
report [REDACTED]
from the Texas A&M
RESEARCH FOUNDATION
College Station, Texas
[REDACTED]

(NASA-CR-194164) FAILURE
PREDICTION OF THIN BERYLLIUM SHEETS
USED IN SPACECRAFT STRUCTURES Final
Technical Report, 1 Jul. 1990 - 30
Jun. 1991 (Texas A&M Univ.) 260 p

N94-11190

Unclass

G3/39 0183093

FAILURE PREDICTION OF THIN BERYLLIUM SHEETS USED IN SPACECRAFT STRUCTURES

Final Report

Period: July 1, 1990, to June 30, 1991

Principal Investigator: Dr. Paul N. Roschke
Research Assistants: Edward Mascorro, Photios Papados, Oscar R. Serna

Texas A&M University
Department of Civil Engineering
College Station, Texas 77843-3136

NASA Grant Number: NAG 9-280

ABSTRACT

Primary objective of this study is to develop a method for prediction of failure of thin beryllium sheets that undergo complex states of stress. Major components of the research include experimental evaluation of strength parameters for cross-rolled beryllium sheet, application of the Tsai-Wu failure criterion to plate bending problems, development of a high order failure criterion, application of the new criterion to a variety of structures, and incorporation of both failure criteria into a finite element code.

A Tsai-Wu failure model for SR-200 sheet material is developed from available tensile data, experiments carried out by NASA on two circular plates, and compression and off-axis experiments performed in this study. The failure surface obtained from the resulting criterion forms an ellipsoid.

By supplementing experimental data used in the the two-dimensional criterion and modifying previously suggested failure criteria, a multi-dimensional failure surface is proposed for thin beryllium structures. The new criterion for orthotropic material is represented by a failure surface in six-dimensional stress space. In order to determine coefficients of the governing equation, a number of uniaxial, biaxial, and triaxial experiments are required. Details of these experiments and a complementary ultrasonic investigation are described in detail. Finally, validity of the criterion and newly determined mechanical properties is established through experiments on structures composed of SR-200 sheet material. These experiments include a plate-plug arrangement under a complex state of stress and a series of plates with an out-of-plane central point load.

Both criteria have been incorporated into a general purpose finite element analysis code. Numerical simulation incrementally applied loads to a structural component that is being designed and checks each nodal point in the model for exceedance of a failure criterion. If stresses at all locations do not exceed the failure criterion, the load is increased and the process is repeated. Failure results for the plate-plug and clamped plate tests are accurate to within 2%.

TABLE OF CONTENTS

	<i>Page</i>
ABSTRACT.....	ii
LIST OF FIGURES	vii
LIST OF TABLES	xii
1. INTRODUCTION.....	1
1.1 Background and Motivation.....	1
1.2 Physical Properties.....	4
1.2.1 Cross-Rolled Sheet Preparation.....	4
1.2.2 Atomic Structure	4
1.2.3 Density	4
1.2.4 Elastic Moduli.....	5
1.3 Thermal Properties	6
1.3.1 Specific Heat	6
1.3.2 Coefficient of Thermal Expansion	6
1.3.3 Thermal Conductivity	7
1.4 Transparency to Electromagnetic Radiation	7
1.5 Mechanical Properties.....	8
1.6 Disadvantages in Using Beryllium	9
2. HISTORICAL BACKGROUND.....	11
2.1 Objectives.....	11
2.2 Attributes of a Failure Criterion	11
2.3 Isotropic Yielding	12
2.4 Tresca's Criterion.....	13
2.5 von Mises' Criterion.....	13
2.6 Hill's Criterion	14
2.7 Gol'denblat and Kopnov's Criterion.....	17
2.8 Hoffman's Criterion	17
2.9 Tsai-Wu Criterion.....	19
2.10 Priddy's Criterion.....	21
2.11 Jiang and Tennyson's Criterion.....	23
3. FAILURE PREDICTION WITH CLOSURE OF CUBIC TENSOR.....	24
3.1 Failure Prediction with Hydrostatic Dependence	24
3.1.1 General State of Stress.....	24
3.1.2 Investigation of Necessary Conditions.....	29
3.1.3 Evaluation of F_{ij} and F_{ijj} for i, j	33
3.1.4 Evaluation of F_{ijj} for $i = 1, 2, 3$, and $j = 4$ or 5 or 6	37
3.2 Failure Prediction without Hydrostatic Dependence	39
3.2.1 General State of Stress.....	39
3.2.2 Investigation of Necessary Conditions.....	40
3.2.3 Evaluation of F_{ij} and F_{ijj} for i, j	41
3.2.4 Evaluation of F_{ijj} for $i = 1, 2, 3$, and $j = 4$ or 5 or 6	43
4. EXPERIMENTAL INVESTIGATIONS.....	46

4.1	Introduction.....	46
4.2	Tensile State of Stress.....	52
4.2.1	Specimens Aligned with Material Axes.....	52
4.2.2	Specimens with Material Axes Rotated 45°.....	53
4.3	In-Plane Shear State of Stress.....	56
4.4	In-Plane Biaxial State of Stress.....	64
4.4.1	25.4-mm Ring Load.....	66
4.4.2	50.4-mm Ring Load.....	73
5.	EXPERIMENTAL DETERMINATION OF PRINCIPAL FAILURE COEFFICIENTS	84
5.1	Introduction.....	84
5.2	In-Plane Compressive State of Stress.....	86
5.2.1	Laboratory Experiments.....	86
5.2.2	Numerical Simulation.....	91
5.2.2.1	Plane Stress Elements.....	92
5.2.2.2	Three-Dimensional Elements.....	92
5.2.3	Comparison of Failure Strain with Elasticity Solution.....	96
5.2.4	Determination of Principal Coefficients F_1 , F_{11} , F_2 , and F_{22}	103
5.3	In-Plane Shearing Stress.....	103
5.3.1	Titanium Experiment and Simulation.....	103
5.3.2	Beryllium Experiment.....	107
5.3.3	Numerical Simulation of Beryllium Experiment.....	108
5.3.4	Determination of Principal Coefficients F_6 and F_{66}	117
5.4	Through-Thickness Shear.....	118
5.4.1	Experiments.....	118
5.4.3	Determination of Failure Coefficients F_{44} and F_{55}	128
5.5	Through-Thickness Compression State of Stress.....	128
5.5.1	Experiments.....	128
5.5.2	Numerical Simulation.....	131
5.5.3	Determination of Failure Coefficients F_3 and F_{33}	132
6.	EXPERIMENTAL DETERMINATION OF INTERACTION FAILURE COEFFICIENTS	134
6.1	Introduction.....	134
6.2	Multiaxial State of Stress: σ_1 , σ_3 , and σ_5	134
6.2.1	Laboratory Experiments.....	135
6.3	Multiaxial State of Stress: σ_2 , σ_3 , and σ_4	145
6.3.1	Laboratory Experiments.....	145
6.3.2	Numerical Simulation.....	146
6.4	Evaluation of Interaction Coefficients.....	147
6.4.1	Theoretical Considerations.....	148
6.4.2	Determination of F_{13} , F_{113} , F_{133} , F_{155} , and F_{355}	149
6.4.3	Interaction Coefficients F_{23} , F_{223} , F_{233} , F_{244} , and F_{344}	150
6.4.4	Determination of F_{12} , F_{112} , F_{122} , F_{166} , and F_{266} , and F_{144} , F_{255} , and F_{366}	150
6.5	State of Stress with In-Plane Compression and Out-of-Plane Shear.....	151

6.5.1	Experimental Investigation.....	151
6.5.2	Theoretical Considerations.....	152
6.5.3	Interaction Coefficients F_{155} and F_{244}	158
7.	NON-DESTRUCTIVE EVALUATION TESTS	159
7.1	Introduction.....	159
7.2	Hardness Test.....	159
7.3	Ultrasonic Test	163
7.3.1	Background	163
7.3.2	Determination of Elastic Constants for Each Layer.....	165
7.3.3	Numerical Simulation.....	167
8.	FAILURE SURFACES FOR SR-200 BERYLLIUM SHEET STRUCTURES	172
8.1	Closure and Convexity of Failure Surfaces.....	172
8.1.1	Closure of a Failure Surface.....	172
8.1.2	Convexity of a Failure Surface	173
8.2	Failure Surfaces	177
8.2.1	In-Plane State of Stress (σ_1 , σ_2 , and σ_6)	181
8.2.2	Combinations of In-Plane Normal Stresses (σ_1 , σ_2) and Out-of- Plane Shearing Stress (σ_4 or σ_5)	182
8.2.3	Combination of Normal Stresses σ_1 , σ_3 and Planar Shearing Stress σ_4	182
8.2.4	Combination of Normal Stresses σ_2 , σ_3 and Planar Shearing Stress σ_5	183
8.2.5	Combination of Shearing Stresses σ_4 , σ_5 , and σ_6	183
9.	NUMERICAL MODELING AND FAILURE PREDICTION FOR SR-200 BERYLLIUM STRUCTURES	184
9.1	Introduction.....	184
9.2	Numerical Model Specification	184
9.3	Automation of Numerical Simulation	186
9.4	Verification of Failure Prediction	189
9.4.1	Plate-Plug Experiment	189
9.4.1.1	Description of Laboratory Experiment	189
9.4.1.2	Numerical Simulation.....	192
9.4.1.3	Observations.....	196
9.4.2	Clamped Plates under Influence of Concentrated Load	197
9.4.2.1	101.6-mm \times 50.8-mm (4.0-in. \times 2.0-in.) Plate	199
9.4.2.2	50.8-mm \times 25.4-mm (2.0-in. \times 1.0-in.) Plate	201
10.	CONCLUSION.....	202
	REFERENCES.....	206

APPENDIX I. Failure Coefficients for Tsai and Wu's Criterion.....	209
APPENDIX II. Overview of Jiang and Tennyson's Criterion.....	211
APPENDIX III. Derivation of Equations 74, 75, And 76	216
APPENDIX IV. Derivation of Equations 115 Through 118	218
APPENDIX V. Theoretical Determination of Normal-Shear Interaction Coefficients.....	220
APPENDIX VI. 45 In-Plane Stress Transformation.....	224
APPENDIX VII. Stress Transformation for Rotation of In-Plane Material Axes	228
APPENDIX VIII. Least Squares Scheme for Evaluation of Unknown Coefficients.....	230
APPENDIX IX. Listing of C-Program to Compute Maximum Stress	233
APPENDIX X. Sample Input ABAQUS Model.....	235
APPENDIX XI. Selective Listing of FORTRAN Program CHECK.....	241
APPENDIX XII. Notation.....	245

LIST OF FIGURES

<i>Figure</i>	<i>Page</i>
1 Structural Application of Beryllium.....	1
2 Optical/Reflective Application of Beryllium	2
3 Density Histogram for Selected Metals	5
4 Histogram of Young's Modulus for Various Metals	6
5 Rotation of Material Axes with Respect to Center-Line of the Specimen.....	16
6 General Body with Surface Forces.....	25
7 Stress Components Acting at a Point	25
8 Constraint and Asymptotic Equations Bounding Open and Closed Two- Dimensional Surfaces	29
9 Open, Non-Convex Failure Surface	35
10 Closed Failure Surface.....	36
11 Experimental Determination of Failure Coefficients - A.....	47
12 Experimental Determination of Failure Coefficients - B.....	48
13 Experimental Determination of Failure Coefficients - C.....	49
14 Experimental Determination of Failure Coefficients - D.....	50
15 In-Plane Tensile Specimen	52
16 Off-Axis In-Plane Tensile Specimen.....	54
17 In-Plane Shear Specimen	57
18 Loading Arrangement for In-Plane Shear Test	58
19 Fracture Pattern for Unsanded Shear Specimens	59
20 Shear Specimen Fringe Plot of Axial Displacement	59
21 Shear Specimen Fringe Plot of Transverse Displacement.....	60
22 Shear Specimen Fringe Plot of Axial Strain, ϵ_1	60
23 Shear Specimen Fringe Plot of Transverse Strain, ϵ_2	61
24 Shear Specimen Fringe Plot of Shearing Strain, ϵ_6	61
25 Shear Specimen Fringe Plot of Axial Stress, σ_1	62
26 Shear Specimen Fringe Plot of Transverse Stress, σ_2	62
27 Shear Specimen Fringe Plot of Shearing Stress, σ_6	63
28 25.4-mm (1.0-in.) and 50.8-mm (2.0-in.) Ring Loadings	65
29 Gage and LVDT Locations for Circular Plate Specimens	65
30 Vertical Displacement along a Radial Line at Yield and Ultimate Stress for 25.4-mm (1.0-in) Load.....	67
31 Plate with 25.4-mm Ring at Ultimate Load Fringe Plot of Vertical Displacement	67
32 Plate with 25.4-mm Ring at Ultimate Load Fringe Plot of In-Plane Displacement in the X-Direction	68
33 Plate with 25.4-mm Ring at Ultimate Load Fringe Plot of In-Plane Displacement in the Y-Direction	68
34 Radial Strains at Yield and Ultimate Stress for 25.4-mm (1.0-in) Load.....	69
35 Plate with 25.4-mm Ring at Ultimate Load Fringe Plot of ϵ_1 Strain.....	69

36	Plate with 25.4-mm Ring at Ultimate Load Fringe Plot of ϵ_2 Strain.....	70
37	Plate with 25.4-mm Ring at Ultimate Load Fringe Plot of ϵ_6 Strain.....	71
38	Plate with 25.4-mm Ring at Ultimate Load Fringe Plot of ϵ_3 Strain.....	71
39	Plate with 25.4-mm Ring at Ultimate Load Fringe Plot of ϵ_4 Strain.....	72
40	Plate with 25.4-mm Ring at Ultimate Load Fringe Plot of ϵ_5 Strain.....	72
41	Plate with 25.4-mm Ring at Ultimate Load Fringe Plot of σ_1 Stress	73
42	Plate with 25.4-mm Ring at Ultimate Load Fringe Plot of σ_2 Stress	74
43	Plate with 25.4-mm Ring at Ultimate Load Fringe Plot of σ_3 Stress	74
44	Plate with 25.4-mm Ring at Ultimate Load Fringe Plot of σ_4 Stress	75
45	Plate with 25.4-mm Ring at Ultimate Load Fringe Plot of σ_5 Stress	75
46	Plate with 25.4-mm Ring at Ultimate Load Fringe Plot of σ_6 Stress	76
47	Vertical Displacement along a Radial Line at Yield and Ultimate Stress for 50.8-mm (2.0-in) Load.....	77
48	Plate with 50.8-mm Ring at Ultimate Load Fringe Plot of Vertical Displacement	77
49	Plate with 50.8-mm at Ultimate Load Fringe Plot of Displacement in the X- Direction.....	78
50	Plate with 50.8-mm at Ultimate Load Fringe Plot of Displacement in the Y- Direction.....	78
51	Radial Strain at Yield and Ultimate Stress for 50.8-mm (2.0-in) Ring Load	80
52	Plate with 50.8-mm Ring at Ultimate Load Fringe Plot of ϵ_1 Strain.....	80
53	Plate with 50.8-mm Ring at Ultimate Load Fringe Plot of ϵ_2 Strain.....	81
54	Plate with 50.8-mm Ring at Ultimate Load Fringe Plot of ϵ_6 Strain.....	81
55	Plate with 50.8-mm Ring at Ultimate Load Fringe Plot of σ_1 Stress	82
56	Plate with 50.8-mm Ring at Ultimate Load Fringe Plot of σ_2 Stress	82
57	Plate with 50.8-mm Ring at Ultimate Load Fringe Plot of σ_6 Stress	83
58	Compression Specimen Longitudinal Axis Aligned with Principal Material Axis.....	88
59	Compression Specimen Transverse Axis Aligned with Principal Material Axis.....	88
60	Fixtures for Compression Testing	89
61	Normal Stress-Strain Curve for Specimen Loaded Along the Principal Direction of Cross Rolling.....	89
62	Normal Stress-Strain Curve for Specimen Loaded Perpendicular to the Principal Direction of Cross Rolling	90
63	Stress-Strain Curve for Specimen Loaded Parallel to Principal Direction of Cross Rolling	90
64	Failed Compression Specimen.....	91
65	Finite Element Discretization for Compression Specimens (a) Two- Dimensional Plane Stress Elements; (b) Three-Dimensional Hexahedral Elements.....	93
66	Distribution of Axial Displacement for 2-D Compression Model	94
67	Distribution of Transverse Displacement for 2-D Compression Model.....	94
68	Distribution of Transverse Stress, σ_2 , for 2-D Compression Model	95
69	Distribution of In-Plane Shearing Stress, σ_6 , for 2-D Compression Model.....	95

70	Distribution of Axial Displacement for 3-D Compression Model	97
71	Distribution of Transverse Displacement for 3-D Compression Model.....	97
72	Distribution of Through-Thickness Displacement for 3-D Compression Model	98
73	Distribution of Normal Strain, ϵ_1 , for 3-D Compression Model	98
74	Distribution of Normal Stress, σ_1 , for 3-D Compression Model	99
75	Distribution of Transverse Stress, σ_2 , for 3-D Compression Model	99
76	Distribution of Through-Thickness Stress, σ_3 , for 3-D Compression Model	100
77	Distribution of Out-of-Plane Shearing Stress, σ_4 , for 3-D Compression Model	100
78	Distribution of Out-of-Plane Shearing Stress, σ_5 , for 3-D Compression Model	101
79	Distribution of In-Plane Shearing Stress, σ_6 , for 3-D Compression Model.....	101
80	Geometry of Beryllium Shear Specimen.....	104
81	Experimental and Numerical Results for (a) Titanium and (b) Beryllium Shear Specimens.....	105
82	Titanium and (b) Beryllium Shear Specimens after Failure.....	106
83	Location Differential Element for Transformation to a State of Stress of Pure Shear	108
84	Finite Element Mesh for Critical Region of Two-Dimensional Shear Specimen.....	109
85	Distribution of Longitudinal Displacement for 2-D Beryllium Shear Specimen	110
86	Distribution of Transverse Displacement for 2-D Beryllium Shear Specimen	111
87	Distribution of Longitudinal Strain for 2-D Beryllium Shear Specimen	111
88	Distribution of Transverse Strain for 2-D Beryllium Shear Specimen.....	112
89	Distribution of In-Plane Shearing Strain for 2-D Beryllium Shear Specimen	112
90	Distribution of Longitudinal Normal Stress for 2-D Beryllium Shear Specimen	113
91	Distribution of In-Plane Shearing Stress for 2-D Beryllium Shear Specimen	113
92	Distribution of Transverse Normal Stress for 2-D Beryllium Shear Specimen	114
93	Finite Element Model of Three-Dimensional Shear Specimen.....	114
94	Distribution of Longitudinal Displacement for 3-D Beryllium Shear Specimen	115
95	Distribution of Axial Strain for 3-D Beryllium Shear Specimen	115
96	Distribution of In-Plane Shearing Strain for 3-D Beryllium Shear Specimen	116
97	Distribution of Axial Stress for 3-D Beryllium Shear Specimen	116
98	Distribution of In-Plane Shearing Stress for 3-D Beryllium Shear Specimen	117
99	Dimensions of Specimens for Double Shear Test	119
100	Setup for Through-Thickness Shearing Stress Test	119
101	Shearing Stress (σ_4) versus Strain (ϵ_1 and ϵ_2) for Through-Thickness Shearing Test.....	121
102	Shearing Stress (σ_5) versus Strain (ϵ_1 and ϵ_2) for Through-Thickness Shearing Test.....	121
103	Top View of Through-Thickness Shear Specimen 1 after Failure	122
104	Top View of Through-Thickness Shear Specimen 2 after Failure	123
105	Side view of Through-Thickness Shear Specimen 1 after Failure.....	123
106	Side view of Through-Thickness Shear Specimen 2 after Failure.....	124
107	Distribution of Short Transverse Displacement for Through-Thickness Shearing Test.....	124
108	Distribution of Shearing Strain, ϵ_4 , for Through-Thickness Shearing Test	125
109	Distribution of Longitudinal Stress for Through-Thickness Shearing Test	125

110	Distribution of Shearing Stress, σ_4 , for Through-Thickness Shearing Test.....	126
111	Distribution of Short Transverse Normal Stress for Through-Thickness Shearing Test.....	126
112	Experimental Setup for Through-Thickness Compression Test.....	129
113	Stress versus Deformation for Through-Thickness Compression.....	130
114	Magnified Photograph of Failed Through-Thickness Compression Specimen	131
115	Distribution of Through-Thickness Compressive Stress from 2-D Simulation.....	132
116	Distribution of Through-Thickness Compressive Stress from 3-D Simulation.....	133
117	Distribution of Axisymmetric Through-Thickness Compressive Stress	133
118	Experimental Fixtures for Combined Normal and Shearing Stress Tests.....	135
119	Load versus Displacement for 30°, 35°, 37°, 40°, and 45° Planes of Inclination (σ_1 , σ_3 , and σ_5).....	138
120	Histogram of Maximum Compressive Load and Maximum Vertical Deflection for 30°, 35°, 37°, 40°, and 45° Planes of Inclination (σ_1 , σ_3 , and σ_5).....	138
121	Magnified Photograph of Failed Specimen that is Inclined 37°	139
122	Magnified Photograph of Failed Specimen that is Inclined 40°	139
123	Magnified Photograph of Failed Specimen that is Inclined 45°	140
124	Distribution of Through-Thickness Normal Stress from 2-D Simulation for 30° Specimen.....	141
125	Distribution of Through-Thickness Normal Stress from 3-D Simulation for 30° Specimen.....	142
126	Distribution of In-Plane Normal Stress from 2-D Simulation for 30° Specimen.....	142
127	Distribution of Shearing Stress from 2-D Simulation for 30° Specimen	143
128	Distribution of Through-Thickness Normal Stress from 2-D Simulation for 35° Specimen.....	143
129	Distribution of Through-Thickness Normal Stress from 2-D Simulation for 37° Specimen.....	144
130	Distribution of Through-Thickness Normal Stress from 2-D Simulation for 40° Specimen.....	144
131	Distribution of Through-Thickness Normal Stress from 2-D Simulation for 45° Specimen.....	145
132	Histogram of Maximum Compressive Load and Maximum Vertical Deflection for 30°, 35°, 37°, 40°, and 45° Planes of Inclination (σ_2 , σ_3 , and σ_4).....	148
133	Failed Compression-Torsion Specimen	153
134	Torsional Moment versus Angle of Twist.....	154
135	Torsional Moment versus Normal and Transverse Strain for Specimen with (a) Principal and (b) Secondary Material Axes Aligned with Loading Orientation.....	155
136	Free Body Diagram of Compression-Torsion Specimen	156
137	Hardness Testing Machine	161
138	Indentations from Through-Thickness Hardness Test.....	162

139	Hardness Test Indentations in SR-200 Beryllium Used to Determine σ_1	162
140	Experimental Setup for Ultrasonic Testing.....	165
141	Location and Dimension of Through-Thickness Layers.....	166
142	Two Independent Layers with Different Elastic Properties E_3 , ν_{13} , and ν_{23} in Undeformed and Deformed Configurations	168
143	Undeformed Medium of Two Connected Layers with Different E_3 , ν_{13} , and ν_{23}	168
144	Deformed Medium of Two Connected Layers with Different E_3 , ν_{13} , and ν_{23}	169
145	Variation of Through-Thickness Modulus with Distance from Middle Plane.....	171
146	Failure Surface for σ_1 , σ_2 , σ_6	178
147	Contours of Failure Surface for σ_1 , σ_2 , σ_4	179
148	Contours of Failure Surface for σ_1 , σ_2 , σ_5	179
149	Failure Surface for σ_1 , σ_3 , σ_4	180
150	Failure Surface for σ_1 , σ_3 , σ_5	180
151	Failure Surface for σ_4 , σ_5 , σ_6	181
152	Finite Elements Used for Numerical Simulation.....	185
153	Flow Chart for Batch Submission.....	187
154	Flow Chart for FORTRAN Program.....	188
155	Hierarchical File Sequence of Failure Prediction Scheme.....	189
156	Plug-Plate Arrangement.....	190
157	Pressure Calibration of Hydraulic Actuator	191
158	Location of Strain Gages on Plate-Plug Specimen.....	191
159	Hydraulic Pressure versus Normal Strain for Gage 2	193
160	Hydraulic Pressure versus Normal Strain for Gages 3 and 4	193
161	Hydraulic Pressure versus Normal Strain for Gages 5, 6, and 7	194
162	Finite Element Mesh for Plate-Plug Structure.....	194
163	Distribution of Through-Thickness Displacement, u_z	195
164	Distribution of Normal Stress in Global x-Direction	195
165	Scanning Electron Microscope Photograph 1	196
166	Scanning Electron Microscope Photograph 2	197
167	Clamped Plate with Load Applicator.....	198
168	Load Distribution for 101.6-mm \times 50.8-mm (4.0-in. \times 2.0-in.) Plate	199
169	Distribution of Normal Stress along Principal Material Axis for 101.6-mm \times 50.8-mm (4.0-in. \times 2.0-in.) Plate.....	200
170	Distribution of Normal Stress along Principal Material Axis for 50.8-mm \times 25.4-mm (2.0-in. \times 1.0-in.) Plate.....	201
171	Rotation of In-Plane Axes.....	225
172	Rotation of an In-Plane Axis	228

LIST OF TABLES

<i>Table</i>	<i>Page</i>
1 Physical Properties of Beryllium	8
2 Elastic Properties of 1.96-mm (0.08-in.) SR-200 Sheet (Fenn et al. 1967).....	9
3 Uniaxial Strength Properties of 1.96-mm (0.08-in.) SR-200 Sheet (Fenn et al. 1967).....	9
4 Elastic Properties of 25.4-mm (0.10-in.) Thick SR-200 Sheet1	51
5 Uniaxial Tensile Strength of 25.4-mm (0.10-in.) Thick SR-200 Sheet1.....	51
6 Normal In-Plane Tensile Strengths for Cross-Rolled Beryllium	53
7 Comparison of Transformed Engineering Constants with Computed Stiffness	55
8 45° Off-Axis Tensile Strengths under In-Plane Load	55
9 In-Plane Shearing Strengths (Henkener et al. 1991)	58
10 Experimental In-Plane Biaxial Stress Output - NASA	66
11 Chemical Composition of Beryllium Specimens.....	85
12 Experiments Required for Evaluation of Failure Coefficients.....	85
13 Experiments Used for Evaluation of Failure Coefficients.....	86
14 Failure Strength for Compression Specimens	91
15 Numerical and Theoretical Comparison of Failure Strain Components	102
16 Failure Strength for In-Plane Shear Specimens.....	107
17 Failure Strength for Out-of-Plane Shear	122
18 Failure Strength for Through-Thickness Compression Specimens.....	130
19 Failure Strengths for Disk Specimens with σ_1 , σ_3 , and σ_5 State of Stress.....	137
20 Failure Strengths of Disk Specimens with σ_2 , σ_3 , and σ_4 State of Stress	147
21 Failure Strength for Compression-Torsion Specimens	153
22 Tensile Strengths from Hardness Testing for Principal Material Axes	164
23 Elastic Constants for Specimens from NDE Measurements	166
24 Elastic Constants for Layers from NDE Measurements	170

1. INTRODUCTION

1.1 BACKGROUND AND MOTIVATION

In the design of complex structures, material selection is usually based upon a variety of physical characteristics, such as strength, and the interaction between materials within the system. Beryllium possesses a unique combination of properties that makes it desirable for a number of applications, especially in the aerospace industry. For example, no other material matches beryllium's advantageous combination of high modulus and low density. Due to this characteristic, beryllium is manufactured in a sheet form that is used extensively to encase spacebound payloads and for structural purposes in the space shuttle itself (see Fig. 1). Integral components of satellite structures that are manufactured from beryllium sheets serve structural, reflective, and thermal functions (see Fig. 2).

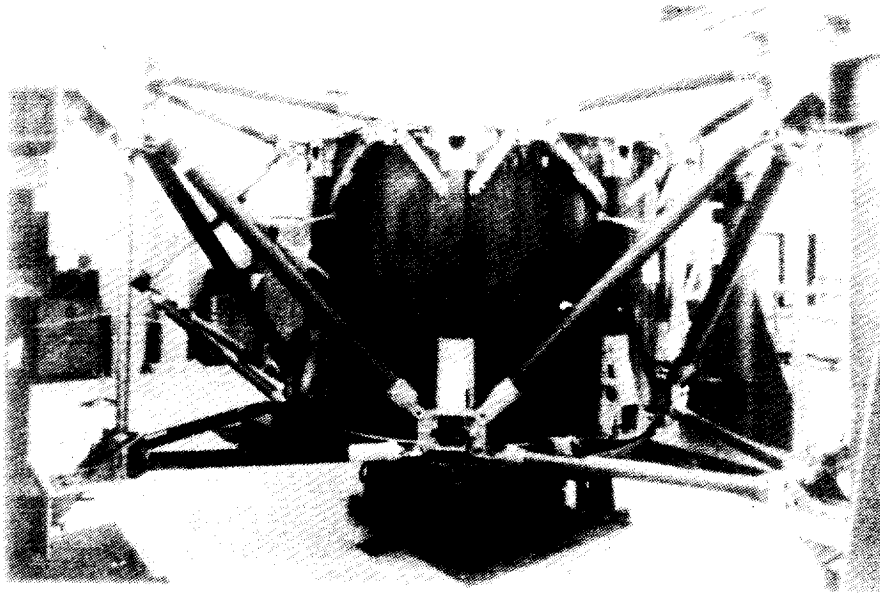


FIG. 1. Structural Application of Beryllium

Substantial research efforts toward property identification and material characterization of beryllium sheets were made in the late 1960s and early 1970s by commercial firms and governmental agencies. Subsequently, beryllium components made from beryllium sheet were successfully applied in a number of aerospace structural applications. At the end of this period, the number of technical publications related to

research on use of beryllium as a structural element diminished considerably. In 1981, a conical beryllium section of the Insat C spacecraft failed catastrophically during certification procedures for flight as a Space Transportation System payload. Failure was attributed to excessive out-of-plane stresses. This unexpected failure rekindled research interest and concern for use of beryllium as a structural element (Henkener et al. 1991). If a beryllium sheet component fails in a spacecraft structure, especially by out-of-plane loadings, the results could be catastrophic since the brittle nature of the material usually causes the formation of fragments that, subsequently, may invoke human injury and jeopardize the structural integrity of the spacecraft. NASA, whose primary motivation is the safety of the crew, is concerned about the behavior of the material under a variety of loadings and especially under complex states of stress.

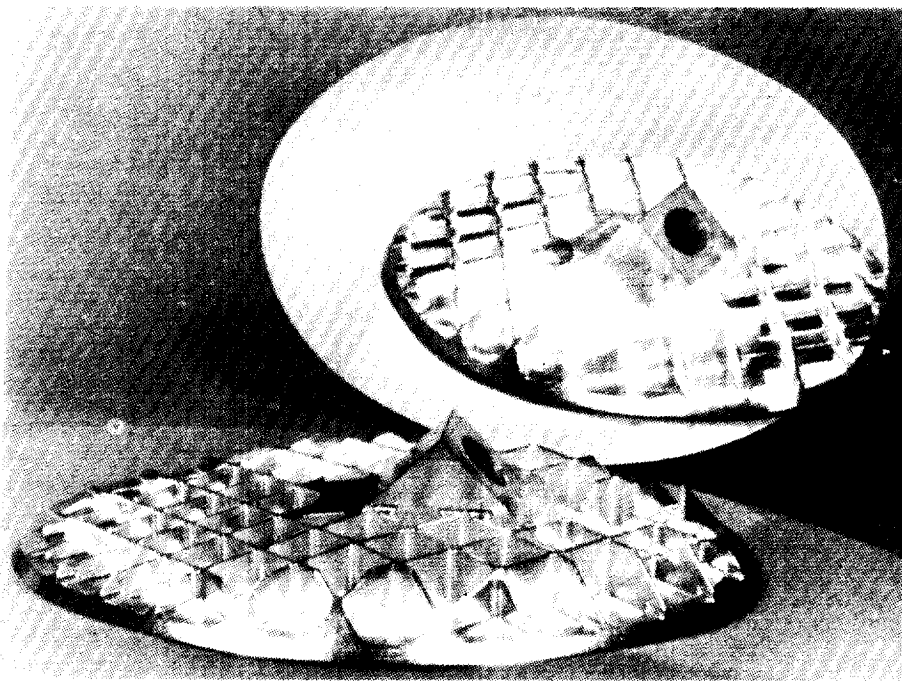


FIG. 2. Optical/Reflective Application of Beryllium

It became apparent that the theoretical and experimental work accomplished in the 1960s and 1970s provides inadequate information for establishing design guidelines. This is due to two factors: the material properties of beryllium are not constant in the through-thickness direction and the criteria that are most commonly used for predicting failure consider only two-dimensional analyses. Moreover, these criteria neglect normal and shear stress interactions.

NASA, the aerospace industry, and the beryllium manufacturing companies are showing a renewed interest for development of a failure prediction method that can be used in design of safe beryllium sheet structures. Most of the published research dedicated to beryllium as a structural material approaches the subject from a microscopic point of view. By contrast, the current effort considers the macroscopic nature of the material. Results obtained are compared, whenever possible, with those obtained by other investigators who use either a microscopic or a macroscopic approach.

The goal in what follows is to describe two numerical techniques for failure prediction of beryllium sheets that have been verified by laboratory experiments. The first technique uses laboratory tests to establish coefficients of the well-known Tsai-Wu failure criterion. Applicability of this theory is measured through a series of tests on beryllium plates deformed by a central point load. Second, a new failure prediction criterion is presented that takes into account multi-dimensional states of stress. These stresses include normal and shearing stress at failure. Various combinations of these stresses are used to calculate the necessary interaction coefficients that define an equation of failure for cross-rolled beryllium. After determining these coefficients, the new criteria is applied for prediction of failure of several other experimental tests.

The remainder of this chapter outlines the physical, thermal, electromagnetic, and mechanical properties of beryllium. Chapter 2 reviews existing criteria that are used to predict failure. Chapter 3 presents a new, multi-dimensional failure criterion that incorporates closure of the cubic polynomial strength tensor. The criterion calls for a number of principal and interaction strength coefficients. Chapters 4 through 7 give an account of the experimental investigations conducted for cross-rolled beryllium sheets. More specifically, chapter 4 reviews experimental accomplishments of other investigators. Some of the failure coefficients for the proposed criterion are based on results of these tests. Chapter 5 describes uniaxial and shear tests used to compute the principal strength coefficients, while chapter 6 includes experiments for determining the interaction coefficients. The next chapter deals with non-destructive evaluations: hardness and ultrasonic tests. The former provides a verification of the uniaxial tensile testing while the latter provides an estimation of the variation of the elastic modulus in the through-thickness direction. The coefficients obtained from experiments described in chapters 5 and 6 are refined via constrained and asymptotic conditions derived from the criterion. The result is a failure surface in six-dimensional stress space. Certain combinations of stresses and the resulting failure surfaces are presented. Application of the failure criterion is provided in chapter 8 for two distinct cases: a plate-plug arrangement subjected to a complex state of stress and a clamped plate subjected to a point load.

1.2 PHYSICAL PROPERTIES

Since material properties affect the behavior of beryllium sheets under load, a brief survey of some of the natural and physical properties are presented and compared with those of other structural metals. Properties discussed in what follows include: material preparation, density, elastic moduli, thermal properties (such as specific heat, coefficient of thermal expansion, and thermal conductivity), and X-ray transparency. The discussion is restricted to cross-rolled beryllium sheet although some of the properties presented may be applicable to other forms of beryllium.

1.2.1 Cross-Rolled Sheet Preparation

SR-200 cross-rolled sheet is manufactured from high purity SR grade powder. Initially, the fabrication consists of hot pressing (simultaneous application of heat and pressure) high purity beryllium powder contained in a suitable die into vacuum hot-pressed block. Subsequently, the block is hot worked at temperatures ranging from 200 to 590° C (400 to 1,100° F) by rolling at reductions of 3:1 to 13:1. The SR-200 sheet is formed by rolling at 90° angles (Brush Wellman 1986; Cooke et al. 1971).

In what follows, references to beryllium are equivalent to references of cross-rolled beryllium sheet unless otherwise stated.

1.2.2 Atomic Structure

The microstructure of beryllium is hexagonal close-packed (HCP) (Asceland 1989). Mechanical properties, as with most such lattice metals, are anisotropic. Two independent bonding systems predominate in beryllium structures: a metallic bond that connects atoms within a basal plane and a metallic-covalent bonding system that acts normal to the basal plane. The two bonding mechanisms act independently from each other. An indication of this is the fact that Poisson's ratios are close to zero for certain directions. The former of the two bonding systems accounts for ductile behavior of the material when stress is applied parallel to the basal plane while the latter system accounts for the brittle nature of beryllium when stress is applied normal to the basal plane (Pollock 1977).

1.2.3 Density

The density of beryllium is 1.85 g/cm³ (0.067 lb/in.³) (Asceland 1989), which makes it the least dense structural metal. An exception is magnesium that has a density of 1.76 g/cm³ (0.064 lb/in.³). A comparison of densities for a number of structural metals is provided in the histogram of Fig. 3.

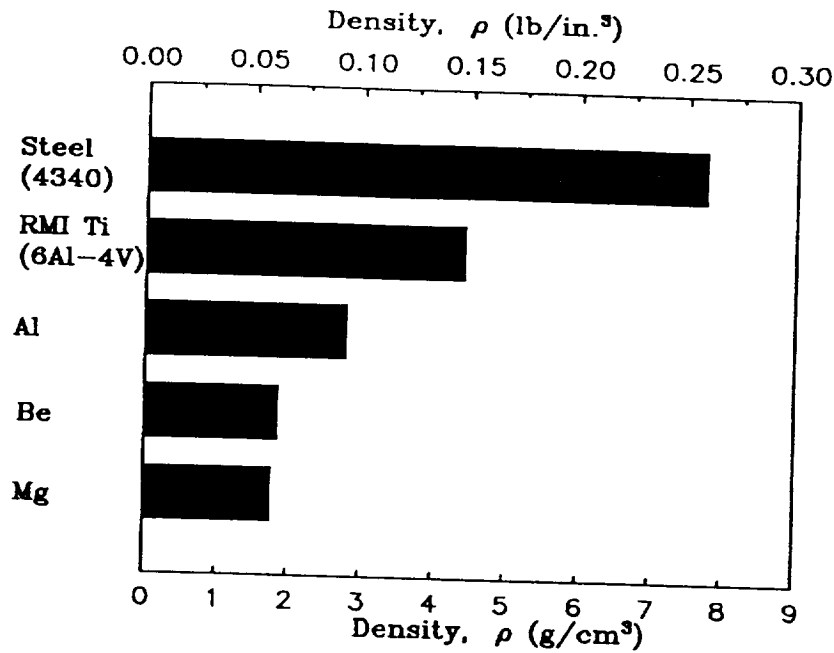


FIG. 3. Density Histogram for Selected Metals

1.2.4 Elastic Moduli

A measure of stiffness is given by Young's modulus and elastic moduli for isotropic and anisotropic material, respectively. Cross-rolled beryllium sheets possess orthotropic material properties. The in-plane moduli of elasticity, E_x and E_y , for SR-200 cross-rolled beryllium sheets have magnitudes of approximately 297 GPa (43×10^3 ksi) and 303 GPa (44×10^3 ksi), respectively. The out-of-plane elastic modulus E_z and, thus, the out-of-plane stiffness, is even higher at 345 GPa (50×10^3 ksi), which makes the material desirable for applications where out-of-plane deformations need to be minimized (Marder 1986). This is important since a high stiffness in the direction normal to the plane of the sheet coupled with low Poisson's ratios implies relatively small out-of-plane deformation and, thus, high dimensional stability. Specific stiffness or the modulus-to-density ratio provides another measure of the commendable properties of beryllium (Fenn et al. 1967). For simple geometric configurations, the deflection of a structure is inversely proportional to the specific modulus of a load free structure deflecting under its own weight. For specialized engineering applications, such as optical supports, it is necessary to minimize distortions. This is obtained by using a high specific modulus material, such as beryllium, in order to increase dimensional stability of the overall structure.

Fig. 4 compares in-plane Young's moduli for selected structural materials. Beryllium's in-plane stiffness is one and one-half times greater than that of steel and several times higher than that of other, so-called, lightweight materials, such as aluminum, titanium, and graphite/epoxy composites.

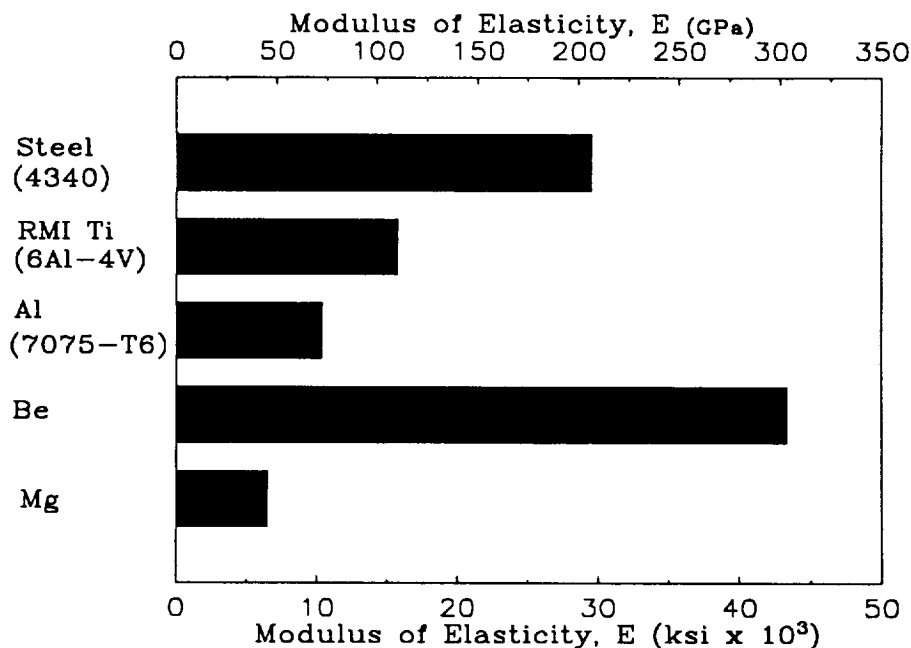


FIG. 4. Histogram of Young's Modulus for Various Metals

1.3 THERMAL PROPERTIES

1.3.1 Specific Heat

Beryllium has an average specific heat of 18.3 kJ/(kg K) (0.46 BTU/lb-°F), the highest among common structural materials (Brush Wellman 1986). The highest specific heat value occurs at its melting point of 1,285°C (2,345°F) (Marder 1986). This is very important due to the fact that the low density and high heat capacity combine to make beryllium a lightweight, high efficiency, heat pool. At the same time, the high melting point of beryllium allows the structure to withstand melting. Striking applications of these characteristics of beryllium are found in high performance aircraft and the space shuttle brake system.

1.3.2 Coefficient of Thermal Expansion

A wider view of the thermal properties of beryllium may be obtained by examining the coefficient of thermal expansion. The value at room temperature is $11.5 \times 10^{-6}/^{\circ}\text{C}$ ($6.4 \times 10^{-6}/^{\circ}\text{F}$), the lowest for any structural metal (Marder 1986). Thus, beryllium has a

combination of high specific heat, which makes it difficult to raise the temperature, and a low coefficient of expansion, so that even when the temperature is elevated, less elongation takes place than for other metals. This combination gives dimensional stability to structures, especially in applications where energy may be absorbed or radiated, as in satellite structural members that go in and out of solar shadows during orbit. As an example, the stiffeners of the solar array on RCA Spacenet satellites were constructed of brazed beryllium. Primary considerations in the design were light weight, accuracy of pointing, and dimensional stability during changes in solar shadowing (Marder 1986).

It should be mentioned that the coefficient of thermal expansion varies with beryllium oxide (BeO) content and, consequently, from grade-to-grade of beryllium. However, increasing BeO content reduces the coefficient of thermal expansion and, therefore, increases stability.

1.3.3 Thermal Conductivity

The thermal conductivity of beryllium, 165 W/(m K) (104 BTU/lb-ft²-°F), is relatively high compared to that of steel, 43 W/(m K) (27 BTU/lb-ft²-°F), and is somewhat less than that of aluminum, 203 W/(m K) (128 BTU/lb-ft²-°F) (Marder 1986). This property allows heat to be conducted readily and, thus, temperature differences between various locations in a structure are ameliorated. Again, as heat is conducted away from higher temperature regions, thermal gradients are reduced, and dimensional stability of the structure is improved.

1.4 TRANSPARENCY TO ELECTROMAGNETIC RADIATION

Not only does beryllium conduct heat well, but it also does not hinder passage of electromagnetic radiation. For example, beryllium is used in x-ray tubes as a window through which x-rays readily pass. A mechanical vacuum seal is maintained between the x-ray tube and the environment. In general, beryllium absorbs very little x-ray, gamma, electron, or other electromagnetic radiation. The transmitted x-ray intensity, I , is described by the equation

$$I = I_o e^{\frac{-m}{\rho} \chi \rho} \dots \dots \dots (1)$$

where, I_o is the intensity of the incoming beam in percent, $-m/\rho$ is the mass absorption coefficient (cm²/g), ρ is the density (g/cm³), χ is the thickness of the material (cm).

The quantity m/ρ is known as the mass absorption coefficient that not only depends on the absorbing material, but also upon the x-ray wavelength. The advantage of using

beryllium is that 95% of the original intensity is transmitted, as compared to $3.3 \times 10^{-8}\%$ and $4.4 \times 10^{-8}\%$ for aluminum and titanium, respectively.

Beryllium is also an excellent reflector of infra-red (I.R.) radiation. It is 96% reflective at 10.6 μ m, and can be an effective optical component in I.R. systems (Grant 1983). Often, advantageous physical properties are useful only when accompanied by sufficient mechanical strength; i.e., beryllium would not be used as an x-ray window if it were not strong enough to withstand the stress imposed by having a vacuum on one side and air pressure on the other.

To summarize, Table 1 lists some of the important physical properties of beryllium.

TABLE 1. Physical Properties of Beryllium

Property (1)	Value (2)
Atomic number	4
Atomic weight	9.02
Specific gravity	1.85 g/cm ³
Melting point	1,285 °C
Specific heat	1.83 J/ °K
Thermal conductivity	165 W/(m K)
Coefficient of thermal expansion	$11.5 \times 10^{-6}/\text{°C}$
Reflectivity	
Optical	50%
Ultraviolet	55%
Infrared	98%
Sonic velocity	12.6×10^3 m/s

1.5 MECHANICAL PROPERTIES

Mechanical properties of beryllium vary considerably from grade-to-grade (Grant 1983). References to beryllium in the following chapters only consider properties of SR-200 cross-rolled beryllium sheet due to its widespread use in space applications. Table 2 summarizes elastic properties for SR-200 sheet that has a thickness of 1.96-mm (0.077-in.). Testing used to obtain most of these parameters was conducted by Lockheed Missiles and Space Company (Fenn et al. 1967). A number of these values have been recently verified for 2.54-mm (0.10-in.) thick cross-rolled beryllium sheet as reported in later chapters of this report and elsewhere (Roschke and Papados 1989; Henkener et al. 1991). Identical in-plane uniaxial mechanical properties for the 1.96-mm (0.077-in.) and the 2.54-mm (0.10-in.)

thick SR-200 sheet are observed. Table 3 lists yield and ultimate failure strengths (Fenn et al. 1967).

TABLE 2. Elastic Properties of 1.96-mm (0.08-in.) SR-200 Sheet (Fenn et al. 1967)

Direction of Loading (1)	Elastic Modulus (GPa) (2)	Poisson's Ratio (3)
Longitudinal	298.7	$\nu_{12} = 0.0768$ $\nu_{13} = 0.0137$
Long transverse	293.6	$\nu_{21} = 0.0752$ $\nu_{23} = 0.0190$
Short transverse (Through-thickness)	347.5	$\nu_{31} = 0.0162$ $\nu_{32} = 0.0230$

TABLE 3. Uniaxial Strength Properties of 1.96-mm (0.08-in.) SR-200 Sheet (Fenn et al. 1967)

Direction of Loading (1)	Yield Stress (MPa) (2)	Ultimate Stress (MPa) (3)
Longitudinal Tension Compression	383.4 379.2	537.6 659.1
Long transverse Tension Compression	386.1 382.7	564.0 591.5
Short transverse Tension		200.0

1.6 DISADVANTAGES IN USING BERYLLIUM

Despite numerous advantages that beryllium provides as a structural material, a number of disadvantages need to be kept in mind. One of the primary drawbacks of beryllium sheet material is that it exhibits brittle behavior when loaded to failure under complex states of stress. For example, in regions of stress concentration beryllium fractures with little or no evidence of plastic deformation, i.e., the material is not capable of redistributing localized stresses by gross deformation before cracking occurs. In addition,

beryllium lacks toughness when exposed to high strain rates due to its inability to absorb energy by plastic deformation prior to fracture (Kojola 1967).

Another disadvantage in using beryllium is the fact that it can not be mechanically machined without special precautions. This is due to toxicity of the metal; i.e., it has been shown by experiments on laboratory animals that inhaling beryllium dust can cause chronic diseases. In addition, machining can cause microscopic surface flaws that radically affect the strength of the material (Henkener et al. 1991). Depending on the stress state, the reduction in strength can be dramatic in the sense that the ultimate strength becomes equal to the yield strength.

Finally, the cost of beryllium cross-rolled sheets is considerably higher than that of other structural metals. Important economic factors in the manufacturing process include mining, purification of beryllium powder, forming hot press blocks, cross-rolling into beryllium sheets, and costly chemical etching and cutting into desired geometrical shapes. Nevertheless, use of beryllium sheet material is often competitive in space applications when all economic factors are taken into account.

2. HISTORICAL BACKGROUND

2.1 OBJECTIVES

Contemporary applications of failure criteria frequently incorporate two-dimensional or simplified three-dimensional methodology for prediction of failure stresses and/or strains. Motivation behind the development of a new multi-dimensional failure criterion is due mainly to the lack of a sufficiently accurate mathematical tool that accounts for the behavior of brittle material with anisotropic properties. Such a criterion should be able to provide a reliable maximum load estimate so that design of the structure is not penalized in terms of excessive weight requirements. The failure criterion developed in the following chapters is represented by a fracture surface in a six-dimensional stress space.

The term "brittleness" is taken here to refer to material failure which is preceded with either negligible or, preferably, no inelastic deformation. Moreover, development of at least one separation surface within the body is required. By definition, first-order criteria involve only first-order terms, quadratic criteria consider combinations of first and second-order terms, and higher-order criteria include cubic-order terms. Incorporation of cubic terms usually yields a non-convex, non-closed, mathematically complex surface.

2.2 ATTRIBUTES OF A FAILURE CRITERION

In general, criteria for failure prediction of a brittle anisotropic material are required to satisfy the following (Roschke and Papados 1989; Gol'denblat and Kopnov 1965; Hill 1950):

- (a) Stability conditions and a smooth, continuous, convex, non-singular surface are required to satisfy uniqueness.
- (b) The criterion should be invariant with respect to coordinate axis transformations.
- (c) The failure surface resulting from the criterion should be a potential function, a function that is independent of the loading path.
- (d) Strength interaction coefficients should be used that depend on mechanical properties of the material at different ultimate strengths.
- (e) Applicability of the criterion for multiaxial and complex states of stress is necessary.
- (f) Only a finite number of tests can be required to evaluate strength coefficients.
- (g) Each complex state of stress should be described by a combination of strength parameters, not only by one component of the strength tensor.

A large number of theories have been proposed that deal with failure prediction. None fully satisfies these conditions. Several of the most important and influential failure theories are presented in the following sections.

It is considered expedient, at this point, to differentiate between failure and yield. Early criteria, such as that of Rankine and Coulomb (Karr and Das 1983) predicted the stress levels at which yielding begins. At that time most structures were designed to perform up to the onset of yield. In this case, any stress outside the loci of points defining the yield surface was considered failure. More recent investigators define a two-dimensional isotropic yield surface and via a flow rule, subsequently, attempt to reach the ultimate strength limit surface (von Mises 1913) which they define as the failure surface. Due to the confusion introduced by conflicting use of the terms yield and failure, failure is defined here as the inability of a structure to perform at its intended design whether that is its yield or ultimate failure limit state. Hill (1951) proposed an orthotropic yield criterion in conjunction with a set of flow rules to define the in-plane ultimate failure surface. This was an effort to predict ultimate failure of ductile material. These approaches, although adequate for ductile material, fail to describe failure surfaces for non-isotropic brittle material since no flow rule can be associated with a material that does not exhibit inelastic or plastic deformation. Gol'denblat and Kopnov (1965) first introduced the idea of a strength failure criterion based directly on ultimate stress. Their work forms the basis of most modern failure criteria for brittle material.

A brief account of the major yield and ultimate failure criteria is provided in chronological order in the following sections.

2.3 ISOTROPIC YIELDING

For isotropic material the phenomenon of yielding is independent of the orientation of the material with respect to the applied stresses. In this case any criterion may be expressed in the form,

$$f_y(J_1, J_2, J_3) = 0 \dots\dots\dots (2)$$

where J_1 , J_2 , and J_3 are the invariants of the stress tensor σ_{ij} (Karr and Das 1983). The invariants are defined in terms of principal components of stress σ_1 , σ_2 , and σ_3 as follows:

$$J_1 = \sigma_1 + \sigma_2 + \sigma_3 \dots\dots\dots (3)$$

$$J_2 = -(\sigma_1\sigma_2 + \sigma_1\sigma_3 + \sigma_2\sigma_3) \dots\dots\dots (4)$$

$$J_3 = \sigma_1\sigma_2\sigma_3 \dots\dots\dots (5)$$

2.4 TRESCA'S CRITERION

Tresca proposed the first yield criterion in 1864 (Hill 1948). Influenced by the general failure theory proposed for soils by Coulomb, Tresca suggested that yielding occurs when the maximum shear stress reaches a certain threshold. This criterion can be expressed in the form:

$$\sigma_1 - \sigma_3 = C \dots\dots\dots (6)$$

where $\sigma_1 \geq \sigma_2 \geq \sigma_3$ are principal components of stress and C is a constant. This corresponds to a hexagonal yield locus on the octahedral plane. Tresca's attempts to analyze the distribution of stress in the plastic region are far from accurate and often crude (Karr and Das 1983).

2.5 VON MISES' CRITERION

It is commonly accepted that the yield strength of metals is unaffected by application of hydrostatic pressure that is applied either alone or in combination with the stress situations. von Mises (1913) used this concept to simplify the yield function. Using the deviatoric stress tensor, σ'_{ij} , instead of σ_{ij} , the yield surface function, f_y , becomes:

$$f_y(J'_2, J'_3) = 0 \dots\dots\dots (7)$$

where,

$$J'_2 = -(\sigma'_1 \sigma'_2 + \sigma'_1 \sigma'_3 + \sigma'_2 \sigma'_3) = \frac{1}{2}(\sigma'_{ij} \sigma'_{ij}) \dots\dots\dots (8)$$

$$J'_3 = \sigma'_1 \sigma'_2 \sigma'_3 = \frac{1}{3}(\sigma'_{ij} \sigma'_{jk} \sigma'_{ki}) \dots\dots\dots (9)$$

The deviatoric components are given by:

$$\sigma'_{ij} = \sigma_{ij} - \sigma \delta_{ij} \dots\dots\dots (10)$$

where

$$\sigma = \sigma_{ii} / 3 = J_1 / 3 \dots\dots\dots (11)$$

for $i, j, k = 1, 2, 3$ and customary indicial notation (Sokolnikoff 1964). Moreover, exploiting the assumption that ideal isotropic/plastic bodies do not exhibit the Bauschinger phenomenon, i.e., the magnitude of yield stress is the same in tension and compression, and since J'_3 changes sign with stress reversals, it follows that f_y must be an even function of this invariant.

In 1913 von Mises also presented a criterion, known as the J_2 -theory, that suggests that yielding occurs when J'_2 reaches a critical value (Karr and Das 1983). This approach

completely neglects the influence of the J'_3 invariant. The criterion produces a circular yield locus on the octahedral plane. Its governing equations are:

$$2J'_2 = \sigma'_{ij} \sigma'_{ij} = \sigma'^2_1 + \sigma'^2_2 + \sigma'^2_3 = 2\kappa^2 \dots\dots\dots (12)$$

or

$$(\sigma'_1 - \sigma'_2)^2 + (\sigma'_2 - \sigma'_3)^2 + (\sigma'_3 - \sigma'_1)^2 = 6\kappa^2 \dots\dots\dots (13)$$

or

$$(\sigma'_x - \sigma'_y)^2 + (\sigma'_y - \sigma'_z)^2 + (\sigma'_z - \sigma'_x)^2 + 6(\tau'^2_{xy} + \tau'^2_{xz} + \tau'^2_{yz}) = 6\kappa^2 \dots\dots\dots (14)$$

where κ is a constant parameter that depends on the pre-strain state of the material. The octahedral shear stress at yield is assumed to have a value of:

$$\sigma_i^o = \frac{\sqrt{2}}{3} \kappa \quad (i = 1, 2, 3) \dots\dots\dots (15)$$

By letting $\sigma_1^o = -\sigma_2^o$ and $\sigma_3^o = 0$, κ can be correlated to the maximum shear at yield. The uniaxial tensile yield stress, Y , is obtained by substitution of $\sigma_1^o = Y$ and $\sigma_2^o = 0$ into Eq. 14. This yields:

$$Y = \sqrt{2} \kappa \dots\dots\dots (16)$$

Hencky provides a physical interpretation of this criterion (Hill 1950). Eqs. 12-14 imply that yielding is initiated only when the elastic distortional energy acquires a critical value. On the other hand, Huber suggests that there are two distinct cases depending upon whether hydrostatic pressure is in tension or compression (Hill 1950). In the former case, yielding is a function of the total distortional energy while in the latter case yielding becomes a function of the elastic distortional energy. Nevertheless, von Mises' criterion provides a reasonably good correlation between experimental and theoretical results for a number of ductile metals such as copper, aluminum, iron, and mild to medium carbon steels (Hill 1950).

2.6 HILL'S CRITERION

von Mises' criterion is generalized by Hill in one of the first attempts to account for tensile and compressive strength variations (Hill 1950). For orthotropic polycrystalline metals Hill proposes the following quadratic equation for yield prediction:

$$F(\sigma_x - \sigma_y)^2 + G(\sigma_x - \sigma_z)^2 + H(\sigma_y - \sigma_z)^2 + 2L\sigma_x^2 + 2M\sigma_y^2 + 2N\sigma_z^2 = 1 \dots\dots\dots (17)$$

where F , G , H , L , M , and N are material constants. The criterion reduces to von Mises' theory provided that any anisotropy is insignificant. Coefficients F , G , H , L , M , and N are

parameters that are characteristic of the material anisotropy. In view of assumed symmetry conditions, only quadratic shear terms are included. In addition, the Bauschinger effect is not taken into account since linear terms are excluded from the criterion. Assuming that hydrostatic pressure, or its superposition, does not influence failure, Hill only uses the difference of the normal components of stress.

Letting X , Y , and Z be the principal tensile yield stresses that correspond to the three mutually perpendicular principal axes of anisotropy, and R , S , and T be the yield shearing stresses with respect to the same three axes, it can be shown that the coefficients F , G , H , L , M , and N should satisfy the following set of equations (Hill 1950):

$$\begin{aligned} \frac{1}{X^2} &= G + H, & 2F &= \frac{1}{Y^2} + \frac{1}{Z^2} - \frac{1}{X^2} \\ \frac{1}{Y^2} &= H + F, & 2G &= \frac{1}{Z^2} + \frac{1}{X^2} - \frac{1}{Y^2} \\ \frac{1}{Z^2} &= F + G, & 2H &= \frac{1}{X^2} + \frac{1}{Y^2} - \frac{1}{Z^2} \\ 2L &= \frac{1}{R^2}, & 2M &= \frac{1}{S^2}, & 2N &= \frac{1}{T^2} \end{aligned} \quad (18)$$

In the event that rotational symmetry is observed about the z -axis, viz. the material is in-plane isotropic and generally quasi-orthotropic, then Eq. 18 becomes:

$$\begin{aligned} &[(G + H)\sigma_x^2 - 2H\sigma_x\sigma_z + (F + H)\sigma_y^2 + 2N\tau_{xy}^2] - 2(G\sigma_x + F\sigma_y)\sigma_z \\ &+ 2(L\tau_{yz}^2 + M\tau_{zx}^2) + 2(F + G)\sigma_x^2 = 1 \end{aligned} \quad (19)$$

The necessary and sufficient conditions for the material to be rotationally symmetric with respect to the out-of-plane axis of rotation are:

$$\begin{aligned} N &= G + 2H = F + 2H \\ L &= M \end{aligned} \quad (20)$$

In the case of global symmetry and complete isotropy, the coefficients are related as follows:

$$L = M = N = 3F = 3G = 3H \quad (21)$$

and Eq. 19 is equivalent to the von Mises' criterion when F is equal to $1/Y^2$.

It is apparent that for the implementation of Hill's criterion the values of the yield stresses X , Y , Z , R , S , and T are required. In other words, six independent experiments are necessary for determining the constant coefficients.

For orthotropic material, such as cross-rolled beryllium sheets, Hill's criterion can be further specialized. Considering only in-plane stresses Eq. 19 becomes:

$$(G+H)\sigma_x^2 - 2H\sigma_x\sigma_y + (F+H)\sigma_y^2 + 2N\tau_{xy}^2 = 1 \dots\dots\dots (22)$$

In the event that the material is cut at an angle α , with respect to the principal rolling direction (Fig. 5), the transformed stress components for a tensile specimen are

$$\begin{aligned} \sigma_x &= \sigma \cos^2(\alpha) \\ \sigma_y &= \sigma \sin^2(\alpha) \\ \tau_{xy} &= \sigma \sin(\alpha)\cos(\alpha) \end{aligned} \dots\dots\dots (23)$$

where σ is the tensile yield stress. In this case Eq. 19 becomes:

$$\sigma = \frac{1}{\sqrt{[F \sin^2(\alpha) + G \cos^2(\alpha) + H + (2N - F - G - 4H) \sin^2(\alpha)\cos^2(\alpha)]}} \dots\dots\dots (24)$$

From Eq. 24 it can be shown that maxima and minima of σ can occur along the orthotropic axes as well as in directions α_{MAX} that are given by

$$\tan^2(\alpha_{MAX}) = \frac{N - G - 2H}{N - F - 2H} \dots\dots\dots (25)$$

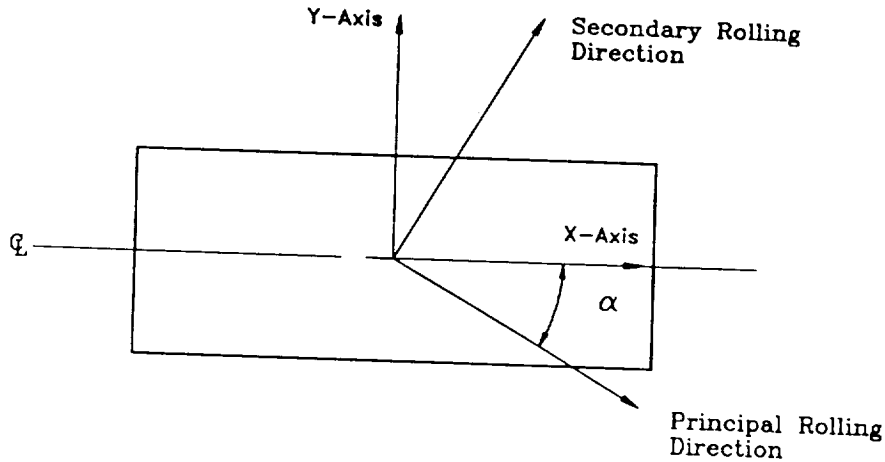


FIG. 5. Rotation of Material Axes with Respect to Center-Line of the Specimen

The yield stress, σ , acquires maximum values in the x and y directions if $N > F + 2H$ and $N > F + 2H$ and minima in the α_{MAX} directions. If $N < F + 2H$ and $N < F + 2H$ then σ attains maxima in the α_{MAX} directions and minima along the x and y axes.

Hill's criterion is the first serious attempt to predict yield surfaces for non-isotropic materials. It is very effective in predicting the behavior of ductile material, both isotropic and orthotropic, although the original intention was to describe yielding of anisotropic

material. Because of the oversimplified assumptions and the omission of certain phenomena, such as the Bauschinger effect, the criterion becomes unreliable for prediction of yielding and, subsequently, failure of brittle material.

2.7 GOL'DENBLAT AND KOPNOV'S CRITERION

A generalized tensorial form of available failure criteria is given by Eq. 26 (Gol'denblat and Kopnov 1965):

$$f(\sigma_k) = (F_i \sigma_i)^\alpha + (F_{ij} \sigma_i \sigma_j)^\beta + (F_{ijk} \sigma_i \sigma_j \sigma_k)^\gamma + \dots = 1 \dots \dots \dots (26)$$

where, $\sigma_1 = \sigma_{11}$, $\sigma_2 = \sigma_{22}$, $\sigma_3 = \sigma_{33}$, $\sigma_4 = \sigma_{13}$, $\sigma_5 = \sigma_{23}$, $\sigma_6 = \sigma_{12}$, and $i, j, k = 1, \dots, 6$; F_i , F_{ij} , and F_{ijk} are contracted equivalents of the second-, fourth-, and sixth-order strength tensors, respectively; and α , β , and γ represent real numbers.

This is the first failure criterion proposed as opposed to yield criteria presented in the earlier sections. It forms the basis for criteria that are subsequently developed.

Gol'denblat and Kopnov's failure criterion was applied to prediction of failure for glass-reinforced plastics. The original generalized criterion of Eq. 26 is simplified for application to these plastics to include only linear and quadratic terms of the stress tensor components, and is applied to in-plane stress situations. For $\alpha = 1$ and $\beta = 0.5$ it becomes

$$f(\sigma_k) = F_i \sigma_i + (F_{ij} \sigma_i \sigma_j)^{0.5} = 1 \dots \dots \dots (27)$$

The power term of Eq. 27 leads to complicated mathematics that do not contribute to the generality of the criterion (Tsai and Wu 1971).

2.8 HOFFMAN'S CRITERION

An orthotropic fracture criterion that uses six stress components, and follows the pattern of yield conditions proposed by von Mises and Hill is proposed by Hoffman (1967). The criterion, which includes terms that are odd functions of the material strengths, is described by the following equation:

$$C_1(\sigma_x - \sigma_z)^2 + C_2(\sigma_z - \sigma_x)^2 + C_3(\sigma_x - \sigma_y)^2 + C_4\sigma_x + C_5\sigma_y + C_6\sigma_z + C_7\tau_{yz}^2 + C_8\tau_{xz}^2 + C_9\tau_{xy}^2 = 1 \dots \dots \dots (28)$$

where C_1 through C_9 are independent coefficients that are determined from nine independent, uniaxial and pure shear experiments.

Letting F_{tx} , F_{ty} , F_{tz} , and F_{cx} , F_{cy} , F_{cz} be the three orthonormal, uniaxial, tensile and compressive strengths, respectively, and F_{syx} , F_{syz} , F_{sxy} the pure shear strengths, then the coefficients of Eq. 28 are given by

$$\begin{aligned}
2C_1 &= \left[(F_y F_{cy})^{-1} + (F_x F_{cx})^{-1} - (F_x F_{cy})^{-1} \right] \\
2C_2 &= \left[(F_x F_{cx})^{-1} + (F_y F_{cy})^{-1} - (F_x F_{cy})^{-1} \right] \\
2C_3 &= \left[(F_x F_{cx})^{-1} + (F_y F_{cy})^{-1} - (F_x F_{cy})^{-1} \right] \\
C_4 &= (F_x)^{-1} - (F_{cx})^{-1} \\
C_5 &= (F_y)^{-1} - (F_{cy})^{-1} \dots \dots \dots (29) \\
C_6 &= (F_x)^{-1} - (F_{cx})^{-1} \\
C_7 &= (F_{yz})^{-2} \\
C_8 &= (F_{sx})^{-2} \\
C_9 &= (F_{sy})^{-2}
\end{aligned}$$

If it is assumed that ultimate strength and fracture are one and the same for brittle material, i.e., the terms "fracture" and "failure" are equivalent, for the case of plane stress, i.e. $\sigma_z = \tau_{yz} = \tau_{xz} = 0$ and Eq. 28 becomes

$$\frac{\sigma_x^2 - \sigma_x \sigma_y}{F_x F_{cx}} + \frac{\sigma_y^2}{F_y F_{cy}} + \frac{F_{cx} - F_x}{F_x F_{cx}} \sigma_x + \frac{F_{cy} - F_y}{F_y F_{cy}} \sigma_y + \frac{\tau_{xy}^2}{F_{sy}^2} = 1 \dots \dots \dots (30)$$

In three-dimensional stress space (σ_x , σ_y , and τ_{xy}) Eq. 30 is represented by an ellipsoidal surface that is symmetric about the x - y plane and has its center at

$$\begin{aligned}
X_c &= \frac{(F_x - F_{cx})}{2} + \frac{(F_y - F_{cy})}{4} \\
Y_c &= \frac{(F_x - F_{cx})}{2} + \frac{(F_x - F_{cx})(F_y F_{cy})}{4 F_x F_{cx}} \dots \dots \dots (31) \\
Z_c &= 0
\end{aligned}$$

Incorporation of linear terms in Hoffman's criterion provides a first formulation for failure prediction of brittle anisotropic material that takes into account differing tensile and compressive strengths. Moreover, first-order tension and compression terms partly account for the Bauschinger phenomenon. Hoffman's criterion contains symmetry and is consistent with other well-established isotropic and anisotropic failure conditions. It provides a smooth and adoptable formula for interpolating between basic strength data. However, only normal interaction coefficients, such as $2C_1$ which relates σ_x and σ_y , are used. Interaction coefficients relating normal and shear strength are omitted. Thus, the limited

interaction terms included in this criterion do not provide the generality required for reliable failure prediction of brittle material.

2.9 TSAI-WU CRITERION

A more general approach is presented by Tsai and Wu (1971, 1974), who propose the following tensor formulation for the failure surface:

$$f(\sigma_k) = F_i \sigma_i + F_{ij} \sigma_i \sigma_j = 1 \dots\dots\dots (32)$$

The difference between positive and negative stress-induced failures is described by the linear terms. Quadratic terms of the criterion describe an ellipsoid in the stress space. The investigators claim that if higher-order terms, such as sixth-order strength tensors, were to be included not only does the mathematics become complicated but also the resultant failure surface can be open ended and thereby predict infinite strengths. Therefore, cubic terms are omitted from this criterion. The main assumptions incorporated in the Tsai-Wu criterion are as follows:

(a) The criterion is itself a scalar equation and, thus, automatically invariant. Contrary to Tresca's, von Mises', and Hill's criteria that require interactions among stress components to be fixed and dependent on material properties, the Tsai-Wu criterion considers these interactions to be independent of material properties.

(b) All stress components are expressed in tensorial notation and, therefore, their transformations and associated invariants are well established. The criterion is invariant for all coordinate systems (i.e. Cartesian, spherical, and cylindrical).

(c) The criterion exploits symmetry properties of the strength tensor. General anisotropy and three dimensional space present no mathematical difficulty.

(d) Off-axes transformation properties are well established. Therefore, behavior of material under application of off-axes stresses can be obtained with relative ease.

(e) Stability conditions are incorporated in such a way as to ensure that the shape of the failure surface is ellipsoidal and, at the same time, the surface is precluded from being open-ended under conditions of hydrostatic pressure. Thus, a positive definite requirement is imposed on both the contracted second- and fourth-order strength tensors, F_i and F_{ij} , respectively. Conditions of constraint are as follows:

$$F_{ii}F_{jj} - F_{ij}^2 \geq 0 \dots\dots\dots (33)$$

$$F_i F_j - F_k^2 \geq 0 \text{ for } i, j = 1, 2, 3 \text{ and } k = 4, 5, 6 \dots\dots\dots (34)$$

For a truly anisotropic material, the Tsai-Wu criterion requires determination of twenty-seven independent coefficients: six for the F_i tensor and twenty-one for the F_{ij}

tensor. For orthotropic material, symmetry reduces the number of coefficients to twelve: three for F_i and nine for F_{ij} . These coefficients are shown in matrix form in Appendix I.

The principal strength tensor coefficients (F_i and F_{ii}) can be readily calculated from experimentally determined values of the uniaxial tensile and compressive failure strengths ($X, Y, Z, X', Y',$ and Z') in the three orthonormal coordinate axes. These axes are chosen to coincide with the axes of orthotropy. Also, results of tests for the three (positive or negative) shear failure stresses (S, R, T), provided that the absolute value of shear strengths is identical, are necessary. If the latter assumption is not valid then six shear strength values are required ($S, R, T, S', R',$ and T'). Eq. 35 shows the relations among strength and tensorial coefficients.

$$\begin{aligned}
 F_1 &= \frac{1}{X} - \frac{1}{X'}, & F_2 &= \frac{1}{Y} - \frac{1}{Y'}, & F_3 &= \frac{1}{Z} - \frac{1}{Z'}, \\
 F_4 &= 0, & F_5 &= 0, & F_6 &= 0 \\
 F_{11} &= \frac{1}{XX'}, & F_{22} &= \frac{1}{YY'}, & F_{33} &= \frac{1}{ZZ'}, & \dots\dots\dots (35) \\
 F_{44} &= \frac{1}{SS'}, & F_{55} &= \frac{1}{RR'}, & F_{66} &= \frac{1}{TT'}
 \end{aligned}$$

The interaction strength coefficients, F_{12} , F_{13} , and F_{23} , can be derived from a variety of biaxial, or combined biaxial and shear experiments. For example, the following stress combinations can be used to estimate interaction coefficient F_{12} (Tsai and Wu 1971; Wu and Scheublein 1974):

$$\begin{aligned}
 \text{For } \sigma_1 = \sigma_2 = P & & F_{12} &= \frac{[1 - P(F_1 + F_2) - P^2(F_{11} + F_{22})]}{2P^2} \\
 \text{For } \sigma_1 = -\sigma_2 = Q & & F_{12} &= -\frac{[1 - Q(F_1 - F_2) - Q^2(F_{11} + F_{22})]}{2Q^2} \\
 \text{For } \sigma_1 = -\sigma_2 = -Q' & & F_{12} &= -\frac{[1 + Q(F_1 - F_2) - Q'^2(F_{11} + F_{22})]}{2Q'^2} & \dots\dots\dots (36) \\
 \text{For } \sigma_1 = \sigma_2 = \sigma_6 = 0.5U & & F_{12} &= \frac{[4 - 2U(F_1 + F_2) - U^2(F_{11} + F_{22} + F_{66})]}{2U^2} \\
 \text{For } \sigma_1 = \sigma_2 = \sigma_6 = -0.5U' & & F_{12} &= \frac{[4 + 2U(F_1 + F_2) - U'^2(F_{11} + F_{22} + F_{66})]}{2U'^2}
 \end{aligned}$$

where P , Q , and $-Q'$ are normal biaxial strengths, and U , and $-U'$ are normal-shear biaxial strengths. Similar equations can be obtained for normal interaction coefficients related to the (1-3) and (2-3) planes.

Special care must be taken when determining interaction coefficients. It has been shown that sensitivity of principal coefficients is not affected by experimental scatter, i.e., the magnitude of the ratio of positive to negative strength measurements does not affect the magnitude of the tensor coefficient (Wu and Scheublein 1974). However, this is not valid for the case of scatter in the experimental results for estimating interaction coefficients F_{ij} for $i \neq j$. An optimal ratio of σ_1/σ_2 is required for this estimation. This ratio depends primarily on the sign of the interaction coefficient, the magnitude of the biaxial strength, and the magnitude of the interaction coefficient itself (Wu and Scheublein 1974, Wu 1974).

The main advantage of the Tsai-Wu criterion compared to earlier failure theories is that it accounts for multi-dimensional stress space as well as different material symmetries. Only first and second-order contracted strength tensors are incorporated in order to achieve mathematical simplicity and to maintain a determinate number of linear equations that provide strength coefficients. After taking symmetry conditions of the strength tensors into consideration, twenty-seven coefficients describe the behavior of anisotropic materials. This approach avoids incorporation of higher-order tensors that lead to mathematical complexity in evaluating strength interaction coefficients, and indeterminacy of the linear system of equations that arises from such an inclusion.

Although widely used, the Tsai-Wu envelope, which yields an ellipsoid, does not give accurate correlations with experimental data for tension-tension and compression-compression quadrants of the failure surface (Priddy 1974; Jiang and Tennyson 1989). Furthermore, a shortcoming of this criterion is the fact that tension-tension and compression-compression interactions may not be treated independently (Jiang and Tennyson 1989). Application of this criterion to cross-rolled beryllium sheet has been established for failure prediction of in-plane stresses (Mascorro et al. 1991).

2.10 PRIDDY'S CRITERION

In an attempt to obtain more generality, Priddy (1974) includes products of stress components of order greater than two in a failure criterion. For a generalized, accurate, and complete criterion, products of stresses of order greater than two are considered in a failure prediction equation for brittle, orthotropic material. These terms induce noncircular octahedral shear envelopes that tend to agree with experimental findings. The general expression describing the criterion is given by the equation:

$$f(\sigma_k) = F_i \sigma_i + F_{ij} \sigma_i \sigma_j + F_{ijk} \sigma_i \sigma_j \sigma_k = 1 \dots\dots\dots (37)$$

Due to complexity of the contracted sixth-order tensor only a limited number of mathematically independent cubic terms are used. An allotropic representation of Eq. 38 leads to the following special form:

$$W = I + I' + I' \times II + f \times III \dots\dots\dots (38)$$

where,

$$\begin{aligned} W &= \{\sigma\}^T [A] \{\sigma\} = \sum \sum (\sigma_i \sigma_j \sigma_k) \quad \text{for } i, j = 1, 2, \text{ and } 3 \\ I &= \{d\}^T \{a\} = \sum d_i \sigma_i \quad \text{for } i, j = 1, 2, \text{ and } 3 \\ I &= \{e\}^T \{\sigma\} = \sum e_i \sigma_i \quad \text{for } i, j = 1, 2, \text{ and } 3 \end{aligned} \quad (39)$$

II = second stress invariant; III = third stress invariant; $\{\sigma\}$ = vector form of stress tensor; W has the form of strain energy density; $[A]$ is a matrix similar to the elastic compliance of the material; and d_i , e_i , and f are undetermined scalar coefficients.

For the special case of orthotropic material that has the principal coordinate axes of the material coinciding with the orthotropic axes, Eq. 38 becomes:

$$\begin{aligned} &a_1 \tau_{12}^2 + a_2 \tau_{23}^2 + a_3 \tau_{13}^2 + b_1 \sigma_1^2 + b_2 \sigma_2^2 + b_3 \sigma_3^2 + c_1 \sigma_1 \sigma_2 + c_2 \sigma_2 \sigma_3 + c_3 \sigma_1 \sigma_3 \\ &= I + d_1 \sigma_1 + d_2 \sigma_2 + d_3 \sigma_3 + (e_1 \sigma_1 + e_2 \sigma_2 + e_3 \sigma_3) (\sigma_1 \sigma_2 + \sigma_2 \sigma_3 + \sigma_1 \sigma_3 - \tau_{12}^2 - \tau_{23}^2 - \tau_{13}^2) \dots (40) \\ &+ f (\sigma_1 \sigma_2 \sigma_3 + 2 \tau_{12} \tau_{23} \tau_{13} - \sigma_1 \tau_{23}^2 - \sigma_2 \tau_{13}^2 - \sigma_3 \tau_{12}^2) \end{aligned}$$

in which

$$\begin{aligned} a_i &= \frac{I}{(F_{ij})^2} \\ b_i &= \frac{I}{(F_n F_{ci})} \dots (41) \\ d_i &= \frac{F_{ci} - F_n}{(F_n F_{ci})} \end{aligned}$$

are strength coefficients obtained from uniaxial strength tests, and F_u and F_{ci} are the tensile and compressive strengths, respectively, of the material. $F_{ij} (i \neq j)$ are shear strength parameters.

In order to reduce the number of coefficients required to describe the failure surface, approximations for both biaxial compression and tension as well as triaxial strengths are used. For example, the triaxial tensile strength is considered to be linearly related to the biaxial strength. These coefficients are represented in Eq. 40 by c_i , e_i , and f . Furthermore, the following stability condition is introduced such that the failure surface is forced to be open for the case of hydrostatic pressure:

$$f = -3 \sum (e_i) \dots (42)$$

It should be noted that Eq. 40 leads to a system of inconsistent equations when shear stresses are considered. Correctly, the criterion considers positive and negative shear strengths acting on any given plane to be identical; this yields expressions for the σ_i

coefficients. However, in the event that the following states of stress are imposed on a structure Eq. 40 becomes:

State of stress: $\tau_{12}, \tau_{23}, \tau_{13}$

$$a_1 \tau_{12}^2 + a_2 \tau_{23}^2 + a_3 \tau_{13}^2 = 1 + 2f \tau_{12} \tau_{23} \tau_{13} \dots \dots \dots (43)$$

State of stress: $-\tau_{12}, \tau_{23}, \tau_{13}$

$$a_1 \tau_{12}^2 + a_2 \tau_{23}^2 + a_3 \tau_{13}^2 = 1 - 2f \tau_{12} \tau_{23} \tau_{13} \dots \dots \dots (44)$$

State of stress: $-\tau_{12}, -\tau_{23}, \tau_{13}$

$$a_1 \tau_{12}^2 + a_2 \tau_{23}^2 + a_3 \tau_{13}^2 = 1 + 2f \tau_{12} \tau_{23} \tau_{13} \dots \dots \dots (45)$$

State of stress: $-\tau_{12}, -\tau_{23}, -\tau_{13}$

$$a_1 \tau_{12}^2 + a_2 \tau_{23}^2 + a_3 \tau_{13}^2 = 1 - 2f \tau_{12} \tau_{23} \tau_{13} \dots \dots \dots (46)$$

Sets of Eqs. 44 to 46 are inconsistent unless the value of the coefficient f is set to zero. Moreover, if f is set to zero then the stability condition introduced by Eq. 42 must always be equal to zero. This yields a secondary condition that states:

$$\Sigma(e_i) = 0 \dots \dots \dots (47)$$

2.11 JIANG AND TENNYSON'S CRITERION

Other higher-order criteria include those of Tennyson and Elliott (1983), and Jiang and Tennyson (1989). The former contribution is similar to that of Priddy in the sense that independent biaxial tests are required for calculation of interaction coefficients. Although the latter model only considers specially orthotropic material, such as composites under in-plane loading, it serves as a fundamental reference for the new, proposed criterion. A general overview of this criterion is found in Appendix II.

Jiang and Tennyson formulate a criterion for failure prediction of orthotropic material, such as composites. They successfully employ closure of the sixth-order strength tensor. This criterion, however, is limited to in-plane stress failure situations. Through-thickness effects are completely neglected. Although it is effective in predicting failure for material that exhibits extensive in-plane ductile behavior, it fails to accurately predict failure of brittle material, such as cross-rolled beryllium sheets, under complex states of stress.

3. FAILURE PREDICTION WITH CLOSURE OF CUBIC TENSOR

3.1 FAILURE PREDICTION WITH HYDROSTATIC DEPENDENCE

The criteria reviewed in chapter 2 are, to varying degrees, approximations of criteria involving higher-order tensors and, consequently, overall failure predictions are not expected to be accurate for all possible states of stress. Moreover, previously proposed cubic polynomial formulations do not guarantee closure of the failure surface in multi-dimensional space. Thus, situations where infinite strengths are predicted can occur that lead to unconservative estimates of material strength.

In what follows, a new criterion is proposed to overcome these limitations. A cubic form of the tensor polynomial surface is forced to satisfy a number of constraints that are associated with the image of this failure surface. The function is projected onto the three orthogonal, mutually perpendicular Cartesian planes (σ_1, σ_2) , (σ_2, σ_3) , and (σ_1, σ_3) to ensure satisfaction of the constraints. Coefficients of the high-order function for beryllium sheet material are determined by a combination of laboratory experiments and numerical simulation (see chapters 4, 5, and 6). For simplicity, only orthotropic materials are considered. It is shown in chapter 8 that the cubic polynomial adequately describes the failure surface for cross-rolled beryllium sheets.

3.1.1 GENERAL STATE OF STRESS

Consider a general three-dimensional solid body that is loaded by external body and surface forces and embedded in a fixed Cartesian coordinate system (Fig. 6). Application of these forces causes the body to deform from the unstrained state; also, a system of internal stresses is set up at each point in the body that oppose deformation. Fig. 7 shows the nine independent components of stress acting on a differential element located at a general point in the solid. These components are listed in matrix form in Eq. 48.

$$[\sigma] = \begin{bmatrix} \sigma_{xx} & \sigma_{xy} & \sigma_{xz} \\ \sigma_{yx} & \sigma_{yy} & \sigma_{yz} \\ \sigma_{zx} & \sigma_{zy} & \sigma_{zz} \end{bmatrix} \dots\dots\dots (48)$$

Application of equations of equilibrium to the differential element reduces the number of unique stress terms from nine to six (Sokolnikoff 1964). This reduces Eq. 48 to the diagonally symmetric form:

$$[\sigma] = \begin{bmatrix} \sigma_{xx} & \sigma_{xy} & \sigma_{xz} \\ \sigma_{xy} & \sigma_{yy} & \sigma_{yz} \\ \sigma_{xz} & \sigma_{yz} & \sigma_{zz} \end{bmatrix} \dots\dots\dots (49)$$

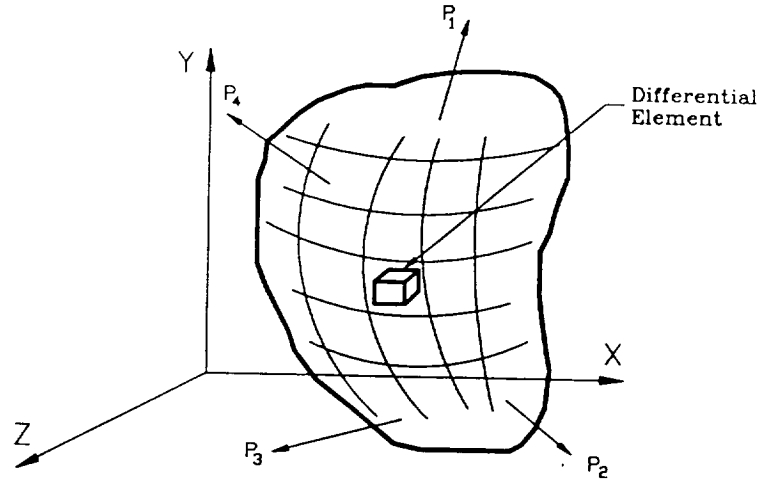


FIG. 6. General Body with Surface Forces

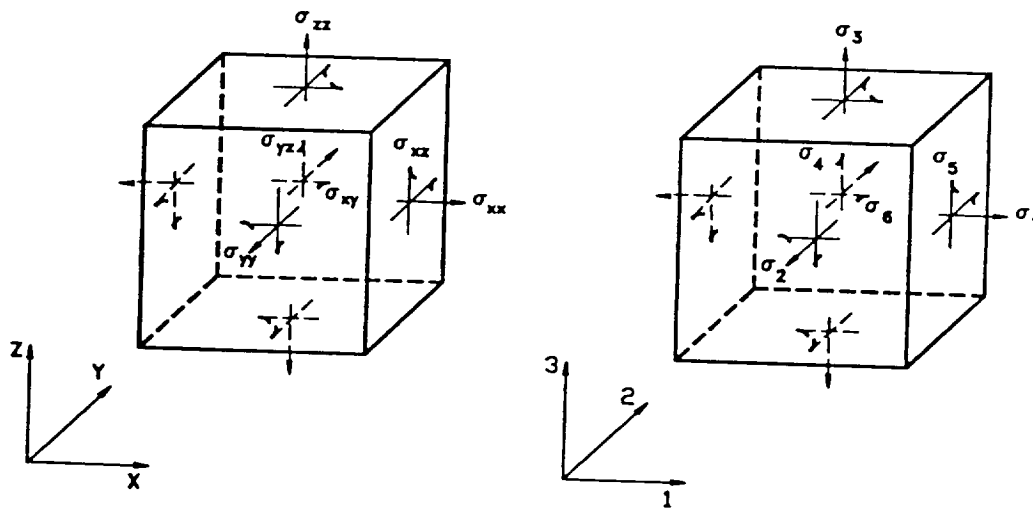


FIG. 7. Stress Components Acting at a Point

Also shown in Fig. 7 are the contracted notational equivalents of the second-order stress tensor. Contracted terms are used for convenience and compact representation. That is, an alternative, single subscript form of Eq. 49 is

$$[\sigma_i] = \begin{bmatrix} \sigma_1 & \sigma_6 & \sigma_4 \\ \sigma_6 & \sigma_2 & \sigma_5 \\ \sigma_4 & \sigma_5 & \sigma_3 \end{bmatrix} \dots\dots\dots (50)$$

Often the contracted stress entries are arranged in a vector format as follows

$$\{\sigma_i\} = \{\sigma_1, \sigma_2, \sigma_3, \sigma_6, \sigma_5, \sigma_4\}^T \dots\dots\dots (51)$$

The σ_i components represent a second-order tensor. However, σ_i itself is not a first-order tensor.

The loads on the body increase in magnitude until failure occurs. Failure is taken here to be the ultimate stress capacity of the structure. At the time of failure the stress at a point in the body reaches a threshold level that is taken to be the failure stress. In the general case, from one to all six components of stress may be nonzero when the body reaches the failure stress.

Furthermore, a fundamental assumption is made that failure can be predicted to occur when the following equation is satisfied at any point in the loaded body

$$F_{ij}\sigma_{ij} + F_{ijkl}\sigma_{ij}\sigma_{kl} + F_{ijklmn}\sigma_{ij}\sigma_{kl}\sigma_{mn} \geq 1 \quad (i, j, k, l, m, n = 1, 2, 3) \dots\dots\dots (52)$$

where σ_{ij} are second-order components of the stress tensor at the point, and F_{ij} , F_{ijkl} , and F_{ijklmn} are second, fourth, and sixth-order tensors, respectively. The tensor character of these coefficients follows from the quotient rule (Sokolnikoff 1964). When the left hand side of Eq. 52 is less than 1.0 the stresses are not high enough to cause failure. When a single stress or combination of stresses cause the left hand side to equal or exceed unity, failure occurs.

Loading of the body may be monotonic or non-monotonic. In other words, satisfaction of Eq. 52 is independent of the path of loading. Yielding of the material is also not explicitly considered, although Eq. 52 implicitly accounts for material flow by means of the F_{ij} , F_{ijkl} , and F_{ijklmn} terms. As an example, a long sample of the material may yield considerably when loaded along one of its principal material axes, but behave in a brittle manner when loaded in pure shear. Both cases can be successfully predicted with Eq. 52, although the yield stress has been greatly exceeded in one case and not at all in a brittle failure.

Eq. 52 is a scalar equation and homogeneity of a tensor equation requires that each term on the left-hand side is also a scalar. Since σ_{ij} are symmetric (Sokolnikoff 1964) it can be shown that there are, in reality, six independent F_{ij} terms, namely F_{11} , F_{22} , F_{33} , F_{12} , F_{13} , and F_{23} . In the same manner, symmetry of σ_{ij} leads to 21 independent F_{ijkl} constants, rather than $3^4 = 81$ that are required when there is no symmetry. Finally, the F_{ijklmn} term has a total of 56 independent terms as a result of symmetry. Altogether there are 83 independent failure coefficients in Eq. 52.

Furthermore, many of the coefficients can be combined and eliminated. For example, if all components of stress at a point in a stressed body are zero except that the normal stress in a principal material direction, σ_{11} , is at its strength level, X , Eq. 52 reduces to:

$$F_{11}X + F_{1111}X^2 + F_{111111}X^3 \geq 1 \dots\dots\dots (53)$$

Similarly, for the case of uniaxial compression strength $\sigma_{11} = -X$ along the same axis, Eq. 52 becomes

$$-F_{11}X' + F_{1111}X'^2 - F_{111111}X'^3 \geq 1 \dots\dots\dots (54)$$

The three material constants F_{11} , F_{1111} , and F_{111111} are computed from two distinct uniaxial experiments: tension and compression. Thus, one of the material coefficients must be redundant. It has been shown by Wu and Scheublein (1974) that F_{111111} is the redundant term. A similar consideration applies for F_{222222} , F_{333333} , F_{121212} , F_{131313} , and F_{232323} . In summary,

$$F_{111111} = F_{222222} = F_{333333} = F_{444444} = F_{555555} = F_{666666} = 0 \dots\dots\dots (55)$$

The number of independent coefficients, consequently, reduces from 83 to 77.

A significant reduction of the number of coefficients in the tensor polynomial is due to the assumption that a change in sign of the shearing stress does not affect failure strength of a general orthotropic material (Leknintskii 1981; Wu and Scheublein 1974). Thus, for the case of all components of stress being zero except for the shearing stress σ_{12} , Eq. 52 reduces to:

$$F_{12}\sigma_{12} + F_{1212}\sigma_{12}^2 \geq 1 \dots\dots\dots (56)$$

Similarly, reversing the sign of the shearing stress gives

$$F_{12}(-\sigma_{12}) + F_{1212}(-\sigma_{12})^2 \geq 1 \dots\dots\dots (57)$$

It follows from Eqs. 56 and 57 and analogous equations for the other shearing stress components, that

$$F_{12} = F_{13} = F_{23} = 0 \dots\dots\dots (58)$$

Using the same assumption of invariance of failure due to a change in the sign of the shearing stress leads to:

$$\begin{aligned} F_{1112} = F_{1113} = F_{1123} = F_{2212} = F_{2213} = F_{2223} = F_{3312} = \\ F_{3313} = F_{3323} = F_{1213} = F_{1223} = F_{1323} = 0 \end{aligned} \quad \dots\dots\dots (59)$$

and,

$$\begin{aligned} F_{111112} = F_{112212} = F_{113312} = F_{111213} = F_{111223} = F_{222212} = F_{223312} = F_{221213} = F_{221223} = \\ F_{333312} = F_{331213} = F_{331223} = F_{121213} = F_{121223} = F_{122323} = F_{121323} = F_{122323} = F_{111113} = \\ F_{112213} = F_{113313} = F_{111323} = F_{222213} = F_{223313} = F_{221323} = F_{333313} = F_{333123} = F_{131323} = \dots\dots\dots (60) \\ F_{132323} = F_{111123} = F_{112223} = F_{113323} = F_{222223} = F_{223323} = F_{333323} = 0 \end{aligned}$$

Application of Eqs. 55, 58, 59, and 60 reduces Eq. 52 to 28 independent coefficients.

Using the contracted stresses of Eq. 50 and an analogous contraction of F_{ij} , F_{ijkl} , and F_{ijklmn} terms, allows Eq. 52 to be expressed in compact form as follows:

$$\begin{aligned} F_1\sigma_1 + F_2\sigma_2 + F_3\sigma_3 + F_{11}\sigma_1^2 + F_{22}\sigma_2^2 + F_{33}\sigma_3^2 + F_{44}\sigma_4^2 + F_{55}\sigma_5^2 + F_{66}\sigma_6^2 \\ + 2F_{12}\sigma_1\sigma_2 + 2F_{13}\sigma_1\sigma_3 + 2F_{23}\sigma_2\sigma_3 + 3F_{112}\sigma_1^2\sigma_2 + 3F_{113}\sigma_1^2\sigma_3 + 3F_{122}\sigma_1\sigma_2^2 \\ + 3F_{223}\sigma_2^2\sigma_3 + 3F_{133}\sigma_1\sigma_3^2 + 3F_{233}\sigma_2\sigma_3^2 + 3F_{144}\sigma_1\sigma_4^2 + 3F_{244}\sigma_2\sigma_4^2 \\ + 3F_{344}\sigma_3\sigma_4^2 + 3F_{155}\sigma_1\sigma_5^2 + 3F_{255}\sigma_2\sigma_5^2 + 3F_{355}\sigma_3\sigma_5^2 + 3F_{166}\sigma_1\sigma_6^2 \\ + 3F_{266}\sigma_2\sigma_6^2 + 3F_{366}\sigma_3\sigma_6^2 + 6F_{123}\sigma_1\sigma_2\sigma_3 \geq 1 \end{aligned} \quad \dots\dots\dots (61)$$

The constant coefficients, F_i and F_{ii} (no summation on i), are identical to those derived by Tsai and Wu (1971) (for $i = 1, 2, 3$). Therefore, the same laboratory experiments and mathematical manipulations are used to determine the values of these constants.

Closure is ensured if the following two conditions are met by the failure surface (Jiang and Tennyson 1989):

(a) Images of the cubic curve projected onto the (σ_1, σ_2) , (σ_1, σ_3) , and (σ_2, σ_3) planes are closed.

(b) Real values of σ_4 , σ_5 , and σ_6 exist for given values of σ_1 , σ_2 , and σ_3 . For this condition to be met the following asymptotic equations must exist:

$$3F_{144}\sigma_1 + 3F_{244}\sigma_2 + 3F_{344}\sigma_3 + F_{44} = 0 \quad \dots\dots\dots (62)$$

$$3F_{155}\sigma_1 + 3F_{255}\sigma_2 + 3F_{355}\sigma_3 + F_{55} = 0 \quad \dots\dots\dots (63)$$

$$3F_{166}\sigma_1 + 3F_{266}\sigma_2 + 3F_{366}\sigma_3 + F_{66} = 0 \quad \dots\dots\dots (64)$$

In addition, they must not intersect the curves of condition (a).

The analysis that follows takes into consideration the fact that the material fails under a hydrostatic state of stress. Derivation of a modified criterion that excludes the case of failure under hydrostatic stress is presented in section 3.2. The latter approach is incorporated in the equations for predicting failure of cross-rolled beryllium sheets.

3.1.2 INVESTIGATION OF NECESSARY CONDITIONS

To examine failure surface images on the three orthogonal Cartesian axes and to satisfy the set of requirements for condition (a), crossing of the failure surface on the three projection planes must be examined when

$$\sigma_4 = \sigma_5 = \sigma_6 = 0 \dots\dots\dots (65)$$

As an example, Fig. 8, shows projections of bounded and unbounded regions of a failure surface onto the $(\sigma_1-\sigma_2)$ plane. Rearrangement of Eq. 61 to isolate σ_4 , σ_5 , and σ_6 terms leads to the following form:

$$\begin{aligned} & (3F_{144}\sigma_1 + 3F_{244}\sigma_2 + 3F_{344}\sigma_3 + F_{44})\sigma_4^2 + (3F_{155}\sigma_1 + 3F_{255}\sigma_2 + 3F_{355}\sigma_3 + F_{55})\sigma_5^2 \\ & + (3F_{166}\sigma_1 + 3F_{266}\sigma_2 + 3F_{366}\sigma_3 + F_{66})\sigma_6^2 = -(F_1\sigma_1 + F_2\sigma_2 + F_3\sigma_3 + F_{11}\sigma_1^2 \\ & + F_{22}\sigma_2^2 + F_{33}\sigma_3^2 + 2F_{12}\sigma_1\sigma_2 + 2F_{13}\sigma_1\sigma_3 + 2F_{23}\sigma_2\sigma_3 + 3F_{112}\sigma_1^2\sigma_2 + 3F_{113}\sigma_1\sigma_3 \\ & + 3F_{122}\sigma_1\sigma_2^2 + 3F_{223}\sigma_2^2\sigma_3 + 3F_{133}\sigma_1\sigma_3^2 + 3F_{233}\sigma_2\sigma_3^2 + 6F_{123}\sigma_1\sigma_2\sigma_3 - 1) \end{aligned} \dots\dots\dots (66)$$

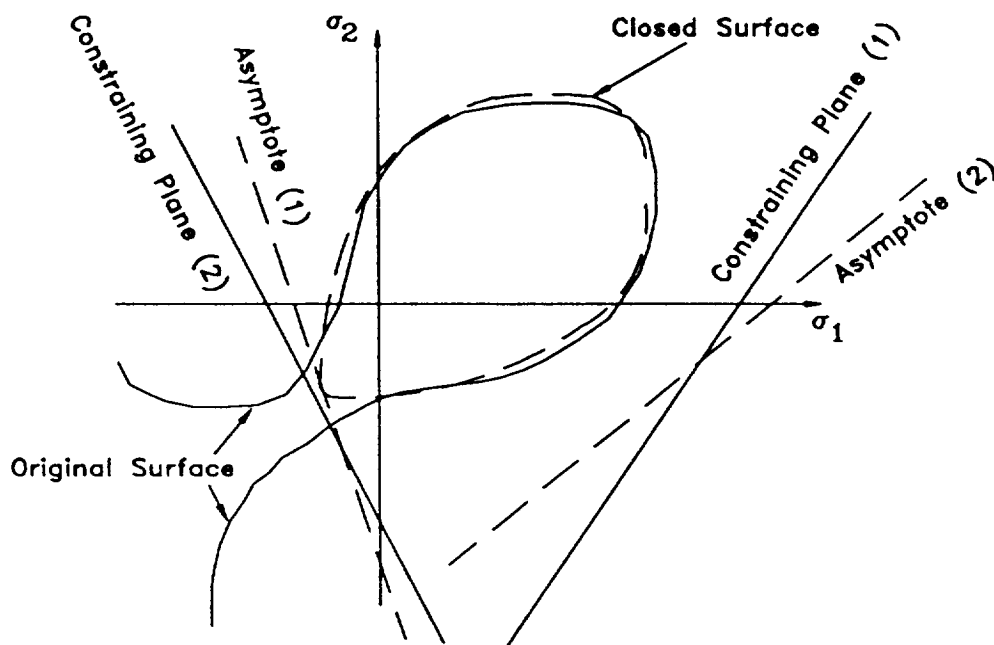


FIG. 8. Constraint and Asymptotic Equations Bounding Open and Closed Two-Dimensional Surfaces

Application of the conditions from Eq. 65 to Eq. 66 gives

$$F_1\sigma_1 + F_2\sigma_2 + F_3\sigma_3 + F_{11}\sigma_1^2 + F_{22}\sigma_2^2 + F_{33}\sigma_3^2 + F_{12}\sigma_1\sigma_2 + 2F_{13}\sigma_1\sigma_3 \\ + 2F_{23}\sigma_2\sigma_3 + 3F_{112}\sigma_1^2\sigma_2 + 3F_{113}\sigma_1^2\sigma_3 + 3F_{122}\sigma_1\sigma_2^2 + 3F_{223}\sigma_2^2\sigma_3 \\ + 3F_{133}\sigma_1\sigma_3^2 + 3F_{233}\sigma_2\sigma_3^2 + 6F_{123}\sigma_1\sigma_2\sigma_3 - 1 = 0 \quad \dots\dots\dots (67)$$

In addition to Eq. 67, criteria need to be specified that are satisfied by interaction terms F_{12} , F_{13} , F_{23} , F_{112} , F_{113} , F_{122} , F_{223} , F_{133} , and F_{233} . This can be accomplished by investigating the constraining planes that apply to Eq. 67. Asymptotes are obtained by collecting quadratic terms of σ_1 , σ_2 , and σ_3 , and setting the coefficients of each term to zero (Jiang and Tennyson 1989). The asymptotic equations that result are given by

$$F_{11} + 3F_{112}\sigma_2 + 3F_{113}\sigma_3 = 0 \quad \dots\dots\dots (68)$$

$$F_{22} + 3F_{122}\sigma_1 + 3F_{223}\sigma_3 = 0 \quad \dots\dots\dots (69)$$

$$F_{33} + 3F_{133}\sigma_1 + 3F_{233}\sigma_2 = 0 \quad \dots\dots\dots (70)$$

$$2F_{12} + 3F_{112}\sigma_1 + 3F_{122}\sigma_2 + 3F_{123}\sigma_3 = 0 \quad \dots\dots\dots (71)$$

$$2F_{13} + 3F_{113}\sigma_1 + 3F_{133}\sigma_3 + 3F_{123}\sigma_2 = 0 \quad \dots\dots\dots (72)$$

$$2F_{23} + 3F_{223}\sigma_2 + 3F_{233}\sigma_3 + 3F_{123}\sigma_1 = 0 \quad \dots\dots\dots (73)$$

As shown in Appendix III, Eqs. 71-73 can be rewritten as:

$$(3F_{112}F_{113} + 3F_{112}F_{223} - 6F_{122}F_{123})\sigma_1 + (3F_{122}F_{113} + 3F_{122}F_{223} - 6F_{112}F_{123})\sigma_2 \\ = 2F_{11}F_{123} + 2F_{22}F_{123} - 2F_{12}F_{113} - 2F_{12}F_{223} \quad \dots\dots\dots (74)$$

$$(3F_{113}F_{112} + 3F_{113}F_{233} - 6F_{133}F_{123})\sigma_1 + (3F_{133}F_{112} + 3F_{133}F_{233} - 6F_{113}F_{123})\sigma_3 \\ = 2F_{11}F_{123} + 2F_{33}F_{123} - 2F_{13}F_{112} - 2F_{13}F_{233} \quad \dots\dots\dots (75)$$

$$(3F_{223}F_{122} + 3F_{223}F_{133} - 6F_{233}F_{123})\sigma_2 + (3F_{233}F_{122} + 3F_{233}F_{133} - 6F_{223}F_{123})\sigma_3 \\ = 2F_{22}F_{123} + 2F_{33}F_{123} - 2F_{23}F_{122} - 2F_{23}F_{133} \quad \dots\dots\dots (76)$$

Thus, the number of independent variables of each equation reduces from three to two; namely, for Eq. 71 the σ_3 dependence is eliminated. For notational simplification the following constants are defined:

$$3F_{112}F_{113} + 3F_{112}F_{223} - 6F_{122}F_{123} = K1 \quad \dots\dots\dots (77)$$

$$3F_{122}F_{113} + 3F_{122}F_{223} - 6F_{112}F_{123} = L1 \quad \dots\dots\dots (78)$$

$$2F_{11}F_{123} + 2F_{12}F_{113} - 2F_{12}F_{223} = M1 \quad \dots\dots\dots (79)$$

$$3F_{113}F_{112} + 3F_{113}F_{233} - 6F_{133}F_{123} = K2 \dots\dots\dots (80)$$

$$3F_{133}F_{112} + 3F_{133}F_{233} - 6F_{113}F_{123} = L2 \dots\dots\dots (81)$$

$$2F_{11}F_{123} + 2F_{33}F_{123} - 2F_{13}F_{112} - 2F_{13}F_{233} = M2 \dots\dots\dots (82)$$

$$3F_{223}F_{122} + 3F_{223}F_{133} - 6F_{233}F_{123} = K3 \dots\dots\dots (83)$$

$$3F_{233}F_{122} + 3F_{233}F_{133} - 6F_{223}F_{123} = L3 \dots\dots\dots (84)$$

$$2F_{22}F_{123} + 2F_{33}F_{123} - 2F_{23}F_{122} - 2F_{23}F_{133} = M3 \dots\dots\dots (85)$$

To ensure closure of Eq. 67 none of the asymptotes given by Eqs. 68 through 73 should intersect the prescribed surface. Considering Eq. 68, for example, it can be seen that the limit values of the coefficients F_{112} and F_{113} depend on the ultimate tensile (Y and Z) or compressive strengths (Y' and Z') of the second and third principal directions, respectively, as well on the magnitude of the coefficient F_{11} . A first estimate of these coefficients, which is obtained via a least-square fit (see section 3.1.3), is necessary. Since the strength values are established from independent uniaxial experiments, the following relations that confine the magnitude of F_{112} and F_{113} are derived.

$$\frac{-F_{11}}{3F_{112}} \leq -Y' \quad \text{for} \quad F_{112} > 0 \dots\dots\dots (86)$$

$$\frac{-F_{11}}{3F_{112}} \geq Y \quad \text{for} \quad F_{112} < 0 \dots\dots\dots (87)$$

$$\frac{-F_{11}}{3F_{113}} \leq -Z' \quad \text{for} \quad F_{113} > 0 \dots\dots\dots (88)$$

$$\frac{-F_{11}}{3F_{113}} \geq Z \quad \text{for} \quad F_{113} < 0 \dots\dots\dots (89)$$

Similarly, from Eqs. 69-73, the following constraint conditions are also necessary to obtain closure:

$$\frac{-F_{22}}{3F_{122}} \leq -X' \quad \text{for} \quad F_{122} > 0 \dots\dots\dots (90)$$

$$\frac{-F_{22}}{3F_{122}} \geq X \quad \text{for} \quad F_{122} < 0 \dots\dots\dots (91)$$

$$\frac{-F_{33}}{3F_{133}} \leq -X' \quad \text{for} \quad F_{133} > 0 \dots\dots\dots (92)$$

$$\frac{-F_{33}}{3F_{133}} \geq X \quad \text{for} \quad F_{133} < 0 \dots\dots\dots (93)$$

$$\frac{-F_{33}}{3F_{233}} \leq -Y' \quad \text{for} \quad F_{233} > 0 \dots\dots\dots (94)$$

$$\frac{-F_{33}}{3F_{233}} \geq Y \quad \text{for} \quad F_{233} < 0 \dots\dots\dots (95)$$

$$\frac{-F_{22}}{3F_{233}} \leq -Z' \quad \text{for} \quad F_{113} > 0 \dots\dots\dots (96)$$

$$\frac{-F_{22}}{3F_{233}} \geq Z \quad \text{for} \quad F_{113} < 0 \dots\dots\dots (97)$$

$$\frac{M1}{K1} \leq -X' \quad \text{for} \quad \frac{M1}{K1} > 0 \dots\dots\dots (98)$$

$$\frac{M2}{K2} \leq -X' \quad \text{for} \quad \frac{M2}{K2} > 0 \dots\dots\dots (99)$$

$$\frac{M1}{L1} \leq -Y' \quad \text{for} \quad \frac{M1}{L1} > 0 \dots\dots\dots (100)$$

$$\frac{M3}{K3} \leq -Y' \quad \text{for} \quad \frac{M3}{K3} > 0 \dots\dots\dots (101)$$

$$\frac{M2}{L2} \leq -Z' \quad \text{for} \quad \frac{M2}{L2} > 0 \dots\dots\dots (102)$$

$$\frac{M3}{L3} \leq -Z' \quad \text{for} \quad \frac{M3}{L3} > 0 \dots\dots\dots (103)$$

$$\frac{M1}{K1} \geq X \quad \text{for} \quad \frac{M1}{K1} < 0 \dots\dots\dots (104)$$

$$\frac{M2}{K2} \geq X \quad \text{for} \quad \frac{M2}{K2} < 0 \dots\dots\dots (105)$$

$$\frac{M1}{L1} \geq Y \quad \text{for} \quad \frac{M1}{L1} < 0 \dots\dots\dots (106)$$

$$\frac{M3}{K3} \geq Y \quad \text{for} \quad \frac{M3}{K3} < 0 \dots\dots\dots (107)$$

$$\frac{M2}{L2} \geq Z \quad \text{for} \quad \frac{M2}{L2} < 0 \dots\dots\dots(108)$$

$$\frac{M3}{L3} \geq Z \quad \text{for} \quad \frac{M3}{L3} < 0 \dots\dots\dots(109)$$

3.1.3 EVALUATION OF F_{ij} AND F_{ijj} FOR $i \neq j$

In the event that there are experimental data from $n1$, $n2$, and $n3$ sets of biaxial load tests that correspond to states of stress lying in the planes $(\sigma_{1i}, \sigma_{2i})$ ($i = 1, 2, \dots, n1$), $(\sigma_{1i}, \sigma_{3i})$ ($i = 1, 2, \dots, n2$), and $(\sigma_{2i}, \sigma_{3i})$ ($i = 1, 2, \dots, n3$), respectively, it is possible to evaluate the interaction coefficients F_{ij} and F_{ijj} for $i \neq j$ by a least-square fit of the cubic Eq. 67. However, this approach may not be sufficient to produce closed curves in the projected (σ_1, σ_2) , (σ_1, σ_3) , and (σ_2, σ_3) subspaces (Fig. 9). In the event that closure is not accomplished, one or more of the constraints that intersect the failure surface are shifted in space (i.e., their coefficients are modified) in such a manner that all constraints are satisfied and the surface is closed.

As an illustration, suppose that the asymptotic plane,

$$F_{22} + 3F_{122}\sigma_1 + 3F_{223}\sigma_3 = 0 \dots\dots\dots(110)$$

which is obtained by rewriting Eq. 67 as a quadratic of σ_2 , is parallel with the σ_2 axis and intersects the open-ended failure surface as shown in Fig. 9. Adjustment in the F_{122} and F_{223} terms orients this plane with respect to the σ_2 axis. Closure is accomplished by requiring that the plane given by Eq. 110 pass through the line $(-X', \sigma_2, -Z')$, where $-X'$ and $-Z'$ are uniaxial compressive strengths along the σ_1 and σ_3 axes, respectively. Thus, by judicious selection of the constants F_{122} and F_{223} , Eq. 110 becomes an asymptotic plane for the failure surface (see Fig. 10). $\sigma_1 = -X'$ and $\sigma_3 = -Z'$ can be substituted into Eq. 67 to obtain the following relation:

$$\begin{aligned} & (-3F_{122}X' - 3F_{223}Z' + F_{22})\sigma_2^2 \\ & + (6F_{123}XZ' + 3F_{112}X^2 + 3F_{233}Z^2 - 2F_{12}X' - 2F_{23}Z' + F_2)\sigma_2 \\ & + (-3F_{133}XZ^2 - 3F_{113}X^2Z' + 2F_{13}XZ' + F_{11}X^2 + F_{33}Z^2 - F_1X' - F_3Z' - I) = 0 \end{aligned} \dots\dots(111)$$

Subsequently, for an infinity of σ_2 roots to exist it follows from Eq. 111 that:

$$-3F_{122}X' - 3F_{223}Z' + F_{22} = 0 \dots\dots\dots(112)$$

$$6F_{123}XZ' + 3F_{112}X^2 + 3F_{233}Z^2 - 2F_{12}X' - 2F_{23}Z' + F_2 = 0 \dots\dots\dots(113)$$

$$-3F_{133}XZ^2 - 3F_{113}X^2Z' + 2F_{13}XZ' + F_{11}X^2 + F_{33}Z^2 - F_1X' - F_3Z' - I = 0 \dots\dots\dots(114)$$

Eq. 114 has the same form that would result if $\sigma_I = -X'$ and $\sigma_3 = -Z'$ were substituted into the cubic criterion of Eq. 66. Thus, it can not be considered to be an asymptote.

Similarly, isolation of quadratic terms σ_I and σ_3 in Eq. 67 leads to constraint planes that are similar in form to Eq. 110 and parallel to the σ_I and σ_3 axes, respectively. This procedure leads to four additional equations (for details see Appendix IV):

$$-3F_{112}Y' - 3F_{113}Z' + F_{11} = 0 \dots\dots\dots (115)$$

$$6F_{123}YZ' + 3F_{122}Y'^2 + 3F_{133}Z'^2 - 2F_{12}Y' - 2F_{13}Z' + F_1 = 0 \dots\dots\dots (116)$$

$$-3F_{133}X' - 3F_{233}Y' + F_{33} = 0 \dots\dots\dots (117)$$

$$6F_{123}XY' + 3F_{113}X'^2 + 3F_{223}Y'^2 - 2F_{13}X' - 2F_{23}Y' + F_3 = 0 \dots\dots\dots (118)$$

Using Lagrange multipliers to incorporate Eqs. 112, 113, and 115-118 as constraint conditions, the following functional is obtained for calculation of the interaction parameters:

$$\begin{aligned} \Phi = & \sum_{i=1}^{n1} (F_1\sigma_{1i} + F_2\sigma_{2i} + F_{11}\sigma_{1i}^2 + F_{22}\sigma_{2i}^2 + 2F_{12}\sigma_{1i}\sigma_{2i} + 3F_{112}\sigma_{1i}^2\sigma_{2i} \\ & + 3F_{122}\sigma_{1i}\sigma_{2i}^2 - 1)^2 + \sum_{i=1}^{n2} (F_1\sigma_{1i} + F_3\sigma_{3i} + F_{11}\sigma_{1i}^2 + F_{33}\sigma_{3i}^2 + 2F_{13}\sigma_{1i}\sigma_{3i} + 3F_{113}\sigma_{1i}^2\sigma_{3i} \\ & + 3F_{133}\sigma_{1i}\sigma_{3i}^2 - 1)^2 + \sum_{i=1}^{n3} (F_2\sigma_{2i} + F_3\sigma_{3i} + F_{22}\sigma_{2i}^2 + F_{33}\sigma_{3i}^2 + 2F_{23}\sigma_{2i}\sigma_{3i} + \\ & + 3F_{223}\sigma_{2i}^2\sigma_{3i} + 3F_{233}\sigma_{2i}\sigma_{3i}^2 - 1)^2 + \lambda_1(-3F_{122}X' - 3F_{223}Z' + F_{22}) + \lambda_2(6F_{123}X'Z' \dots\dots\dots (119) \\ & + 3F_{112}X'^2 + 3F_{233}Z'^2 - 2F_{12}X' - 2F_{23}Z' + F_2) + \lambda_3(-3F_{112}Y' - 3F_{113}Z' + F_{11}) \\ & + \lambda_4(6F_{123}Y'Z' + 3F_{122}Y'^2 + 3F_{133}Z'^2 - 2F_{12}Y' - 2F_{13}Z' + F_1) \\ & + \lambda_5(-3F_{133}X' - 3F_{233}Y' + F_{33}) + \lambda_6(6F_{123}XY' + 3F_{113}X'^2 + 3F_{223}Y'^2 - 2F_{13}X' - 2F_{23}Y' + F_3) \end{aligned}$$

where λ_i for $i = 1, 2, \dots, 6$ represent Lagrange multipliers, and summation indices $n1$, $n2$, and $n3$ range over the number of experimental tests carried out.

Interaction coefficients F_{ij} and F_{iij} for $i \neq j$ are determined by minimizing the functional Φ . A total of sixteen equations are obtained with an identical number of unknowns. Coefficients F_i and F_{ii} ($i = 1, 2, 3$) need not be obtained from this expression since they are identical to the Tsai-Wu coefficients stated earlier. The first ten minimizations are as follows:

$$\begin{aligned} \frac{\partial \Phi}{\partial F_{12}} = & -2\lambda_2X' - 2\lambda_4Y' + 4\sigma_{1i}\sigma_{2i} \sum_{i=1}^{n1} (F_1\sigma_{1i} + F_2\sigma_{2i} + F_{11}\sigma_{1i}^2 + F_{22}\sigma_{2i}^2 \\ & + 2F_{12}\sigma_{1i}\sigma_{2i} + 3F_{112}\sigma_{1i}^2\sigma_{2i} + 3F_{122}\sigma_{1i}\sigma_{2i}^2 - 1) = 0 \dots\dots\dots (120) \end{aligned}$$

$$\frac{\partial \Phi}{\partial F_{13}} = -2\lambda_4 Z' - 2\lambda_6 X' + 4\sigma_{1i}\sigma_{3i} \sum_{i=1}^{n2} (F_1\sigma_{1i} + F_3\sigma_{3i} + F_{11}\sigma_{1i}^2 + F_{33}\sigma_{3i}^2 + 2F_{13}\sigma_{1i}\sigma_{3i} + 3F_{113}\sigma_{1i}^2\sigma_{3i} + 3F_{133}\sigma_{3i}^2\sigma_{1i} - 1) = 0 \quad \dots\dots\dots(121)$$

$$\frac{\partial \Phi}{\partial F_{23}} = -2\lambda_2 Z' - 2\lambda_6 Y' + 4\sigma_{2i}\sigma_{3i} \sum_{i=1}^{n3} (F_2\sigma_{2i} + F_3\sigma_{3i} + F_{22}\sigma_{2i}^2 + F_{33}\sigma_{3i}^2 + 2F_{23}\sigma_{2i}\sigma_{3i} + 3F_{223}\sigma_{2i}^2\sigma_{3i} + 3F_{233}\sigma_{3i}^2\sigma_{2i} - 1) = 0 \quad \dots\dots\dots(122)$$

$$\frac{\partial \Phi}{\partial F_{112}} = -3\lambda_3 Y' + 3\lambda_2 X' + 6\sigma_{1i}^2\sigma_{2i} \sum_{i=1}^{n1} (F_1\sigma_{1i} + F_2\sigma_{2i} + F_{11}\sigma_{1i}^2 + F_{22}\sigma_{2i}^2 + 2F_{12}\sigma_{1i}\sigma_{2i} + 3F_{112}\sigma_{1i}^2\sigma_{2i} + 3F_{122}\sigma_{2i}^2\sigma_{1i} - 1) = 0 \quad \dots\dots\dots(123)$$

$$\frac{\partial \Phi}{\partial F_{113}} = -3F\lambda_3 Z' + 3\lambda_6 X' + 6\sigma_{1i}^2\sigma_{3i} \sum_{i=1}^{n2} (F_1\sigma_{1i} + F_3\sigma_{3i} + F_{11}\sigma_{1i}^2 + F_{33}\sigma_{3i}^2 + 2F_{13}\sigma_{1i}\sigma_{3i} + 3F_{113}\sigma_{1i}^2\sigma_{3i} + 3F_{133}\sigma_{3i}^2\sigma_{1i} - 1) = 0 \quad \dots\dots\dots(124)$$

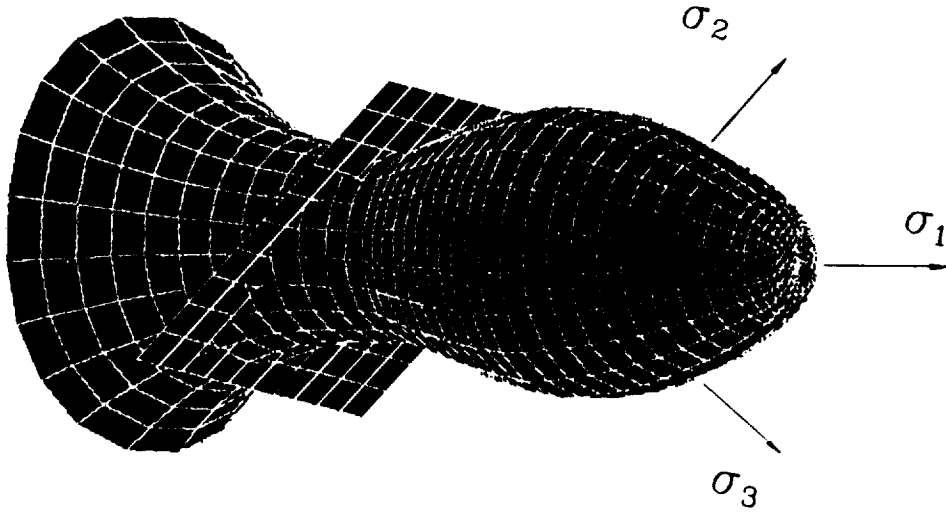


FIG. 9. Open, Non-Convex Failure Surface

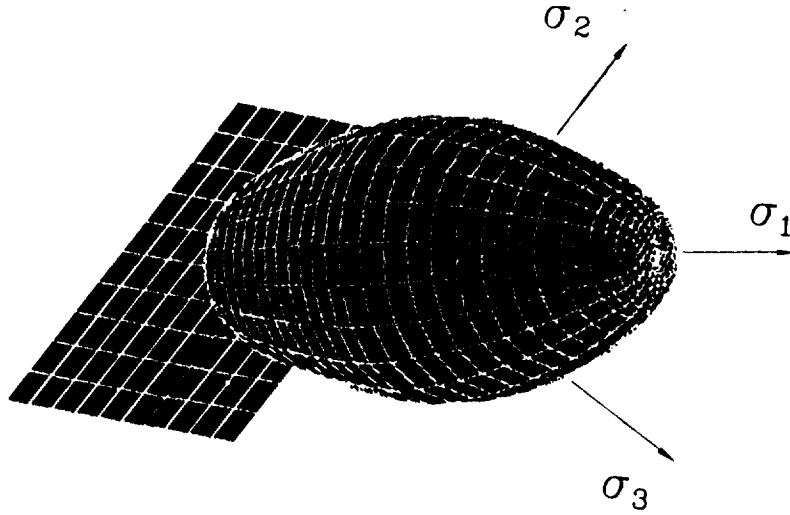


FIG. 10. Closed Failure Surface

$$\frac{\partial \Phi}{\partial F_{122}} = -3F\lambda_1 X' + 3\lambda_4 Y'^2 + 6\sigma_{2i}^2 \sigma_{li} \sum_{i=1}^{n1} (F_1 \sigma_{li} + F_2 \sigma_{2i} + F_{11} \sigma_{li}^2 + F_{22} \sigma_{2i}^2 + 2F_{12} \sigma_{li} \sigma_{2i} + 3F_{112} \sigma_{li}^2 \sigma_{2i} + 3F_{122} \sigma_{2i}^2 \sigma_{li} - I) = 0 \quad (125)$$

$$\frac{\partial \Phi}{\partial F_{223}} = -3\lambda_1 Z' + 3\lambda_4 Y'^2 + 6\sigma_{2i}^2 \sigma_{3i} \sum_{i=1}^{n3} (F_2 \sigma_{2i} + F_3 \sigma_{3i} + F_{22} \sigma_{2i}^2 + F_{33} \sigma_{3i}^2 + 2F_{23} \sigma_{2i} \sigma_{3i} + 3F_{223} \sigma_{2i}^2 \sigma_{3i} + 3F_{233} \sigma_{3i}^2 \sigma_{2i} - I) = 0 \quad (126)$$

$$\frac{\partial \Phi}{\partial F_{133}} = -3\lambda_6 X' + 3\lambda_4 Z'^2 + 6\sigma_{3i}^2 \sigma_{li} \sum_{i=1}^{n2} (F_1 \sigma_{li} + F_3 \sigma_{3i} + F_{11} \sigma_{li}^2 + F_{33} \sigma_{3i}^2 + 2F_{13} \sigma_{li} \sigma_{3i} + 3F_{113} \sigma_{li}^2 \sigma_{3i} + 3F_{133} \sigma_{3i}^2 \sigma_{li} - I) = 0 \quad (127)$$

$$\frac{\partial \Phi}{\partial F_{233}} = -3\lambda_6 X' + 3\lambda_2 Z'^2 + 6\sigma_{3i}^2 \sigma_{2i} \sum_{i=1}^{n2} (F_2 \sigma_{2i} + F_3 \sigma_{3i} + F_{22} \sigma_{2i}^2 + F_{33} \sigma_{3i}^2 + 2F_{23} \sigma_{2i} \sigma_{3i} + 3F_{223} \sigma_{2i}^2 \sigma_{3i} + 3F_{233} \sigma_{3i}^2 \sigma_{2i} - I) = 0 \quad (128)$$

$$\frac{\partial \Phi}{\partial F_{123}} = 6\lambda_2 X Z' + 6\lambda_4 Y Z' + 6\lambda_6 X Y' = 0 \dots\dots\dots (129)$$

The remaining six equations are obtained by taking derivatives of the functional, Φ , with respect to $\lambda_1, \lambda_2, \lambda_3, \lambda_4, \lambda_5$, and λ_6 . The resulting equations are identical to those of Eqs. 112, 113, and 115 through 118.

The system of Eqs. 112-113, 115-118, and 120-129 is determinate and calculation of the F_{ij} and F_{ijj} coefficients is feasible. Thus, it is possible to construct a closed cubic surface for the particular quadrant (compression-compression) under consideration. The same approach can be applied for each of the other seven quadrants of the failure surface.

3.1.4 EVALUATION OF F_{ijj} FOR $i = 1, 2, 3$, AND $j = 4$ OR 5 OR 6

For the condition (b) to be met the following asymptotic equations must exist:

$$3F_{144}\sigma_1 + 3F_{244}\sigma_2 + 3F_{344} + F_{44} = 0 \dots\dots\dots (130)$$

$$3F_{155}\sigma_1 + 3F_{255}\sigma_2 + 3F_{355} + F_{55} = 0 \dots\dots\dots (131)$$

$$3F_{166}\sigma_1 + 3F_{266}\sigma_2 + 3F_{366} + F_{66} = 0 \dots\dots\dots (132)$$

Also these planes must not intersect the projected images of the failure surface on the three planes (σ_1, σ_2) , (σ_1, σ_3) , and (σ_2, σ_3) . For this condition to be satisfied Eqs. 130-132 should not intersect the failure surface defined by Eq. 67. This condition occurs only if the planes described by these three equations are, at most, tangent to the cubic surface. For simplicity, only one of these conditions is explicitly considered in the present discussion. Later, the concept is generalized to incorporate equations for the other two planes.

As an example Eq. 132 is written as follows:

$$\sigma_3 = -\frac{(3F_{166}\sigma_1 + 3F_{266}\sigma_2 + F_{66})}{3F_{366}} \dots\dots\dots (133)$$

The following form of Eq. 67 is obtained by substitution of σ_3 from Eq. 133 into Eq. 67 and rearrangement of the result:

$$\begin{aligned} & (A_{16}\sigma_1^3 + A_{26}\sigma_1^2 + A_{36}\sigma_1 + A_{46}) + (B_{16}\sigma_2^3 + B_{26}\sigma_2^2 + B_{36}\sigma_2 + B_{46}) \\ & + (C_{16}\sigma_1^2\sigma_2 + C_{26}\sigma_1\sigma_2^2 + C_{36}\sigma_1\sigma_2) = 0 \end{aligned} \dots\dots\dots (134)$$

where, $A_{16}, A_{26}, A_{36}, A_{46}, B_{16}, B_{26}, B_{36}, B_{46}, C_{16}, C_{26}$, and C_{36} are constants that are functions of F_i, F_{ij} , and F_{i66} for $i = 1, 2, 3$. Explicitly, these constants are given by the following expressions (Roschke et al. 1990).

$$A_{16} = 27(F_{166}^2 F_{133} - F_{166} F_{366} F_{113}) \dots \dots \dots (135)$$

$$A_{26} = 9(F_{166}^2 F_{33} + 2F_{166} F_{66} F_{133} - F_{366} F_{66} F_{113} - 2F_{366} F_{166} F_{13} + F_{366}^2 F_{11}) \dots \dots \dots (136)$$

$$A_{36} = 3(F_{66}^2 F_{133} + 2F_{166} F_{66} F_{33} - 3F_{366} F_{166} F_3 - 2F_{366} F_{66} F_{13} + 3F_{366}^2 F_1) \dots \dots \dots (137)$$

$$A_{46} = 0.5(F_{66}^2 F_{33} - 3F_{366} F_{66} F_3 - 9F_{366}^2) \dots \dots \dots (138)$$

$$B_{16} = 27(F_{266}^2 F_{233} - F_{366} F_{266} F_{223}) \dots \dots \dots (139)$$

$$B_{26} = 9(F_{266}^2 F_{33} + 2F_{266} F_{66} F_{233} - F_{366} F_{66} F_{223} - 2F_{366} F_{266} F_{23} + F_{366}^2 F_{22}) \dots \dots \dots (140)$$

$$B_{36} = 3(F_{66}^2 F_{233} + 2F_{266} F_{33} - 3F_{366} F_{266} F_3 - 2F_{366} F_{66} F_{23} + 3F_{366}^2 F_2) \dots \dots \dots (141)$$

$$B_{46} = 0.5(F_{66}^2 F_{33} - 3F_{366} F_{66} F_3 - 9F_{366}^2) \dots \dots \dots (142)$$

$$C_{16} = 27(F_{166}^2 F_{233} + 2F_{166} F_{266} F_{133} - F_{366} F_{266} F_{113} + F_{366}^2 F_{112} - 2F_{366} F_{166} F_{123}) \dots \dots \dots (143)$$

$$C_{26} = 27(F_{266}^2 F_{133} + 2F_{166} F_{266} F_{233} - F_{366} F_{166} F_{223} + F_{366}^2 F_{122} - 2F_{366} F_{266} F_{123}) \dots \dots \dots (144)$$

$$C_{36} = 18(F_{166} F_{266} F_{33} + F_{166} F_{66} F_{233} + F_{266} F_{66} F_{133} - F_{166} F_{366} F_{23} - F_{266} F_{366} F_{13} + F_{366}^2 F_{12} - F_{366} F_{66} F_{123}) \dots \dots \dots (145)$$

The closed-form solution of the bicubic Eq. 134 yields repeating, real σ_1 and σ_2 roots at the points of tangency with some side conditions. The repeating roots and side conditions are given by the relations (Jiang and Tennyson 1989; MIT Publications 1988):

$$27 A_{16}^2 A_{46}^2 - 18 A_{16} A_{26} A_{36} A_{46} + 4 A_{16} A_{36}^3 - A_{26}^2 A_{36}^2 + A_{26}^3 A_{46} = 0 \dots \dots \dots (146)$$

$$27 B_{16}^2 B_{46}^2 - 18 B_{16} B_{26} B_{36} B_{46} + 4 B_{16} B_{36}^3 - B_{26}^2 B_{36}^2 + B_{26}^3 B_{46} = 0 \dots \dots \dots (147)$$

$$C_{16} = 0 \dots \dots \dots (148)$$

$$C_{26} = 0 \dots \dots \dots (149)$$

$$C_{36} = 0 \dots \dots \dots (150)$$

A functional, Ψ , is defined from the closed-form solution of the bicubic Eq. 134, that yields repeating σ_1 and σ_2 roots at points of tangency, and side conditions $C_{16} = C_{26} =$

$C_{36} = 0$. Assuming that there are $n1$ sets of failure data, $(\sigma_{1i}, \sigma_{2i}, \sigma_{6i})$ for $i = 1, 2, \dots, n1$, Ψ takes the following form:

$$\begin{aligned} \Psi = \sum_{i=1}^{n1} & (F_1 \sigma_{1i} + F_2 \sigma_{2i} + F_{11} \sigma_{1i}^2 + F_{22} \sigma_{2i}^2 + F_{66} \sigma_{6i}^2 + 2F_{12} \sigma_{1i} \sigma_{2i} + 3F_{112} \sigma_{1i}^2 \sigma_{2i} + F_{122} \sigma_{1i} \sigma_{2i}^2 \\ & + 3F_{166} \sigma_{1i} \sigma_{6i}^2 + 3F_{266} \sigma_{2i} \sigma_{6i}^2 + 3F_{366} \sigma_{3i} \sigma_{6i}^2 - 1)^2 + \mu_1 (27A_{16}^2 A_{46}^2 - 18A_{16} A_{26} A_{36} A_{46} \\ & + 4A_{16} A_{36}^3 - A_{26}^2 A_{36}^2 + A_{26}^3 A_{46}) + \mu_2 (27B_{16}^2 B_{46}^2 - 18B_{16} B_{26} B_{36} B_{46} + 4B_{16} B_{36}^3 \\ & - B_{26}^2 B_{36}^2 + B_{26}^3 B_{46}) - B_{26}^2 B_{36}^2 + B_{26}^3 B_{46}) + \mu_3 C_{16} + \mu_4 C_{26} + \mu_5 C_{36} \end{aligned} \quad ..(151)$$

where μ_1 through μ_5 are Lagrange multipliers.

The functional, Ψ , reaches an extreme value (maximum or minimum) when:

$$\begin{aligned} \frac{\partial \Psi}{\partial F_{166}} = 0, \quad \frac{\partial \Psi}{\partial F_{266}} = 0, \quad \frac{\partial \Psi}{\partial F_{366}} = 0, \quad \frac{\partial \Psi}{\partial \mu_1} = 0, \\ \dots\dots\dots(152) \\ \frac{\partial \Psi}{\partial \mu_2} = 0, \quad \frac{\partial \Psi}{\partial \mu_3} = 0, \quad \frac{\partial \Psi}{\partial \mu_4} = 0, \quad \frac{\partial \Psi}{\partial \mu_5} = 0 \end{aligned}$$

A set of eight nonlinear simultaneous equations is obtained that yields coefficients F_{166} , F_{266} , and F_{366} and numerical values for the five Lagrange multipliers.

Similarly, Eqs. 130 and 131 may be rearranged as follows:

$$\sigma_2 = -\frac{(3F_{144}\sigma_1 + 3F_{344}\sigma_3 + F_{44})}{3F_{244}} \dots\dots\dots(153)$$

$$\sigma_1 = -\frac{(3F_{255}\sigma_2 + 3F_{355}\sigma_3 + F_{55})}{3F_{155}} \dots\dots\dots(154)$$

Relationships similar to Eq. 134 can be derived by incorporating Eqs. 153 and 154 in the event that biaxial test data, $(\sigma_{1i}, \sigma_{3i}, \sigma_{4i})$ for $i = 1, 2, \dots, n2$ and $\sigma_{2i}, \sigma_{3i}, \sigma_{5i}$ for $i = 1, 2, \dots, n3$, respectively, exist. By an analogous analysis the interaction coefficients F_{144} , F_{244} , F_{344} , F_{155} , F_{255} , and F_{355} may be obtained, thus, yielding all interaction coefficients necessary for determining the failure surface. Details of these derivations are in Appendix V.

3.2 FAILURE PREDICTION WITHOUT HYDROSTATIC DEPENDENCE

3.2.1 GENERAL STATE OF STRESS

Expansion of terms in Eq. 52 and application of the assumption that excludes failure under a hydrostatic state of stress, leads to the following equation in terms of the contracted notational form:

$$\begin{aligned}
 &F_1\sigma_1 + F_2\sigma_2 + F_3\sigma_3 + F_{11}\sigma_1^2 + F_{22}\sigma_2^2 + F_{33}\sigma_3^2 + F_{44}\sigma_4^2 + F_{55}\sigma_5^2 + F_{66}\sigma_6^2 \\
 &+ 2F_{12}\sigma_1\sigma_2 + 2F_{13}\sigma_1\sigma_3 + 2F_{23}\sigma_2\sigma_3 + 3F_{112}\sigma_1^2\sigma_2 + 3F_{113}\sigma_1^2\sigma_3 \\
 &+ 3F_{122}\sigma_1\sigma_2^2 + 3F_{223}\sigma_2^2\sigma_3 + 3F_{133}\sigma_1\sigma_3^2 + 3F_{233}\sigma_2\sigma_3^2 + 3F_{114}\sigma_1^2\sigma_4^2 \dots\dots\dots (155) \\
 &+ 3F_{244}\sigma_2^2\sigma_4^2 + 3F_{344}\sigma_3^2\sigma_4^2 + 3F_{155}\sigma_1\sigma_5^2 + 3F_{255}\sigma_2\sigma_5^2 + 3F_{355}\sigma_3\sigma_5^2 \\
 &+ 3F_{166}\sigma_1\sigma_6^2 + 3F_{266}\sigma_2\sigma_6^2 + 3F_{366}\sigma_3\sigma_6^2 = 1
 \end{aligned}$$

Eq. 155 can be rearranged as follows:

$$\begin{aligned}
 &(3F_{144}\sigma_1 + 3F_{244}\sigma_2 + 3F_{344}\sigma_3 + F_{44})\sigma_4^2 \\
 &+ (3F_{155}\sigma_1 + 3F_{255}\sigma_2 + 3F_{355}\sigma_3 + F_{55})\sigma_5^2 \\
 &+ (3F_{166}\sigma_1 + 3F_{266}\sigma_2 + 3F_{366}\sigma_3 + F_{66})\sigma_6^2 \\
 &= - (F_1\sigma_1 + F_2\sigma_2 + F_3\sigma_3 + F_{11}\sigma_1^2 + F_{22}\sigma_2^2 \dots\dots\dots (156) \\
 &+ F_{33}\sigma_3^2 + 2F_{12}\sigma_1\sigma_2 + 2F_{13}\sigma_1\sigma_3 + 2F_{23}\sigma_2\sigma_3 \\
 &+ 3F_{112}\sigma_1^2\sigma_2 + 3F_{113}\sigma_1^2\sigma_3 + 3F_{122}\sigma_1\sigma_2^2 \\
 &+ 3F_{223}\sigma_2^2\sigma_3 + 3F_{133}\sigma_1\sigma_3^2 + 3F_{233}\sigma_2\sigma_3^2 - 1)
 \end{aligned}$$

Again, closure of this failure surface is accomplished by imposing conditions (a) and (b) of section 3.1.1.

3.2.2 INVESTIGATION OF NECESSARY CONDITIONS

The images of the failure surface on the three planes must be examined when $\sigma_4 = \sigma_5 = \sigma_6 = 0$. Thus, Eq. 156 becomes

$$\begin{aligned}
 &F_1\sigma_1 + F_2\sigma_2 + F_3\sigma_3 + F_{11}\sigma_1^2 + F_{22}\sigma_2^2 + F_{33}\sigma_3^2 + 2F_{12}\sigma_1\sigma_2 + 2F_{13}\sigma_1\sigma_3 \\
 &+ 2F_{23}\sigma_2\sigma_3 + 3F_{112}\sigma_1^2\sigma_2 + 3F_{113}\sigma_1^2\sigma_3 + 3F_{122}\sigma_1\sigma_2^2 + 3F_{223}\sigma_2^2\sigma_3 \dots\dots\dots (157) \\
 &+ 3F_{133}\sigma_1\sigma_3^2 + 3F_{233}\sigma_2\sigma_3^2 - 1 = 0
 \end{aligned}$$

The asymptotes correlating the interaction coefficients are obtained by rewriting this equation as a quadratic in terms of either σ_1 , σ_2 , or σ_3 and setting the result equal to zero. The resulting equations are given by

$$F_{11} + 3F_{112}\sigma_2 + 3F_{113}\sigma_3 = 0 \dots\dots\dots (158)$$

$$F_{22} + 3F_{122}\sigma_1 + 3F_{223}\sigma_3 = 0 \dots\dots\dots (159)$$

$$F_{33} + 3F_{133}\sigma_1 + 3F_{233}\sigma_2 = 0 \dots\dots\dots (160)$$

$$2F_{12} + 3F_{112}\sigma_1 + 3F_{122}\sigma_2 = 0 \dots\dots\dots (161)$$

$$2F_{13} + 3F_{113}\sigma_1 + 3F_{133}\sigma_3 = 0 \dots\dots\dots (162)$$

$$2F_{23} + 3F_{223}\sigma_2 + 3F_{233}\sigma_3 = 0 \dots\dots\dots (163)$$

The last three equations can be rewritten as (see Appendix III for $F_{123} = 0$):

$$\begin{aligned} & (3F_{112}F_{113} + 3F_{112}F_{223})\sigma_1 + (3F_{122}F_{113} + 3F_{122}F_{223})\sigma_2 \\ & = -2F_{12}F_{113} - 2F_{12}F_{223} \dots\dots\dots (164) \end{aligned}$$

$$(3F_{113}F_{112} + 3F_{113}F_{233})\sigma_1 + (3F_{133}F_{112} + 3F_{133}F_{233})\sigma_3 = -2F_{13}F_{112} - 2F_{13}F_{233} \dots\dots\dots (165)$$

$$(3F_{223}F_{122} + 3F_{223}F_{133})\sigma_2 + (3F_{233}F_{122} + 3F_{233}F_{133})\sigma_3 = -2F_{23}F_{122} - 2F_{23}F_{133} \dots\dots\dots (166)$$

This is done to facilitate comparison with section 3.2.1. However, it is not a simplification since the number of independent variables remains the same for each equation. For notational compactness the following constants are defined:

$$3F_{112}F_{113} + 3F_{112}F_{223} = K1' \dots\dots\dots (167)$$

$$3F_{122}F_{113} + 3F_{122}F_{223} = L1' \dots\dots\dots (168)$$

$$-2F_{12}F_{113} - 2F_{12}F_{223} = M1' \dots\dots\dots (169)$$

$$3F_{113}F_{112} + 3F_{113}F_{233} = K2' \dots\dots\dots (170)$$

$$3F_{133}F_{112} + 3F_{133}F_{233} = L2' \dots\dots\dots (171)$$

$$-2F_{13}F_{112} - 2F_{13}F_{233} = M2' \dots\dots\dots (172)$$

$$3F_{223}F_{122} + 3F_{223}F_{133} = K3' \dots\dots\dots (173)$$

$$3F_{233}F_{122} + 3F_{233}F_{133} - 6F_{223}F_{123} = L3' \dots\dots\dots (174)$$

$$2F_{22}F_{123} + 2F_{33}F_{123} - 2F_{23}F_{122} - 2F_{23}F_{133} = M3' \dots\dots\dots (175)$$

To ensure closure of Eq. 157 the same asymptotes given by Eqs. 68 through 73 in section 3.1.2 should not intersect the prescribed surface.

3.2.3 EVALUATION OF F_{ij} AND F_{ij} FOR $i \neq j$

Assuming that there are experimental data from $n1$, $n2$, and $n3$ sets of biaxial load tests that correspond to $(\sigma_{1i}, \sigma_{2i})$ ($i = 1, 2, \dots, n1$), $(\sigma_{1i}, \sigma_{3i})$ ($i = 1, 2, \dots, n2$), and $(\sigma_{2i}, \sigma_{3i})$ ($i = 1, 2, \dots, n3$), respectively, it is possible to evaluate the interaction coefficients by a least-square fit of the cubic Eq. 157. Assuming that closure is not accomplished, one or more of the constraints that intersect the failure surface are shifted in space (i.e., their coefficients are modified) in such a manner that all constraints are satisfied and the surface is closed.

To use the same illustration as in section 3.1.3, suppose that the asymptotic plane is given by:

$$F_{22} + 3F_{122}\sigma_1 + 3F_{223}\sigma_3 = 0 \dots\dots\dots (176)$$

that is parallel with the σ_2 axis and intersects the open-ended failure surface shown in Fig. 9. Closure is accomplished by requiring that the plane given by Eq. 176 pass through the line $(-X', \sigma_2, -Z')$. Eq. 176 becomes an asymptotic plane for the failure surface (see Fig. 10). $\sigma_1 = -X'$ and $\sigma_3 = -Z'$ can be substituted into Eq. 157 to obtain the following relation:

$$\begin{aligned} &(-3F_{122}X' - 3F_{223}Z' + F_{22})\sigma_2^2 + (3F_{112}X'^2 + 3F_{233}Z'^2 - 2F_{12}X' - 2F_{23}Z' + F_2)\sigma_2 \\ &+ (-3F_{133}XZ'^2 - 3F_{113}X'^2Z' + 2F_{13}XZ' + F_{11}X'^2 + F_{33}Z'^2 - F_1X' - F_3Z' - I) = 0 \dots\dots (177) \end{aligned}$$

For an infinity of σ_2 roots to exist it follows from Eq. 177 that:

$$-3F_{122}X' - 3F_{223}Z' + F_{22} = 0 \dots\dots\dots (178)$$

$$3F_{112}X'^2 + 3F_{233}Z'^2 - 2F_{12}X' - 2F_{23}Z' + F_2 = 0 \dots\dots\dots (179)$$

$$-3F_{133}XZ'^2 - 3F_{113}X'^2Z' + 2F_{13}XZ' + F_{11}X'^2 + F_{33}Z'^2 - F_1X' - F_3Z' - I = 0 \dots\dots\dots (180)$$

Eq. 180 has the same form that would result if $\sigma_1 = -X'$ and $\sigma_3 = -Z'$ were substituted into the cubic criterion of Eq. 155.

Isolation of σ_1 and σ_3 quadratic terms in Eq. 157 leads to equations of constraint planes that are similar in form to Eq. 176 and are parallel to the σ_1 and σ_3 axes, respectively. These equations are:

$$-3F_{112}Y' - 3F_{113}Z' + F_{11} = 0 \dots\dots\dots (181)$$

$$3F_{122}Y'^2 + 3F_{133}Z'^2 - 2F_{12}Y' - 2F_{13}Z' + F_1 = 0 \dots\dots\dots (182)$$

$$-3F_{133}X' - 3F_{233}Y' + F_{33} = 0 \dots\dots\dots (183)$$

$$3F_{113}X'^2 + 3F_{223}Y'^2 - 2F_{13}X' - 2F_{23}Y' + F_3 = 0 \dots\dots\dots (184)$$

Using Lagrange multipliers to incorporate Eqs. 178, 179, and 181-184 as constraint conditions, the following functional is obtained for calculation of the interaction parameters:

$$\begin{aligned} \Phi = & \sum_{i=1}^{n1} (F_1 \sigma_{1i} + F_2 \sigma_{2i} + F_{11} \sigma_{1i}^2 + 2F_{12} \sigma_{1i} \sigma_{2i} + 3F_{112} \sigma_{1i}^2 \sigma_{2i} + 3F_{122} \sigma_{1i} \sigma_{2i}^2 - 1)^2 \\ & + \sum_{i=1}^{n2} (F_1 \sigma_{1i} + F_3 \sigma_{3i} + F_{11} \sigma_{1i}^2 + F_{33} \sigma_{3i}^2 + 2F_{13} \sigma_{1i} \sigma_{3i} + 3F_{113} \sigma_{1i}^2 \sigma_{3i} + 3F_{133} \sigma_{1i} \sigma_{3i}^2 - 1)^2 \\ & + \sum_{i=1}^{n3} (F_2 \sigma_{2i} + F_3 \sigma_{3i} + F_{22} \sigma_{2i}^2 + F_{33} \sigma_{3i}^2 + 2F_{23} \sigma_{2i} \sigma_{3i} + 3F_{223} \sigma_{2i}^2 \sigma_{3i} + 3F_{233} \sigma_{2i} \sigma_{3i}^2 - 1)^2 \dots (185) \\ & + \lambda_1 (-3F_{122} X' - 3F_{223} Z' + F_{22}) + \lambda_2 (3F_{112} X'^2 + 3F_{233} Z'^2 - 2F_{12} X' - 2F_{23} Z' + F_2) \\ & + \lambda_3 (-3F_{112} Y' - 3F_{113} Z' + F_{11}) + \lambda_4 (3F_{122} Y'^2 + 3F_{133} Z'^2 - 2F_{12} Y' - 2F_{13} Z' + F_1) \\ & + \lambda_5 (-3F_{133} X' - 3F_{233} Y' + F_{33}) + \lambda_6 (3F_{113} X'^2 + 3F_{223} Y'^2 - 2F_{13} X' - 2F_{23} Y' + F_3) \end{aligned}$$

where λ_i for $i = 1, 2, \dots, 6$ represent Lagrange multipliers, and summation indices $n1$, $n2$, and $n3$ range over the number of experimental tests carried out.

Minimizing the functional Φ yields the interaction coefficients F_{ij} and F_{ijj} for $i \neq j$. Fifteen equations are obtained with an identical number of unknowns. Coefficients F_i and F_{ii} ($i = 1, 2, 3$) need not be obtained from this expression since they are identical to the Tsai-Wu coefficients stated earlier.

The fifteen equations are the same as those indicated in Eqs. 112, 113, 115 through 118, and 120 through 128 of section 3.1. The sixteenth equation, which would correspond to Eq. 129, does not exist since the modified criterion is independent of hydrostatic failure stress and, thus, the interaction coefficient F_{123} is not part of the contracted tensorial polynomial.

3.2.4 EVALUATION OF F_{ijj} FOR $i = 1, 2, 3$, AND $j = 4$ OR 5 OR 6

For condition (b) in section 3.1.1 to be met the following asymptotic equations must exist:

$$3F_{144}\sigma_1 + 3F_{244}\sigma_2 + 3F_{344}\sigma_3 + F_{44} = 0 \dots\dots\dots(186)$$

$$3F_{155}\sigma_1 + 3F_{255}\sigma_2 + 3F_{355}\sigma_3 + F_{55} = 0 \dots\dots\dots(187)$$

$$3F_{166}\sigma_1 + 3F_{266}\sigma_2 + 3F_{366}\sigma_3 + F_{66} = 0 \dots\dots\dots(188)$$

The resulting asymptotes must not intersect projected images of the failure surface on the three planes (σ_1, σ_2) , (σ_1, σ_3) , and (σ_2, σ_3) . For this condition to be satisfied Eqs. 186-188 should not intersect the failure surface defined by Eq. 157. This condition occurs only if the planes described by these three equations are, at most, tangent to the cubic surface. For

simplicity, only one of these conditions is explicitly considered in the present discussion. Later, the concept is generalized to incorporate equations for the other two planes.

As an example, Eq. 188 is written as follows:

$$\sigma_3 = -\frac{(3F_{166}\sigma_1 + 3F_{266}\sigma_2 + F_{66})}{3F_{366}} \dots\dots\dots (189)$$

The following form of Eq. 157 is obtained by substitution of σ_3 from Eq. 189 and rearrangement of the result:

$$\begin{aligned} & (A_{16}\sigma_1^3 + A_{26}\sigma_1^2 + A_{36}\sigma_1 + A_{46}) + (B_{16}\sigma_2^3 + B_{26}\sigma_2^2 + B_{36}\sigma_2 + B_{46}) \\ & + (C_{16}\sigma_1^2\sigma_2 + C_{26}\sigma_1\sigma_2^2 + C_{36}\sigma_1\sigma_2) = 0 \end{aligned} \dots\dots\dots (190)$$

where, A_{16} , A_{26} , A_{36} , A_{46} , B_{16} , B_{26} , B_{36} , B_{46} , C_{16} , C_{26} , and C_{36} are constants that are functions of F_i , F_{ij} , and F_{i66} for $i = 1, 2, 3$. Only the C_{16} , C_{26} , and C_{36} constants depend on the coefficient F_{123} ; all others are the same as those described by Eqs. 135-142. The relations for the three constants are given by the following expressions (Roschke et al. 1990):

$$C_{16} = 27(F_{166}^2 F_{233} + 2F_{166}F_{266}F_{133} - F_{366}F_{266}F_{113} + F_{366}^2 F_{112}) \dots\dots\dots (191)$$

$$C_{26} = 27(F_{266}^2 F_{133} + 2F_{166}F_{266}F_{233} - F_{366}F_{166}F_{223} + F_{366}^2 F_{122}) \dots\dots\dots (192)$$

$$C_{36} = 18(F_{166}F_{266}F_{33} + F_{166}F_{66}F_{233} + F_{266}F_{66}F_{133} - F_{166}F_{366}F_{23} - F_{266}F_{366}F_{13} + F_{366}^2 F_{12}) \dots\dots\dots (193)$$

The closed-form solution of the cubic Eq. 190 yields repeating, real σ_1 and σ_2 roots at the points of tangency with some side conditions. The repeating roots and the side conditions are given by the relations:

$$27A_{16}^2 A_{46}^2 - 18A_{16}A_{26}A_{36}A_{46} + 4A_{16}A_{36}^3 - A_{26}^2 A_{36}^2 + A_{26}^3 A_{46} = 0 \dots\dots\dots (194)$$

$$27B_{16}^2 B_{46}^2 - 18B_{16}B_{26}B_{36}B_{46} + 4B_{16}B_{36}^3 - B_{26}^2 B_{36}^2 + B_{26}^3 B_{46} = 0 \dots\dots\dots (195)$$

$$C_{16} = 0 \dots\dots\dots (196)$$

$$C_{26} = 0 \dots\dots\dots (197)$$

$$C_{36} = 0 \dots\dots\dots (198)$$

A functional, Ψ , is defined from the closed-form solution of the bicubic Eq. 190, that yields repeating σ_1 and σ_2 roots at points of tangency, and side conditions $C_{16} = C_{26} =$

$C_{36} = 0$. Assuming that there are $n1$ sets of failure data, $(\sigma_{1i}, \sigma_{2i}, \sigma_{6i})$ for $i = 1, 2, \dots, n1$, Ψ takes the following form:

$$\begin{aligned} \Psi = & \sum_{i=1}^{n1} (F_1 \sigma_{1i} + F_2 \sigma_{2i} + F_{11} \sigma_{1i}^2 + F_{22} \sigma_{2i}^2 + F_{66} \sigma_{6i}^2 + 2F_{12} \sigma_{1i} \sigma_{2i} + 3F_{112} \sigma_{1i}^2 \sigma_{2i} \\ & + 3F_{122} \sigma_{1i} \sigma_{2i}^2 + 3F_{166} \sigma_{1i} \sigma_{6i}^2 + 3F_{266} \sigma_{2i} \sigma_{6i}^2 + 3F_{366} \sigma_{3i} \sigma_{6i}^2 - 1)^2 \\ & + \mu_1 (27A_{16}^2 A_{46}^2 - 18A_{16} A_{26} A_{36} A_{46} + 4A_{16} A_{36}^3 - A_{26}^2 A_{36}^2 + A_{26}^3 A_{46}) \dots\dots\dots (199) \\ & + \mu_2 (27B_{16}^2 B_{46}^2 - 18B_{16} B_{26} B_{36} B_{46} + 4B_{16} B_{36}^3 - B_{26}^2 B_{36}^2 + B_{26}^3 B_{46}) \\ & + \mu_3 C_{16} + \mu_4 C_{26} + \mu_5 C_{36} \end{aligned}$$

where μ_1 through μ_5 are Lagrange multipliers.

The functional, Ψ , reaches an extreme value (maximum or minimum) when:

$$\begin{aligned} \frac{\partial \Psi}{\partial F_{166}} = 0, \quad \frac{\partial \Psi}{\partial F_{266}} = 0, \quad \frac{\partial \Psi}{\partial F_{366}} = 0, \quad \frac{\partial \Psi}{\partial \mu_1} = 0, \\ \frac{\partial \Psi}{\partial \mu_2} = 0, \quad \frac{\partial \Psi}{\partial \mu_3} = 0, \quad \frac{\partial \Psi}{\partial \mu_4} = 0 \dots\dots\dots (200) \end{aligned}$$

A set of eight nonlinear simultaneous equations is obtained that yields coefficients F_{166} , F_{266} , and F_{366} and numerical values for the five Lagrange multipliers.

Similarly, Eqs. 186 and 187 may be rearranged as follows:

$$\sigma_2 = -\frac{(3F_{144}\sigma_1 + 3F_{344}\sigma_3 + F_{44})}{3F_{244}} \dots\dots\dots (201)$$

$$\sigma_1 = -\frac{(3F_{255}\sigma_2 + 3F_{355}\sigma_3 + F_{55})}{3F_{155}} \dots\dots\dots (202)$$

Relationships similar to Eq. 190 can be derived from Eqs. 201, 202, and Eq. 156 in the event that biaxial test data, $(\sigma_{1i}, \sigma_{3i}, \sigma_{4i})$ for $i = 1, 2, \dots, n2$ and $\sigma_{2i}, \sigma_{3i}, \sigma_{5i}$ for $i = 1, 2, \dots, n3$, respectively, exist. By an analogous analysis the interaction coefficients F_{144} , F_{244} , F_{344} , F_{155} , F_{255} , and F_{355} may be obtained, thus, yielding all interaction coefficients necessary for determining the failure surface.

4. EXPERIMENTAL INVESTIGATIONS

4.1 INTRODUCTION

In order to use the proposed criterion that is derived in sections 3.1 and 3.2 for failure prediction, the failure strength coefficients need to be experimentally determined. After these coefficients are known, Eq. 61 can be used to predict failure of a structure using components of the second-order stress tensor at each point in the body and assuming that hydrostatic failure can not be induced. The primary focus of the next three chapters is a description of a number of destructive laboratory experiments that have been conducted on cross-rolled beryllium sheet. Results and combinations of the results of these tests provide the failure coefficients for this material.

Figs. 11 through 14 give a complete list of the failure coefficients that are to be determined and a graphical listing of the required stress combinations. Axis labels 1, 2, and 3 correspond to the principal rolling, secondary rolling, and through-thickness directions, respectively. In addition, directions 4, 5, and 6 are associated with stresses acting on the (1-3), (2-3), and (1-2) planes, respectively. Tests in Fig. 11 are designed to place the specimen in a state of stress that causes failure due to normal stresses acting on each of the principal directions of the material. The last experiment shown in Fig. 11 is designed to yield the normal interaction coefficients for an in-plane biaxial state of stress. Each test shown in Fig. 12 induces a state of pure shear in a prescribed orthonormal direction. Figs. 13 and 14 show the experiments necessary for obtaining the normal-shear interaction coefficients.

A seminal reference for the experimental program is a report by Fenn et al. (1967). The report outlines extensive experimental work carried out on cross-rolled beryllium. Results of these tests are used in the current study for both initial constitutive model specifications and for estimation of the strength parameters for beryllium sheet. A summary of primary strength properties from the report by Fenn et al. is listed in Tables 4 and 5. It should be noted, however, that results in these tables were obtained from experimental work for 1.96-mm (0.077-in.) thick cross-rolled beryllium sheets. The current work involves 2.54-mm (0.10-in.) thick plates.

Not only does the report by Fenn et al. list test results for SR-200 material that is thinner than the current investigation, but the technique used for determining the through-thickness tensile strength is questionable. Specimens for this test were made from wafers of beryllium sheet that were diffusion-bonded between two pull rods of beryllium block. The

bonding process was carried out for 10 minutes at 649°C (1,200°F). Interlayers of 0.508-mm (2.0×10^{-3} -in.) copper foil were also used. Although this temperature is well below the recrystallization temperature for beryllium, reheating the material to 649°C causes the residual stresses that are present from the manufacturing process of cold rolling to be relieved. Alterations in the stress state can affect subsequent behavior of the material (Kojola 1961). Although there is no evidence that the moduli are affected by the bonding process, reduction of the ultimate tensile properties have been reported (Asceland 1989).

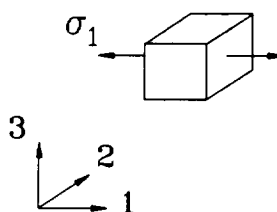
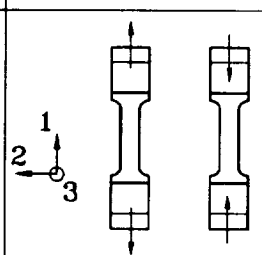
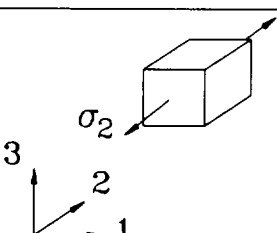
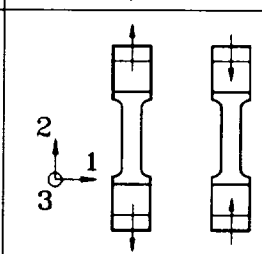
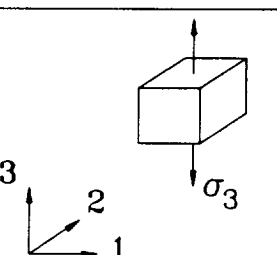
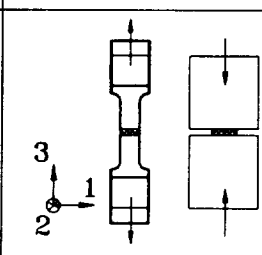
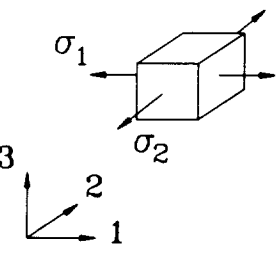
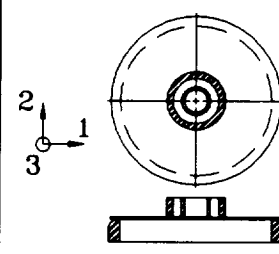
Failure Coefficients	Material Axes and State of Stress	Experiment(s)
F_1 F_{11}		
F_2 F_{22}		
F_3 F_{33}		
F_{12} F_{112} F_{122}		
1, 2, and 3 indicate primary rolling, secondary rolling, and through-thickness directions, respectively.		

FIG. 11. Experimental Determination of Failure Coefficients - A

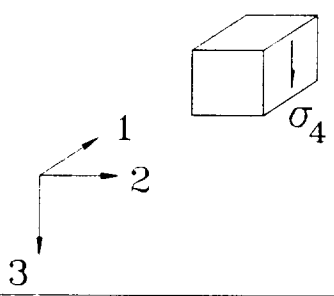
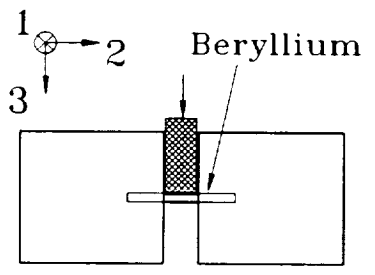
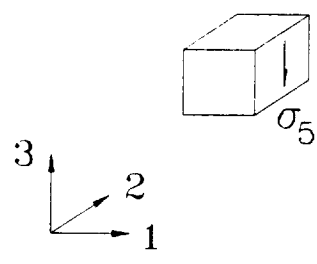
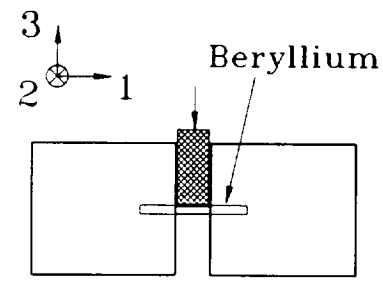
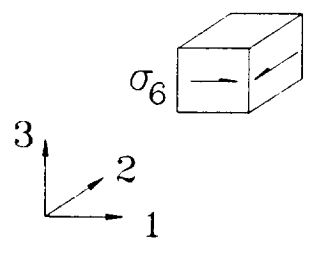
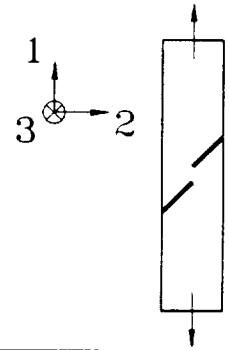
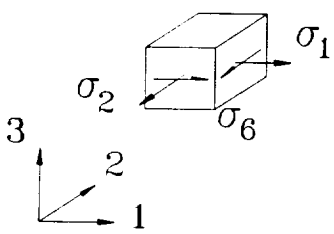
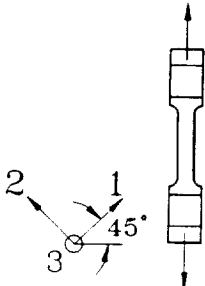
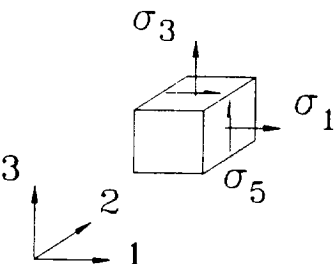
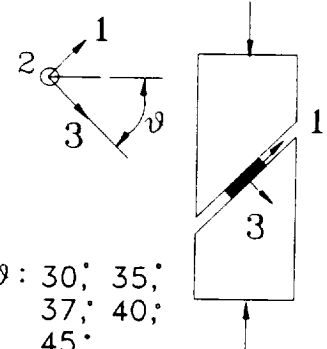
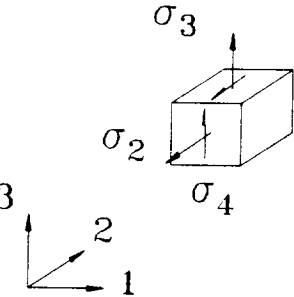
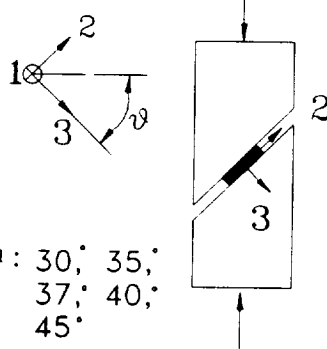
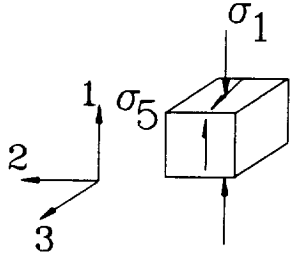
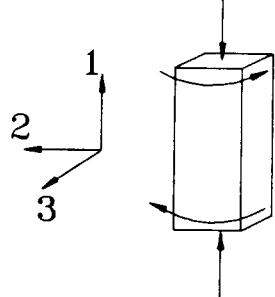
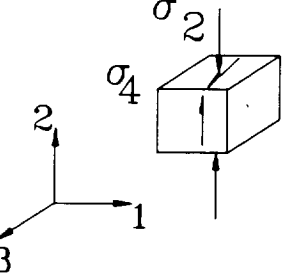
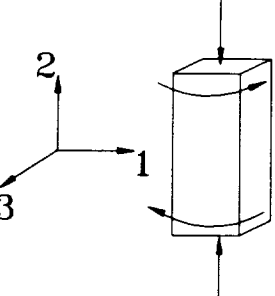
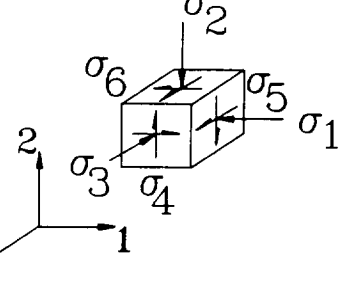
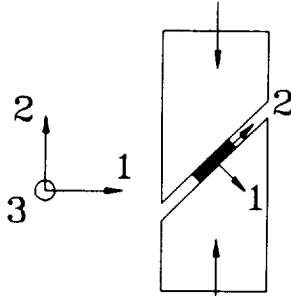
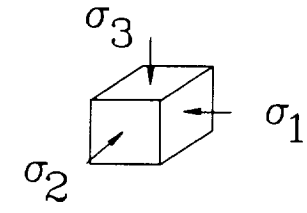
Failure Coefficients	Material Axes and State of Stress	Experiment(s)
F_{44}		
F_{55}		
F_{66}		
1, 2, and 3 indicate primary rolling, secondary rolling, and through-thickness directions, respectively		

FIG. 12. Experimental Determination of Failure Coefficients - B

Failure Coefficient	Material Axes and State of Stress	Experiment(s)
F_{166} F_{266}		
F_{13} F_{113} F_{133} F_{155} F_{355}		 $\varphi: 30^\circ, 35^\circ, 37^\circ, 40^\circ, 45^\circ$
F_{23} F_{223} F_{233} F_{244} F_{344}		 $\varphi: 30^\circ, 35^\circ, 37^\circ, 40^\circ, 45^\circ$

1, 2, and 3 indicate primary rolling, secondary rolling, and through-thickness directions, respectively

FIG. 13. Experimental Determination of Failure Coefficients - C

Failure Coefficients	Material Axes and State of Stress	Experiment(s)
F_{155}		
F_{244}		
F_{144} F_{255} F_{366}		
F_{123}		—

1, 2, and 3 indicate primary rolling, secondary rolling, and through-thickness directions, respectively

FIG. 14. Experimental Determination of Failure Coefficients - D

TABLE 4. Elastic Properties of 25.4-mm (0.10-in.) Thick SR-200 Sheet¹

Direction of Loading (1)	Elastic Modulus (GPa) (2)	Poisson's Ratios (3)
Longitudinal	298.7	$\nu_{12} = 0.0768$ $\nu_{13} = 0.0137$
Long transverse	293.6	$\nu_{21} = 0.0752$ $\nu_{23} = 0.0190$
Short transverse (Through-thickness)	347.5	$\nu_{31} = 0.0162$ $\nu_{32} = 0.0230$

Subscripts 1, 2, and 3 indicate the primary rolling, secondary rolling, and through-thickness directions, respectively.

1.0 ksi = 6.9 MPa

¹Fenn et al. 1967

TABLE 5. Uniaxial Tensile Strength of 25.4-mm (0.10-in.) Thick SR-200 Sheet¹

Direction (1)	Yield Stress (MPa) (2)	Ultimate Stress (MPa) (3)
Longitudinal	383.4	537.6
Long transverse	386.1	564.0
Short transverse	—	200.0

1.0 ksi = 6.9 MPa

¹Fenn et al. 1967

The remainder of this chapter deals with in-plane shear and biaxial experiments carried out at NASA Johnson Space Center (Henkener et al. 1991) and in-plane tensile tests carried out at Texas A&M University (Mascorro 1991; Mascorro et al. 1991) on 2.54-mm (0.10-in.) thick SR-200 sheet material. All experiments were performed in a controlled laboratory environment with constant room temperature and pressure. Experimental strength parameters deduced from these tests are used in conjunction with the results from tests reported in chapters 5 and 6 for estimation of principal and interaction coefficients. Tests in this chapter are presented in a synoptic way for the sake of completeness with respect to using results of known experimental work. Many of the laboratory experiments have also been simulated numerically in order to check or complement information obtained from transducers. Details of the simulation results are presented with each experiment. In many cases the predicted displacements, strains, and stresses for the beryllium specimens are reported by means of gray-scale fringe plots. More information concerning the numerical simulation is available in chapter 8.

4.2 TENSILE STATE OF STRESS

4.2.1 Specimens Aligned with Material Axes

Six plate specimens similar to those shown in Fig. 15 were obtained by NASA (Henkener et al. 1991) from Electrofusion Co. Three specimens have the principal rolling direction aligned with the loading axis and three have the secondary rolling direction aligned with the line of loading. Unfortunately, three of the specimens were sanded either on one or both sides. This is believed to have caused the beryllium to fail prematurely at a load near its yield strength. Results from the other three successful test specimens are listed in Table 6. A comparison of the results obtained by NASA with the ones tested by Fenn et al. (1967) shows that the tensile strengths for the 1.96-mm (0.077-in.) and 2.54-mm (0.10-in.) plate thicknesses are in agreement. However, in the secondary rolling direction the observed tensile strength of 497.1 MPa (72.1 ksi) for the 2.54-mm (0.10-in.) thick plate material is considerably lower than the 564.0 MPa (81.8 ksi) reported by Fenn et al. (1967).

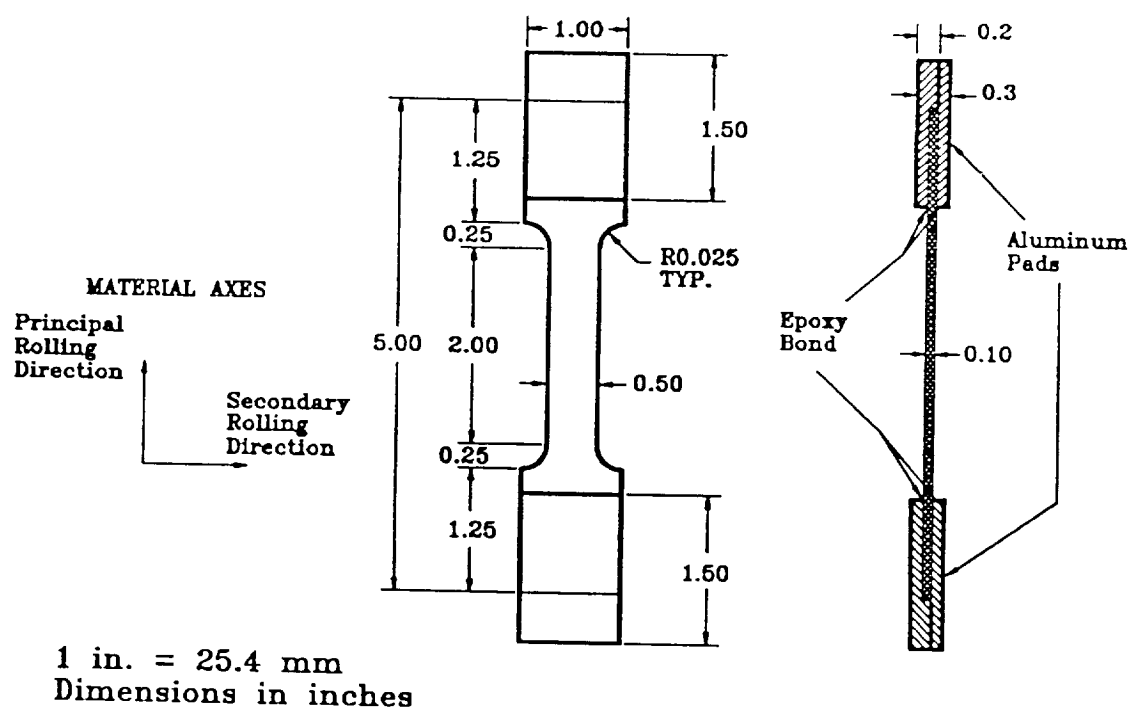


FIG. 15. In-Plane Tensile Specimen

Although two longitudinal and two transverse strain gages are used with three of the tensile specimens (Henkener et al. 1991), inconclusive results are reported for the total elongation. This is due to inconsistent specimen treatment (some specimens were sanded

while others were not) and variations in the rate of loadings for each specimen. In addition, the measured ultimate strengths exhibit significant variations, possibly for the same reasons. Thus, for the estimation of the failure coefficients the tensile results reported by Fenn et al. (1967) are used rather than the results reported by Henkener et al. (1991). Numerical simulation was not carried out for this experiment.

TABLE 6. Normal In-Plane Tensile Strengths for Cross-Rolled Beryllium

Specimen Number (1)	Orientations (2)	Failure Stress	
		MPa (3)	(ksi) (4)
1	Longitudinal	528.8	(76.7)
2		533.0	(77.3)
3 ^a		<u>551.6</u>	<u>(80.0)</u>
Average		537.8	(78.0)
1	Transverse	497.1	(72.1)
2 ^b		551.6	(80.0)
3 ^a		<u>579.2</u>	<u>(83.6)</u>
Average ^c		564.0	(81.8)

^aElectrofusion data; ^bFenn et al. (1967); ^cAverage of last two specimens.

4.2.2 Specimens with Material Axes Rotated 45°

Three beryllium sheet specimens were loaded in a uniaxial testing machine and tested to failure. A biaxial state of stress in the orthotropic material was achieved by orienting the material axes 45° from the direction of the load (Fig. 16). To minimize the possibility of failure at the grips, the three specimens were designed with curved transitions. Each specimen was loaded at a rate of 68.9 N/s (10 lb/s) using an 89-kN (20-kip) capacity MTS uniaxial testing machine. An MTS extensometer (Model 632.86B-03) was used to record through-thickness strains. Details of these tests are reported by Mascorro (1991).

An average Young's modulus for the three specimens is measured to be 29.5×10^4 MPa (42.8×10^6 psi) (Mascorro 1991). The average Poisson's ratio reported for in-plane and through-thickness deformations is 0.09 and 0.15, respectively. The latter number appears to be an order of magnitude larger than the through-thickness Poisson's ratio reported by Fenn et al. (1967) and an estimate from an ultrasonic technique (see section 7.2). It is believed that the inconsistency is due to a miscalibration of the MTS extensometer (clip gage).

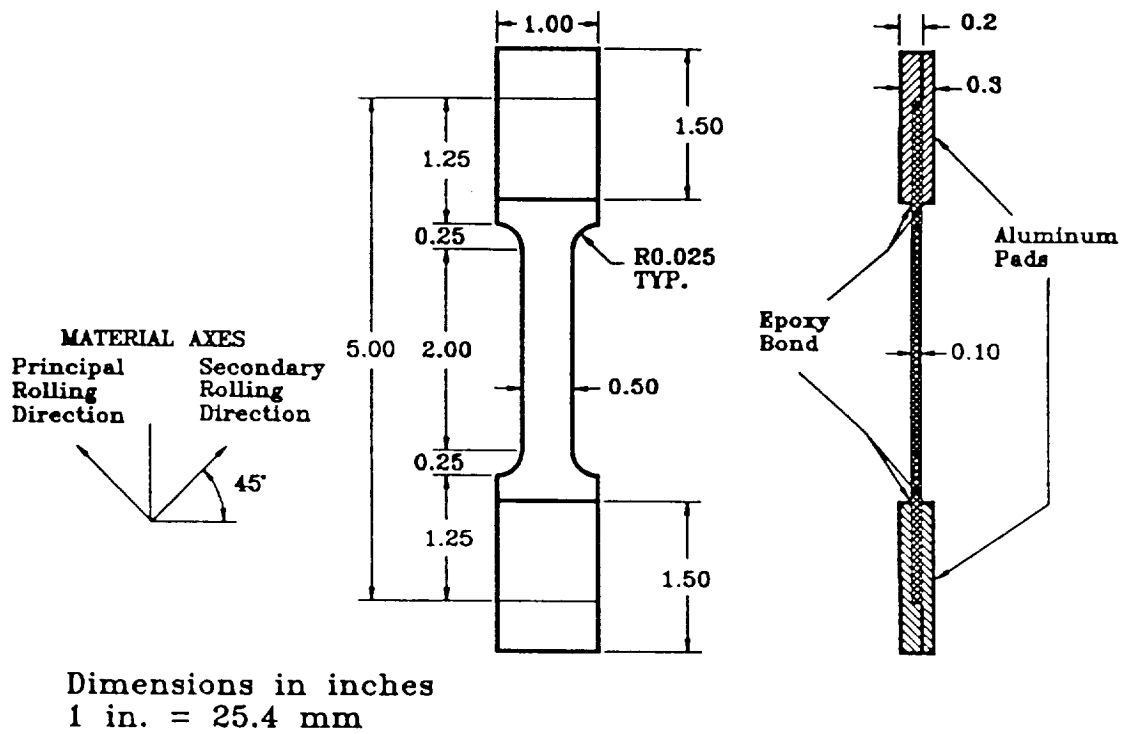


FIG. 16. Off-Axis In-Plane Tensile Specimen

Specimen 1 failed at a very low load of 369.5 MPa (57.7 ksi), that occurred almost immediately after yield. This may have been caused by the MTS clip gage scratching the surface or from a surface flaw in the specimen. To avoid scratching the surface of the second specimen 0.2032-mm (0.0080-in.) thick brass shims were placed between the specimen and the contact points of the MTS clip gage. Brass shims were not placed on specimen 3 because it was loaded to failure chronologically before the other two specimens.

In order to compare elastic properties obtained from an earlier test (Fenn et al. 1967) with data from this experiment, the stress tensor aligned with the loaded axis is transformed to the material axis (Lekhnitskii 1981). Components of the transformed stress tensor (see Appendix VI) are then substituted into the three-dimensional orthotropic elasticity equations that relate stress and strain. This leads to the stiffness equations:

$$S_{1x} = \frac{\sigma_x}{\varepsilon_1} = \frac{2E_1E_2}{E_2 - \nu_{12}E_1} \dots\dots\dots (203)$$

$$S_{2x} = \frac{\sigma_x}{\varepsilon_2} = \frac{2E_1E_2}{E_1 - \nu_{21}E_2} \dots\dots\dots (204)$$

$$S_{3x} = \frac{\sigma_x}{\epsilon_3} = -\frac{2E_1E_2}{\nu_{31}E_2 + \nu_{32}E_1} \dots\dots\dots (205)$$

where E_1 and E_2 are moduli in the longitudinal and long-transverse directions, respectively; S_{1x} and S_{2x} are the measured stiffnesses in the long (principal) rolled and transverse rolled (secondary) directions due to stress in the loaded "x" direction, respectively; and ν_{ij} are Poisson's ratios. Finally, engineering constants reported by Fenn et al. (1967) are substituted into Eqs. 203-205 for comparison with the off-axis tests. Results shown in Table 7 are in satisfactory agreement except for an order of magnitude difference in the short-transverse stiffness as discussed earlier.

Failure stresses for each of the specimens aligned 45° off of the material axes are listed in Table 8. Based on results from the second and third specimens (Mascorro 1991), failure strength under biaxial stress is 533.1 MPa (77.3 ksi). This is 4.7 MPa (0.7 ksi) less than the failure stress observed when the material is loaded only in the long (primary) direction, and 30.9 MPa (4.5 ksi) lower than the failure stress predicted for a specimen loaded only in the transverse (secondary) rolled direction.

TABLE 7. Comparison of Transformed Engineering Constants with Computed Stiffness

Stiffness	Off-Axis Experiment		Fenn et al. (1967)	
	GPa (2)	(10^3 ksi) (3)	GPa (4)	(10^3 ksi) (5)
E_x	295.0	(42.8)	295.2	(42.8)
S_{yx}	-3,062.0	(-444.1)	-3,753.5	(-544.4)
S_{1x}	644.0	(93.3)	646.7	(93.8)
S_{2x}	638.0	(92.5)	635.0	(92.1)
S_{3x}	1,990.0	(288.6)	18,084.0	(2,623.0)
G_{12}	137.1	(19.9)	136.9	(19.9)

TABLE 8. 45° Off-Axis Tensile Strengths under In-Plane Load

Specimen Number (1)	Orientations (2)	Failure Stress	
		MPa (3)	(ksi) (4)
1	45°	397.8	(57.7) ^a
2	45°	529.2	(76.8)
3	45°	<u>537.0</u>	<u>(77.9)</u>
Average		533.1	(77.3)

^aNot used to determine average.

The off-axis test results are useful for computing the failure interaction coefficient F_{12} (see Eqs. 119-120 and Fig. 11), since the stress transformation from the load to the material axes yields stress components in the material directions as follows:

$$\sigma_1 = \sigma_2 = 0.5\sigma_x \dots\dots\dots(206)$$

Appendix VI shows details of this transformation.

For this study, the in-plane tensile strengths in the principal and secondary material axis orientations, are taken to be

$$\begin{aligned} X_1 &= 537.8 \text{ MPa } (78.0 \text{ ksi}) \\ X_2 &= 564.0 \text{ MPa } (81.8 \text{ ksi}) \end{aligned} \dots\dots\dots(207)$$

Numerical simulation was not performed on these tests.

4.3 IN-PLANE SHEAR STATE OF STRESS

NASA conducted an experiment on five cross-rolled beryllium sheets having a special geometry and a load that is designed to induce a shear failure (Henkener et al. 1991). Geometry and loading of the specimens are illustrated in Figs. 17 and 18, respectively. Five nearly identical specimens are tested in order to obtain adequate data for statistical sampling analysis. Three specimens (3, 4, and 5) are deliberately sanded in a specified direction: two are parallel and one is oriented 45° with respect to the loading direction. All specimens are brought to failure via displacement-controlled loading at a rate of 1.1×10^{-2} mm/s (2.0×10^{-2} in./min). The specimens are instrumented with rosette strain gages for determination of yield and ultimate strain components (Henkener et al. 1991). Specifically, strain gages were mounted in the longitudinal, long transverse, and short transverse directions for three specimens. The other three specimens were instrumented using a ladder gage, a line of ten closely-spaced gages, in the direction of the applied load for possible observation of the Luder's band effect.

Table 9 summarizes the yield and ultimate in-plane shearing strengths obtained from this experiment. The fixture-to-specimen bond of one of the unsanded specimens failed during loading (specimen 1) and, thus, the ultimate shearing strength was not attained. The two specimens that were sanded parallel to the loading direction (specimens 3 and 4) did not appear to be affected by this action. However, specimen 5 was sanded 45° off axis and failed prematurely at well below the ultimate shearing strength for an unsanded specimen. Fig. 19 shows the failure pattern of cracks for specimen 3.

Numerical simulation of the loaded structure at failure is used for comparison with experimental results. The simulation is accomplished using eight-noded, plane stress

elements. Special care is taken in modeling the geometry of the region surrounding the notches of the shear specimen. The numerical model considers linear, orthotropic material behavior and effects of large displacement. An average ultimate load of 19.1 kN (4.3 kip) is used for the numerical analysis. Fringe plots of displacements, strains, and stresses are shown in Figs. 20-27 for the ultimate load. Figs. 20 and 21 show components of axial and transverse displacement, respectively. The leftmost point of the structure is restrained from displacement and load is applied parallel to the horizontal axis. Figs. 22-24 display axial (ϵ_1), transverse (ϵ_2), and shear (ϵ_6) components of strain, respectively. The region between the notches has approximately -5.1×10^{-4} m/m (-5.1×10^{-4} in./in.), -3.3×10^{-4} m/m (-3.3×10^{-4} in./in.), and 2.4×10^{-3} m/m (2.4×10^{-3} in./in.) of axial, transverse, and shearing strain, respectively, at failure (Figs. 22-24).

Figs. 25-27 show components of normal (σ_1), transverse (σ_2), and shearing stress (σ_6), respectively. In-plane shearing stresses in the portion between the two notches of the small plate are the prevailing stresses. Moreover, it is observed that the distribution of all components of stress in this region is nearly constant from one notch to the other (see Figs. 25-27). The average in-plane shearing stress in this region is approximately 313.0 MPa (45.4 ksi). The magnitude of the normal and transverse stresses in the same region, although considerably smaller than that of the shearing stress, are not small enough to be neglected. The normal stress is approximately -68.0 MPa (-9.9 ksi) and the transverse stress is approximately -149.6 MPa (-21.7 ksi).

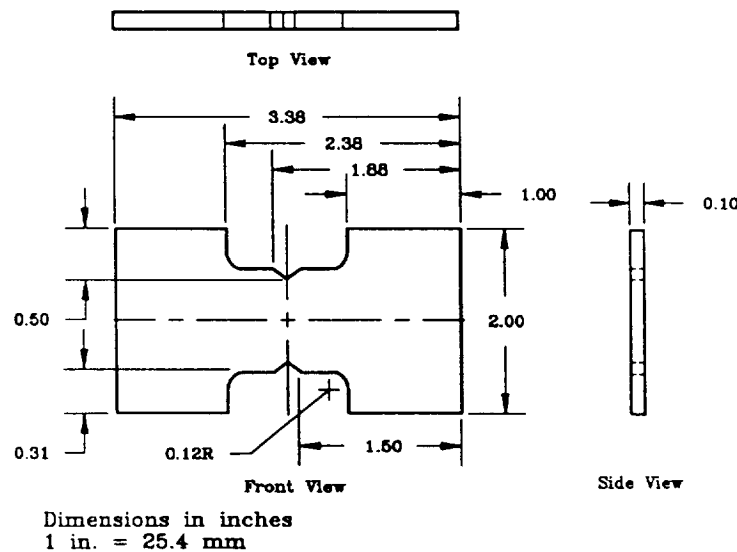


FIG. 17. In-Plane Shear Specimen

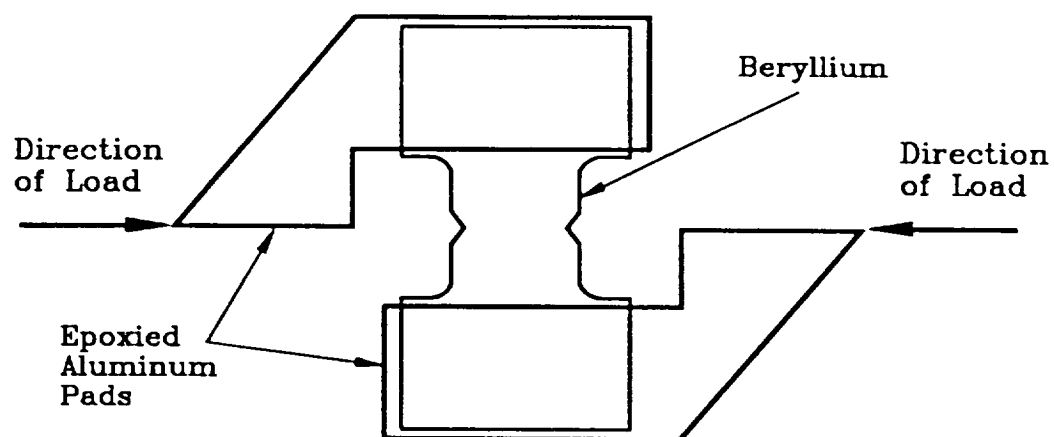


FIG. 18. Loading Arrangement for In-Plane Shear Test

TABLE 9. In-Plane Shearing Strengths (Henkener et al. 1991)

Specimen Number	Surface Finish	Yield		Ultimate	
		MPa	(ksi)	MPa	(ksi)
(1)	(2)	(3)	(4)	(5)	(6)
1	Unsanded	204.8	(29.7)		
2	Unsanded	204.8	(29.7)	300.6	(43.6)
3	Sanded	206.8	(30.0)	311.0	(45.1)
4	Sanded	203.4	(29.5)	307.5	(44.6)
5	Sanded	203.4	(29.5)	265.5	(38.5)

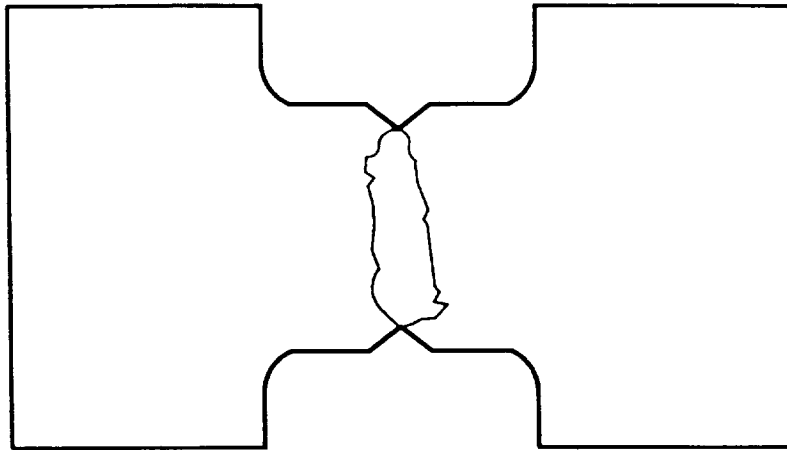


FIG. 19. Fracture Pattern for Unsanded Shear Specimens

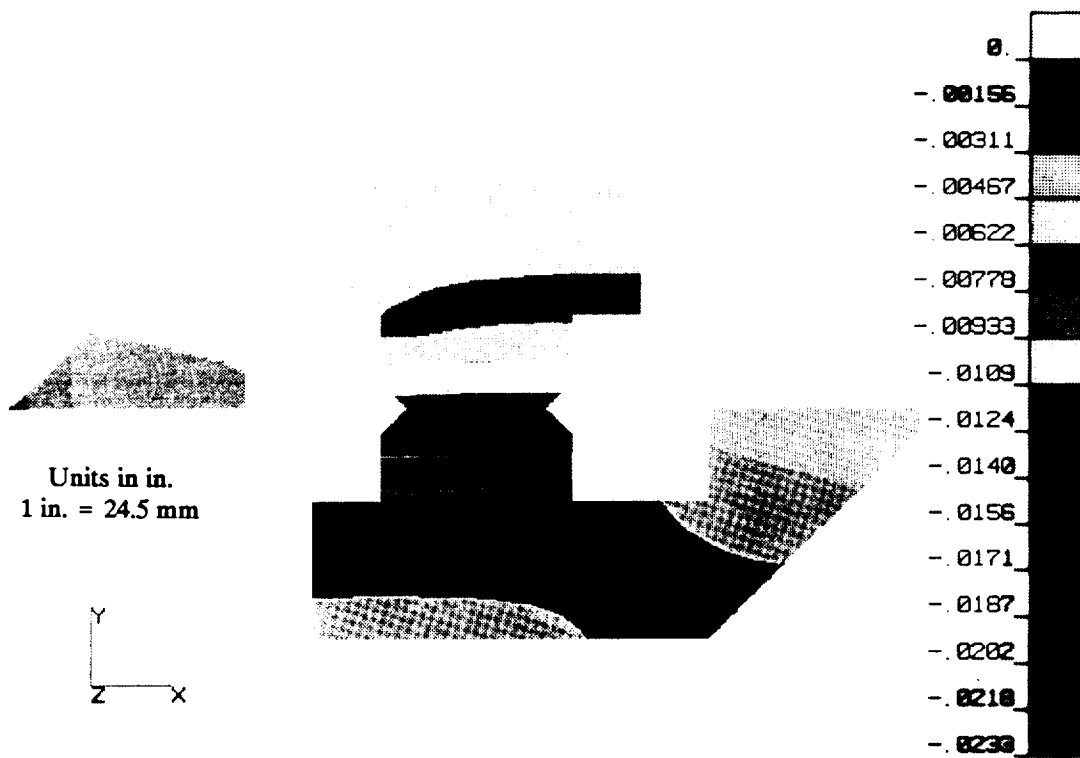


FIG. 20. Shear Specimen Fringe Plot of Axial Displacement

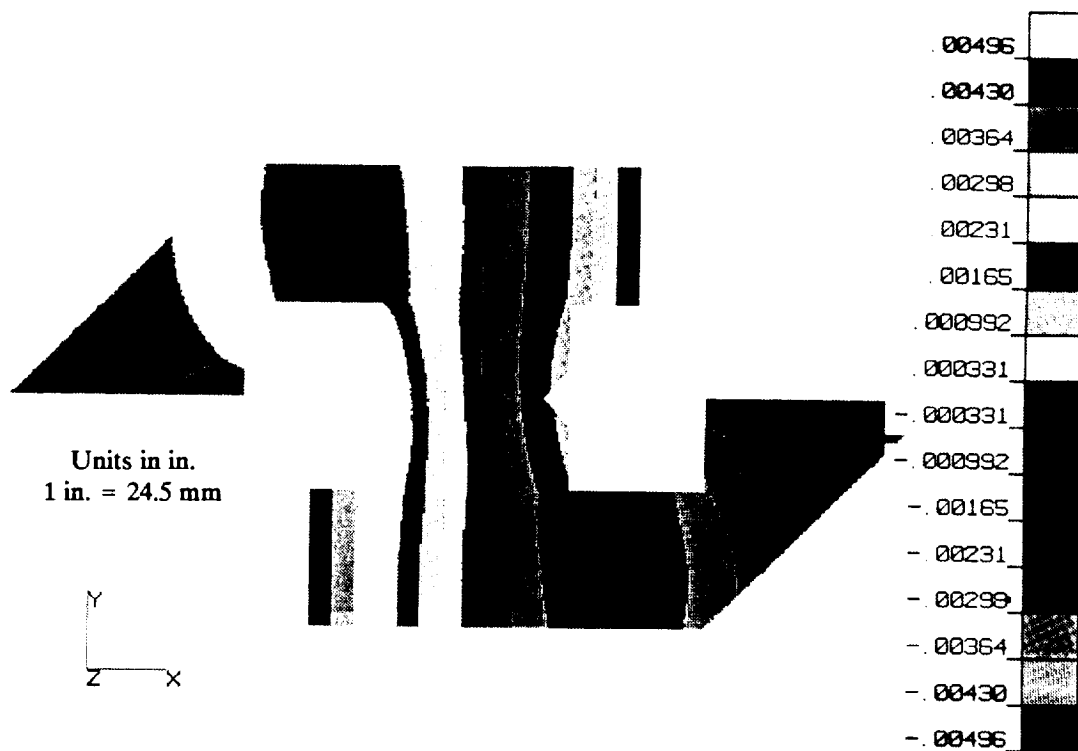


FIG. 21. Shear Specimen Fringe Plot of Transverse Displacement

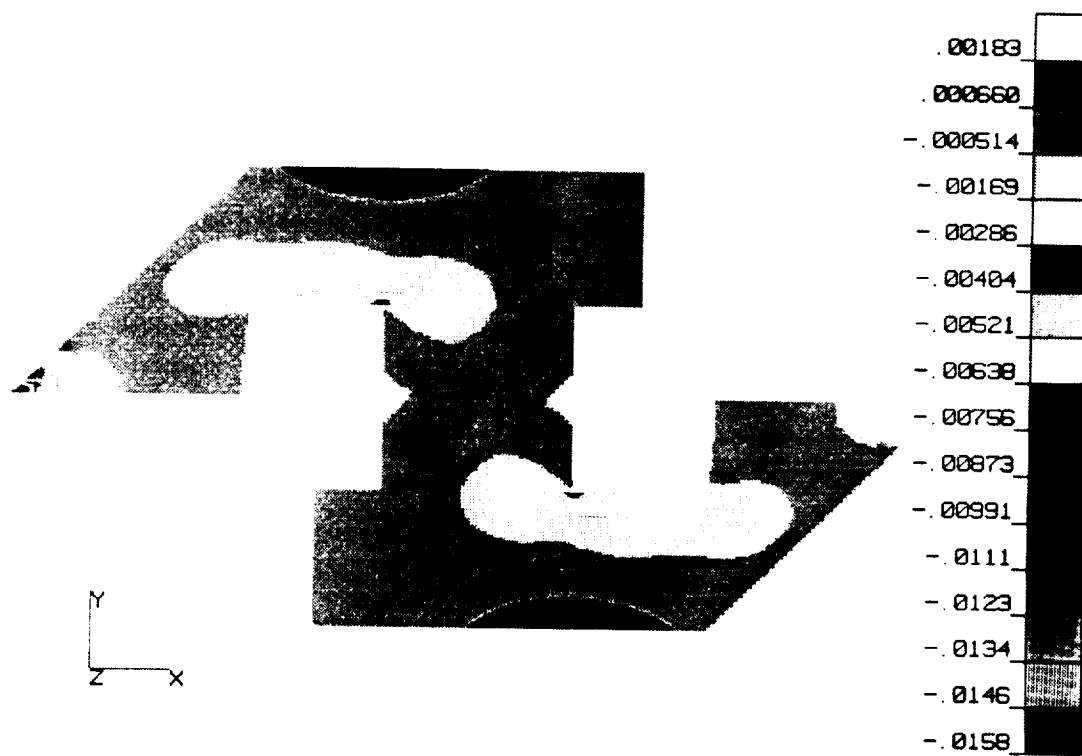


FIG. 22. Shear Specimen Fringe Plot of Axial Strain, ϵ_1

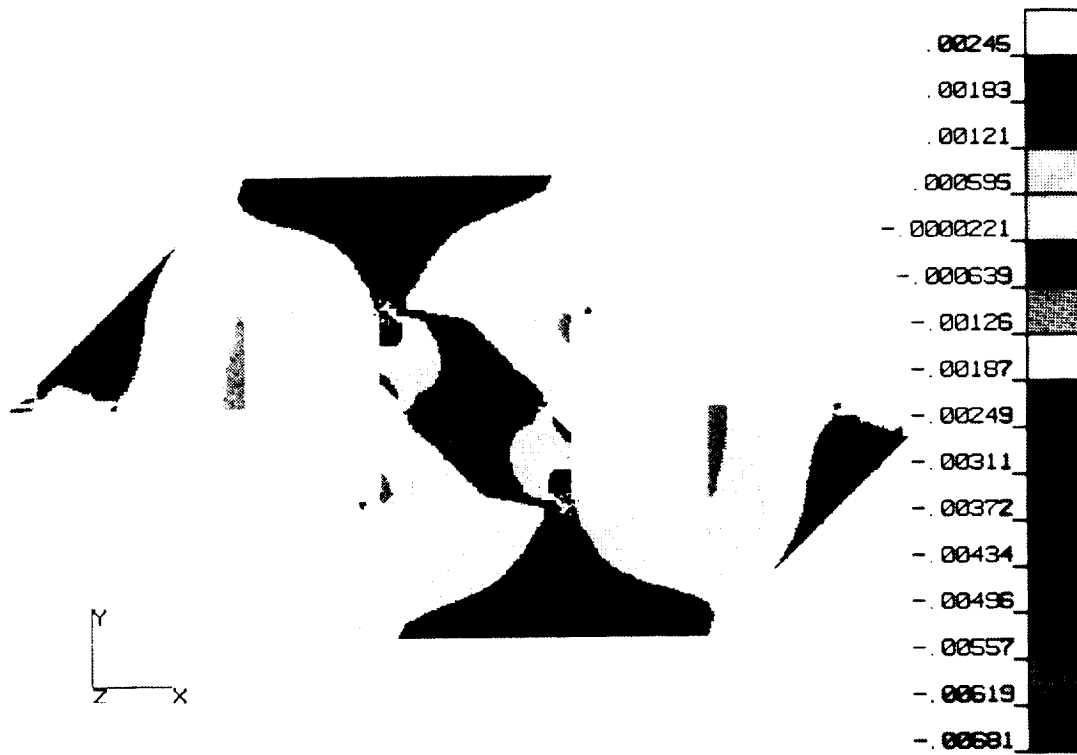


FIG. 23. Shear Specimen Fringe Plot of Transverse Strain, ϵ_2

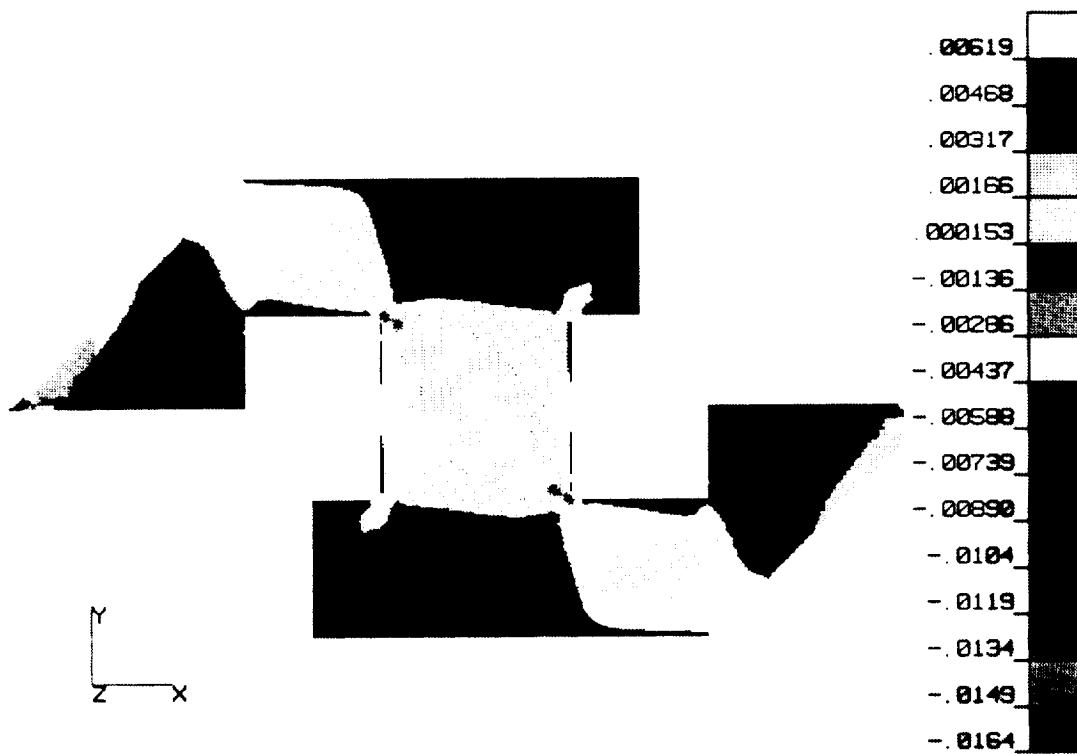


FIG. 24. Shear Specimen Fringe Plot of Shearing Strain, ϵ_6



FIG. 25. Shear Specimen Fringe Plot of Axial Stress, σ_1

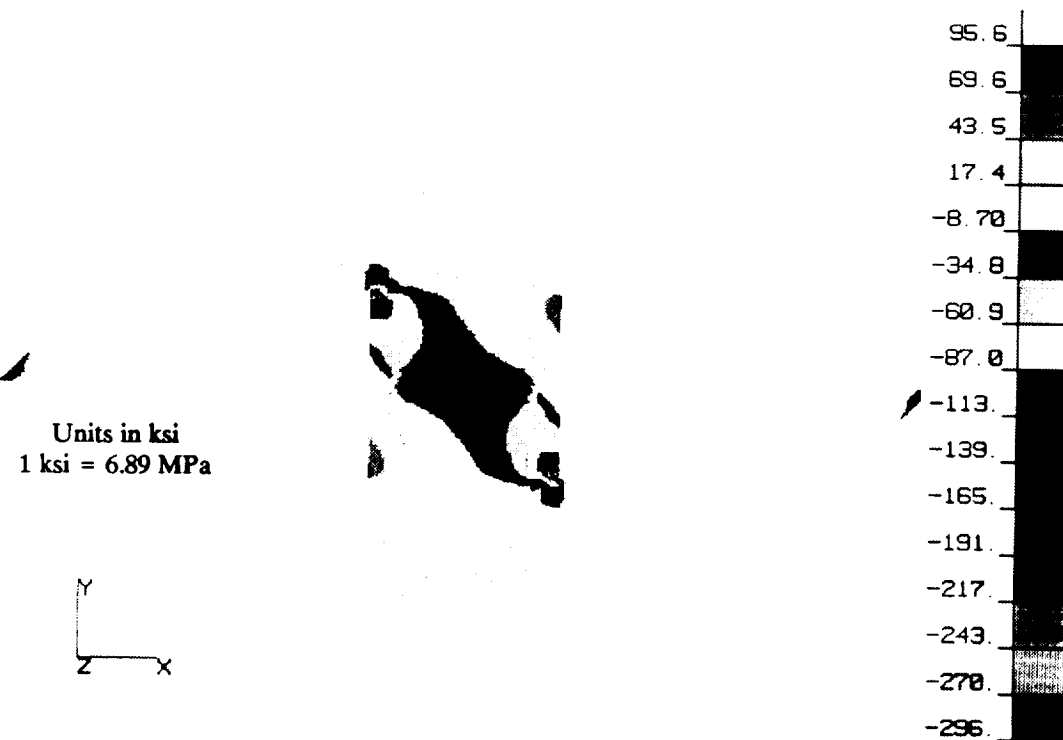


FIG. 26. Shear Specimen Fringe Plot of Transverse Stress, σ_2



FIG. 27. Shear Specimen Fringe Plot of Shearing Stress, σ_x

Although a state of pure shear is not obtained from this experiment, a value of pure shearing stress can be computed on a differential element located equidistant between the notches. Using an elementary stress transformation (Dally and Riley 1978) yields a pure shearing stress of 296.5 MPa (43.0 ksi) on a plane that is 2.0° from the x-axis.

The numerical analysis discussed earlier agrees reasonably well with the results obtained from the experiment. Taking an average of the shearing strength of specimens 2, 3, and 4 yields an ultimate in-plane shearing stress of 306.4 MPa (44.4 ksi). This value is obtained by dividing the ultimate load by the area between the notches for each specimen and averaging the results. It is noted that the experimentally determined ultimate shearing stress is approximately 2% lower than the numerically predicted value. In order to be conservative, the experimental value is chosen to represent the in-plane shearing strength of cross-rolled beryllium. In chapter 5 this failure stress is compared with the average in-plane shearing strength computed from another experiment. The smaller of these two values is used as the final shearing strength to compute principal and interaction strength coefficients.

4.4 IN-PLANE BIAXIAL STATE OF STRESS

Interaction coefficients F_{12} , F_{112} , and F_{122} are established by experimental determination of the in-plane biaxial strength of the material (Fig. 11). A number of experimental arrangements have been proposed for obtaining the biaxial strength of a plate structure. The most recent approach is discussed by Ferron and Makinde (1988). To date all of these techniques require slot or hole drilling and/or a reduced middle section of the structure to ensure that the material fails near the center of the plate. Beryllium cross-rolled sheet can not be adapted to these geometrical requirements due to the sensitivity of its strength to holes and surface flaws that are invariably developed during construction of such specimens.

A different approach is used in the current study to obtain a biaxial state of stress that causes failure in the material. A series of tests on circular plates made of cross-rolled beryllium was conducted at Johnson Space Center (Henkener et al. 1991). Two 165.1-mm (6.5-in.) diameter circular disks were tested to failure. A schematic of the loading arrangement is shown in Fig. 28 for two loading situations. Fig. 29 shows linear-variable-differential-transformers (LVDT) and strain gage locations. The first disk was loaded with a concentric ring that is 25.4 mm (1.0 in.) in diameter. Experimental data were established at 50, 75, and 100 percent of the material's yield stress, as well as at ultimate loading. Transducer output includes readouts from strain gages and LVDTs. A similar procedure was repeated for the second beryllium disk using a 50.8-mm (2.0-in.) concentric ring load.

The purpose of this experiment is to establish a state of stress that closely approximates pure bending moment within the loading rings. Significant shearing stresses and torsional moments are avoided by concentric application of the load ring about the center of the plate. This can be regarded as the two-dimensional extension of the well-known four-point bending test of a simply-supported beam.

Simulation of the 25.4-mm (1.0-in.) and 50.8-mm (2.0-in.) load experiments is carried out using six-hundred twenty-noded isoparametric hexahedral elements with ten elements through the thickness of the plate. Orthotropic material properties for cross-rolled beryllium are used with through-thickness inhomogeneous distribution of material (see chapter 8). In addition, large displacement theory is considered. The numerical model is constrained from displacement in the out-of-plane direction along the cylindrical aluminum support. A uniformly distributed line load is applied in a concentric manner to simulate the ring loadings. Due to symmetry of loading and geometry, only one-quarter of the actual plate structure is modeled with finite elements. A summary of the results of these experiments is shown in Table 10. Each experiment is discussed in the following sections.

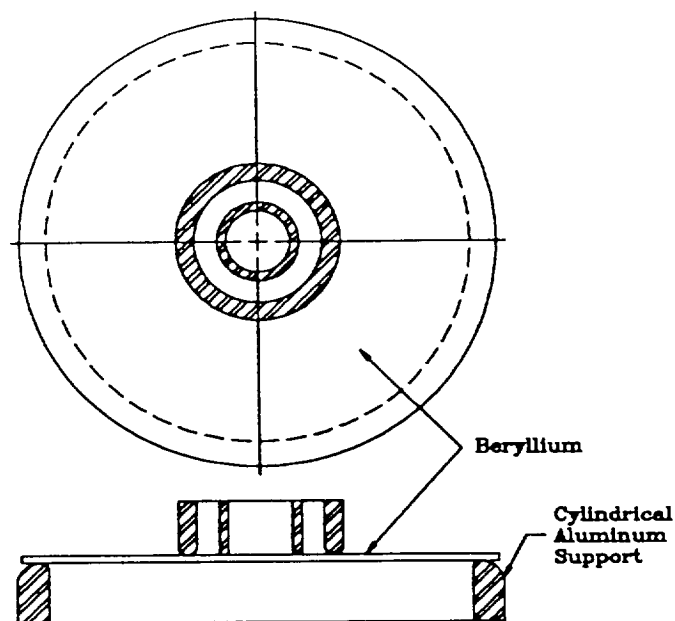


FIG. 28. 25.4-mm (1.0-in.) and 50.8-mm (2.0-in.) Ring Loadings

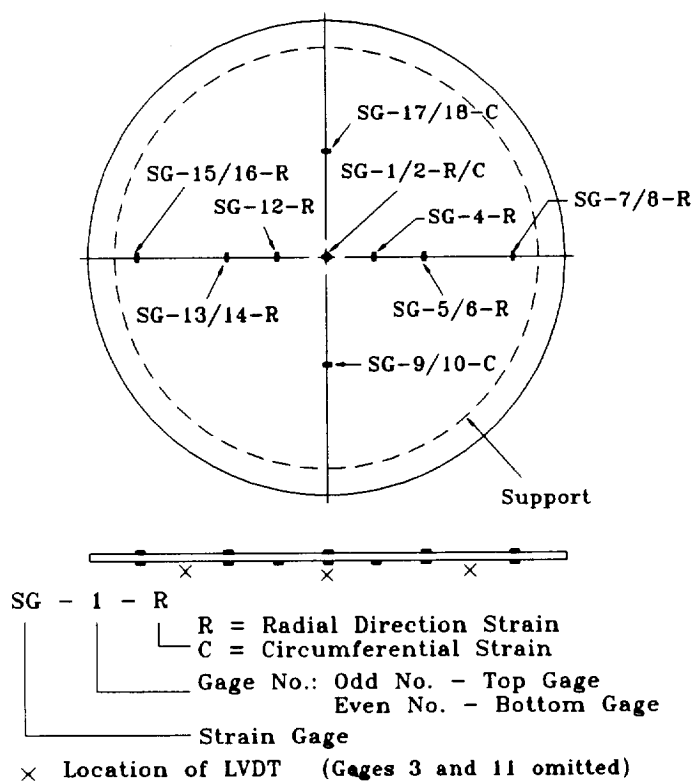


FIG. 29. Gage and LVDT Locations for Circular Plate Specimens

TABLE 10. Experimental In-Plane Biaxial Stress Output - NASA

State of Stress (1)	25.4-mm Ring Load		50.8-mm Ring Load	
	MPa (2)	(ksi) (3)	MPa (4)	(ksi) (5)
50% of yield	191.7	(27.8)	188.2	(27.3)
75% of yield	289.6	(42.0)	283.4	(41.1)
100% of yield	379.9	(55.1)	370.9	(53.8)
Failure	834.3	(121.0)	827.4 ^a	(120.0)

^a Maximum Failure Stress = 930.8 MPa (135.0 ksi)

4.4.1 25.4-mm Ring Load

In order to obtain the components of stress at the failure load, the numerically predicted displacements and strains are compared with those measured by the transducers during the experiment. Fig. 30 compares experimental and numerically predicted vertical displacements along a radial line at the yield and ultimate stress levels. These two cases correspond to loads of 1.9 kN (0.4 kip) and 6.0 kN (1.4 kip), respectively. Experimentally measured displacements at the center and at one intermediate location between the supported edge and the center of the plate are also plotted for comparison with the finite element prediction. Agreement between measured and predicted values is excellent at the load level that causes the yield stress and within 1% at the ultimate load. Fig. 31 shows a fringe plot of vertical deflection that is obtained from the finite element analysis. Figs. 32 and 33 show numerically simulated in-plane displacement components in the two orthogonal x and y directions, respectively. In the vicinity of the 25.4-mm (1.0-in.) ring these in-plane components are several orders of magnitude less than their vertical counterparts.

Fig. 34 shows a graph of strain versus distance from the center of the plate. This figure provides a simple comparison of finite element and experimental results for normal strain at the yield and ultimate stress levels of load. Experimentally determined normal strains at gage locations on the bottom of the plate (Fig. 29) are in good agreement with the finite element simulation.

Distribution of normal strain in the direction of the longitudinal (principal) axis of rolling, ϵ_l , at the ultimate load level is also shown by means of a fringe plot in Fig. 35 for one quadrant of the plate. This figure shows strain on the bottom surface of the plate. A nearly symmetric pattern is observed. The highest gradient of strain occurs well outside of the line of the ring load.

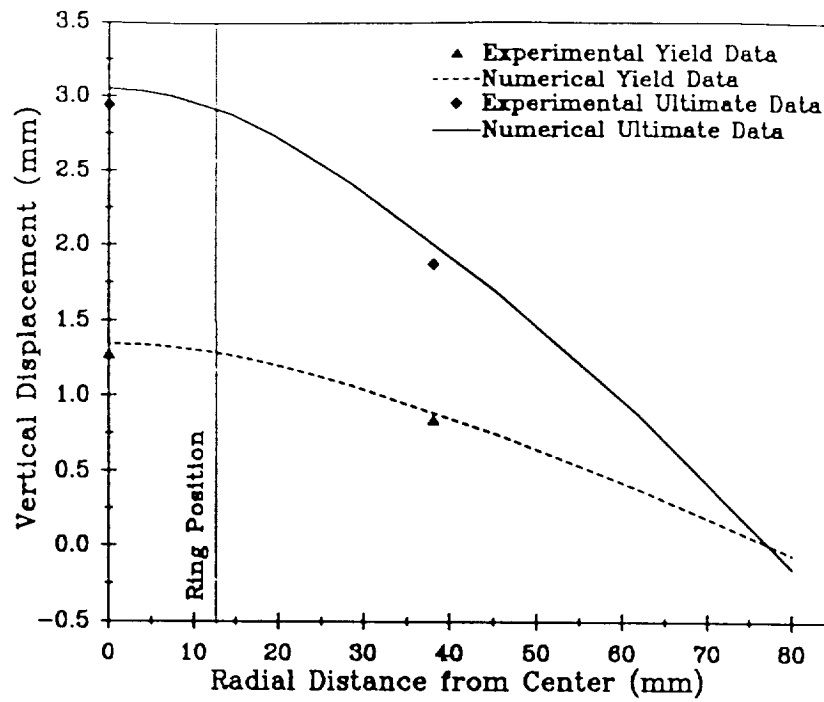


FIG. 30. Vertical Displacement along a Radial Line at Yield and Ultimate Stress for 25.4-mm (1.0-in) Load

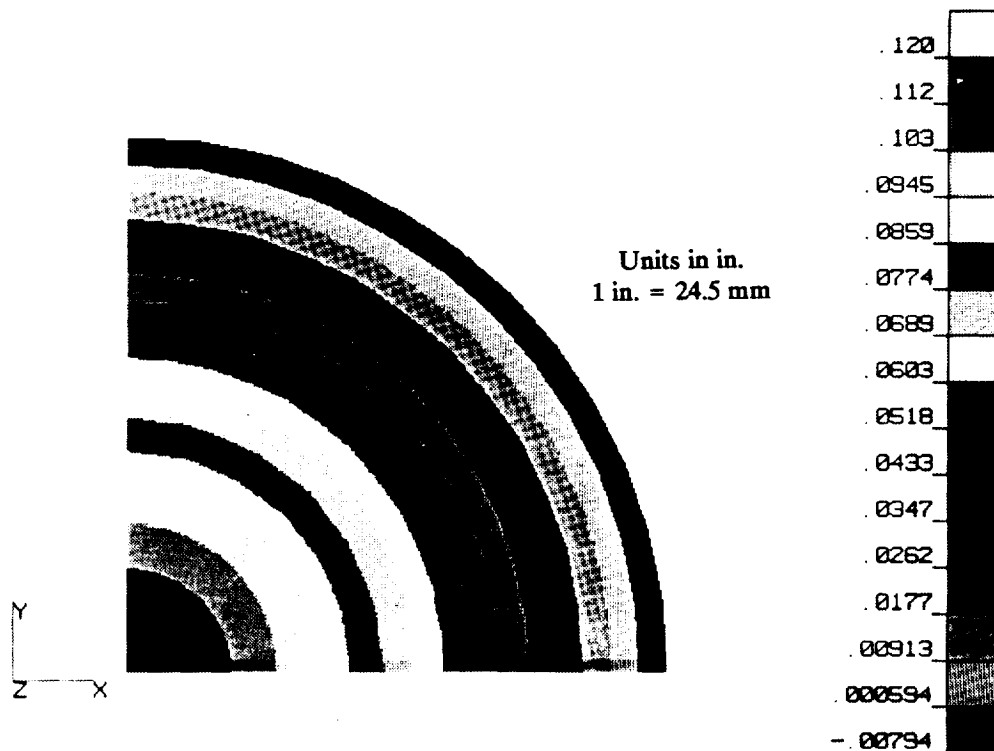


FIG. 31. Plate with 25.4-mm Ring at Ultimate Load Fringe Plot of Vertical Displacement

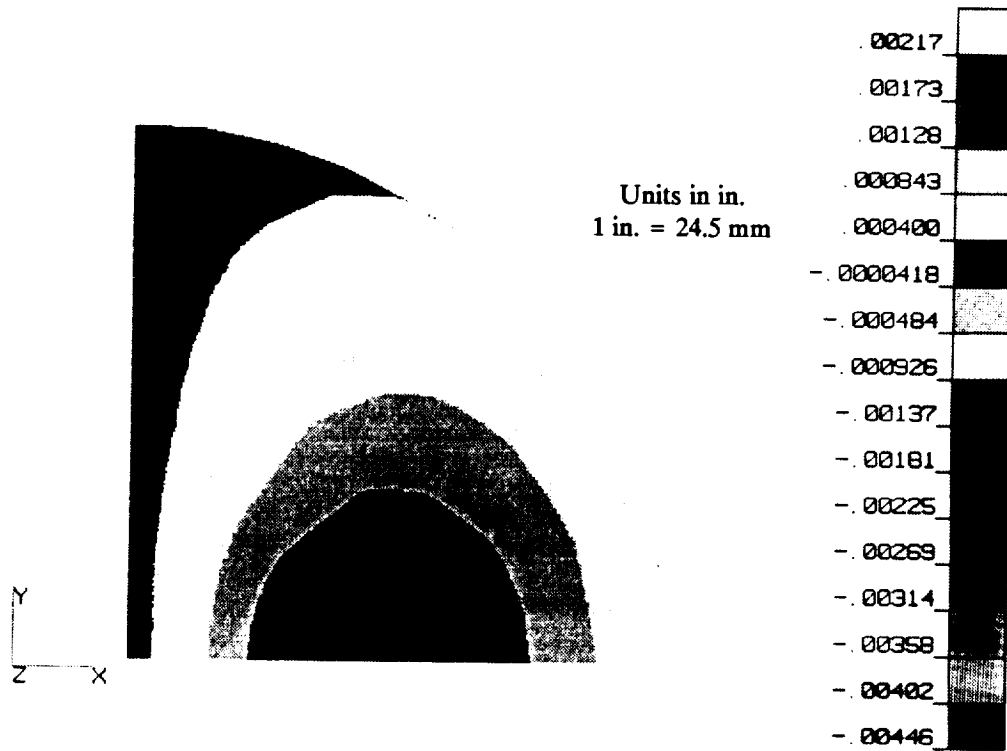


FIG. 32. Plate with 25.4-mm Ring at Ultimate Load Fringe Plot of In-Plane Displacement in the X-Direction

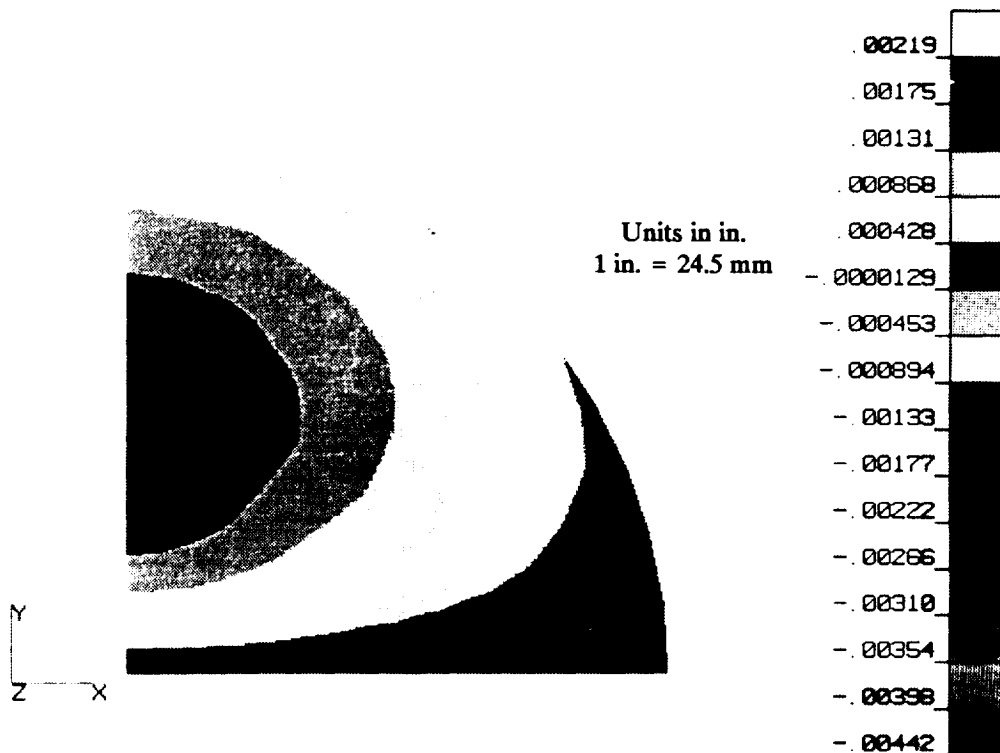


FIG. 33. Plate with 25.4-mm Ring at Ultimate Load Fringe Plot of In-Plane Displacement in the Y-Direction

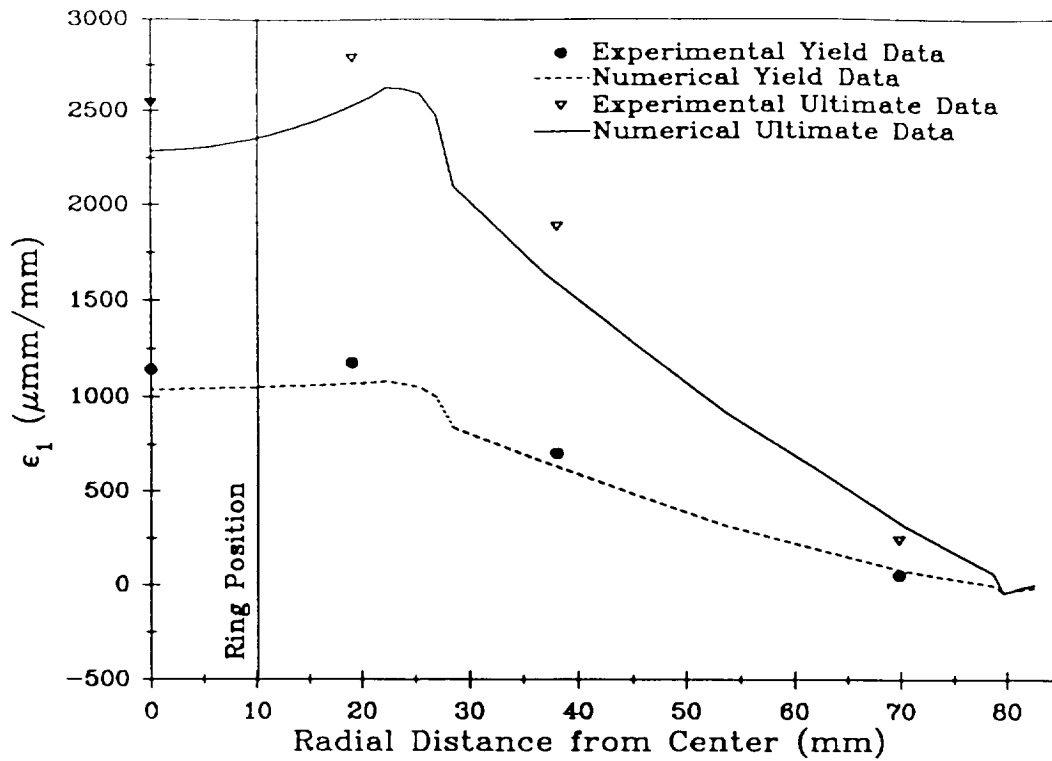


FIG. 34. Radial Strains at Yield and Ultimate Stress for 25.4-mm (1.0-in) Load

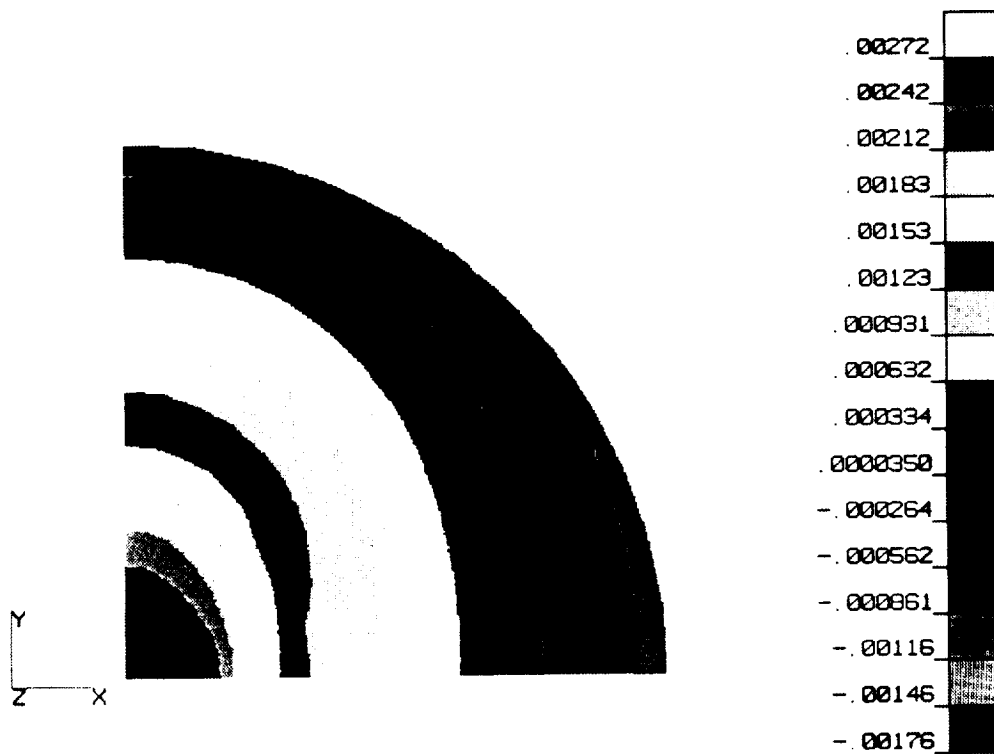


FIG. 35. Plate with 25.4-mm Ring at Ultimate Load Fringe Plot of ϵ_1 Strain

Distribution of normal strain, ϵ_2 , in the transverse direction of cross-rolling at the ultimate load is shown in Fig. 36 for the same quadrant of the plate. The magnitude of this bottom surface strain is approximately the same as the normal strain that occurs in the longitudinal direction of cross-rolling (Fig. 35). The distributions are nearly mirror images of each other.

A gray scale fringe plot of in-plane shearing strain, ϵ_6 , is shown in Fig. 37 for the bottom surface of the plate. This figure illustrates the fact that although this component of strain is significantly large outside of and at the location of the loading ring (-6.3×10^{-4} mm/mm), inside the ring the magnitude of this strain is almost negligible (-3.0×10^{-5} mm/mm). Within the 25.4-mm ring, however, the out-of-plane strain, ϵ_3 , in the through-thickness direction is approximately 20% of ϵ_1 and ϵ_2 as shown in Fig. 38. Although Fig. 38 illustrates this phenomenon only for the bottom surface of the structure, the statement is valid for all the through-thickness, inhomogeneous layers that comprise the plate. Finally, fringe plots in Figs. 39 and 40 show that out-of-plane shearing strains can be readily neglected due to the fact that they are at least an order of magnitude smaller than the in-plane components of strain.

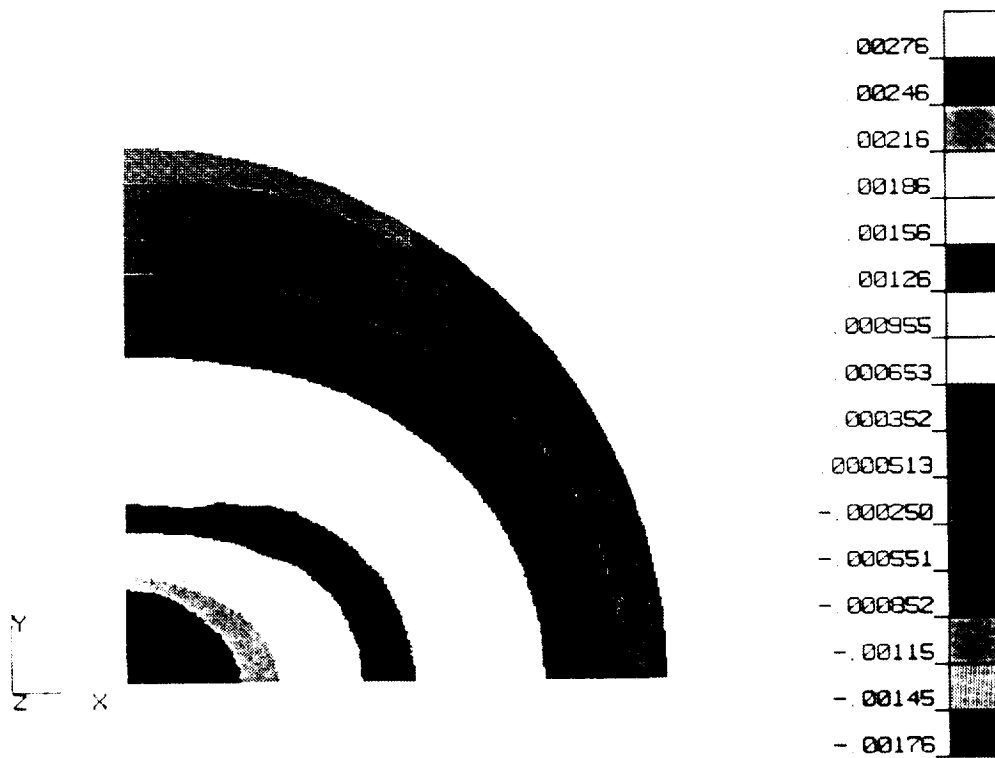


FIG. 36. Plate with 25.4-mm Ring at Ultimate Load Fringe Plot of ϵ_2 Strain

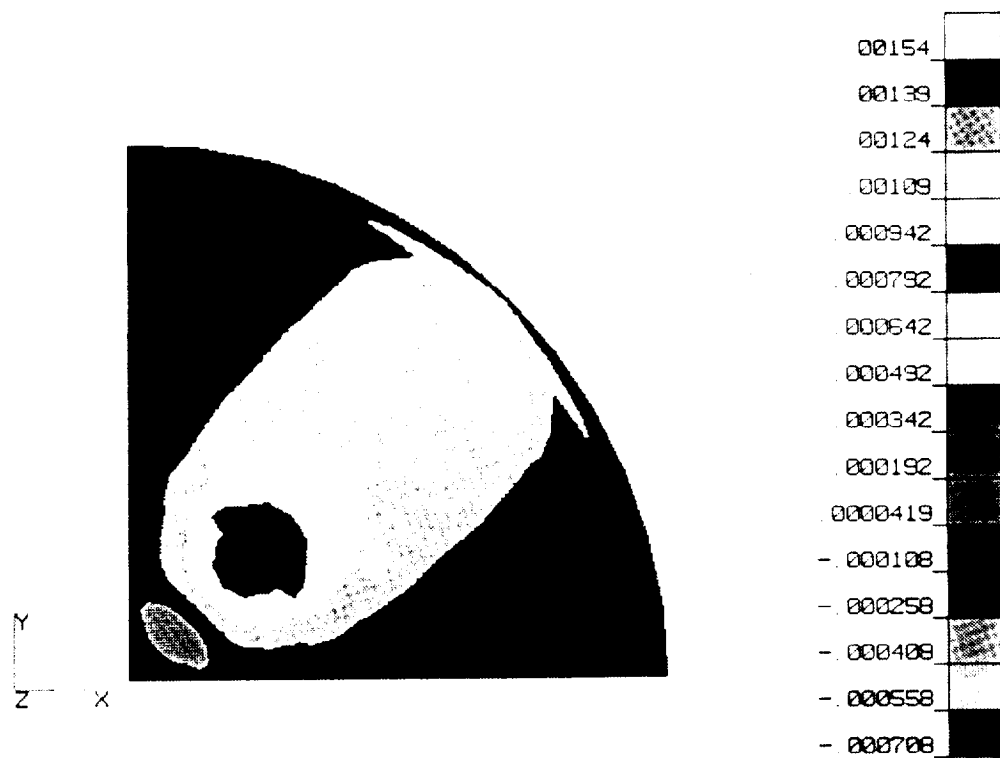


FIG. 37. Plate with 25.4-mm Ring at Ultimate Load Fringe Plot of ϵ_6 Strain

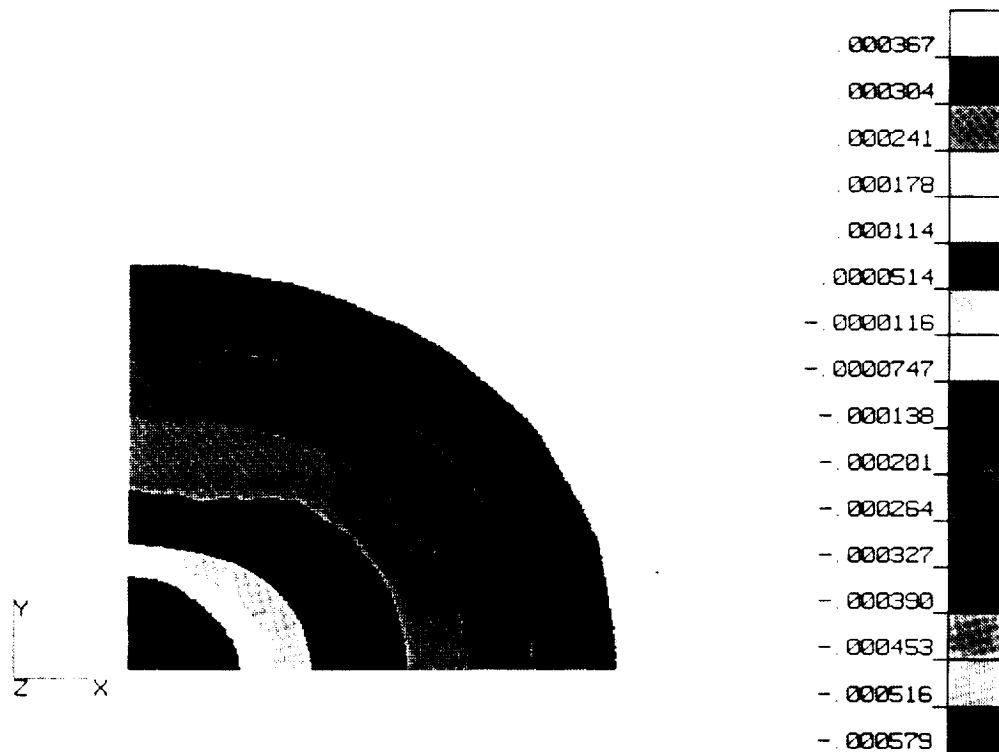


FIG. 38. Plate with 25.4-mm Ring at Ultimate Load Fringe Plot of ϵ_3 Strain

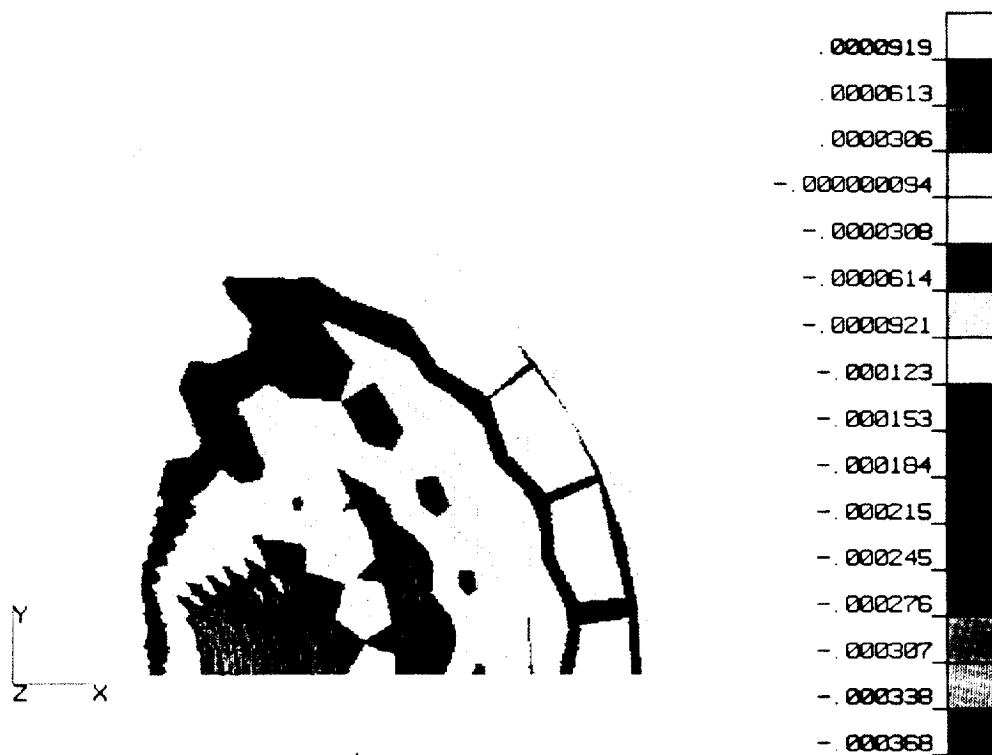


FIG. 39. Plate with 25.4-mm Ring at Ultimate Load Fringe Plot of ϵ_4 Strain

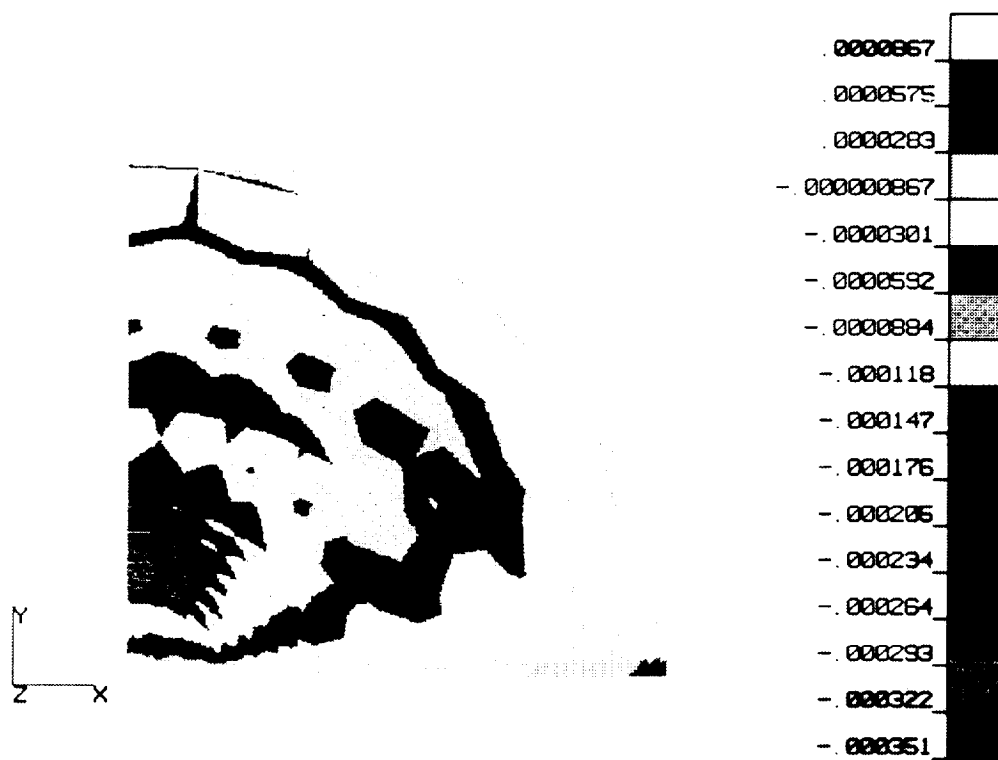


FIG. 40. Plate with 25.4-mm Ring at Ultimate Load Fringe Plot of ϵ_5 Strain

Distributions of stress, obtained numerically, show the same trends as the strain plots discussed earlier. Figs. 41-46 illustrate the variation of each component of stress throughout one-quarter of the plate. From these plots it can be deduced that at the center of the plate there exists what is essentially a state of biaxial normal stress. The numerical model yields biaxial normal stresses of 841.2 MPa (122 ksi) and 820.5 MPa (119 ksi) for σ_1 and σ_2 , respectively, within a radial distance of 2.5 mm (0.1 in.) from the center of the plate. Although, the center zone is not absolutely free from all other components of stress, this test provides a reasonably good means for determining the biaxial failure strength for cross-rolled beryllium sheet.

4.4.2 50.4-mm Ring Load

A second circular plate is loaded to failure by means of a circular ring that is 50.8 mm (2.0 in.) in diameter (Fig. 28). As mentioned earlier, the only difference between the two experimental plates is the diameter of the load ring. Locations of transducers are shown in Fig. 29.

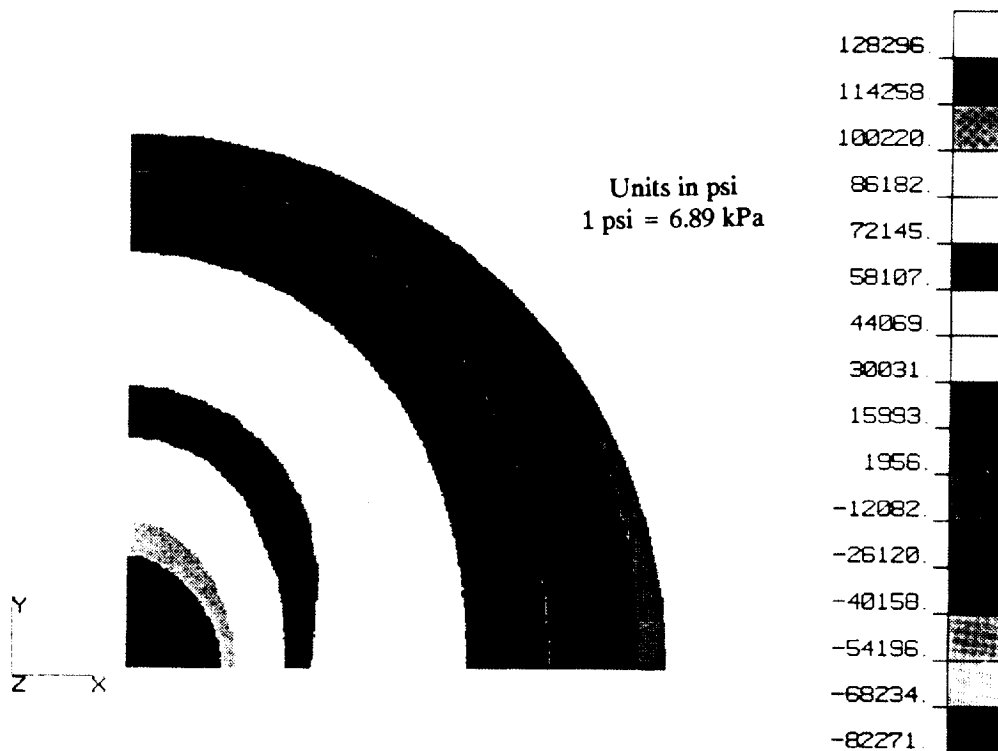


FIG. 41. Plate with 25.4-mm Ring at Ultimate Load Fringe Plot of σ_1 Stress

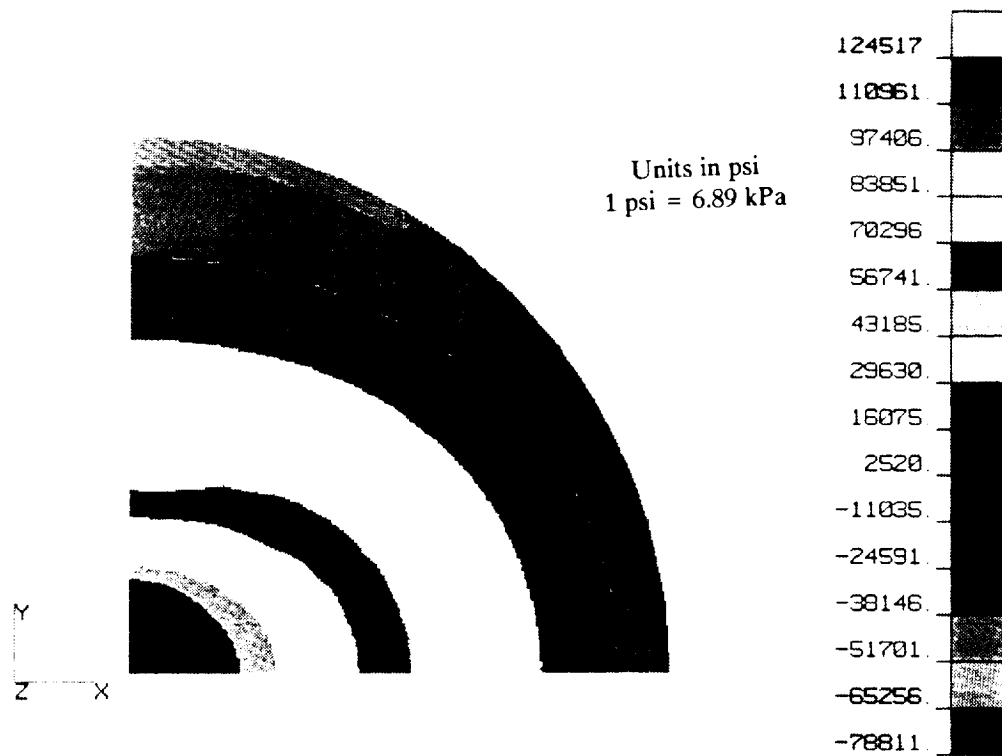


FIG. 42. Plate with 25.4-mm Ring at Ultimate Load Fringe Plot of σ_2 Stress

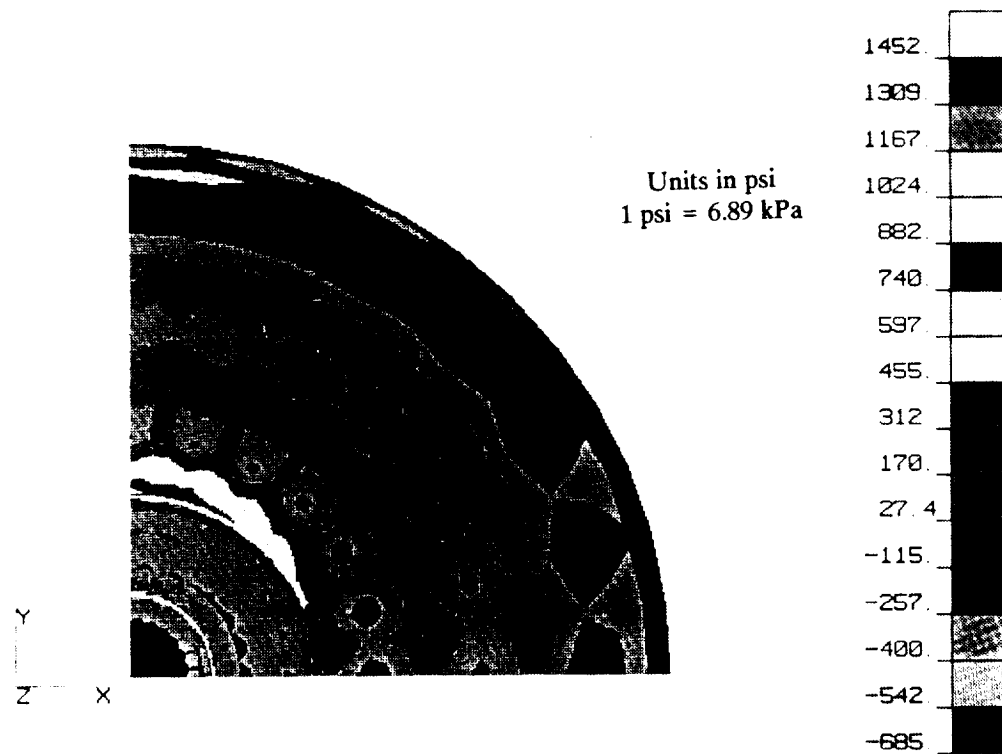


FIG. 43. Plate with 25.4-mm Ring at Ultimate Load Fringe Plot of σ_3 Stress

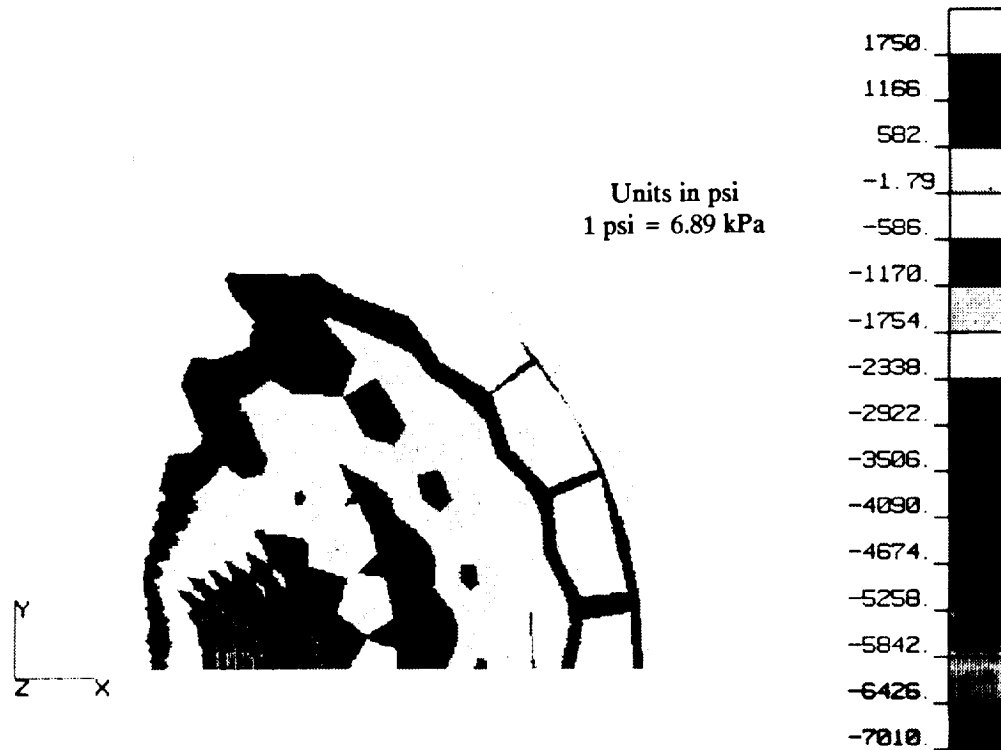


FIG. 44. Plate with 25.4-mm Ring at Ultimate Load Fringe Plot of σ_4 Stress

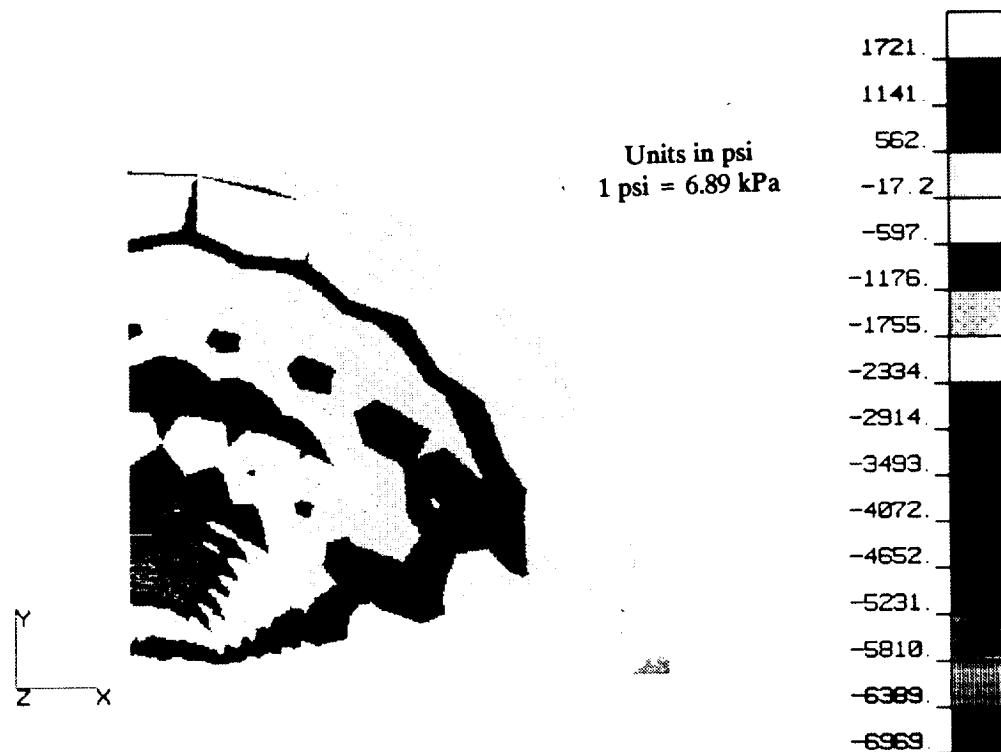


FIG. 45. Plate with 25.4-mm Ring at Ultimate Load Fringe Plot of σ_5 Stress

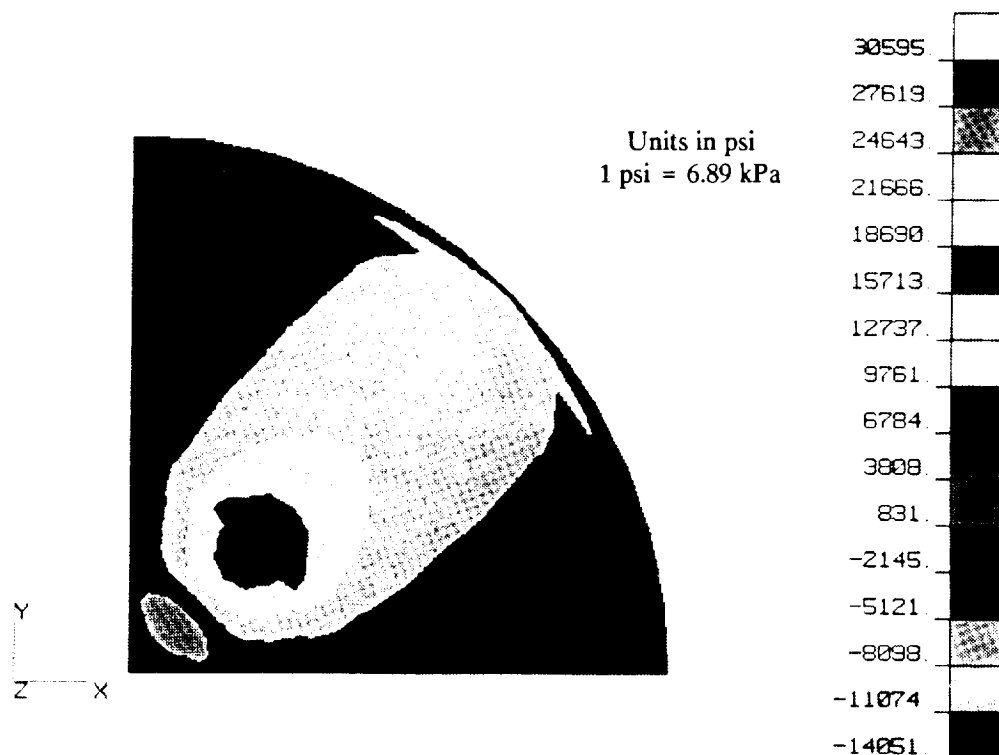


FIG. 46. Plate with 25.4-mm Ring at Ultimate Load Fringe Plot of σ_6 Stress

Results of numerical simulation are verified by comparison with actual displacements and strains measured during the experiment. Fig. 47 compares experimental and numerically predicted vertical displacements along a radial line along the center of the plate. The yield and ultimate load levels are 6.0 kN (1.4 kip) and 9.2 kN (2.1 kip), respectively. Experimentally measured displacements from the center and one intermediate location between the supported edge and the center of the plate are plotted for comparison with the finite element prediction. Agreement between measured and predicted values is excellent at load levels that cause the yield and ultimate stresses.

Fig. 48 shows the distribution of vertical deflection at ultimate load by means of a fringe plot that is generated from finite element results. The vertical deflections are very nearly symmetrical about the center of the plate. Maximum deflection at the center of the plate is 3.5 mm (0.14 in.). Figs. 49 and 50 show distributions of numerically simulated in-plane components of displacement. It is observed that in the central portion of the plate [within the 50.8-mm (2.0-in.) ring] the latter displacements are orders of magnitude less than the vertical component.

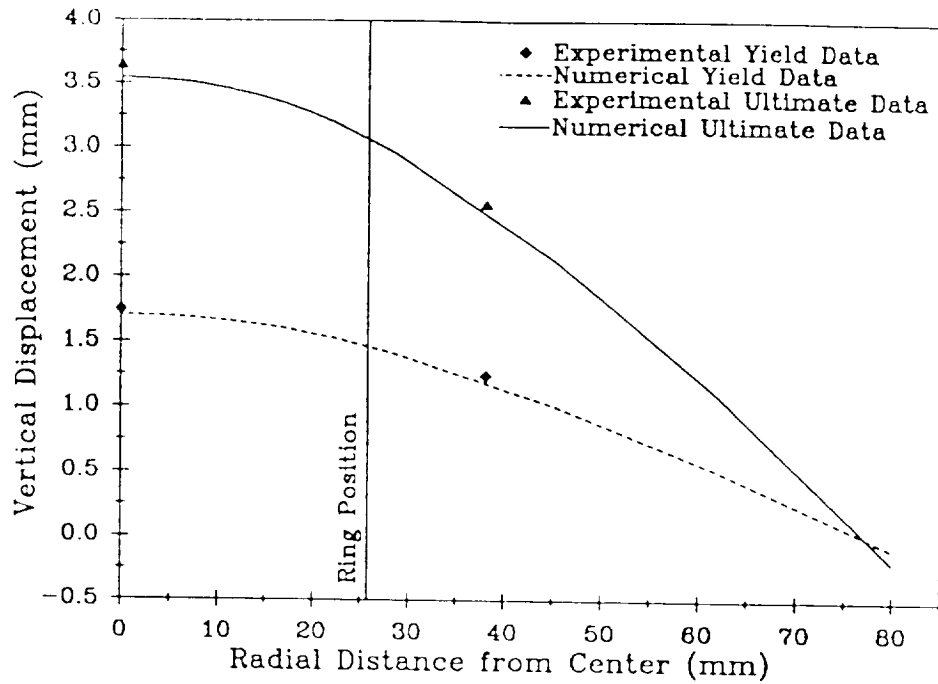


FIG. 47. Vertical Displacement along a Radial Line at Yield and Ultimate Stress for 50.8-mm (2.0-in) Load

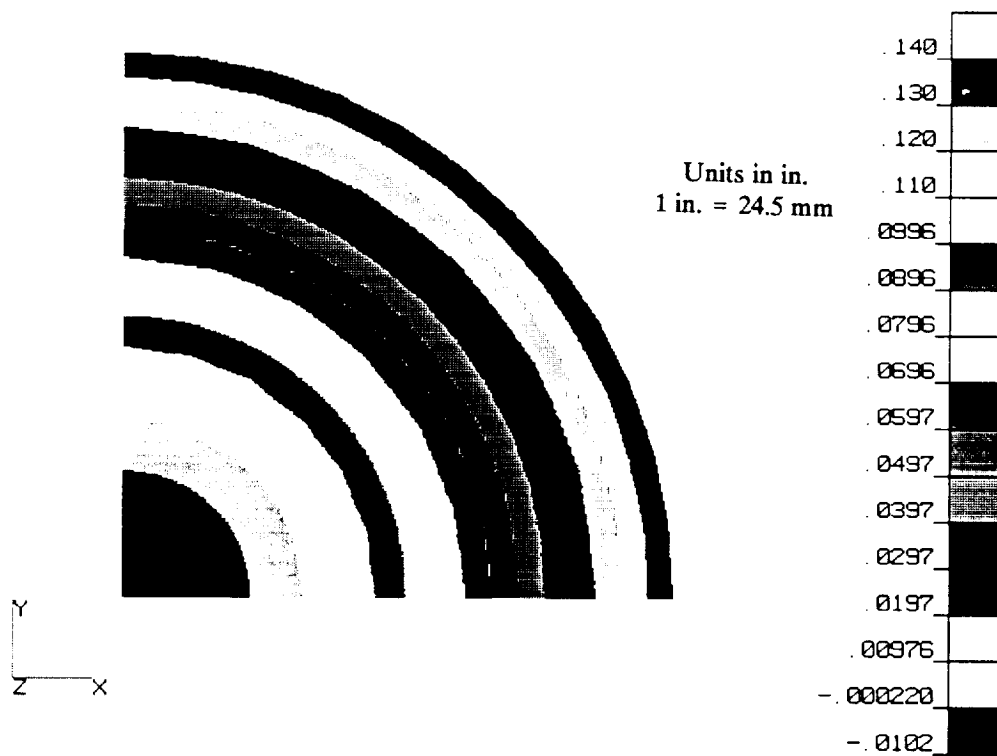


FIG. 48. Plate with 50.8-mm Ring at Ultimate Load Fringe Plot of Vertical Displacement

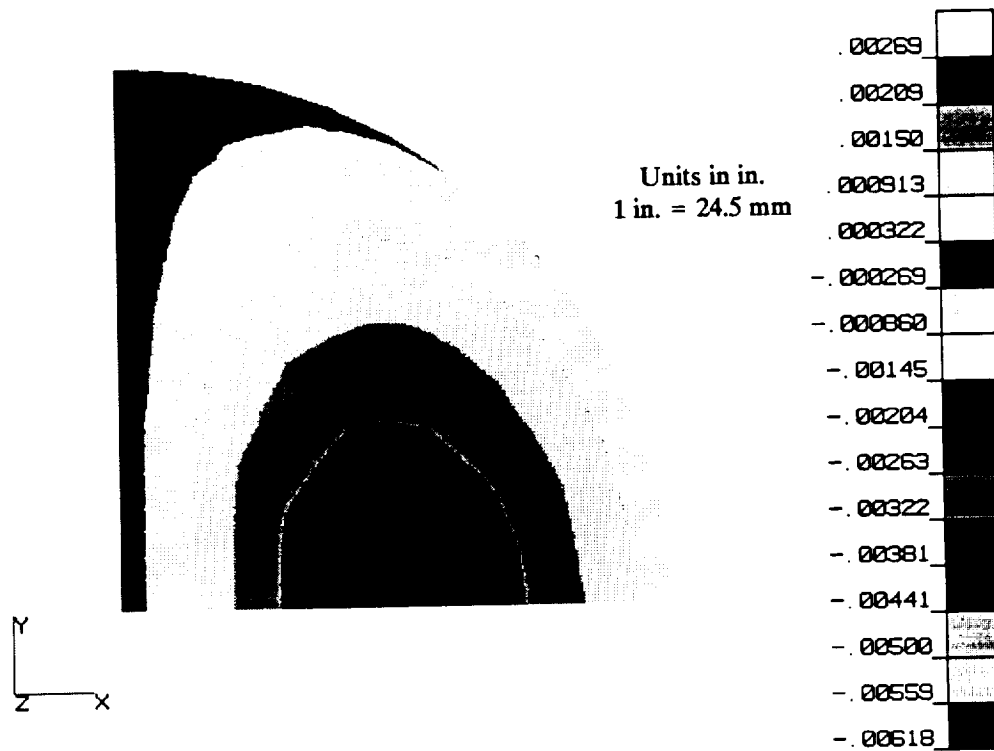


FIG. 49. Plate with 50.8-mm at Ultimate Load Fringe Plot of Displacement in the X-Direction

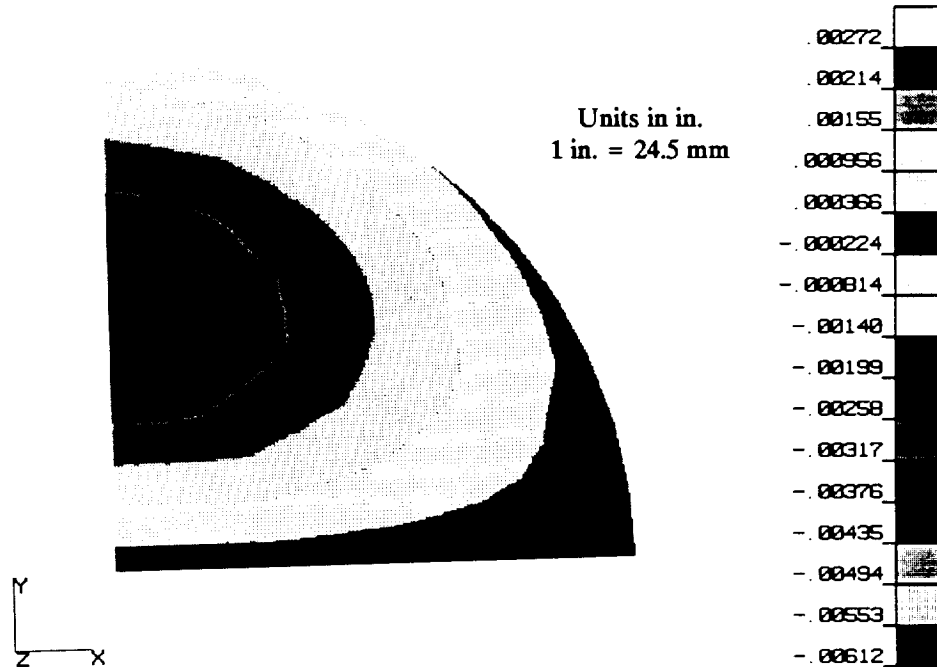


FIG. 50. Plate with 50.8-mm at Ultimate Load Fringe Plot of Displacement in the Y-Direction

A graph of normal strain versus distance from the center of the plate allows a comparison of finite element and experimental results (see Fig. 51). Experimentally determined axial strains at gage locations on the bottom surface shown in Fig. 29 are plotted for comparison with finite element predictions (Fig. 52 illustrates FEA prediction at the ultimate load level). The maximum normal strain does not occur at the center of the plate. Instead, the maximum normal strain is predicted to appear on the bottom surface at a radial distance of 11.5 mm (0.45 in.) from the center. Although this maximum strain was located outside of the ring load when the 25.4-mm (1.0-in.) ring was used, here the maximum occurs well inside the radius of the ring. Excellent agreement is evident at the locations where strains are measured by transducers.

Distribution of normal strain ϵ_1 and ϵ_2 along the longitudinal (principal) axis and transverse (secondary) direction of cross-rolling, respectively, are shown at the ultimate load level for the same quadrant in Figs. 52 and 53. Both ϵ_1 and ϵ_2 acquire an average value of 2.2×10^{-3} mm/mm at the center of the plate. A nearly symmetric pattern about the center of the plate is observed. Although the magnitude of these strains are of the same order, their distributions are mirror images of each other.

In-plane shearing strain, ϵ_6 , as shown in a gray scale fringe plot (Fig. 54) demonstrates that although this component of stress is large enough to be significant outside and at the bounds of the loading ring [7.5×10^{-4} mm/mm (7.5×10^{-4} in./in.)], inside of the ring the magnitude of this strain is almost negligible. Out-of-plane shearing strains, ϵ_4 and ϵ_5 , although not shown graphically, have substantially lower magnitudes than the in-plane strains.

Distribution of stresses, obtained numerically, show similar trends as the strain distributions discussed earlier for the plate loaded with the 25.4-mm (1.0-in.) ring. Fringe plots (Figs. 55-57) illustrate the distribution of the in-plane normal and shearing stress components σ_1 , σ_2 , and σ_6 . Out-of-plane shearing stresses are negligible, as is the case for the 25.4-mm (1.0-in.) ring load. From these plots it can be deduced that near the center of the plate there exists a state of biaxial normal stress. The numerical model shows a biaxial state of stress of 786.0 MPa (114 ksi) and 772.2 MPa (112 ksi) for σ_1 and σ_2 , respectively, at a radial distance of 4.5 mm (0.18 in.) from the center of the plate. At this location the magnitude of all other stress components approach zero.

The numerical simulations indicate that for both plates an average biaxial state of stress of 830.8 MPa (120.5 ksi), obtained by averaging the in-plane normal failure stresses for the 25.4-mm (1.0-in.) and 50.8-mm (2.0-in.) ring loadings, is reached prior to failure of the structure. This value of the in-plane biaxial strength is used in chapter 6 to establish the interaction coefficients.

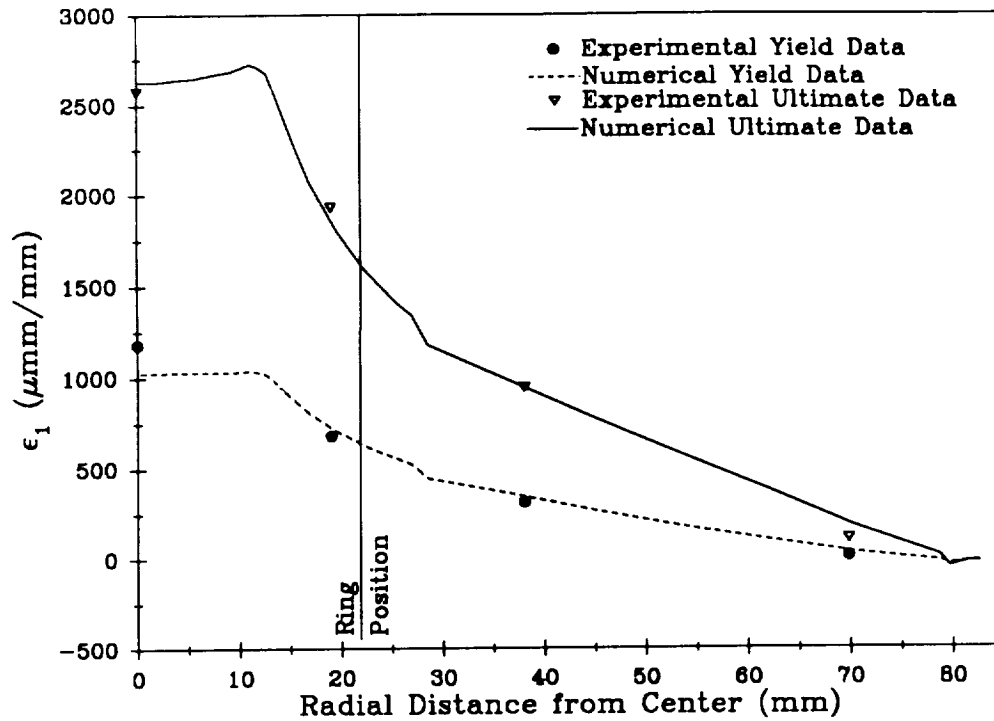


FIG. 51. Radial Strain at Yield and Ultimate Stress for 50.8-mm (2.0-in) Ring Load

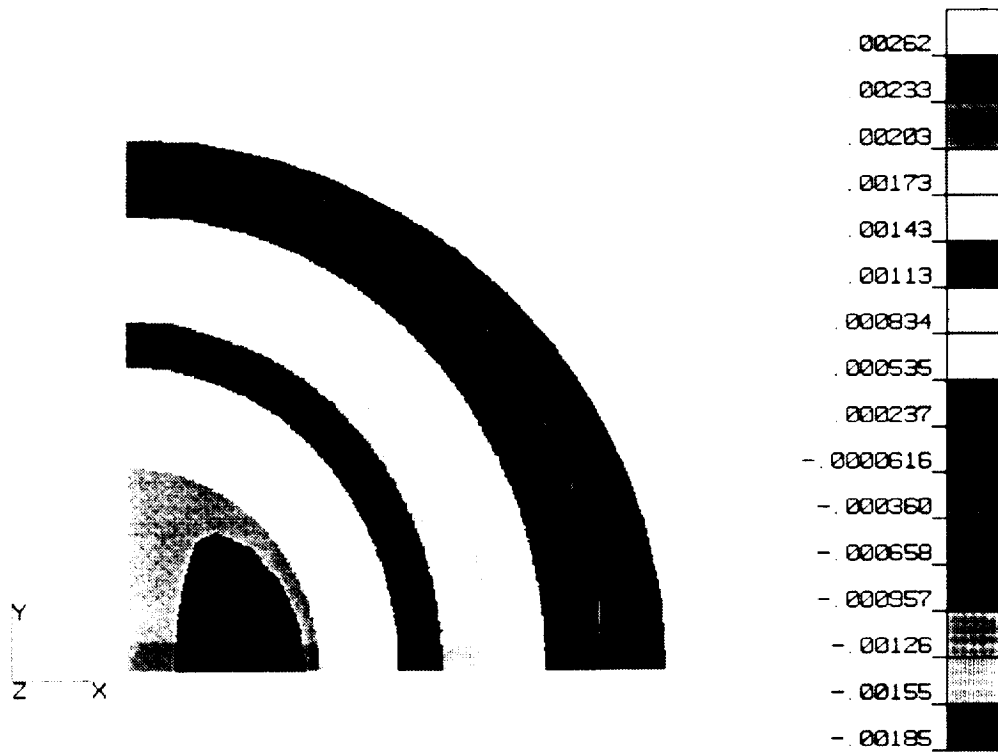


FIG. 52. Plate with 50.8-mm Ring at Ultimate Load Fringe Plot of ϵ_1 Strain

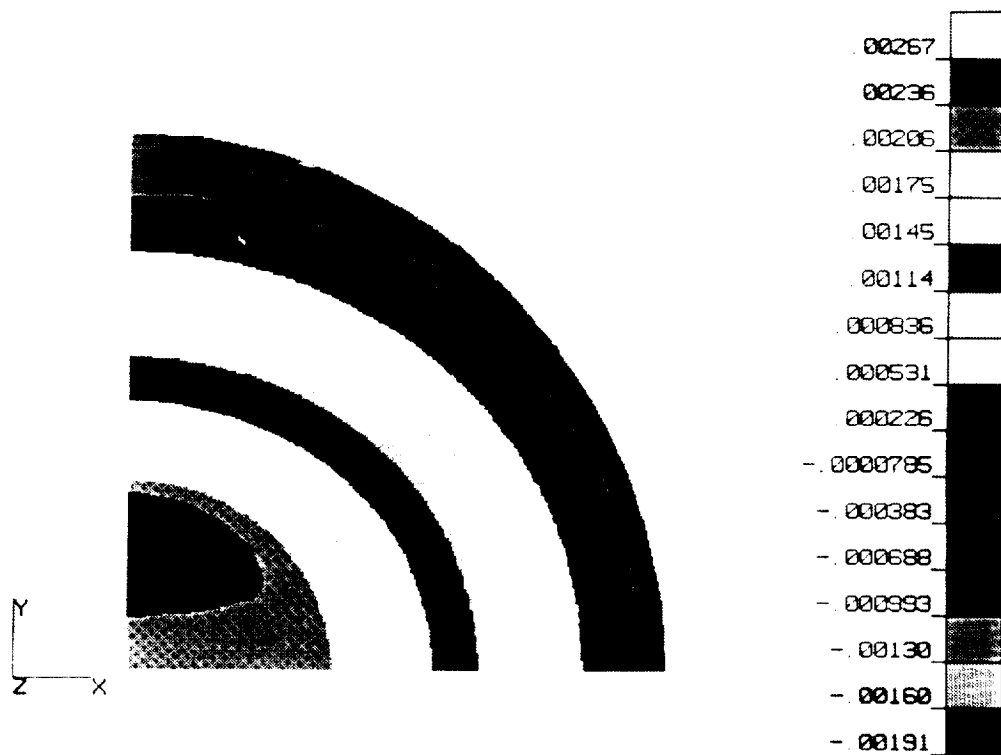


FIG. 53. Plate with 50.8-mm Ring at Ultimate Load Fringe Plot of ϵ_2 Strain

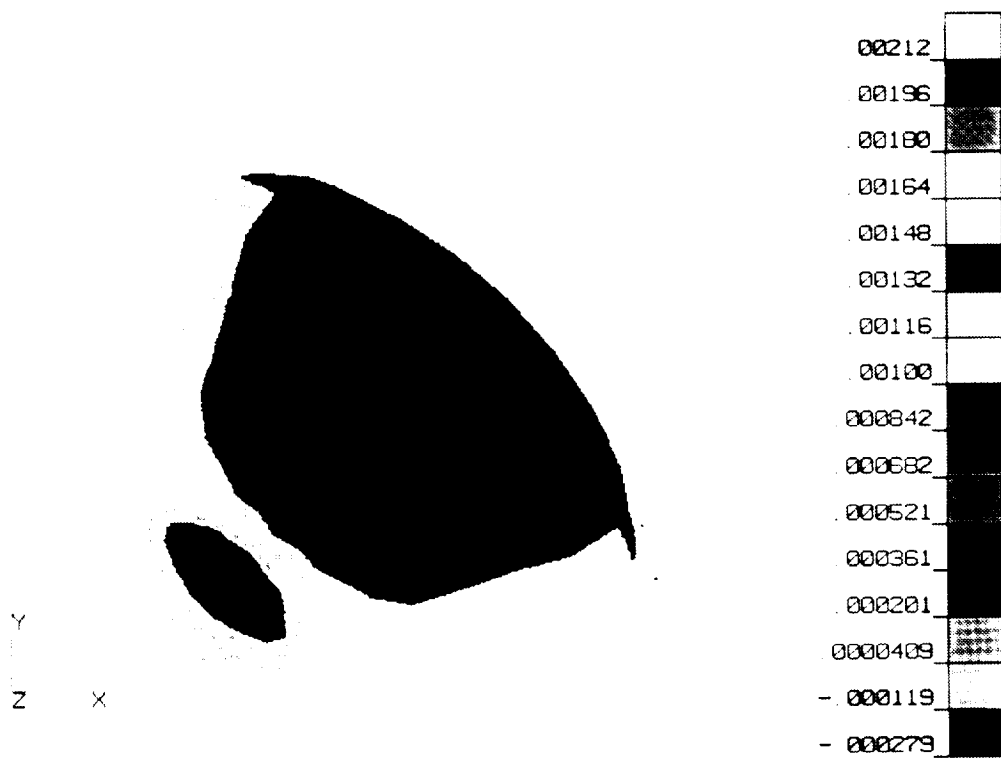


FIG. 54. Plate with 50.8-mm Ring at Ultimate Load Fringe Plot of ϵ_6 Strain

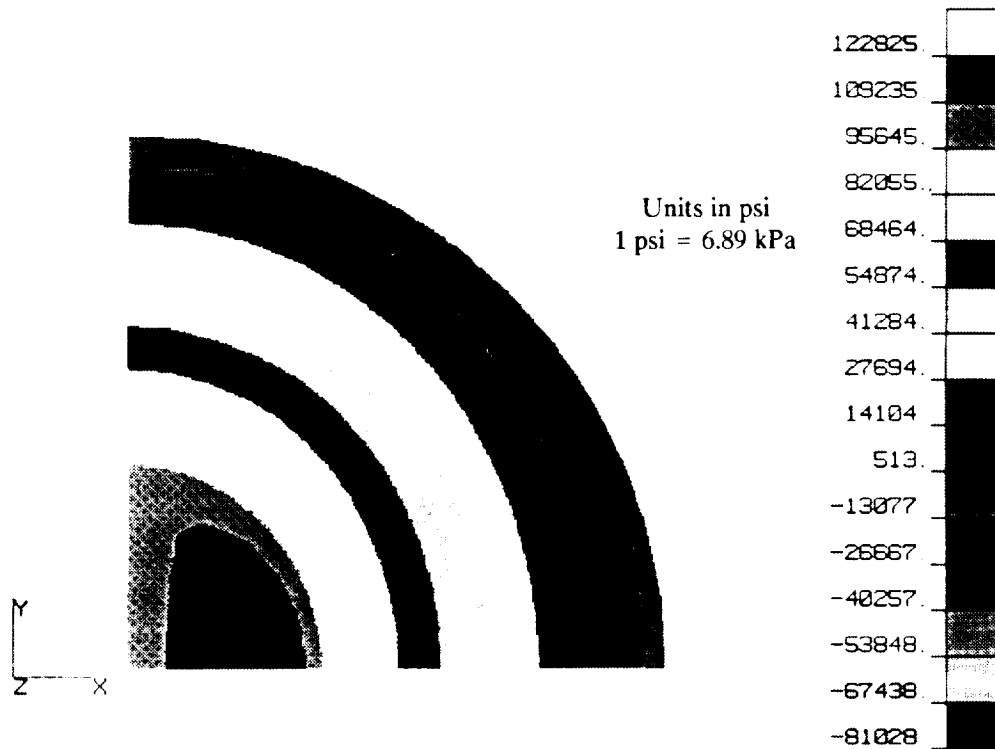


FIG. 55. Plate with 50.8-mm Ring at Ultimate Load Fringe Plot of σ_1 Stress

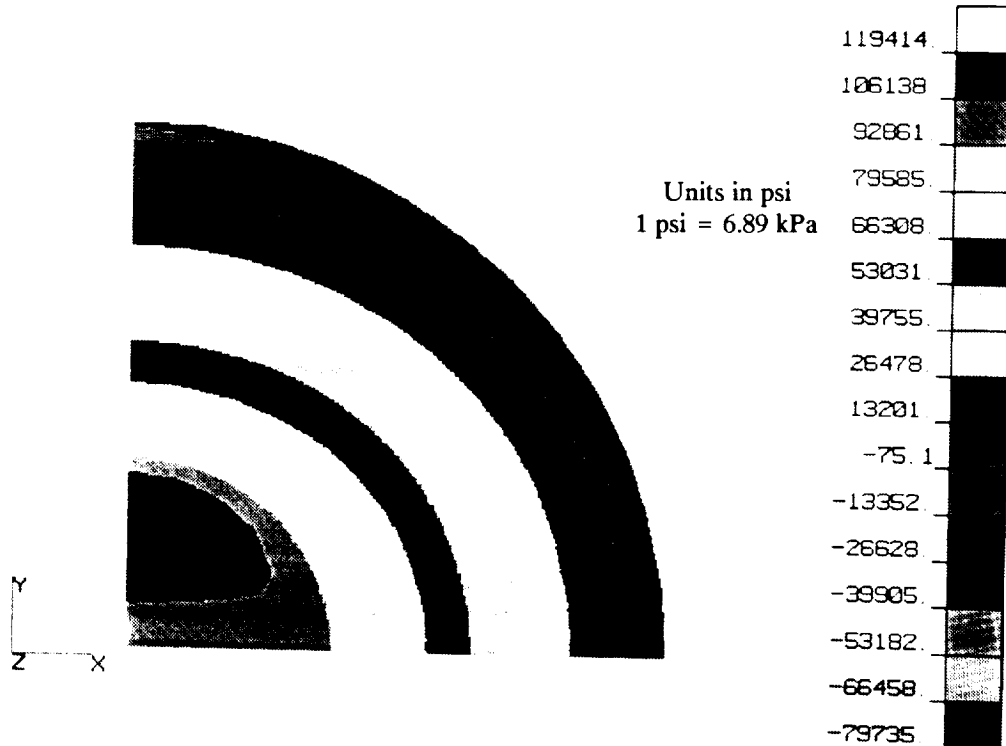


FIG. 56. Plate with 50.8-mm Ring at Ultimate Load Fringe Plot of σ_2 Stress

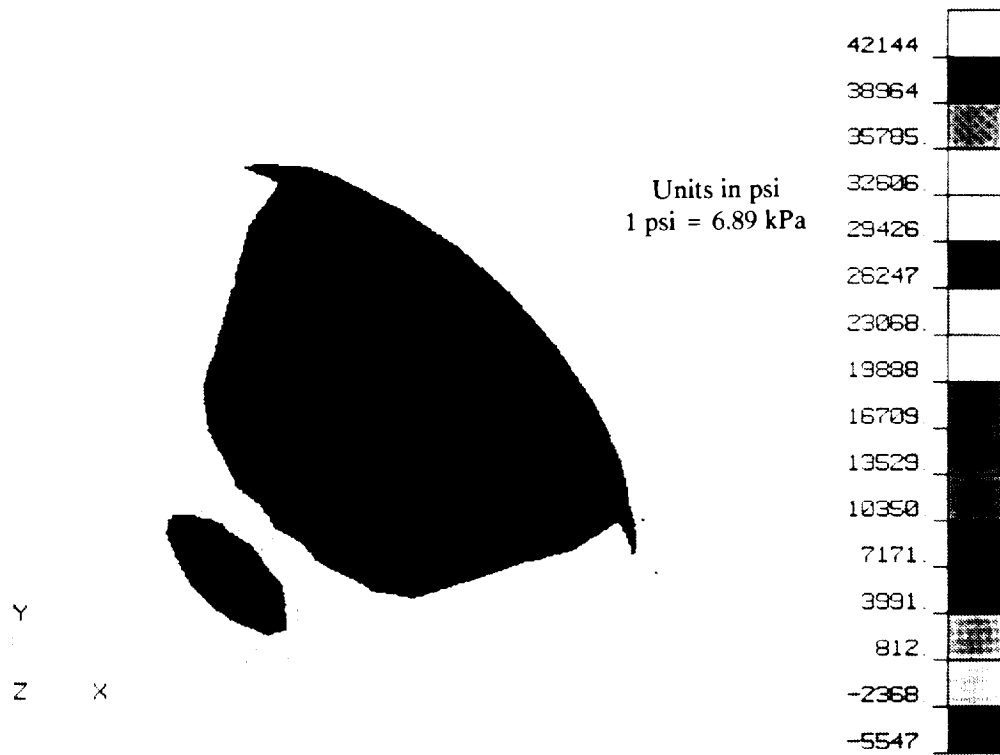


FIG. 57. Plate with 50.8-mm Ring at Ultimate Load Fringe Plot of σ_6 Stress

5. EXPERIMENTAL DETERMINATION OF PRINCIPAL FAILURE COEFFICIENTS

5.1 INTRODUCTION

Chapter 4 presents results of laboratory experiments and complementary numerical simulations carried out on cross-rolled beryllium sheets. Specimen geometry and loading is arranged so that in-plane stresses dominate. An off-axis biaxial specimen places a differential element in a state of biaxial stress even though the loading apparatus applies a uniaxial load. A notched shear plate leads to an in-plane shear failure mechanism. Two circular beryllium plates loaded by a circular ring, placed at the center of each plate, provide a two-dimensional analogue to a beam loaded in pure bending.

In this chapter another set of experiments and numerical simulations is described. The purpose of these experiments is to supplement uniaxial, biaxial, and pure shearing stress data available from the experiments described in chapter 4 in order to obtain the principal failure strength coefficients. These coefficients are obtained from failure tests in which either uniaxial or biaxial stress conditions that are free of shear are imposed, or from conditions of pure shearing stress. After some introductory discussion a series of tests involving simple uniaxial compression, in-plane shear, through-thickness shear, and through-thickness compression is presented. The reader is referred to Fig. 11 to understand how these tests contribute to determination of failure coefficients required by the higher-order macroscopic failure criterion described in chapter 3. All beryllium specimens used in tests described in this chapter have the same chemical composition (see Table 11). In addition, all experimental work is carried out in a controlled laboratory environment.

Both the principal and the interaction coefficients that describe the criterion are determined from a finite number of experiments that include uniaxial, biaxial, and shear tests. For specially orthotropic material, such as cross-rolled beryllium sheet, the minimum number of experiments required to determine all coefficients is fifteen. A summary of tests for an ideal case is presented in Table 12. Limitations arise, however, due to the fact that the SR-200 material is only available in plate form. Thus, modifications of the ideal set of experiments are needed. The experiments used for evaluation of all coefficients for thin plate structures are listed in Table 13 (see also Figs. 11-14). Principal modifications occur for biaxial and multiaxial states of stress that include the through-thickness direction as one of the stress axes. True biaxial failure parameters, such as (σ_1, σ_3) and (σ_2, σ_3) , can not be measured for thin plate structures due to geometrical limitations. A new set of experiments

TABLE 11. Chemical Composition of Beryllium Specimens

Element (1)	Chemical Composition (weight %) (2)
Be	99.00
BeO	1.00
Fe (ppm)	600
C (ppm)	1,200
Al (ppm)	300
Mg (ppm)	Less than 100
Si (ppm)	200
Other Elements (ppm)	Less than 400

ppm = parts per million

TABLE 12. Experiments Required for Evaluation of Failure Coefficients

Experiment (1)	Axis (2)	Coefficients (3)	Number of Tests (4)
Uniaxial:			
Tension and Compression	X	F_1, F_{11}	2
Tension and Compression	Y	F_2, F_{22}	2
Tension and Compression	Z	F_3, F_{33}	2
Pure Shear:			
Positive or Negative	X-Z	F_4, F_{44}	1
Positive or Negative	Y-Z	F_5, F_{55}	1
Positive or Negative	X-Y	F_6, F_{66}	1
Biaxial:			
Tension-Tension, or	X-Y	F_{12}, F_{112}, F_{122}	1
Compression-Compression, or	X-Z	F_{13}, F_{113}, F_{133}	1
Tension-Compression	Y-Z	F_{23}, F_{223}, F_{233}	1
Multiaxial:			
Tension or Compression	X-Z	$F_{144}, F_{244}, F_{344}$	1
and Shear	Y-Z	$F_{155}, F_{255}, F_{355}$	1
	X-Y	$F_{166}, F_{266}, F_{366}$	1

TABLE 13. Experiments Used for Evaluation of Failure Coefficients

Experiment (1)	Axis (2)	Coefficients (3)	Number of Tests (4)
Uniaxial:			
Tension and Compression	X	F_1, F_{11}	2
Tension and Compression	Y	F_2, F_{22}	2
Tension and Compression	Z	F_3, F_{33}	2
Pure Shear:			
Positive or Negative	X-Z	F_4, F_{44}	1
Positive or Negative	Y-Z	F_5, F_{55}	1
Positive or Negative	X-Y	F_6, F_{66}	1
Biaxial:			
Tension-Tension	X-Y	F_{12}, F_{112}, F_{122}	1
Compression-Torsion	X-Z	F_{244}	1
Compression-Torsion	Y-Z	F_{155}	1
Multiaxial:			
Compression, Compression, and Shear	X-Z	$F_{13}, F_{113}, F_{133},$ F_{155}, F_{355}	5
	Y-Z	$F_{23}, F_{223}, F_{233},$ F_{244}, F_{344}	5
Tension, Tension, and Shear	X-Y	F_{166}, F_{266}	1
All six components	X-Y-Z	$F_{144}, F_{255}, F_{366}$	1

is introduced that induces a triaxial state of stress, such as $(\sigma_1, \sigma_3, \sigma_5)$ and $(\sigma_2, \sigma_3, \sigma_4)$. From these experiments both the normal and normal-shearing interaction coefficients can be established provided that the number of tests is increased from one to, at least, three. For the current study five specimens are used for each state of stress.

5.2 IN-PLANE COMPRESSIVE STATE OF STRESS

5.2.1 Laboratory Experiments

Compression testing is carried out using two specimens. One coupon has the longitudinal principal material axis oriented along the loading axis; the other has the long-transverse principal material axis coinciding with the direction of the load (Figs. 58 and 59). Special end fixtures are machined from A-2 tool steel, hardened to Rockwell C 50/55, and oriented to ensure that the specimen does not slip during loading (Fig. 60). In the assembled configuration the unsupported length of the beryllium sheet specimen is 12.7 mm

(0.5 in.). The specimens were loaded using a biaxial Material Testing Machine (MTS) machine that has a 44.5-kN (10.0-kip) tension/compression range and a $\pm 45^\circ$ torsional angle capacity. Only the tension/compression actuator of the MTS is used to achieve the compressive state of stress. In-plane strain was measured using bonded Micro-Measurement precision rosettes (CEA-06-062UR-350) in the middle of the unsupported area of the plate. One rosette was placed on each side of the specimen directly opposite its counterpart. This was done to ensure symmetric distribution of the load. Orientation of these gages is shown in Figs. 58 and 59. As a check prior to actual testing, the specimens were lightly loaded and the stress-strain curves of corresponding rosette strain gages were compared. Both specimens were loaded at a rate of 445 N/s (100 lb/sec).

Although the primary objective of this test is to obtain compressive strength coefficients for the longitudinal and long-transverse directions, the experiments also verify results obtained by other investigators, as well as serve to recalculate and compare the elastic moduli with results acquired from uniaxial tests. Stress-strain curves for specimens loaded with the principal axis of rolling parallel and perpendicular to the load are plotted in Figs. 61 and 62, respectively. Strains plotted are for gages oriented in the direction of the load. Fig. 63 is similar to Figs. 61 and 62 but uses data collected from the rosette gages to compute in-plane normal strain in a direction that is 45° from the loading direction. The primary objective for use of the 45° gages is to show that compressive loading of the structure is symmetric.

Table 14 summarizes the moduli and failure strength determined for each specimen. The modulus of elasticity for compression, as calculated from Figs. 61 and 62, for specimens 1 and 2 is 3.00×10^5 MPa (43.5×10^6 psi) and 3.06×10^5 MPa (44.3×10^6 psi), respectively. These values compare favorably with 3.20×10^5 MPa (46.4×10^6 psi) reported for the average in-plane compressive elastic modulus by Aldinger (Webster and London 1979). Fig. 64 shows one of the specimens after failure. The FEA simulation is described in section 5.2.2.

The longitudinal and long-transverse specimens fail catastrophically and exhibit properties distinctive of brittle material (Fig. 64). For compression, elastic moduli obtained from the stress-strain curves (Figs. 61 and 62) are slightly higher than moduli obtained from uniaxial tensile tests. In each case, compressive strength is approximately 20% higher than the tensile strength in the same direction, which is characteristic of brittle material. Although beryllium is ductile when undergoing an in-plane tensile load, compressive loadings manifest very different behavior. Results obtained suggest that the material exhibits brittle properties for compressive in-plane loadings.

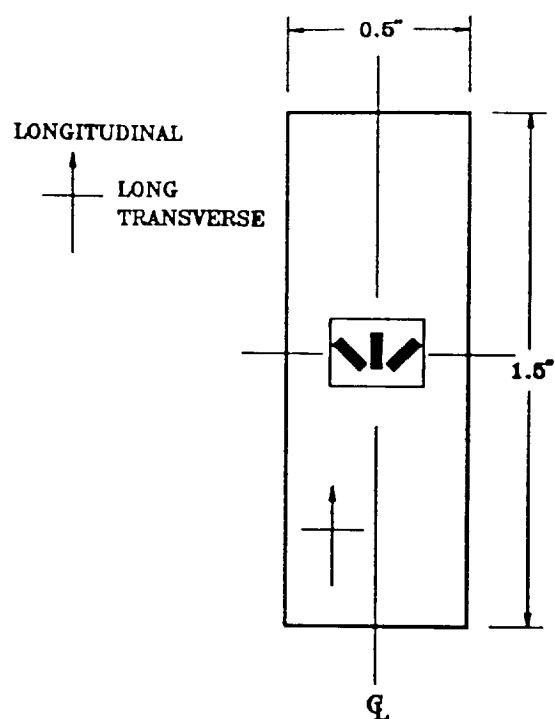


FIG. 58. Compression Specimen Longitudinal Axis Aligned with Principal Material Axis

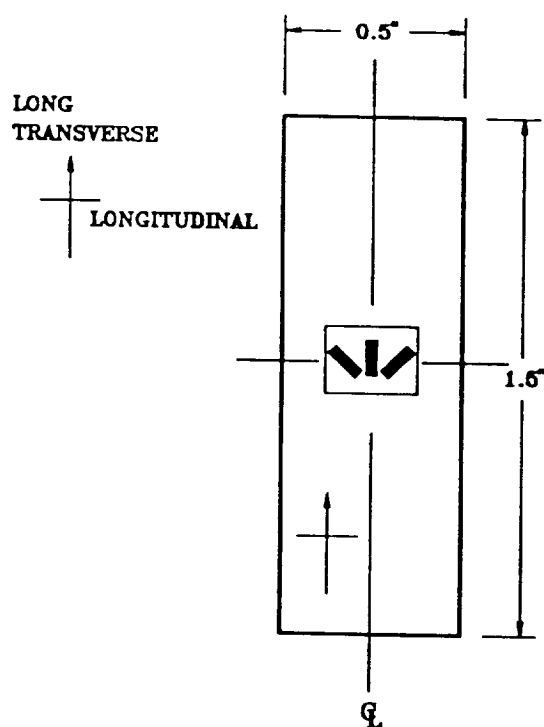


FIG. 59. Compression Specimen Transverse Axis Aligned with Principal Material Axis

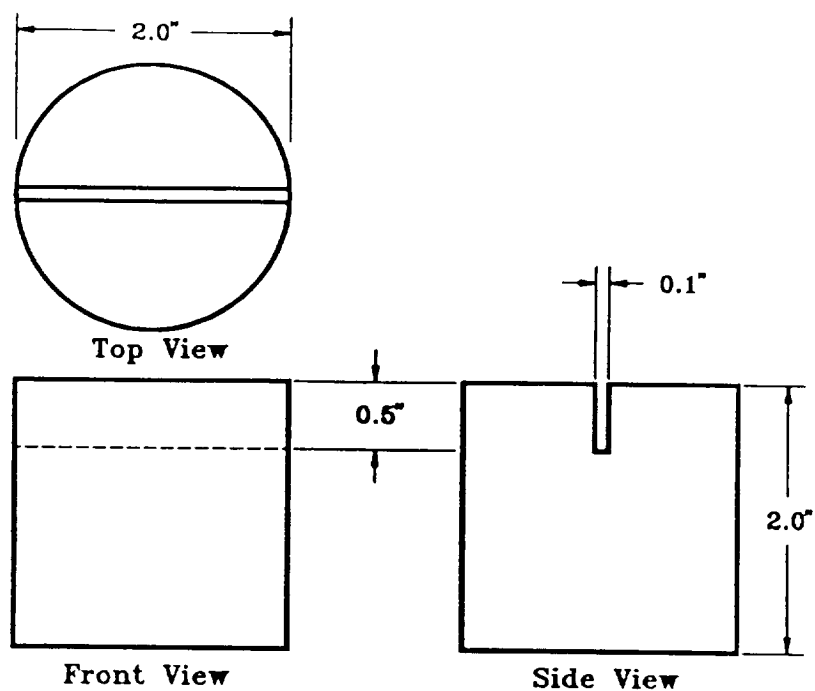


FIG. 60. Fixtures for Compression Testing

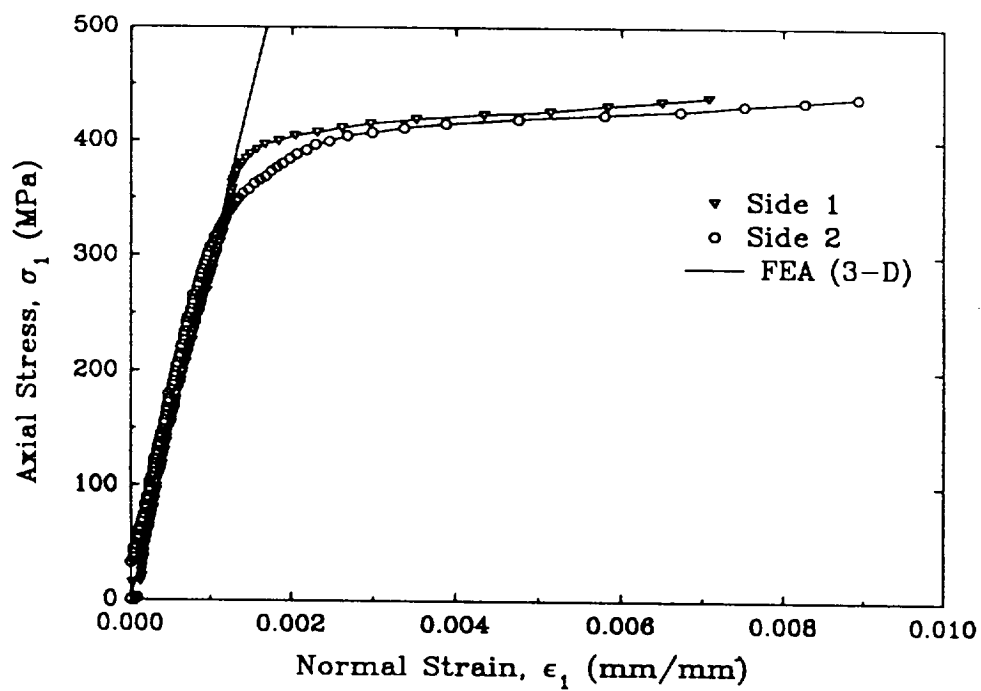


FIG. 61. Normal Stress-Strain Curve for Specimen Loaded Along the Principal Direction of Cross Rolling

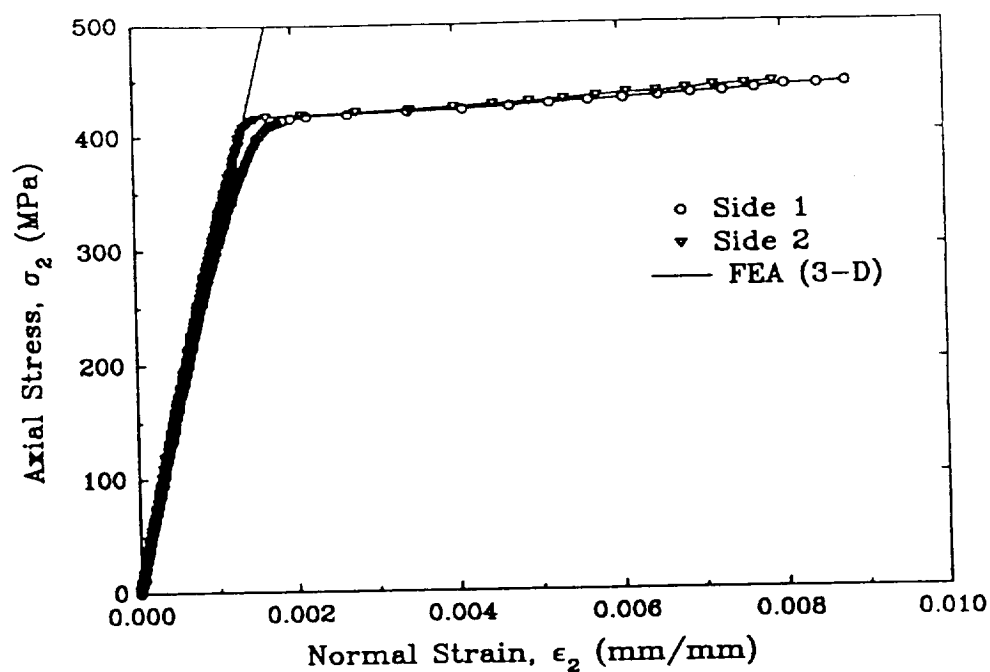


FIG. 62. Normal Stress-Strain Curve for Specimen Loaded Perpendicular to the Principal Direction of Cross Rolling

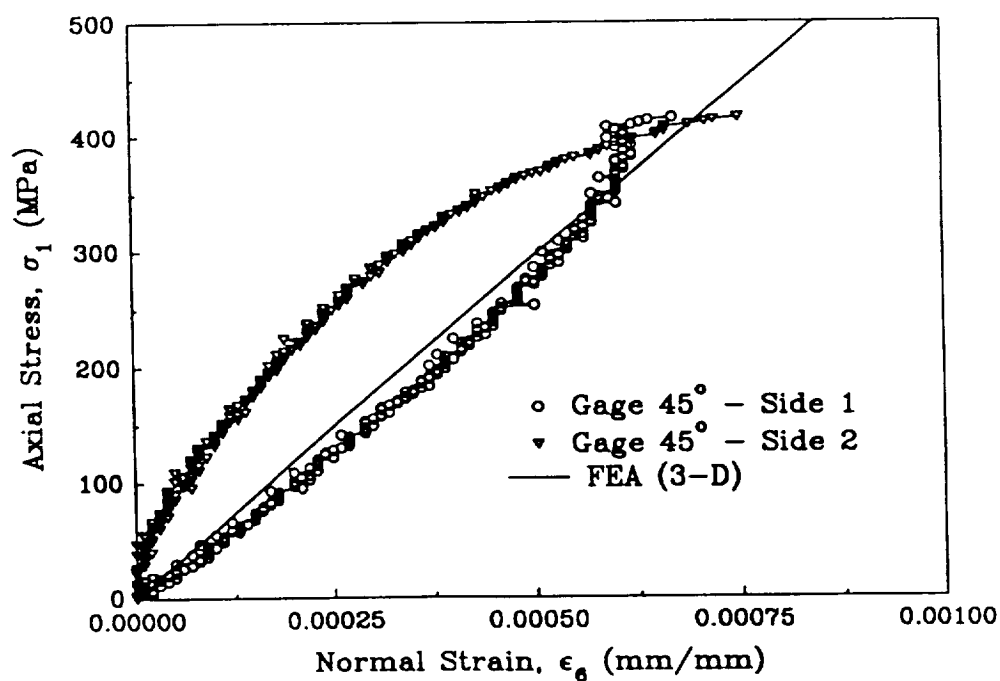


FIG. 63. Stress-Strain Curve for Specimen Loaded Parallel to Principal Direction of Cross Rolling



FIG. 64. Failed Compression Specimen

TABLE 14. Failure Strength for Compression Specimens

Specimen (1)	Orientation of Principal Rolling (2)	Elastic Modulus		Failure Stress	
		GPa (3)	(ksi) (4)	MPa (5)	(ksi) (6)
1	Parallel	300.0	(43,500)	658.8	(95.6)
2	Perpendicular	306.0	(44,300)	691.8	(100.3)

5.2.2 Numerical Simulation

Knowledge of maximum in-plane compressive strengths, σ_1 and σ_2 , is required for estimation of the principal failure coefficients F_I and F_{II} , as well as F_2 and F_{22} (Tsai and Wu 1971; Wu 1974; Priddy 1974; Tennyson and Elliot 1983; Jiang and Tennyson 1989). Numerical models are used prior to laboratory testing to aid in geometrical optimization of the experimental specimens. This preliminary modeling minimizes manufacturing costs of the beryllium specimens and their fixtures and gives a reasonably accurate prediction of the distribution of the stresses throughout the part. Both two- and three-dimensional models of a simple compression specimen are generated (Fig. 65). The final design suggests a 38.1-mm \times 12.7-mm (1.5-in. \times 0.5-in.) experimental plate specimen (see Figs. 58-59). The FEA package ABAQUS (1991a) is used for the numerical simulations.

5.2.2.1 Plane Stress Elements

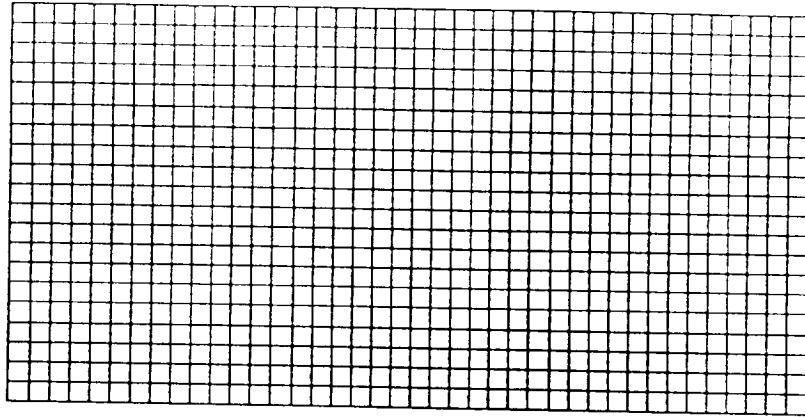
Eight hundred, eight-noded plane stress elements with approximately 16,500 degrees-of-freedom are used in a two-dimensional model of the structure. In order to capitalize on geometry and loading conditions of symmetry only one-fourth of the actual structure is numerically modeled. Predictions of components of strain at five integration points are requested in the through-thickness direction. Output at the top and bottom surfaces of the plate shown in Fig. 58 are compared with data from strain gages (see Figs. 61, 62, and 63). Material is given linear orthotropic properties with average material properties for the through-thickness modulus, while geometric deformation is taken to be nonlinear. Agreement of the strain gage values with FEA is good up to a load level of approximately 400 MPa (57 ksi).

Fringe plots of simulated displacements and stresses at ultimate load for the two-dimensional FEA model having the loading axis parallel with respect to the principal direction of rolling are shown in Figs. 66-69 for one-fourth of the plate. The top and right edges are lines of symmetry for the loaded plate. Figs. 66 and 67 illustrate the distribution of displacement in the principal rolling directions (x- and y- axes, respectively). From these figures it can be seen that in-plane transverse displacements are approximately an order of magnitude smaller than in-plane axial quantities. A combination of the fact that beryllium has small Poisson's ratios and a uniaxial application of the load accounts for this type of behavior.

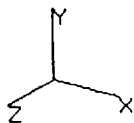
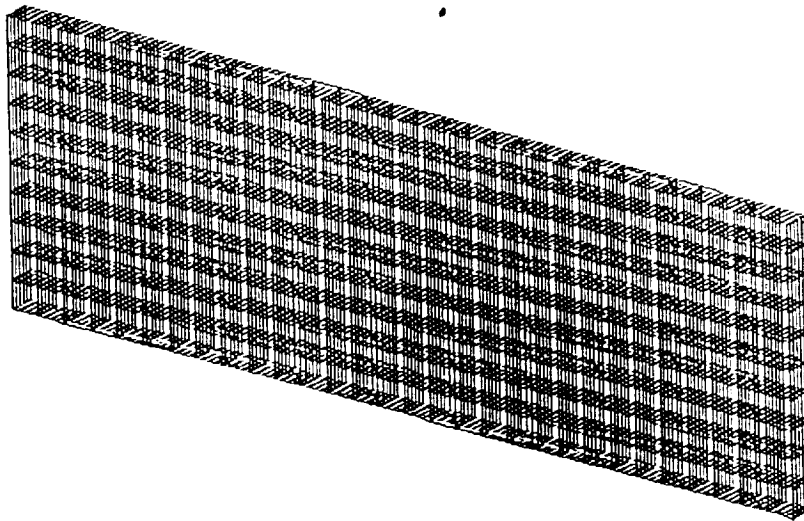
Although not shown by means of fringe plots, in-plane normal strains, ϵ_1 and ϵ_2 , for the failure load are predicted to reach values of 2.03×10^{-3} and 1.7×10^{-4} , respectively, while maximum shearing strain, ϵ_6 , is at least three orders of magnitude smaller than ϵ_1 . The numerical prediction and experimental tests for ϵ_1 yield an ultimate compressive strength of 657.8 MPa (95.4 ksi) and 658.8 MPa (95.6 ksi), respectively, a difference of approximately 0.15%. Figs. 68 and 69 show distribution of the in-plane normal stress in the transverse direction and the in-plane shearing stress, respectively, at the failure load. The former stress component attains a maximum value of 0.6 MPa (0.1 ksi) which, as is to be expected, is two orders of magnitude smaller than the compressive strength. A fringe plot is not shown for the ultimate compressive stress acting in the direction of the load since its value is constant at 657.8 MPa (95.4 ksi) throughout the specimen.

5.2.2.2 Three-Dimensional Elements

Symmetry conditions are partially exploited for three-dimensional analysis. In this case, only one-eighth of the structure is modeled with three thousand, twenty-noded, hexahedral elements (Fig. 65). Five elements are used in the through-thickness direction. Nodes that are located inside of the steel grip are restrained from movement in the through-thickness direction.



(a)



(b)

FIG. 65. Finite Element Discretization for Compression Specimens (a) Two-Dimensional Plane Stress Elements; (b) Three-Dimensional Hexahedral Elements

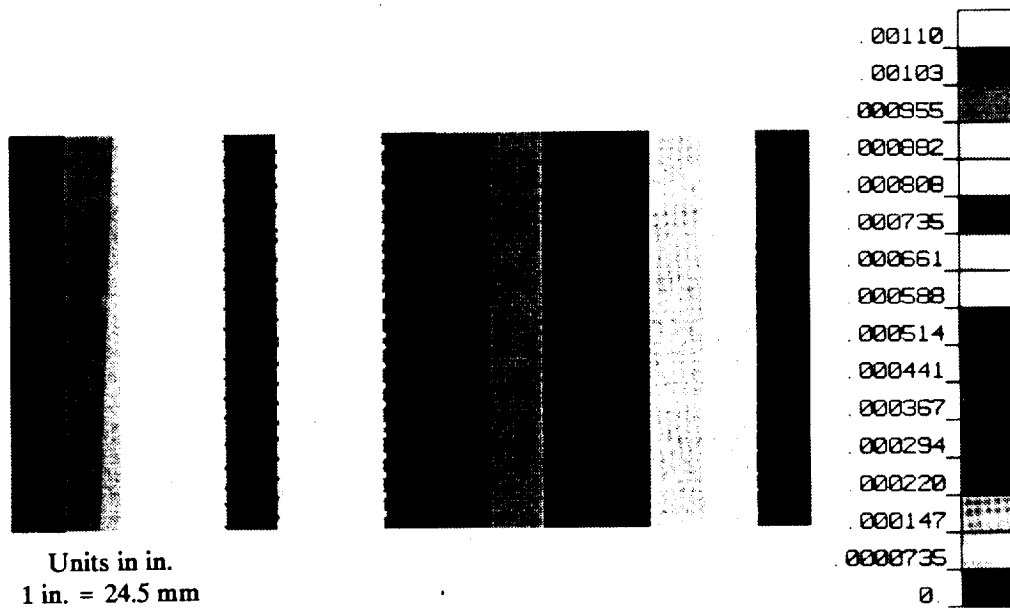


FIG. 66. Distribution of Axial Displacement for 2-D Compression Model

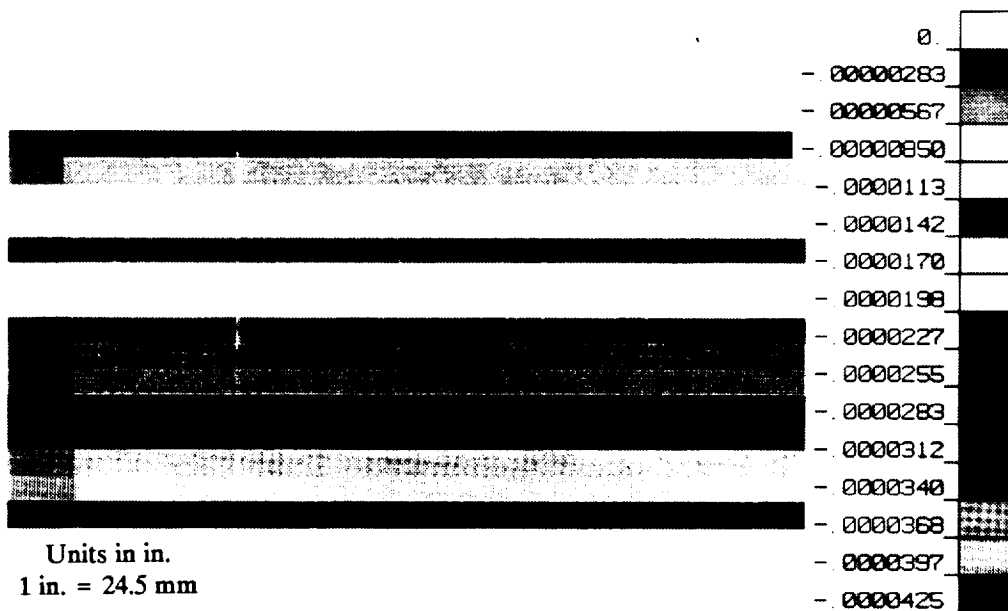


FIG. 67. Distribution of Transverse Displacement for 2-D Compression Model

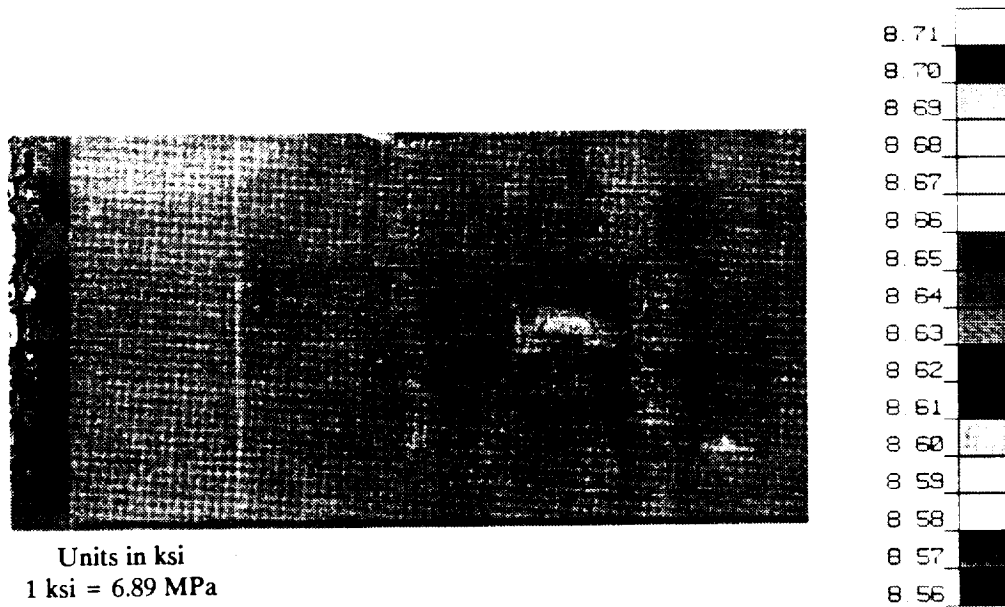


FIG. 68. Distribution of Transverse Stress, σ_2 , for 2-D Compression Model



FIG. 69. Distribution of In-Plane Shearing Stress, σ_6 , for 2-D Compression Model

Results from the two- and three-dimensional analyses are in close agreement. Figs. 70-72 illustrate numerical predictions of u_1 , u_2 , and u_3 displacements, respectively, from the three-dimensional simulation. Physically, u_1 , u_2 , and u_3 correspond to components of displacement in the directions aligned with the load, in the plane of and perpendicular to the load, and in the through-thickness direction, respectively. The values obtained for u_1 are in agreement with those obtained from the two-dimensional analysis. In addition, magnitudes of u_2 and u_3 are significantly smaller than u_1 .

Fig. 73 illustrates distribution of the axial strain, ϵ_1 , at ultimate load. Fringe patterns in Figs. 74 through 79 illustrate distribution of each component of stress resulting from three-dimensional simulation of the compression test. Although σ_2 and σ_6 are non-zero they are at least two orders of magnitude smaller than σ_1 in the region between the steel grips. With the exception of σ_1 the other components of stress can be considered to be negligibly small.

5.2.3 Comparison of Failure Strain with Elasticity Solution

Since beryllium is considered to be an orthotropic material, a closed-form elasticity solution for the strain components ϵ_1 , ϵ_2 , and ϵ_3 can be obtained, provided a non-complex state of stress is applied to a geometrically simple structure. As an independent check on the numerical simulation, components of strain at failure are predicted by an elasticity approach assuming that the material behaves in a linearly elastic manner prior to failure. Although beryllium exhibits non-homogeneous material properties in the through-thickness direction, i.e., the through-thickness modulus E_3 is a function of position, an average value of E_3 can be employed to make the solution tractable. The average value of E_3 used for the theoretical computation of the strain components ϵ_1 , ϵ_2 , and ϵ_3 at failure is 447.5 GPa (50.5×10^3 ksi) (Fenn et al. 1967).

The following generalized expressions relate components of stress and strain for an orthotropic material (Lekhnitskii 1981):

$$\begin{aligned}
 \epsilon_1 &= \frac{1}{E_1} \sigma_1 - \frac{\nu_{21}}{E_2} \sigma_2 - \frac{\nu_{31}}{E_3} \sigma_3 \\
 \epsilon_2 &= -\frac{\nu_{12}}{E_1} \sigma_1 + \frac{1}{E_2} \sigma_2 - \frac{\nu_{32}}{E_3} \sigma_3 \dots\dots\dots (208) \\
 \epsilon_3 &= -\frac{\nu_{13}}{E_1} \sigma_1 - \frac{\nu_{23}}{E_2} \sigma_2 + \frac{1}{E_3} \sigma_3 \\
 \epsilon_{13} &= \frac{1}{G_4} \sigma_4, \quad \epsilon_{23} = \frac{1}{G_5} \sigma_5, \quad \epsilon_{12} = \frac{1}{G_6} \sigma_6
 \end{aligned}$$

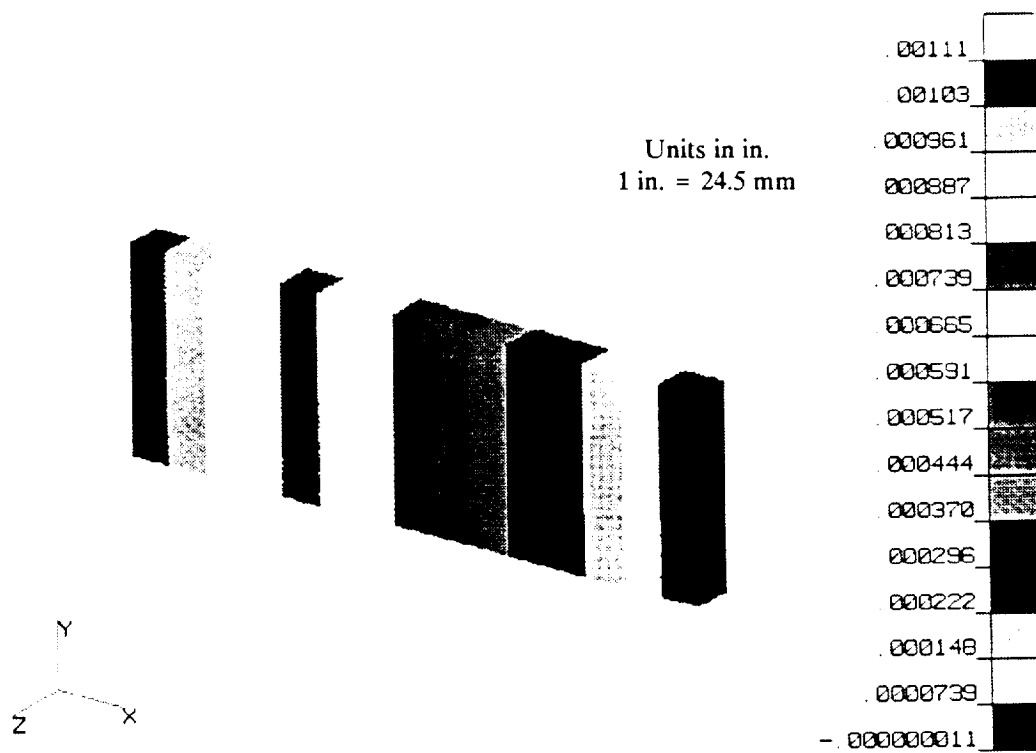


FIG. 70. Distribution of Axial Displacement for 3-D Compression Model

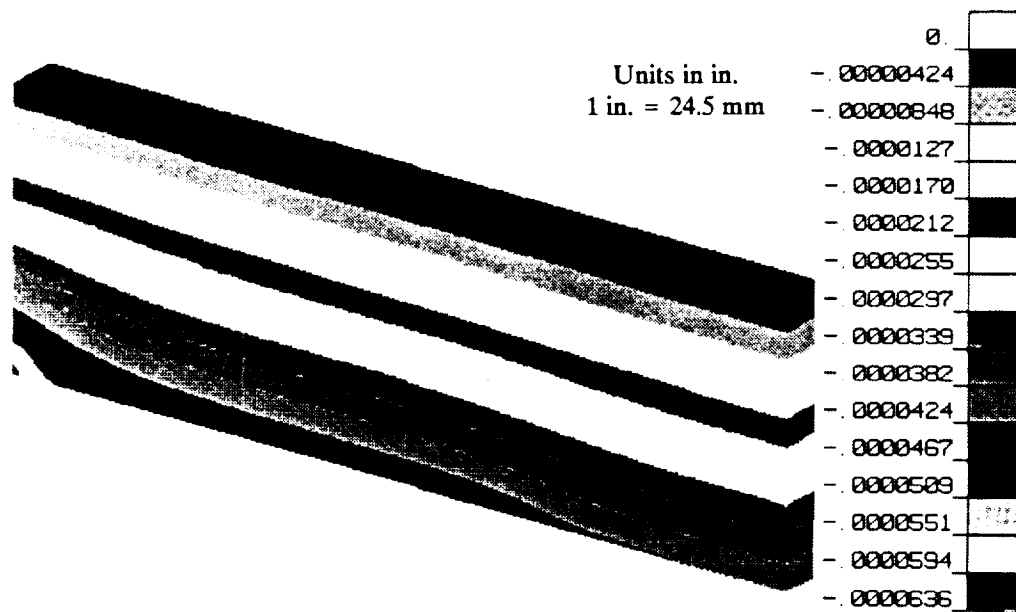


FIG. 71. Distribution of Transverse Displacement for 3-D Compression Model

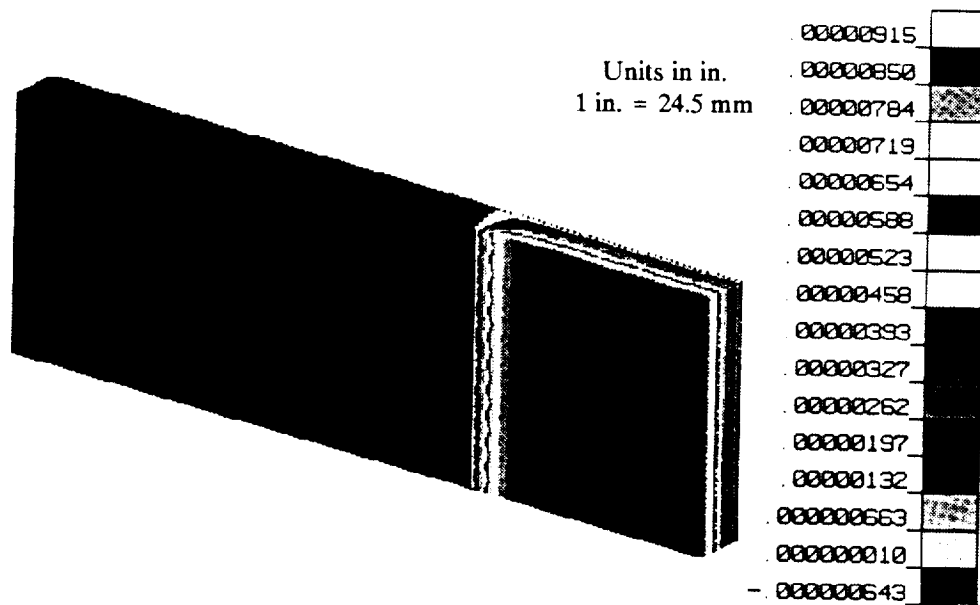


FIG. 72. Distribution of Through-Thickness Displacement for 3-D Compression Model

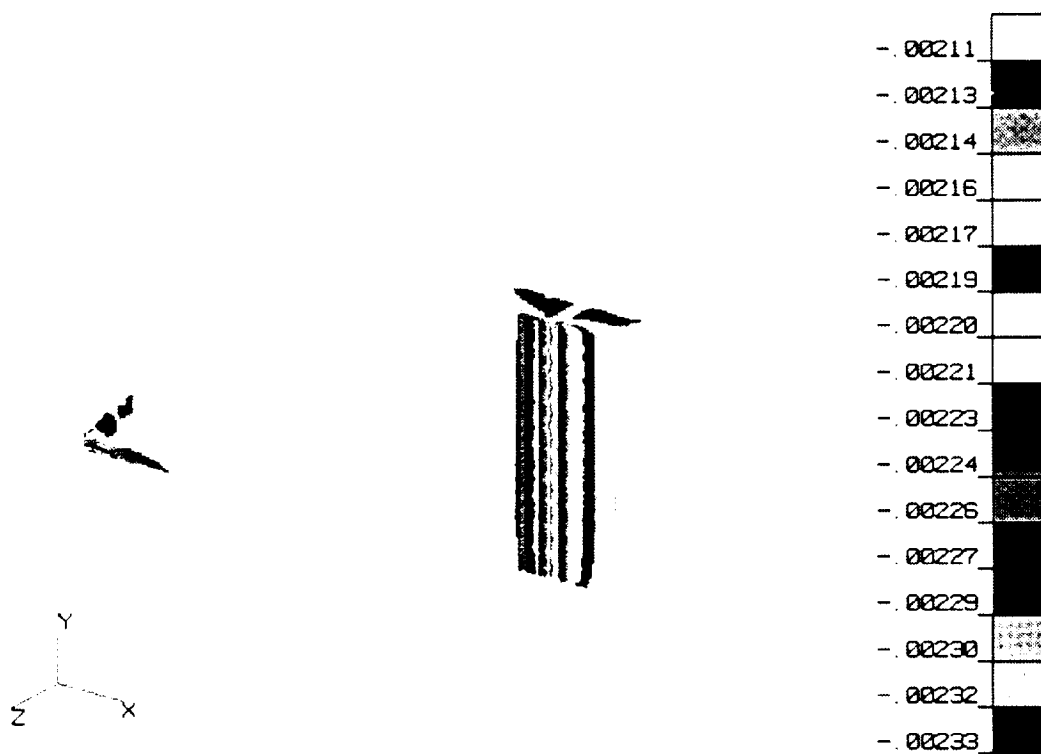


FIG. 73. Distribution of Normal Strain, ϵ_1 , for 3-D Compression Model

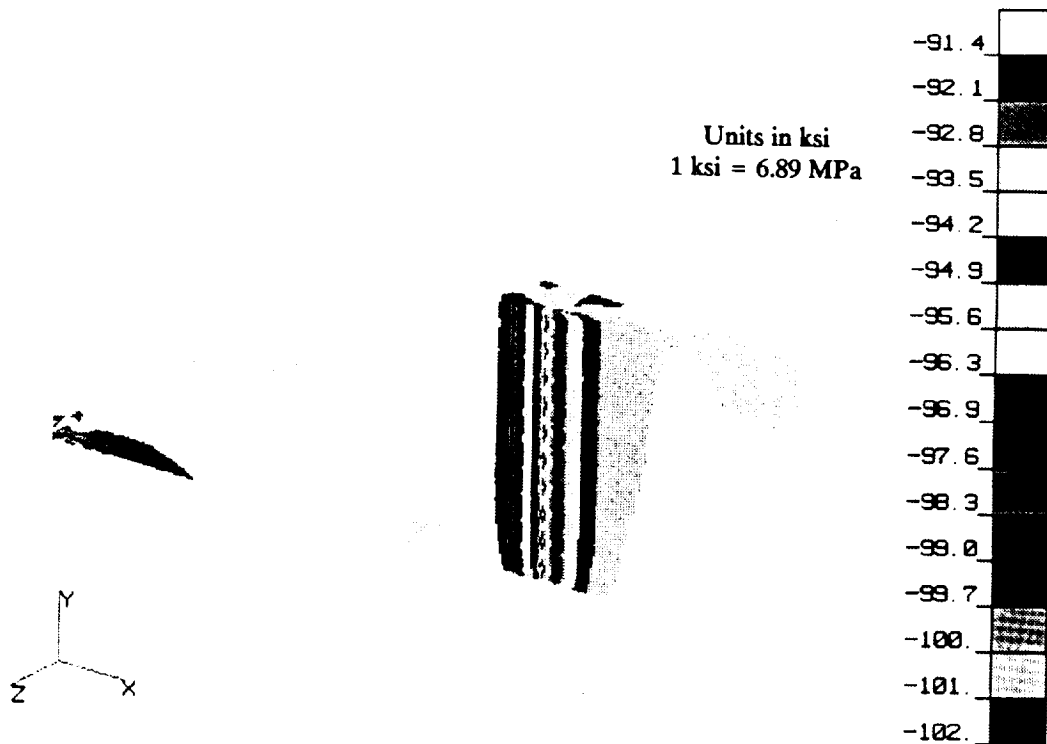


FIG. 74. Distribution of Normal Stress, σ_1 , for 3-D Compression Model

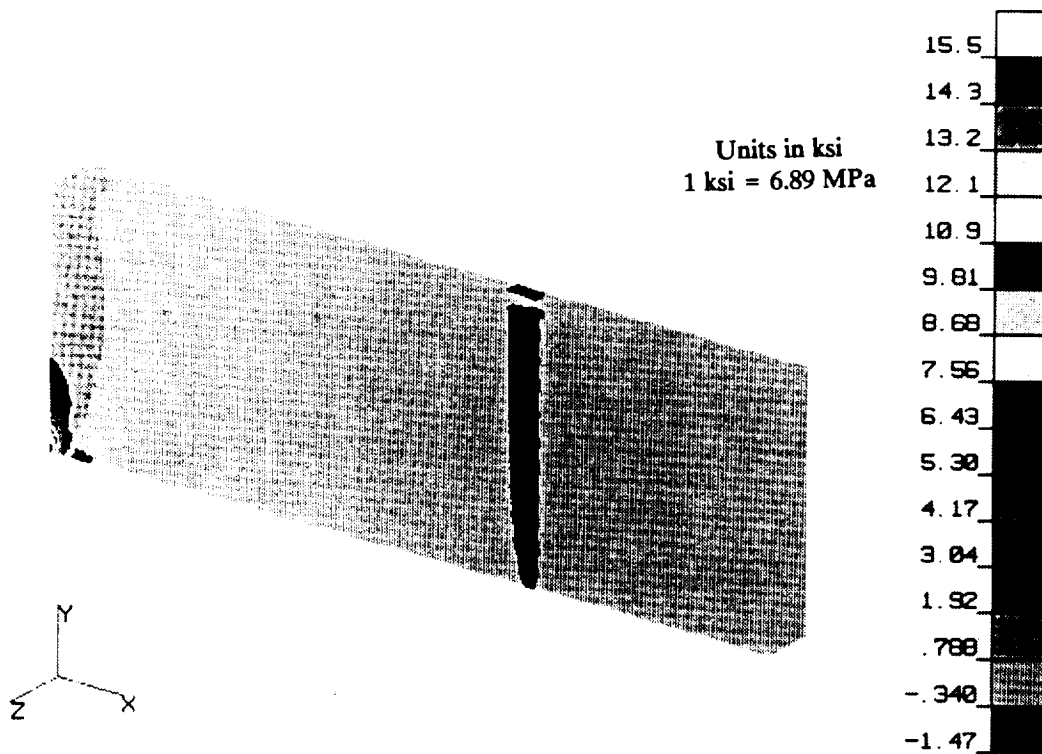


FIG. 75. Distribution of Transverse Stress, σ_2 , for 3-D Compression Model

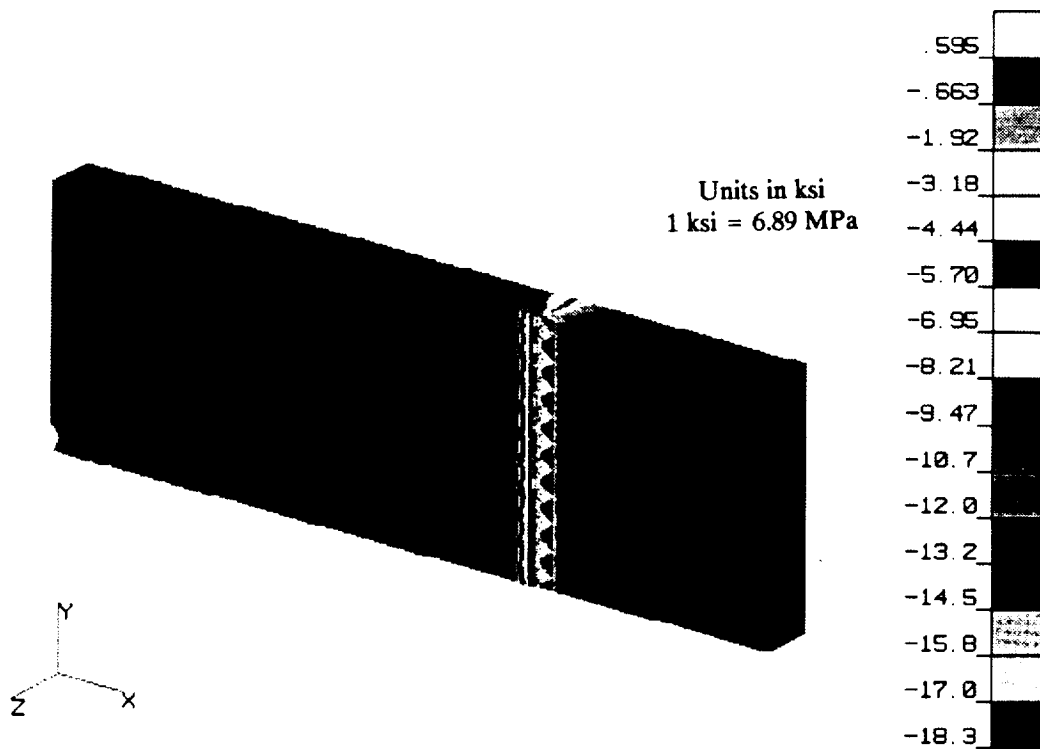


FIG. 76. Distribution of Through-Thickness Stress, σ_3 , for 3-D Compression Model

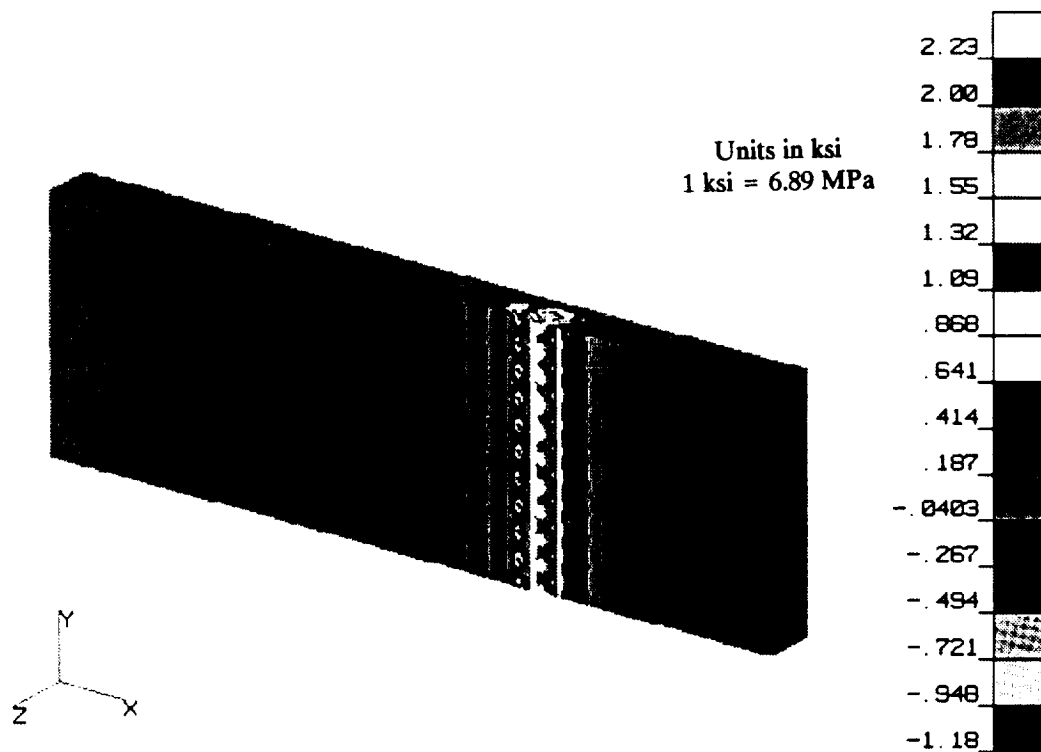


FIG. 77. Distribution of Out-of-Plane Shearing Stress, σ_4 , for 3-D Compression Model

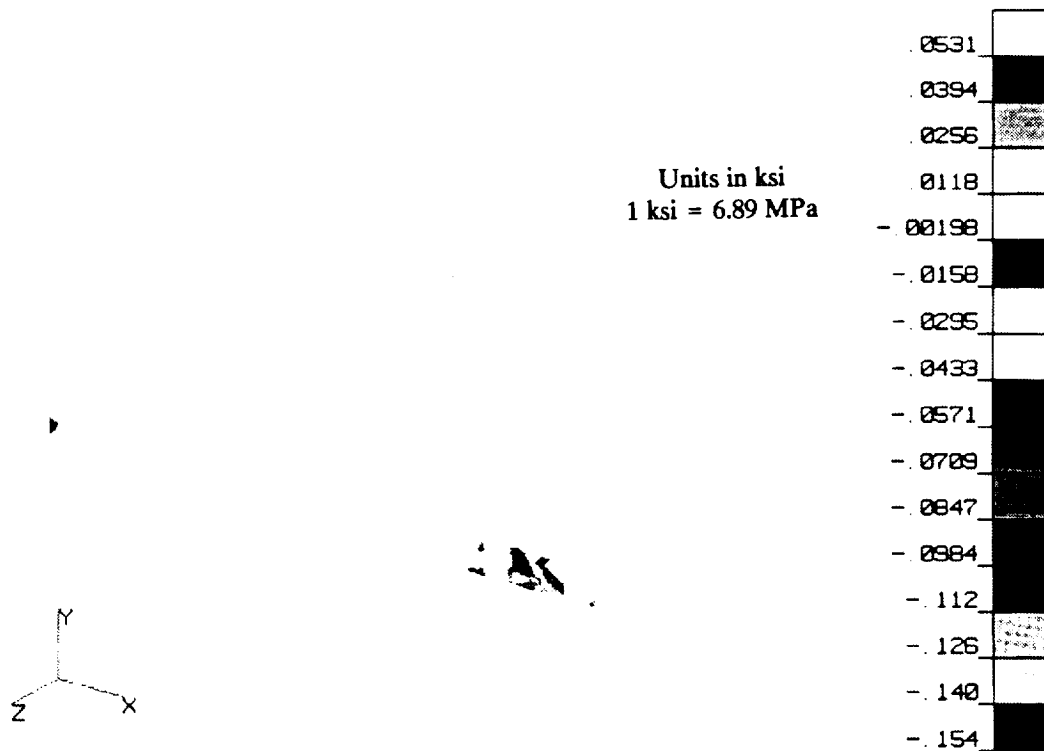


FIG. 78. Distribution of Out-of-Plane Shearing Stress, σ_5 , for 3-D Compression Model

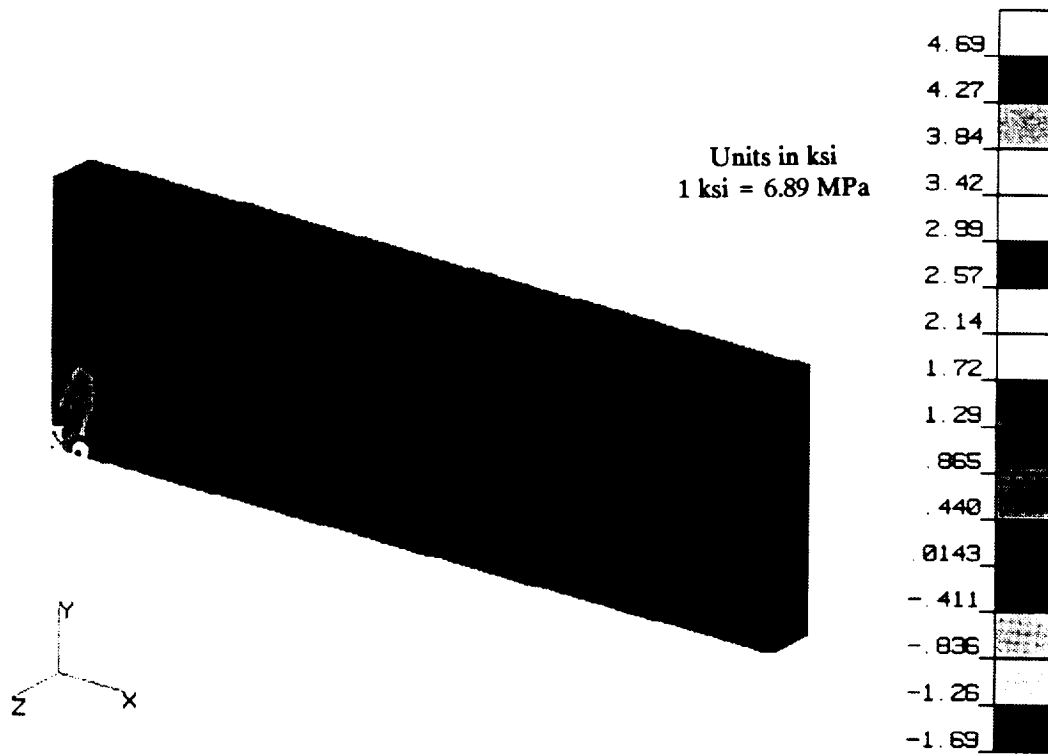


FIG. 79. Distribution of In-Plane Shearing Stress, σ_6 , for 3-D Compression Model

Specialization of these equations for the case of a uniform compressive load, $-\sigma_1$, in the longitudinal direction yields the following relations:

$$\varepsilon_1 = -\frac{\sigma_1}{E_1} \dots\dots\dots (209)$$

$$\varepsilon_2 = \nu_{12} \frac{\sigma_1}{E_1} \dots\dots\dots (210)$$

$$\varepsilon_3 = \nu_{13} \frac{\sigma_1}{E_1} \dots\dots\dots (211)$$

Using the numerically simulated value of $-\sigma_1$ at failure [658.8 MPa (95.6 ksi)] and the material properties in Table 4, the components of strain can be determined from Eqs. 209-211. These components are shown in Table 15.

Similarly, for the case of a uniform compressive load, $-\sigma_2$, in the transverse direction Eqs. 208 become:

$$\varepsilon_1 = \nu_{21} \frac{\sigma_2}{E_2} \dots\dots\dots (212)$$

$$\varepsilon_2 = -\frac{\sigma_2}{E_2} \dots\dots\dots (213)$$

$$\varepsilon_3 = \nu_{23} \frac{\sigma_2}{E_2} \dots\dots\dots (214)$$

Again, using a value for $-\sigma_2$ of 691.8 MPa (100.3 ksi) that is obtained from the numerical analysis, evaluation of Eqs. 212-214 yields the results shown in Table 15.

TABLE 15. Numerical and Theoretical Comparison of Failure Strain Components

Strain Component	Orientation of Principal Rolling from Load	Failure Strain	
		Numerical $\mu\text{mm/mm}$	Elasticity $\mu\text{mm/mm}$
(1)	(2)	(3)	(4)
ε_1	Parallel	0.00227	0.00223
ε_2	Parallel	0.00018	0.00017
ε_3	Parallel	0.00005	0.00005
ε_1	Perpendicular	0.00021	0.00019
ε_2	Perpendicular	0.00238	0.00232
ε_3	Perpendicular	0.00004	0.00004

5.2.4 DETERMINATION OF PRINCIPAL COEFFICIENTS F_1 , F_{11} , F_2 , AND F_{22}

Experimental testing shows good correlation with numerical analysis and suggests that the numerical model is adequate, at least for in-plane loading conditions. Principal failure coefficients F_1 , F_2 , F_{11} , and F_{22} (see Table 13) can be calculated from the following generalized equations provided by Tsai and Wu (1971):

$$F_i = \frac{1}{X_i} - \frac{1}{X_i'} \dots\dots\dots (215)$$

$$F_{ii} = \frac{1}{X_i X_i'}$$

where X_i and X_i' for $i, j = 1, 2$, and 3 are tensile and compressive strengths, respectively, in the three principal directions of orthotropy. In-plane tensile strength data (Fenn et al. 1967) and results of the compression experiment (Table 14) lead to the following coefficients:

$$\begin{aligned} F_1 &= 3.4153 \times 10^{-4} \text{ MPa}^{-1} & (2.3548 \times 10^{-3} \text{ ksi}^{-1}) \\ F_1 &= 3.2762 \times 10^{-4} \text{ MPa}^{-1} & (2.2588 \times 10^{-3} \text{ ksi}^{-1}) \dots\dots\dots (216) \\ F_{11} &= 2.5629 \times 10^{-6} \text{ MPa}^{-2} & (1.2184 \times 10^{-4} \text{ ksi}^{-2}) \\ F_{22} &= 2.5629 \times 10^{-6} \text{ MPa}^{-2} & (1.2184 \times 10^{-4} \text{ ksi}^{-2}) \end{aligned}$$

5.3 IN-PLANE SHEARING STRESS

Determination of the principal coefficient F_{66} (Tsai and Wu 1971; Priddy 1974), as well as interaction coefficients F_{166} and F_{266} (Tennyson and Elliot 1983; Jiang and Tennyson 1989), requires knowledge of the in-plane shearing strength, σ_6 . This section describes a special experiment that is carried out on titanium and beryllium specimens toward this end. Numerical simulation of each test that aids in design of the specimen and determination of the failure stresses is also presented.

5.3.1 Titanium Experiment and Simulation

As a preliminary test, a shear specimen made from a sheet of 6Al-4V titanium alloy is numerically modeled, and then fabricated and loaded to failure. This material is chosen because of its availability and due to the fact that it has a hexahedral-close-packed lattice microstructure that is the same as that of beryllium. Results of numerical modeling suggest a 114.3-mm \times 25.4-mm (4.5-in. \times 1.0-in.) coupon with two 45° slits located similar to those shown in Fig. 80 for a beryllium specimen. However, note that the center ends of the slits of the titanium specimen are aligned with the centerline of the specimen while those of beryllium specimen described in section 5.3.2 are slightly offset from the centerline. After fabrication, the titanium specimen is tested using the 44.5-kN (10.0-kip) MTS testing

machine. The ends of the coupon are subjected to tensile loadings that cause the center of the specimen to predominantly undergo a shearing stress.

A strain gage aligned with the direction of loading is placed between the ends of the two slits at the center of one side of the specimen (similar to Fig. 80). The specimen is loaded in stroke control at a rate of 2.54 mm/s (0.1 in./sec). A comparison of experimental strain gage readings and numerically simulated values are shown in Fig. 81(a). The strain gage fails after the specimen is subjected to a shearing stress of approximately 600 MPa (87 ksi). The failed titanium shear specimen is shown in Fig. 82(a). It should be noted that the specimen fails after attaining considerable normal strain in the direction of the loading and in a manner that suggests ductile behavior. In addition, failure takes place in such manner that two almost identical pieces result with the separation crack linking the bulbs of the slits.

A numerical FEA model that has isotropic material properties and includes effects of non-linear geometry is constructed for the specimen. Material properties are provided by the manufacturers of 6Al-4V alloy (RMI 1967). Satisfactory correlation between numerical simulation and experimental data is determined for the shearing strength of titanium [see Fig. 81(a)]. The shearing strength of this alloy is reported to be 759 MPa (110 ksi) (RMI 1967). Experimentally, the shearing strength of the coupon is determined to be 786 MPa (114 ksi). This value is obtained by dividing the failure load by the cross-sectional area of the region between the bulbs of the 45° slits. Output from numerical simulation suggests a shearing strength of 764 MPa (111 ksi) which is in close agreement with both the experimental results and the information provided by the manufacturer (RMI 1967). Both experimental and numerical studies indicate a pure shear mode of failure for the titanium specimen.

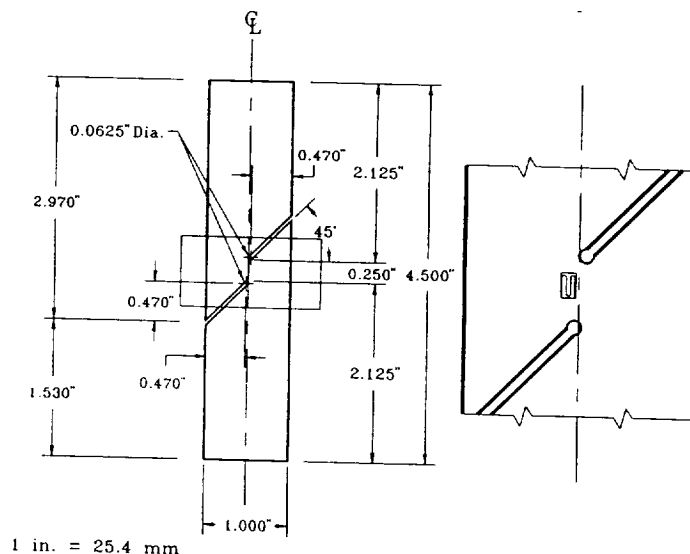
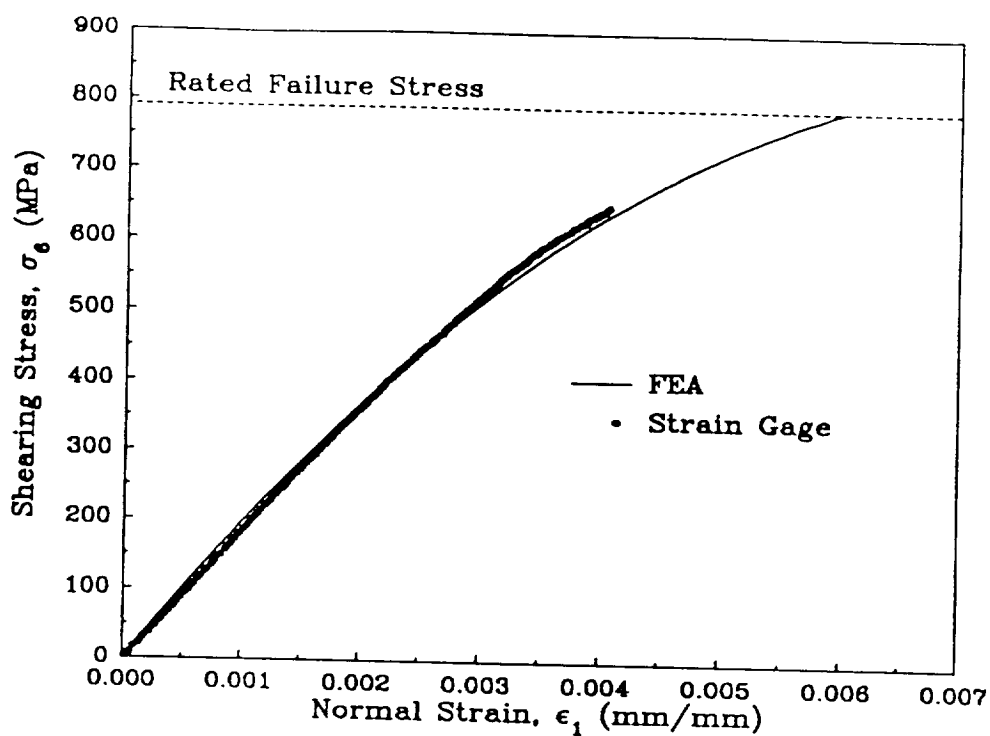
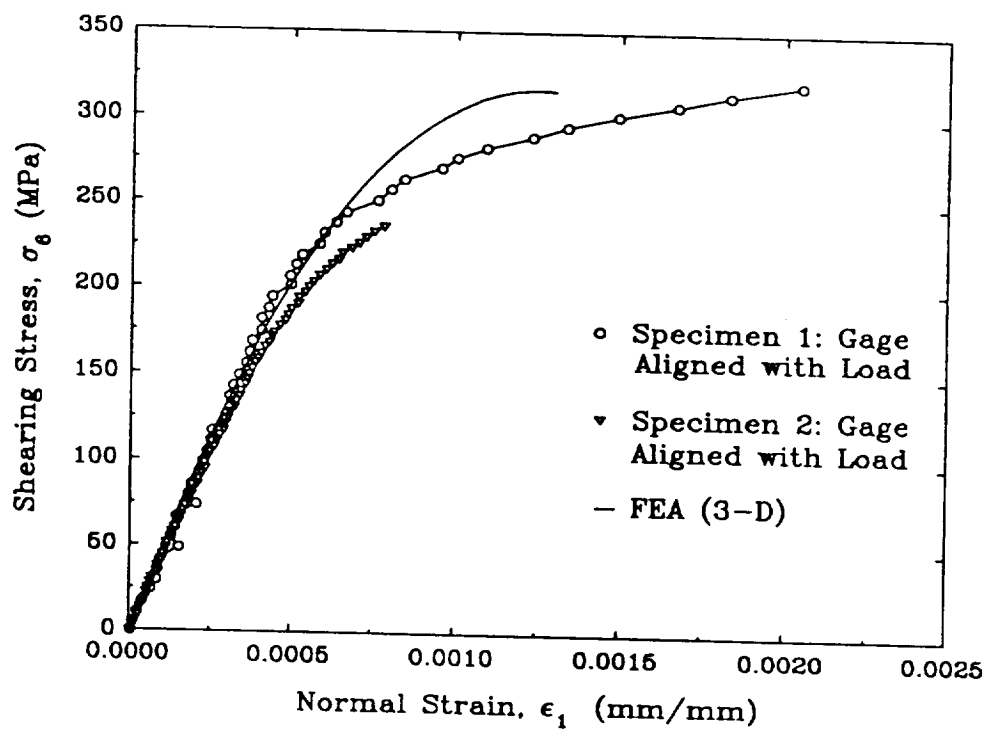


FIG. 80. Geometry of Beryllium Shear Specimen



(a)

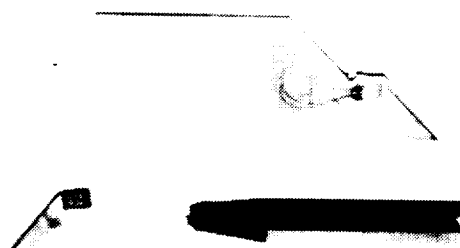


(b)

FIG. 81. Experimental and Numerical Results for (a) Titanium and (b) Beryllium Shear Specimens



(a)



(b)

FIG. 82. (a) Titanium and (b) Beryllium Shear Specimens after Failure

5.3.2 Beryllium Experiment

Two experimental specimens, dimensionally identical to the one shown in Fig. 80, are used to estimate the shearing strength of beryllium. Each specimen is loaded in the same way and at the same rate as the titanium specimen. In addition, each specimen has the principal rolling direction aligned with the load. A strain gage is mounted on each surface of the plate and aligned with the loading direction. Fig. 81(b) shows shearing stress versus the average normal strain at the location of the strain gage for each of the two specimens. The shearing stress is determined by dividing the axial load by the cross-sectional area of the region between the 45° slits. It should be noted that the strain gages mounted on specimen 2 failed prematurely. Table 16 summarizes the failure strengths determined from this experiment for titanium and beryllium. A failed beryllium specimen is shown in Fig. 82(b).

Unlike titanium, a mixed mode of failure appears to dominate for beryllium. This is partly attributed to the fact that the ends of the 45° slits of the titanium specimen are exactly aligned with the centerline that is parallel to the direction of application of the load, while the end slits of beryllium are slightly offset with respect to the centerline. The geometry of the specimen and the direction of loading caused failure in a combined state of shear and axial tension. Thus, the experiment can not be regarded as a totally successful means for estimating shearing strength of beryllium. However, via transformation of the stress tensor at failure, a state of pure shear can be calculated on a rotated differential element (Fig. 83). For the two specimens this yields an average value of pure shearing stress of 322.7 MPa (46.8 ksi). This strength is verified by another experiment recently conducted by NASA (see section 4.3).

After careful examination of the failed specimen, the mixed mode of failure that occurred, namely tension-shear, can be attributed partially to the fact that the through-thickness surfaces of the slits, especially near the center of the specimen, were heavily oxidized. Surface cracks may have formed prematurely at the sites of cavitation due to corrosion and, thus, induced a mixed mode of failure due to pre-orientation. Moreover, the slight offset of the ends of the slits may have contributed to this phenomenon.

TABLE 16. Failure Strength for In-Plane Shear Specimens

Specimen Number (1)	Material (2)	Failure Stress	
		MPa (3)	(ksi) (4)
1	Titanium	786.3	(114.0)
2	Beryllium	322.7	(46.8)
3	A Beryllium	345.9	(50.2)

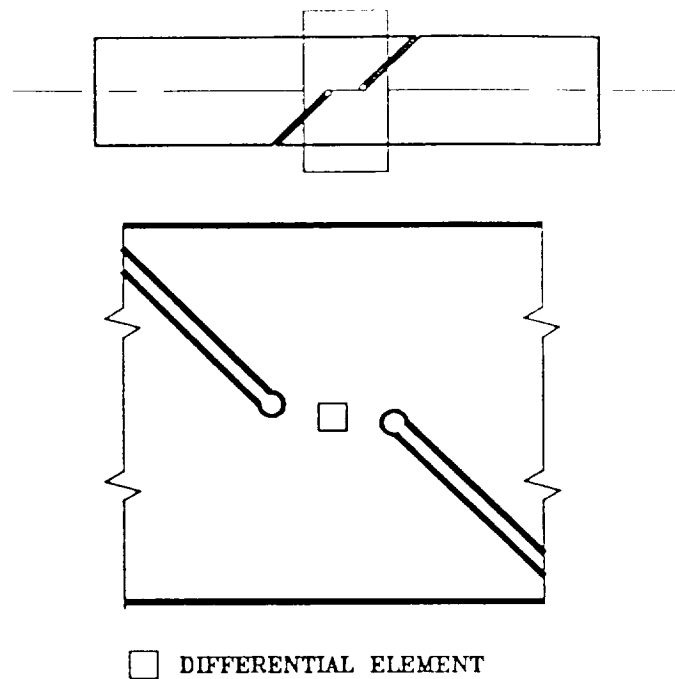


FIG. 83. Location Differential Element for Transformation to a State of Stress of Pure Shear

5.3.3 Numerical Simulation of Beryllium Experiment

Prior to actual fabrication and physical testing an FEA model is used to simulate the proposed in-plane shear test. The actual specimen is a 114.3-mm \times 25.4-mm \times 2.54-mm (4.5-in. \times 1.0-in. \times 0.1-in.) coupon with two 45° slits located anti-symmetrically with respect to the x-x and y-y planes of symmetry (Fig. 80). Two- and three-dimensional models of this specimen are generated. Fig. 84 shows the mesh used for two-dimensional analysis for the critical region at the center of the plate structure. The 2-D model includes orthotropic material behavior as well as non-linear geometric considerations. Inhomogeneous orthotropic material properties and geometrical nonlinearities are incorporated in the 3-D models.

The two-dimensional numerical model simulates the entire specimen. It has two-thousand, eight-noded plate elements, and approximately 40,000 degrees-of-freedom. There are five through-thickness points of integration for each of the nine integration locations per plate element. Numerical output is requested at each of the eight nodes of each element for the top and bottom surface. Fringe plots showing distributions of selected components of displacement, strain, and stress at the failure load of 3.9 kN (875.0 lb) are

presented in Figs. 85-92. Figs. 85 and 86 show distribution of axial and transverse displacement, respectively. They indicate that in the critical region an anti-symmetric pattern occurs about a line that passes through the center points of the rounded regions of the 45° lateral cuts. The same condition of anti-symmetry is indicated for all other components of strain and stress as well (Figs. 87 through 92). From these figures, all three components of strain and stress are significant in the region between the ends of the slots. Maximum values of 44.8 MPa (6.5 ksi), -29.0 MPa (-4.2 ksi), and 312.3 MPa (45.3 ksi) for σ_1 , σ_2 , and σ_6 , respectively, are induced in this region. A state of pure shearing stress at the center of the plate is determined by using a simple stress transformation. This yields an ultimate shearing strength of 314.4 MPa (45.6 ksi) that occurs on a material plane that makes an angle of 1.1° with respect to the loading axis.

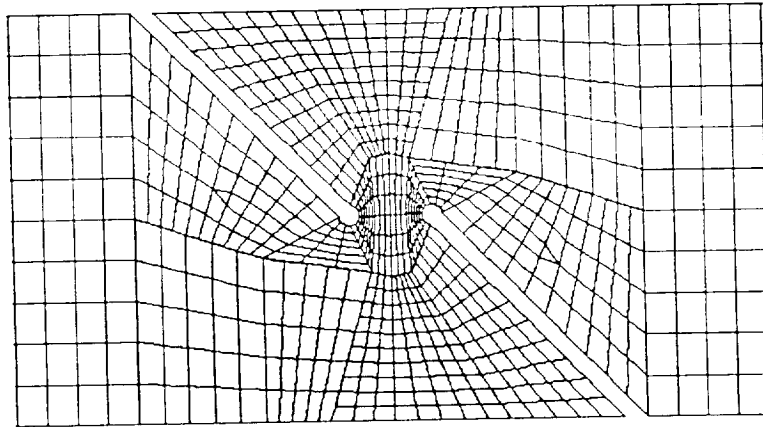


FIG. 84. Finite Element Mesh for Critical Region of Two-Dimensional Shear Specimen

For the three-dimensional model, 5,400 twenty-noded hexahedral elements are used (see Fig. 93). Due to symmetry of the load and anti-symmetry of the geometry of the specimen, only one-fourth of the actual structure is simulated. A plane of anti-symmetry passes through the centroid of the structure and parallel to the loaded end. In addition, special equations are specified in the input to the FEA code so that displacement magnitudes along this plane are antisymmetric. For example, deformation in the longitudinal direction at the top of Fig. 94 are to the right in the middle of the specimen, while those at the bottom are to the left. The overall structure is symmetric about a plane

passing through the center of its thickness direction. Five elements are used to simulate one-half of the thickness of the plate as a consequence of this symmetry. Figs. 94-98 show fringe plots of selected components of displacement, strain, and stress at the top surface at failure load. Results obtained suggest a different stress distribution as compared to the two-dimensional results (Figs. 84-92). This is mainly due to differences in geometry of the bulb ends of the slits as well as the material variation in the through-thickness direction. Stresses σ_1 , σ_2 , and σ_6 acquire values of 313.7 MPa (45.5 ksi), -68.9 MPa (-10.0 ksi), and 255.1 MPa (37.0 ksi), respectively, in the critical region between the two ends of the slits. Out-of-plane quantities are negligible by comparison. A condition of pure shearing stress can be achieved by means of a stress transformation at the centroid of the specimen. The magnitude of this stress is 296.5 MPa (43.0 ksi) which occurs at an angle of 11.3° with respect to the direction of the load.

The shearing stress obtained experimentally at failure shows good correlation with numerical analysis. This suggests that the model utilized for numerical simulation is adequate for the type of analysis performed.



FIG. 85. Distribution of Longitudinal Displacement for 2-D Beryllium Shear Specimen

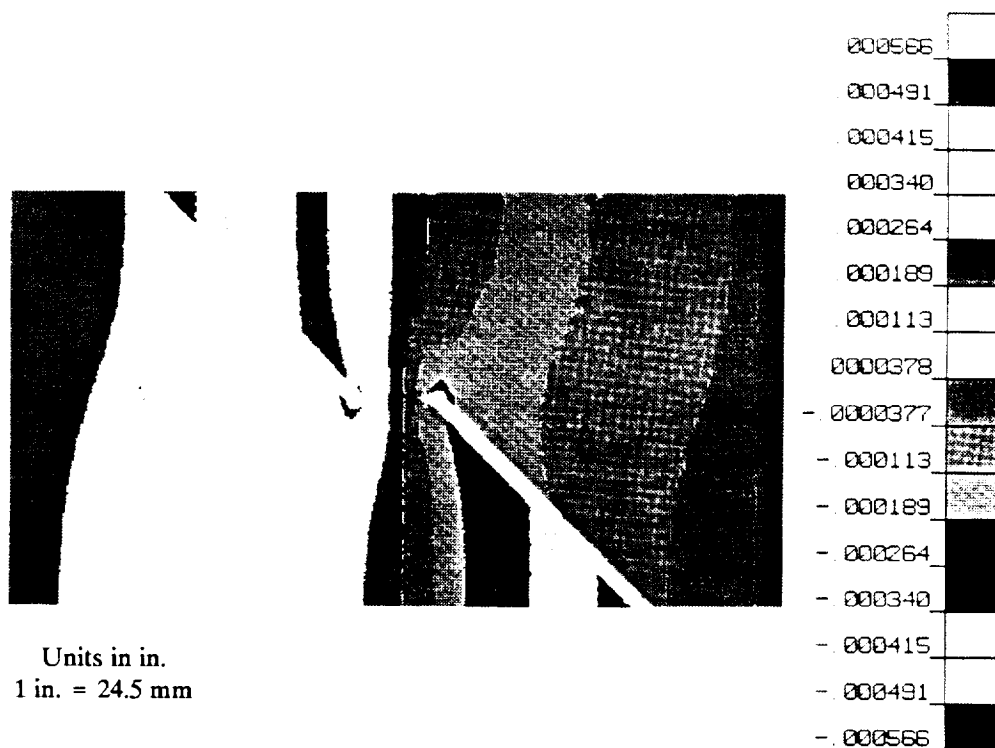


FIG. 86. Distribution of Transverse Displacement for 2-D Beryllium Shear Specimen

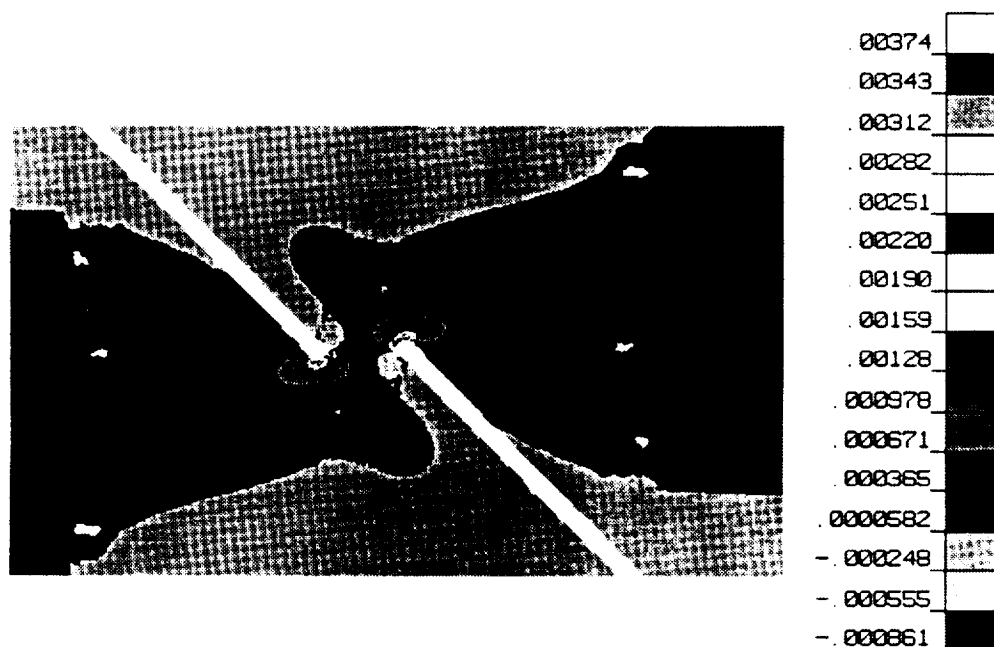


FIG. 87. Distribution of Longitudinal Strain for 2-D Beryllium Shear Specimen

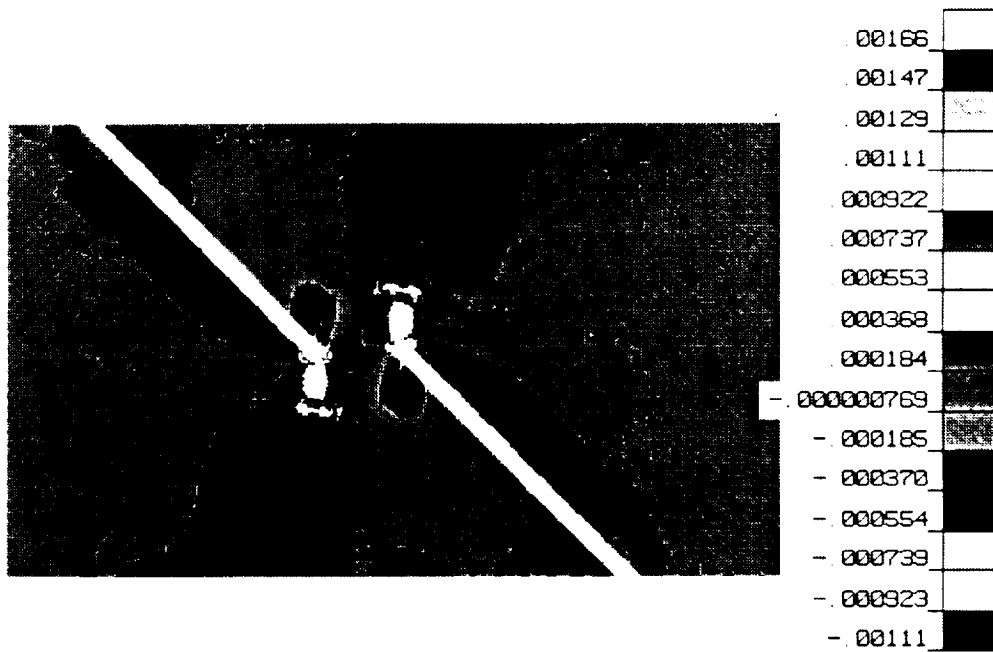


FIG. 88. Distribution of Transverse Strain for 2-D Beryllium Shear Specimen

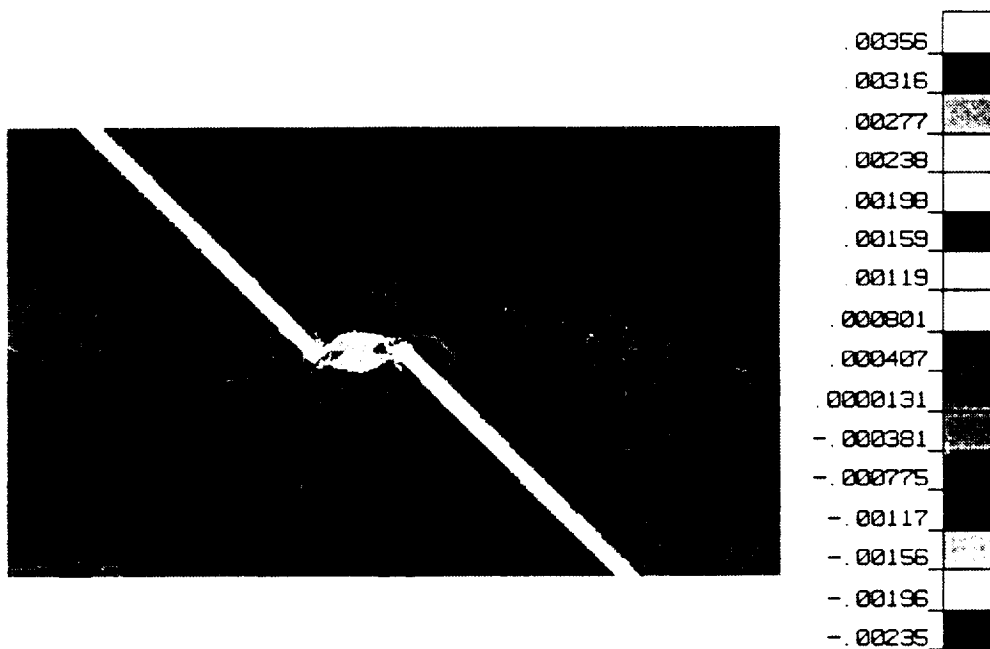


FIG. 89. Distribution of In-Plane Shearing Strain for 2-D Beryllium Shear Specimen

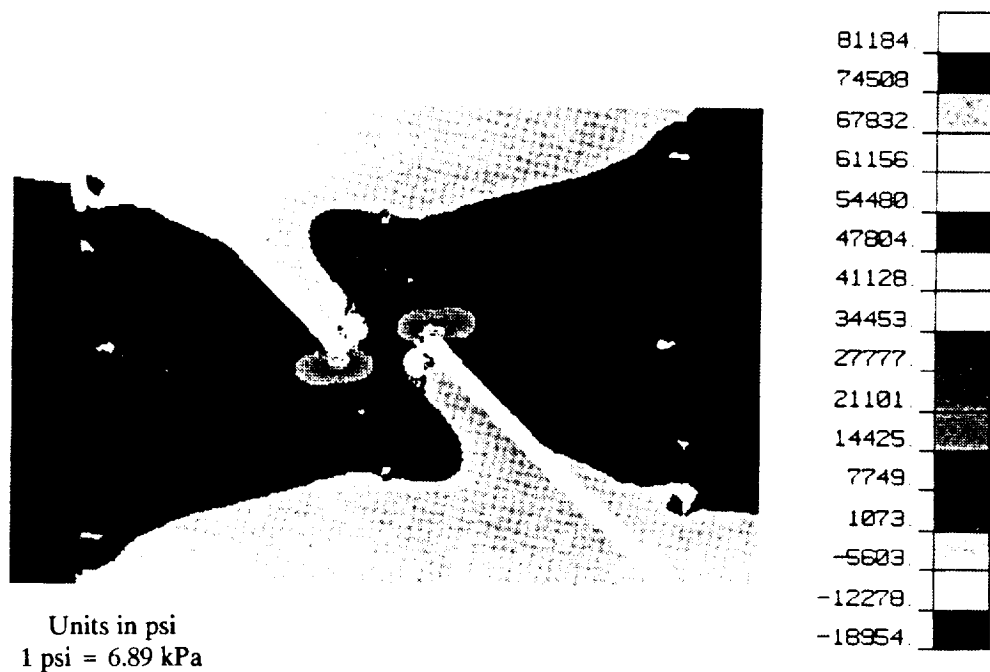


FIG. 90. Distribution of Longitudinal Normal Stress for 2-D Beryllium Shear Specimen

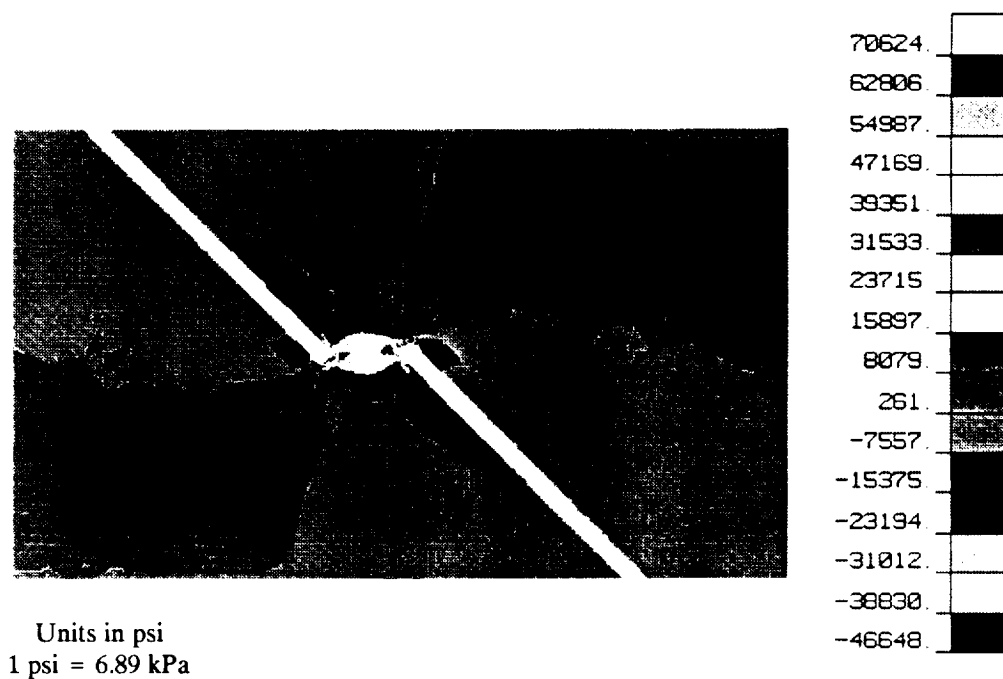


FIG. 91. Distribution of In-Plane Shearing Stress for 2-D Beryllium Shear Specimen

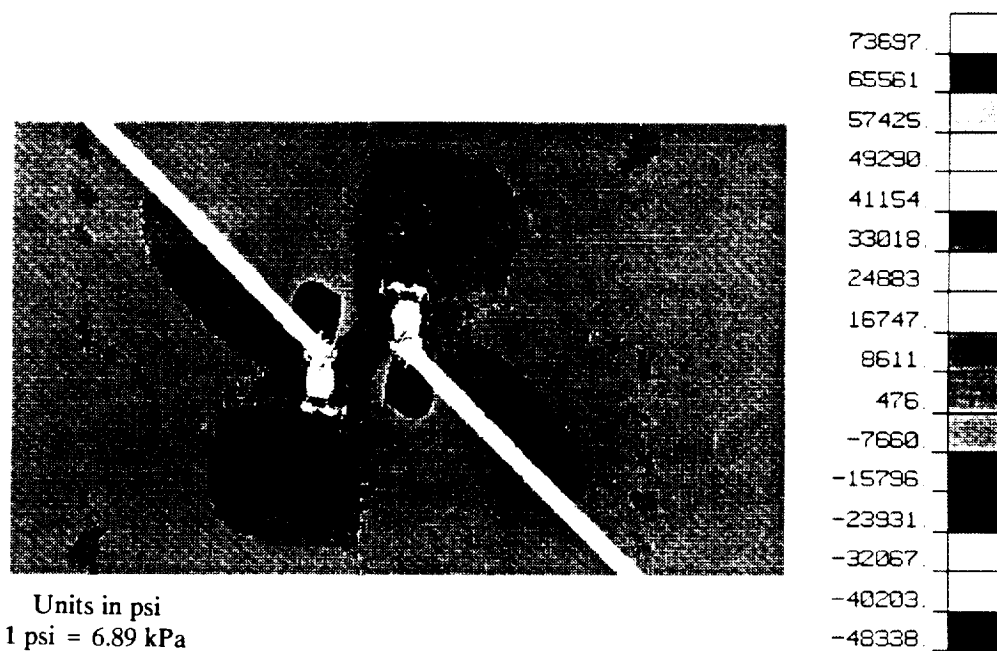


FIG. 92. Distribution of Transverse Normal Stress for 2-D Beryllium Shear Specimen

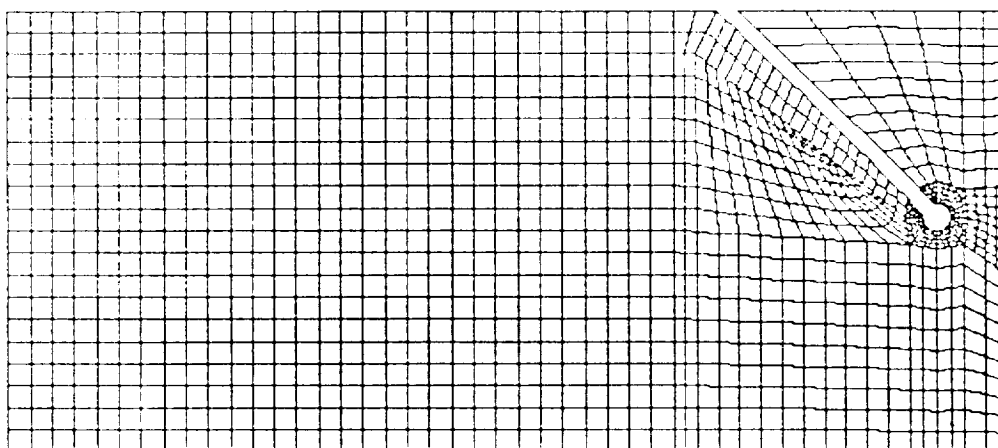


FIG. 93. Finite Element Model of Three-Dimensional Shear Specimen

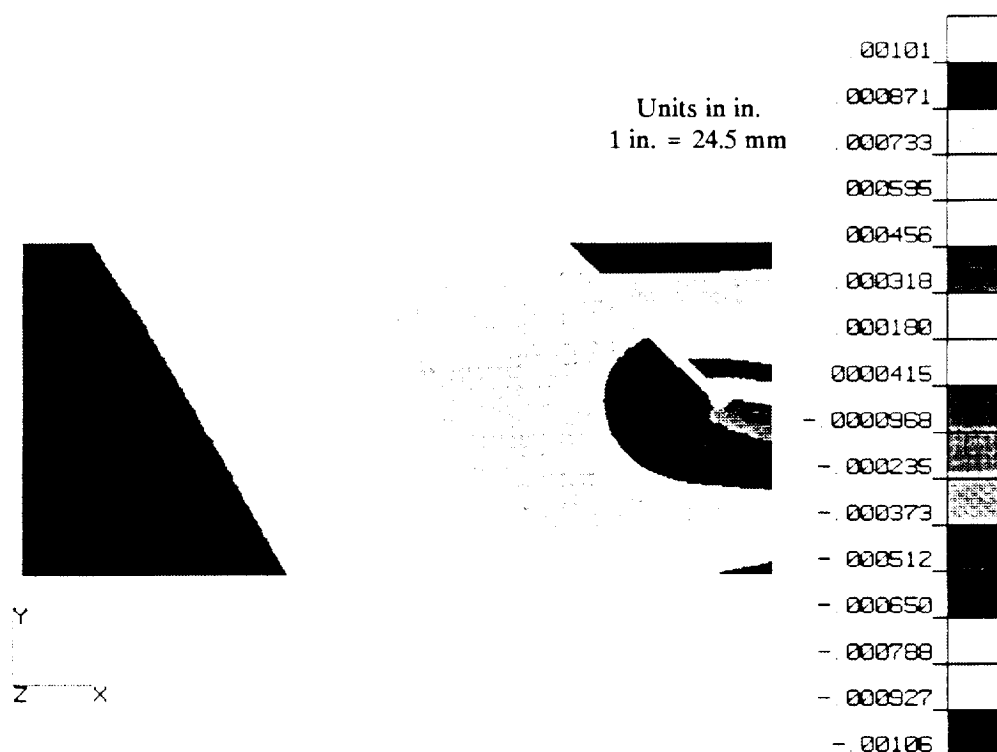


FIG. 94. Distribution of Longitudinal Displacement for 3-D Beryllium Shear Specimen

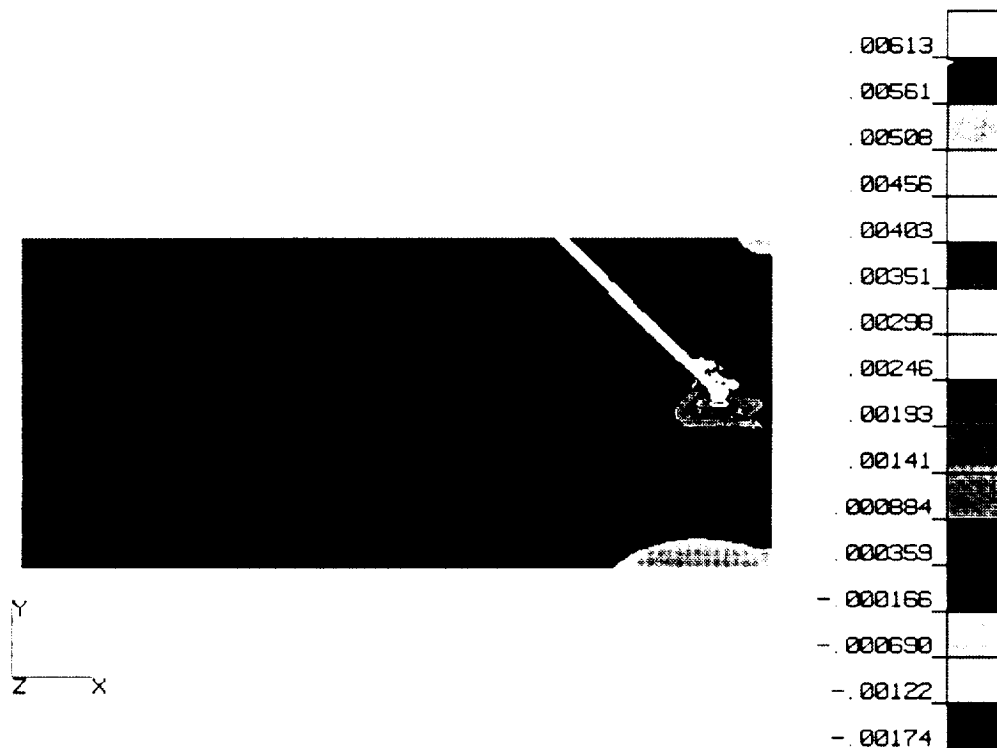


FIG. 95. Distribution of Axial Strain for 3-D Beryllium Shear Specimen

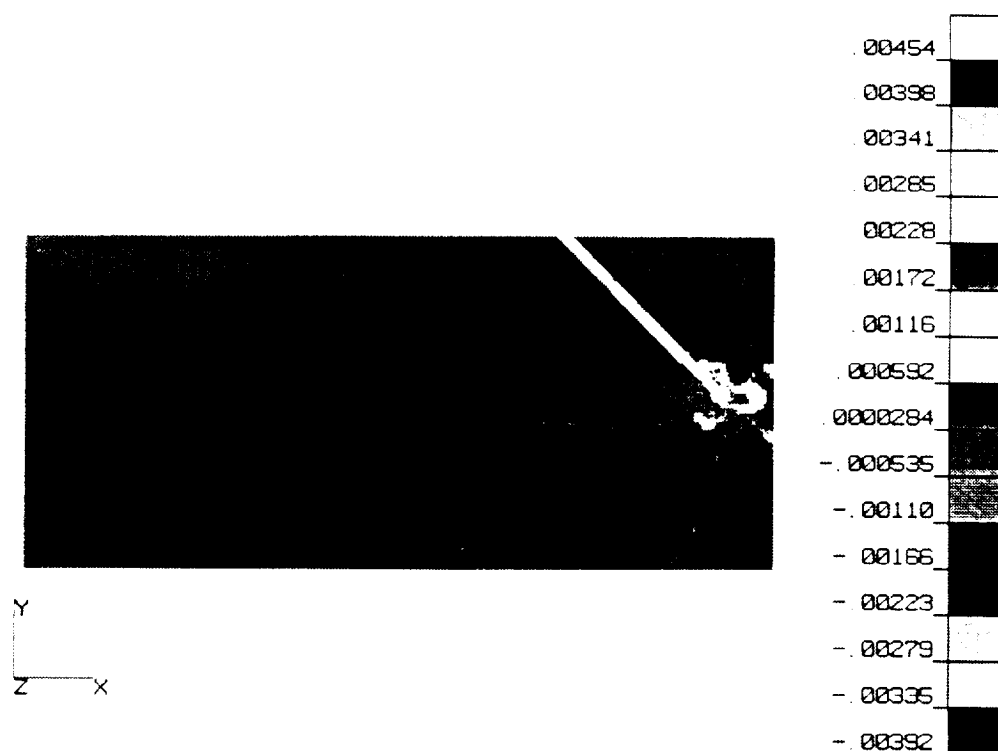


FIG. 96. Distribution of In-Plane Shearing Strain for 3-D Beryllium Shear Specimen

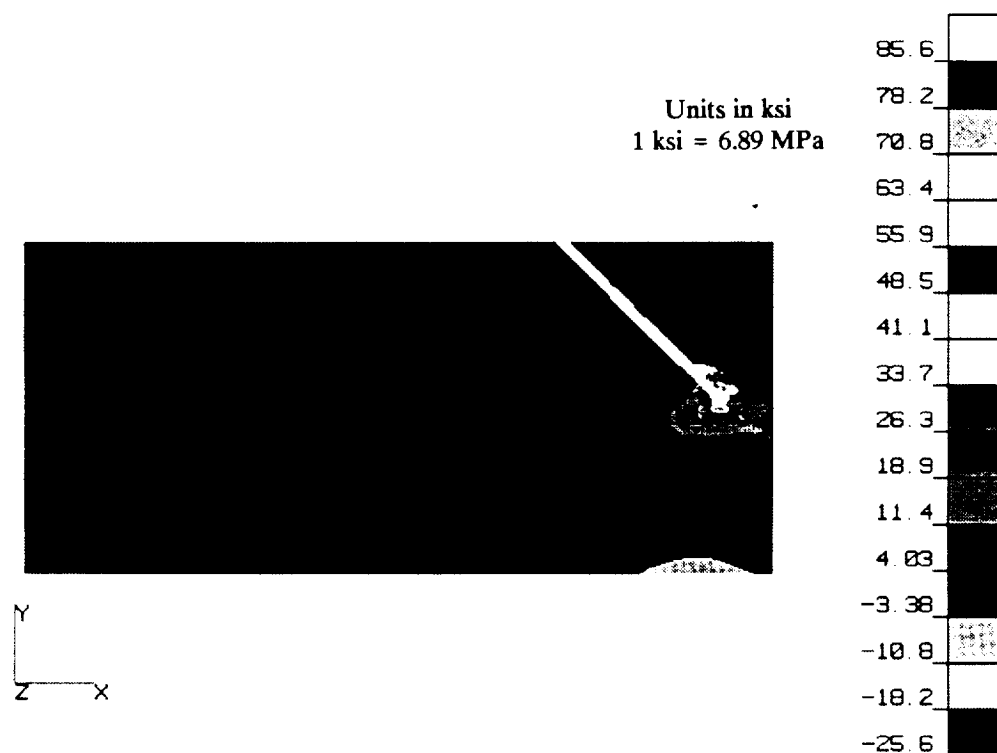


FIG. 97. Distribution of Axial Stress for 3-D Beryllium Shear Specimen

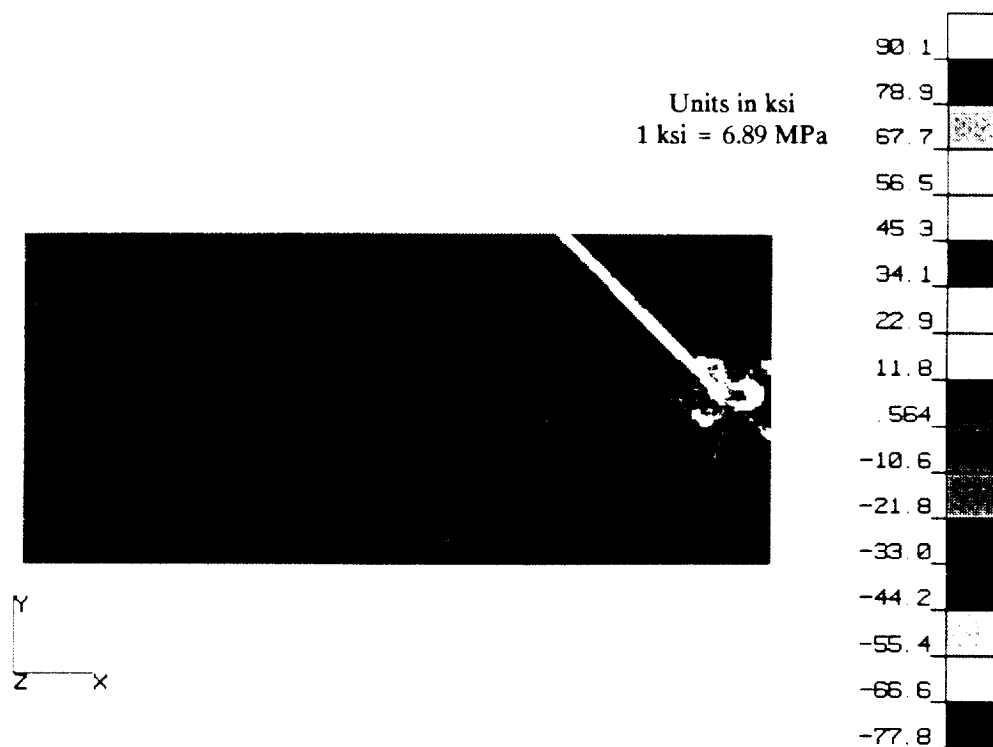


FIG. 98. Distribution of In-Plane Shearing Stress for 3-D Beryllium Shear Specimen

5.3.4 Determination of Principal Coefficients F_6 and F_{66}

The principal failure coefficient F_{66} for beryllium (see Table 3) can be calculated from Eq. 35. The governing equations for determination of the failure strength coefficients are as follows:

$$F_6 = \frac{I}{T} - \frac{I}{T'} \dots\dots\dots (217)$$

$$F_{66} = \frac{I}{TT'}$$

where T and T' are positive and negative in-plane shearing strengths. However, since the material is treated as an orthotropic continuum and positive and negative shearing strengths are assumed to be identical:

$$T = T'$$

$$F_6 = 0 \dots\dots\dots (218)$$

$$F_{66} = \frac{I}{T^2}$$

Substituting $T = 322.7$ MPa (46.8 ksi) into Eq. 218 gives the following coefficient:

$$F_{66} = 9.604 \times 10^{-6} \text{ MPa}^{-2} \quad (4.566 \times 10^{-4} \text{ ksi}^{-2}) \dots\dots\dots (219)$$

If the in-plane shearing strength of 303.4 MPa (44.0 ksi) reported by NASA is used instead (see section 4.3), the F_{66} coefficient becomes:

$$F_{66} = 1.0866 \times 10^{-5} \text{ MPa}^{-2} \quad (5.1653 \times 10^{-4} \text{ ksi}^{-2}) \dots\dots\dots (220)$$

The difference in the two coefficients is approximately 21 percent. For development of the proposed criterion the latter coefficient, NASA's, is used. This decision is based on the fact that the coefficient that results from NASA's tests is more conservative, i.e., it causes the failure surface of the proposed criterion for beryllium to occupy less volume. In addition, results obtained from the experiment that produced the former coefficient (Papados and Roschke 1991) are not as reliable due to surface flaws on the specimen.

5.4 THROUGH-THICKNESS SHEAR

5.4.1 Experiments

Determination of the failure coefficients F_{44} and F_{55} (see Eq. 35 and Table 13) requires knowledge of the through-thickness shearing stresses σ_4 and σ_5 , respectively, at failure. This section describes how these coefficients are obtained experimentally by means of a double shear test.

A schematic of the beryllium plate and clamping steel fixtures used in the laboratory are shown in Figs. 99 and 100. Geometrical dimensions of the beryllium coupons are identical with those used for the compression test discussed in section 5.2 (cf. Figs. 58 and 59). The specimens are again specially oriented: one has the principal direction of cross rolling parallel to the long dimension of the coupon, and the other has the secondary direction of cross rolling parallel to the long dimension of the coupon (see Fig. 99). A special fixture that was designed for testing of beryllium plates (Mascorro et al. 1991) is used to secure each specimen. An area that is 12.7 mm \times 25.4 mm (0.5 in. \times 1.0 in.) at each end of the coupon is clamped. Load is applied in the through-thickness direction. This is accomplished with a 25.4-mm \times 12.7-mm \times 50.8-mm (1.0-in. \times 0.5-in. \times 2.0-in.) A-2 steel puncher that is hardened to the maximum practical permissible limit of 60/62 on the Rockwell C scale. A schematic of the experimental arrangement appears in Fig. 100.

An 8.9-kN (20.0-kip) uniaxial MTS testing machine is used for testing each through-thickness shear specimen. All specimens are loaded in displacement (stroke) control at a rate of 4.2×10^{-2} mm/s (0.1 in./min). The time required for each specimen to fail is less than one minute. Data acquisition includes applied load, time, and strain gage output.

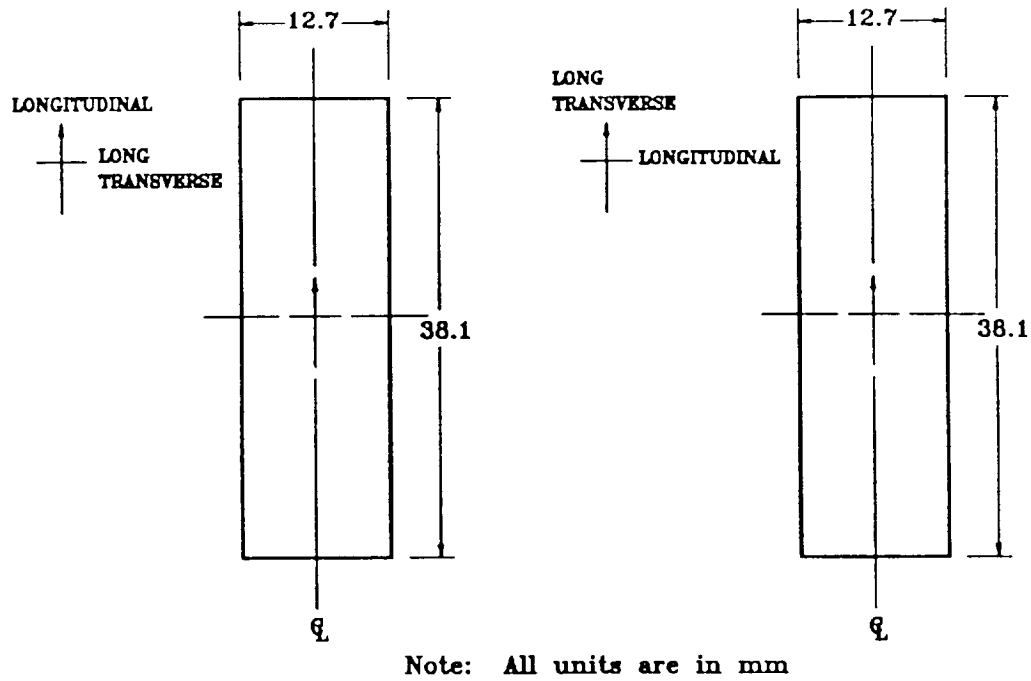


FIG. 99. Dimensions of Specimens for Double Shear Test

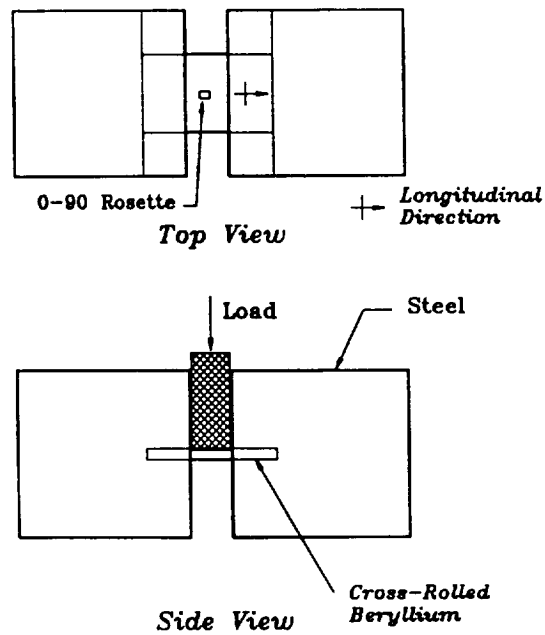


FIG. 100. Setup for Through-Thickness Shearing Stress Test

Two specimens per orientation of the material are used for establishing the out-of-plane shearing strengths of cross-rolled beryllium sheet. Due to satisfactory agreement in the results additional specimens are not tested. A strain gage is mounted at the center of the bottom surface in the longitudinal direction for each specimen. Gages in both test configurations indicated little strain, which shows that no appreciable bending stresses are developed during loading. Figs. 101 and 102 display through-thickness shearing stress versus axial and transverse strain (aligned with and perpendicular to the principal rolling directions), respectively, from transducers mounted on the bottom surface of one of the specimens for each material orientation. The through-thickness shearing strength for each specimen is obtained by dividing the failure load by twice the cross-sectional area of the coupon (RMI 1967). It should be noted that this method is not considered to be accurate. These strengths are in close agreement with the numerical output from Table 17.

Top and side views of the failed specimens for both configurations are shown in Figs. 103 through 105. Figs. 103 and 105 show one of the specimens after failure that has the primary rolling direction aligned with the supporting edge. An example of the opposite orientation is shown in Figs. 104 and 106. For each case, a major crack develops near the supporting edge and propagates through the thickness (Figs. 103 and 104). Secondary cracks can be seen in close proximity as well. This is due to the fact that the edge of the plate is not completely clamped. Therefore, numerical simulation predicts that a combination of axial, shear, and normal through-thickness stresses (see Figs. 109-111), are present in the vicinity of the supported edge. During the experiment it is noted that a single crack initiates at the top one-fourth of the plate in the through-thickness direction at a location approximately 12.7 mm (0.5 in.) from the long side edge of the plate. The crack forms at an early stage of loading (linear elastic). Prior to failure similar cracks are observed at the bottom one-fourth of the plate in the same direction. The "middle" portion of the plate does not show any indication of damage. From Figs. 105 and 106 it can be seen, especially when the principal axis of cross rolling is aligned with the long dimension of the specimen, that although the material develops a central crack it also exhibits material integrity through the middle one-third of the thickness dimension. This suggests a more ductile or "soft" behavior of cross-rolled beryllium sheet within approximately its middle one-third compared to the top and bottom thirds. Variation of material modulus in the through-thickness direction is discussed in more detail and verified experimentally in section 7.3.

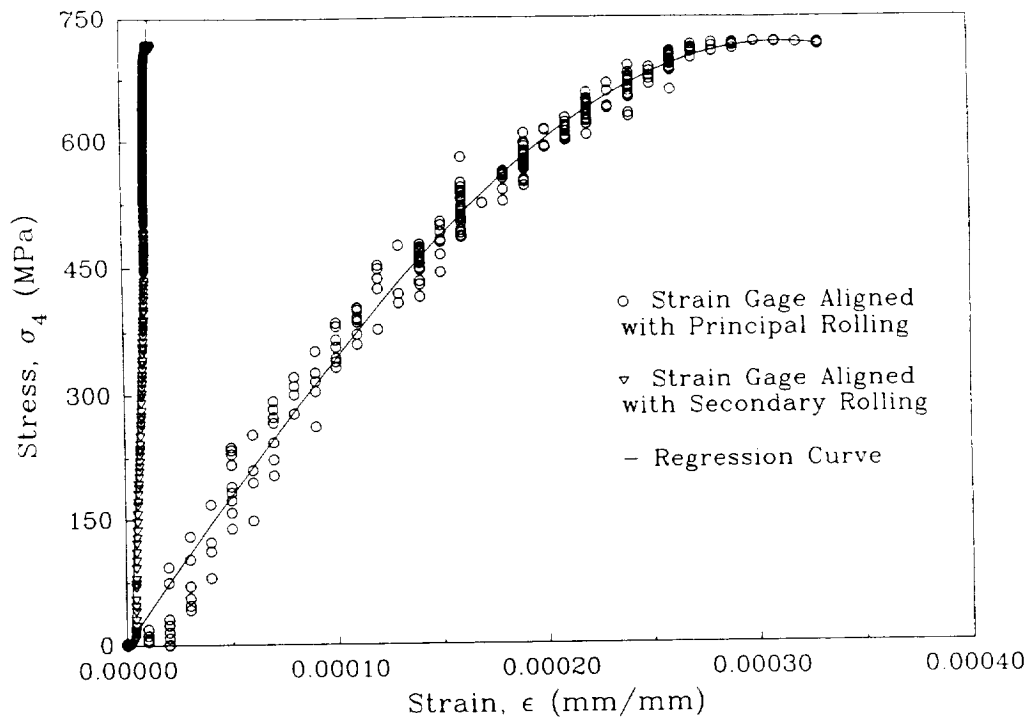


FIG. 101. Shearing Stress (σ_4) versus Strain (ϵ_1 and ϵ_2) for Through-Thickness Shearing Test

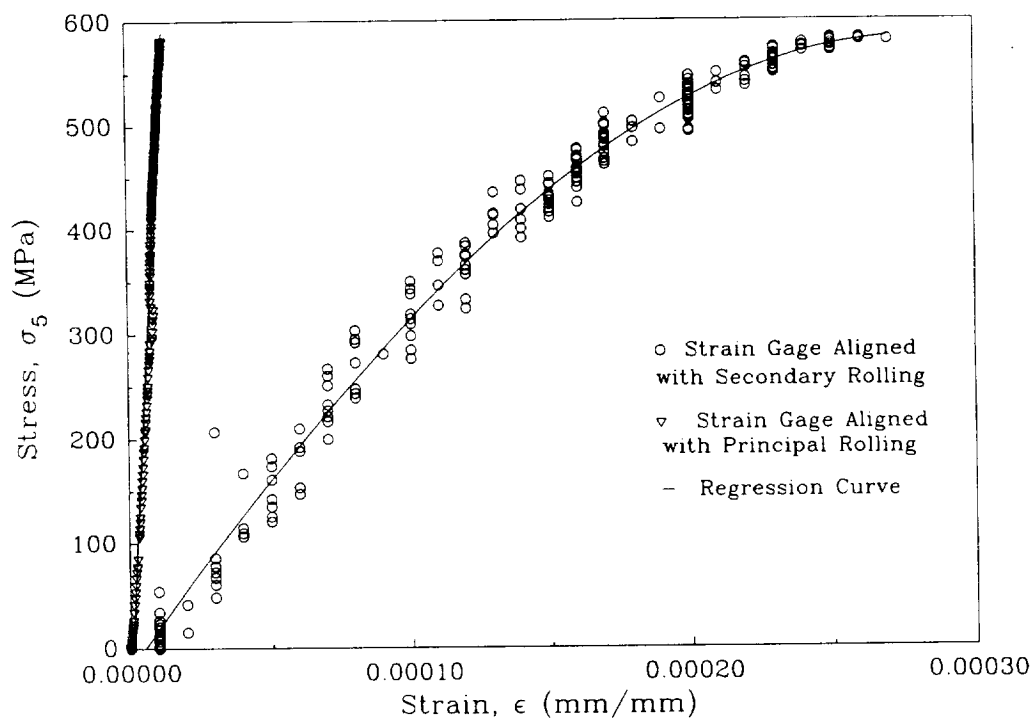
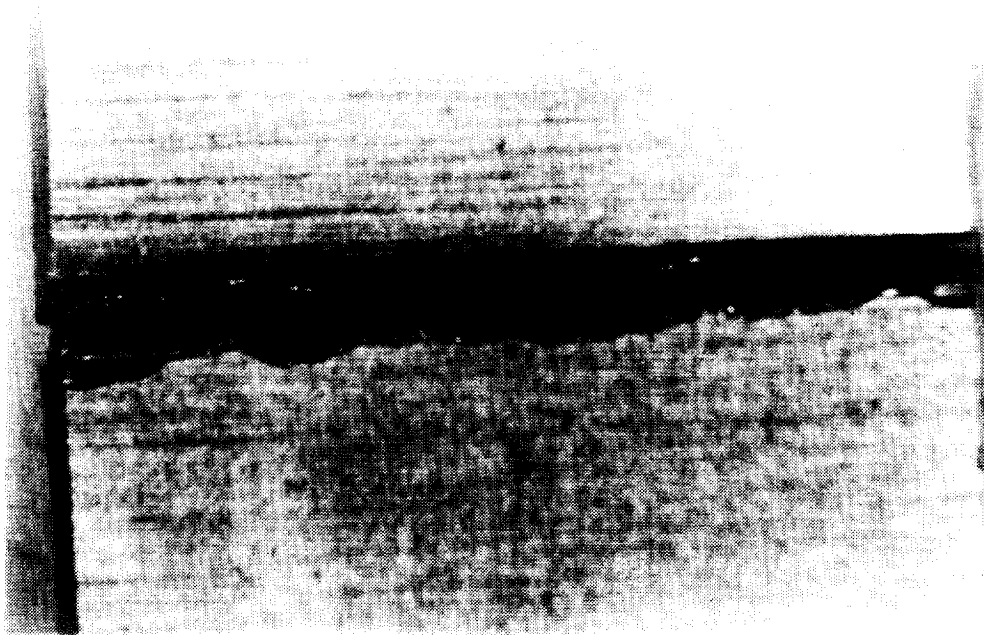


FIG. 102. Shearing Stress (σ_5) versus Strain (ϵ_1 and ϵ_2) for Through-Thickness Shearing Test

TABLE 17. Failure Strength for Out-of-Plane

Specimen Number	Failure Stress from Experimental Data			
	σ_4		σ_5	
	MPa (2)	(ksi) (3)	MPa (4)	(ksi) (5)
(1)				
1	552.3	(80.1)	589.5	(85.5)
2	565.7	(81.1)	595.7	(86.4)
Average	559.5	(80.6)	592.6	(86.1)

Specimen Number	Failure Stress from Numerical Simulation			
	σ_4		σ_5	
	MPa (2)	(ksi) (3)	MPa (4)	(ksi) (5)
(1)				
1	526.8	(76.4)	585.4	(84.9)
2	515.7	(74.8)	588.1	(85.3)
Average	521.3	(75.6)	586.8	(85.1)

**FIG. 103. Top View of Through-Thickness Shear Specimen 1 after Failure**

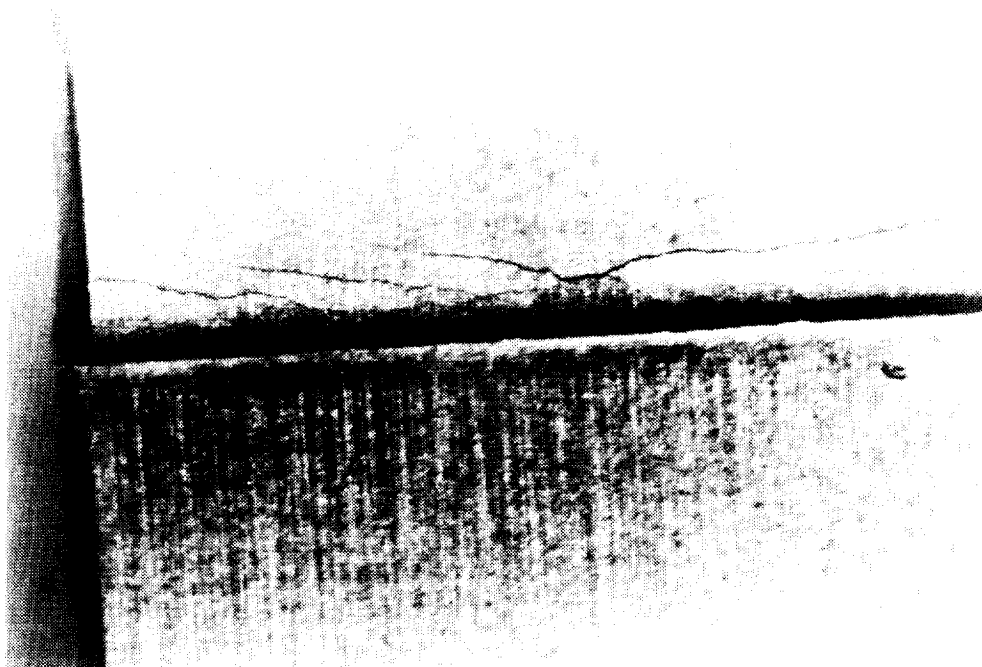


FIG. 104. Top View of Through-Thickness Shear Specimen 2 after Failure

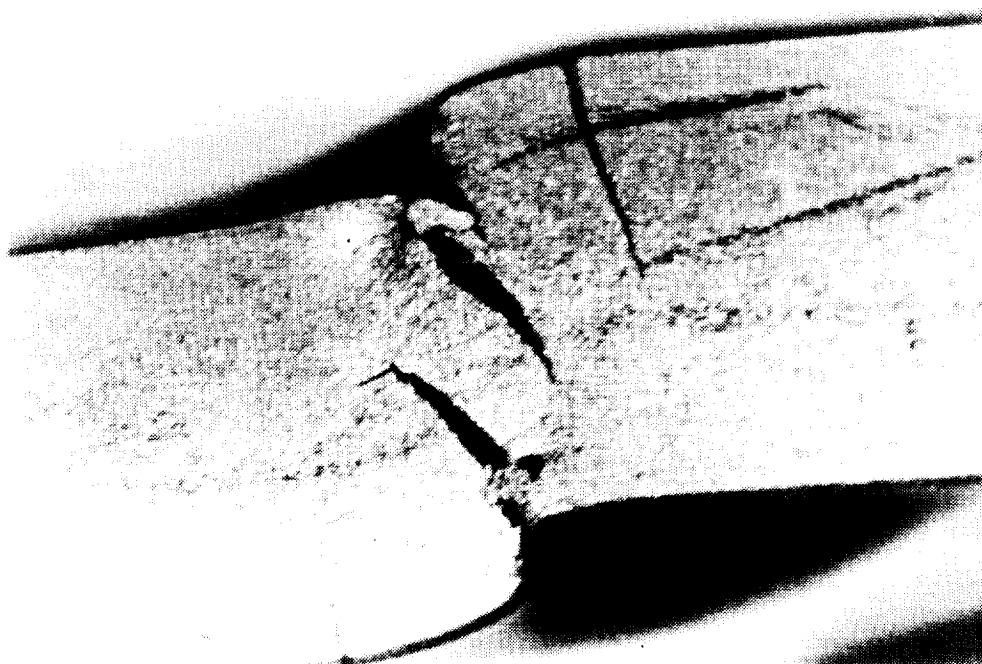


FIG. 105. Side View of Through-Thickness Shear Specimen 1 after Failure

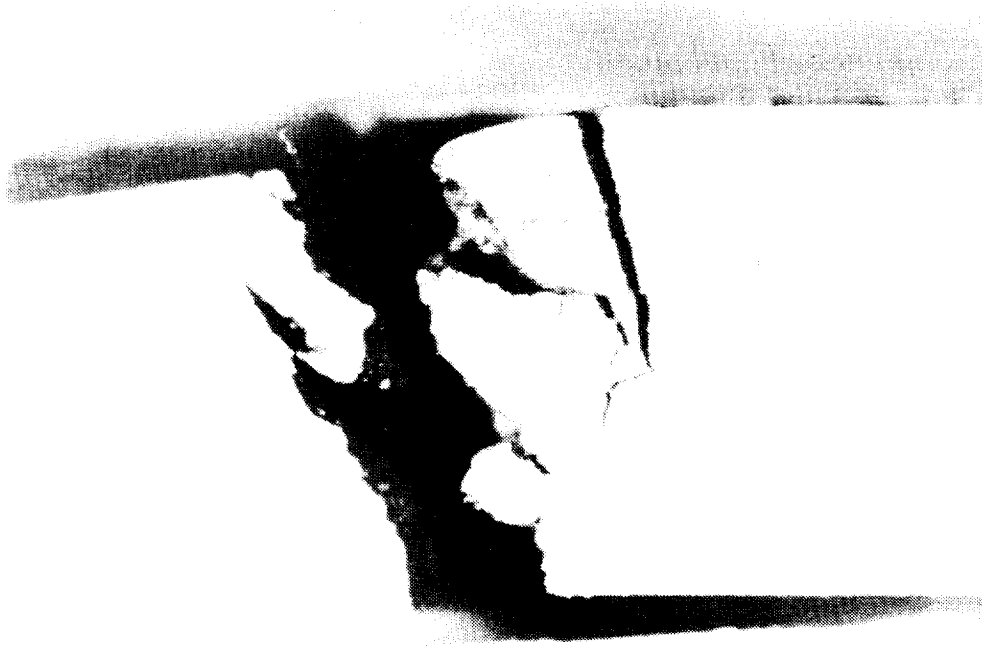


FIG. 106. Side View of Through-Thickness Shear Specimen 2 after Failure

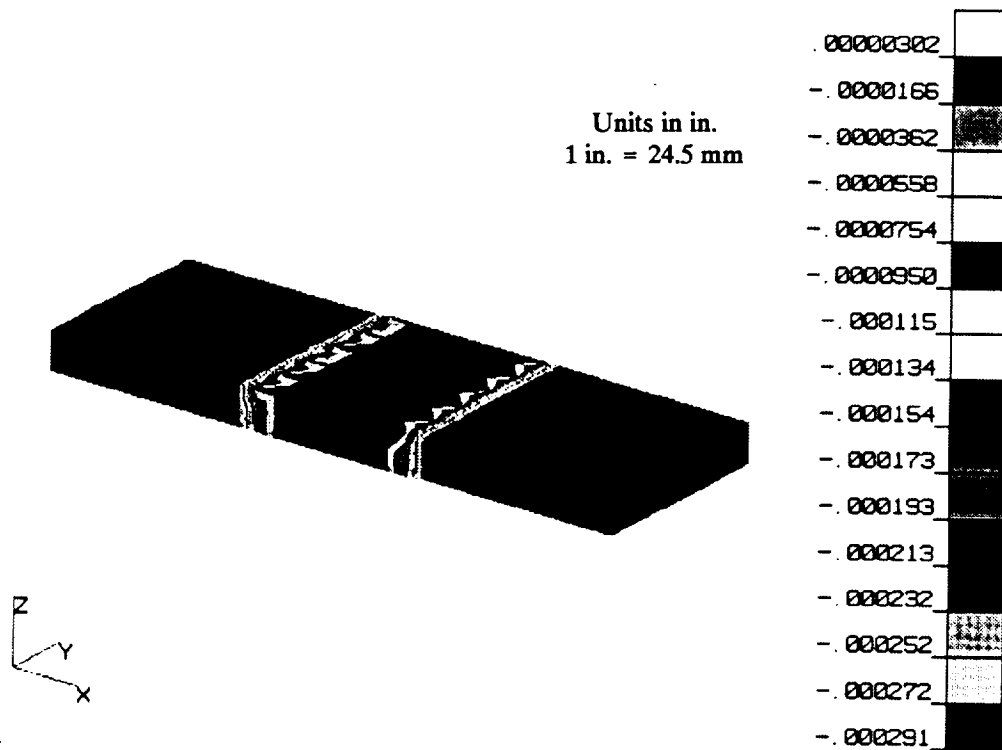


FIG. 107. Distribution of Short Transverse Displacement for Through-Thickness Shearing Test

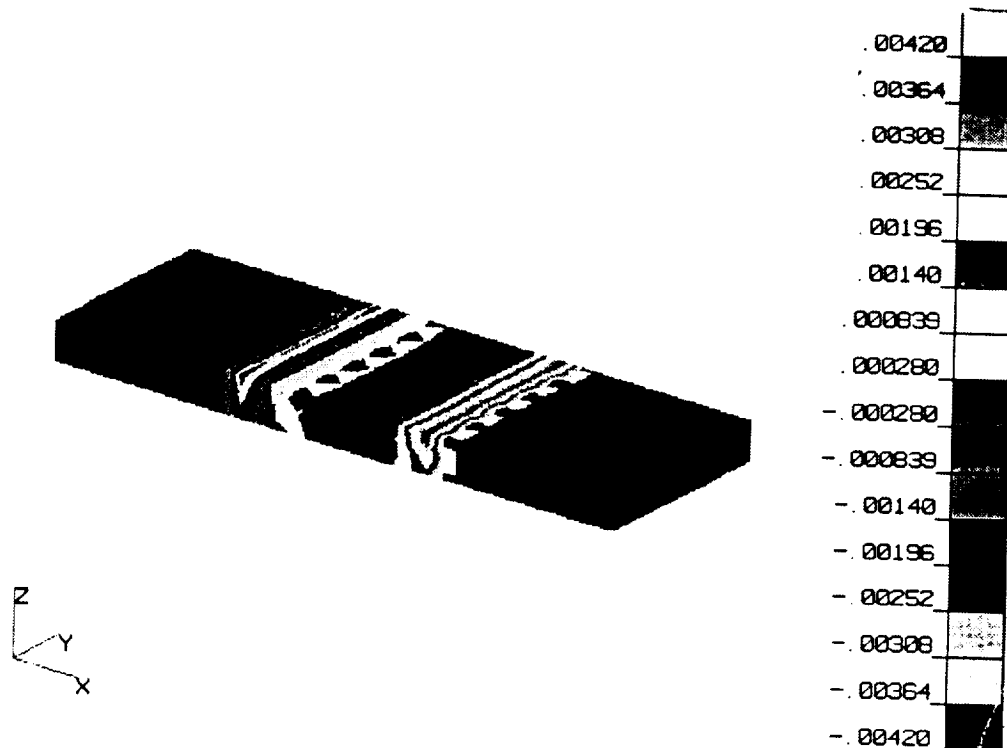


FIG. 108. Distribution of Shearing Strain, ϵ_{xy} , for Through-Thickness Shearing Test

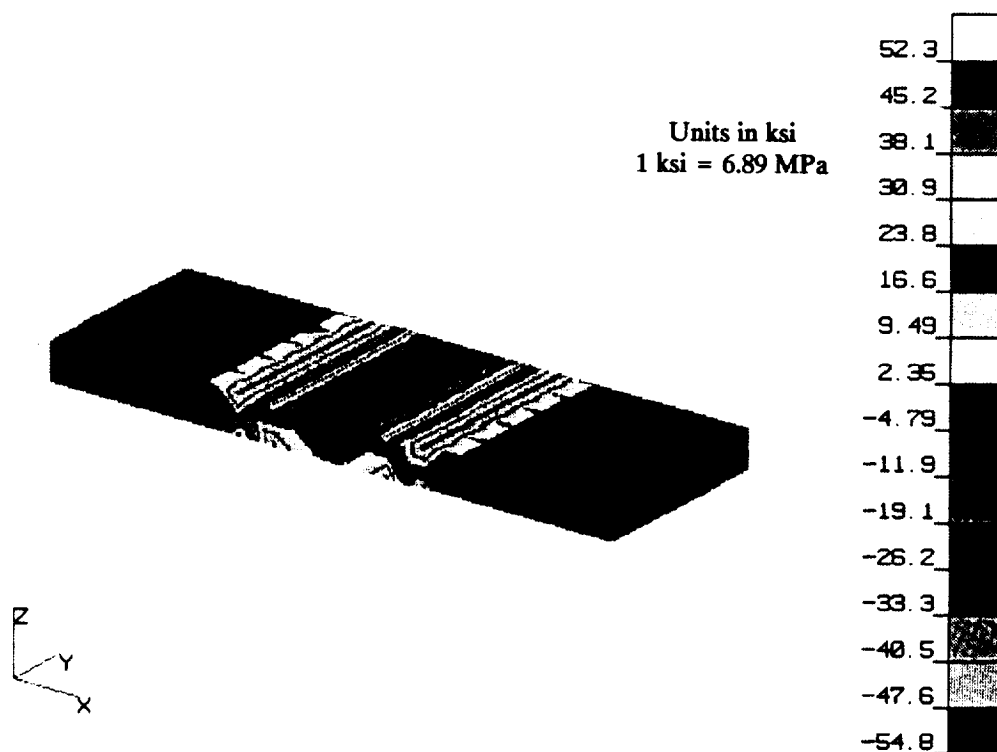


FIG. 109. Distribution of Longitudinal Stress for Through-Thickness Shearing Test

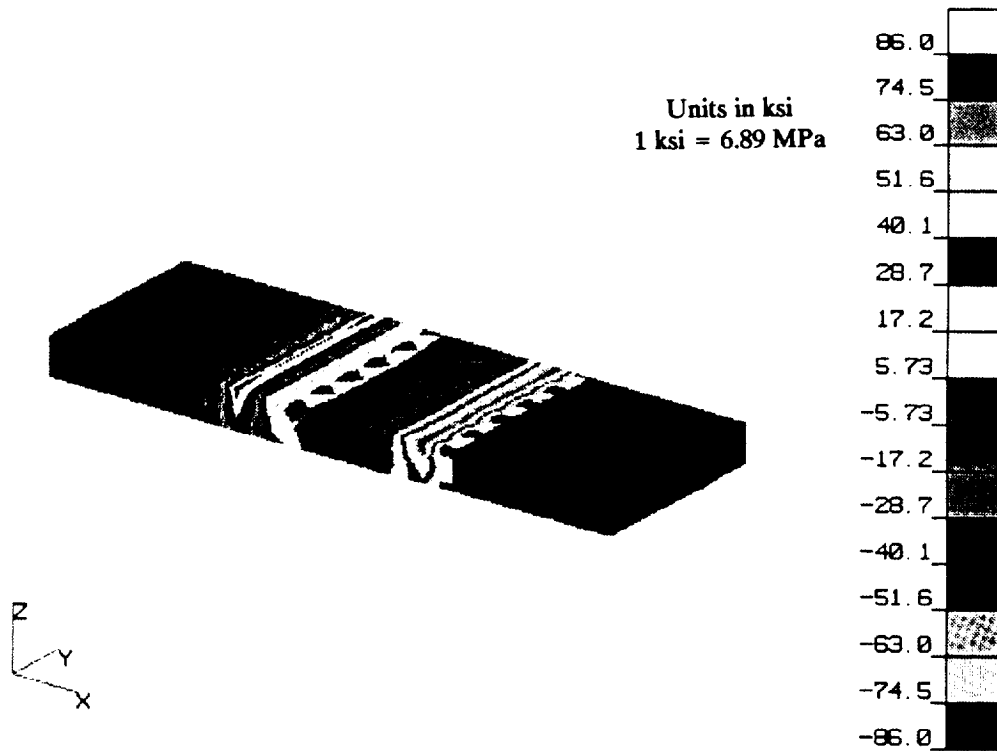


FIG. 110. Distribution of Shearing Stress, σ_{xy} , for Through-Thickness Shearing Test

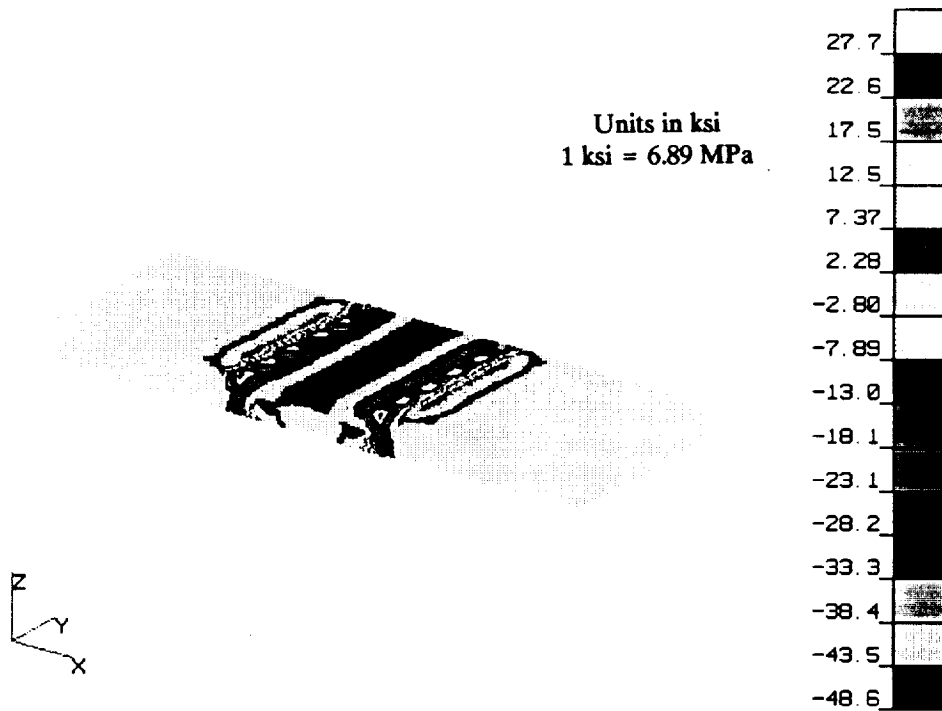


FIG. 111. Distribution of Short Transverse Normal Stress for Through-Thickness Shearing Test

5.4.2 Numerical Simulation

Three-dimensional numerical models are constructed to aid in design of the experimental specimen and to determine the distribution of stresses at the failure load. During preliminary simulation, the major goal is to optimize the physical dimensions of the coupon. After testing, simulation is intended to predict displacement, strain, and stress distributions induced during the experiment. A model with three thousand twenty-noded isoparametric hexahedral elements is used. Ten elements that simulate the through-thickness dimension allow for a variation of the through-thickness modulus as described in chapter 7. Originally, only one-fourth of the structure was modeled using a less refined finite element model that did not take into consideration variations of the through-thickness material properties. Although results obtained were satisfactory it was decided to modify the model to incorporate material variations in the short transverse direction. This is also consistent with all previous three-dimensional numerical models for beryllium.

Through-thickness shearing strengths, σ_4 and σ_5 , are in close agreement with the experimental results (Table 17). The experimental (average) values of strength are compared with the numerical values obtained at a distance of 1.27 mm (0.05 in.) from the top (or bottom) surface of the plate and at a distance of 12.7 mm (0.50 in.) from the edge of the specimen.

Another improvement over the original numerical model is also introduced for the final simulation. Initially, the loading was imposed by means of a uniform out-of-plane stress distribution on the top surface of the specimen, i.e., load was applied in the negative z-direction. The results obtained were not within an acceptable level of agreement with the experimental data. Differences between experimental and numerical values for strain and through-thickness shearing stress were approximately 15%.

In the refined model a contact load is applied instead of a uniform load distribution. In other words, the body that applies the load is considered to be a rigid body. The deformable part of the assembly is restricted to the unconstrained portion of the beryllium sheet. General interface elements are used between the rigid body and the top surface of the beryllium plate that is in contact with it to ensure compatibility of displacements (ABAQUS 1991b). Experimental and numerical results from this analysis are in good agreement. Typical displacement, strain, and stress distributions from numerical simulation of the σ_4 experiment are shown in Figs. 107 through 111. Fig. 107 shows that most of the unsupported beryllium structure experiences a uniform displacement of 6.9×10^{-3} mm (2.7×10^{-4} in.) in the direction of the load. Moreover, as shown by Figs. 108-111, insignificant shearing strain and stresses are experienced by the center portion of the free part of the beryllium plate. This is in agreement with the experimental results.

5.4.3 Determination of Failure Coefficients F_{44} and F_{55}

Experimentally determined values of the out-of-plane failure shearing stresses, σ_4 and σ_5 , are presented in Table 17. The average of these values are used to compute the principal failure strength coefficients, F_{44} and F_{55} , by means of Eq. 35. This simple calculation leads to the following coefficients:

$$F_{44} = 3.5023 \times 10^{-6} \text{ MPa}^{-2} \quad (1.6649 \times 10^{-4} \text{ ksi}^{-2}) \dots\dots\dots (221)$$

$$F_{55} = 2.1950 \times 10^{-6} \text{ MPa}^{-2} \quad (1.3857 \times 10^{-4} \text{ ksi}^{-2}) \dots\dots\dots (222)$$

Note that both F_4 and F_5 are equal to zero (see Eqs. 35 and 58) since beryllium is treated as an orthotropic material.

5.5 THROUGH-THICKNESS COMPRESSION STATE OF STRESS

An important but difficult parameter to measure is the through-thickness compression strength of beryllium. Like the in-plane compression strengths, the through-thickness strength is needed to calculate both principal (F_3 and F_{33}) and interaction (F_{13} , F_{23} , F_{133} , F_{233} , F_{113} , F_{223} , F_{344} , F_{355} , and F_{366}) failure coefficients. The physical limitation of the material geometry, i.e., the fact that it is only available in thin plate form, makes it difficult to test in the through-thickness direction, especially in tension. A tensile test has been reported by Lockheed (Fenn et al. 1967). Results and accuracy of this test have been discussed earlier (see section 5). A test to obtain the compressive strength for cross-rolled beryllium in the through-thickness direction has not been reported in the literature. This section describes a novel experiment devised to determine the failure strength in compression.

5.5.1 Experiments

A special series of tests has been carried out to compute the through-thickness compressive strength of cross-rolled beryllium. The experimental arrangement is shown in Fig. 112. Two right circular steel cylinders that have a diameter of 50.8 mm (2.0 in.) are used to load the specimen. Each is 76.3-mm (3.0-in.) long, made of A-2 tool steel and hardened to 58-60 on the Rockwell "C" hardness scale. The beryllium specimens, a 12.7-mm (0.5-in.) diameter disk and a 12.7-mm (0.5-in.) square plate are sandwiched between the two cylinders. Dimensions of the plate specimens are based on the ultimate capacity of the MTS machine. Top and bottom surfaces of the specimen are perpendicular to the line of the applied load which is provided by a $2.2 \times 10^6\text{-N}$ ($5.0 \times 10^5\text{-lb}$) MTS machine.

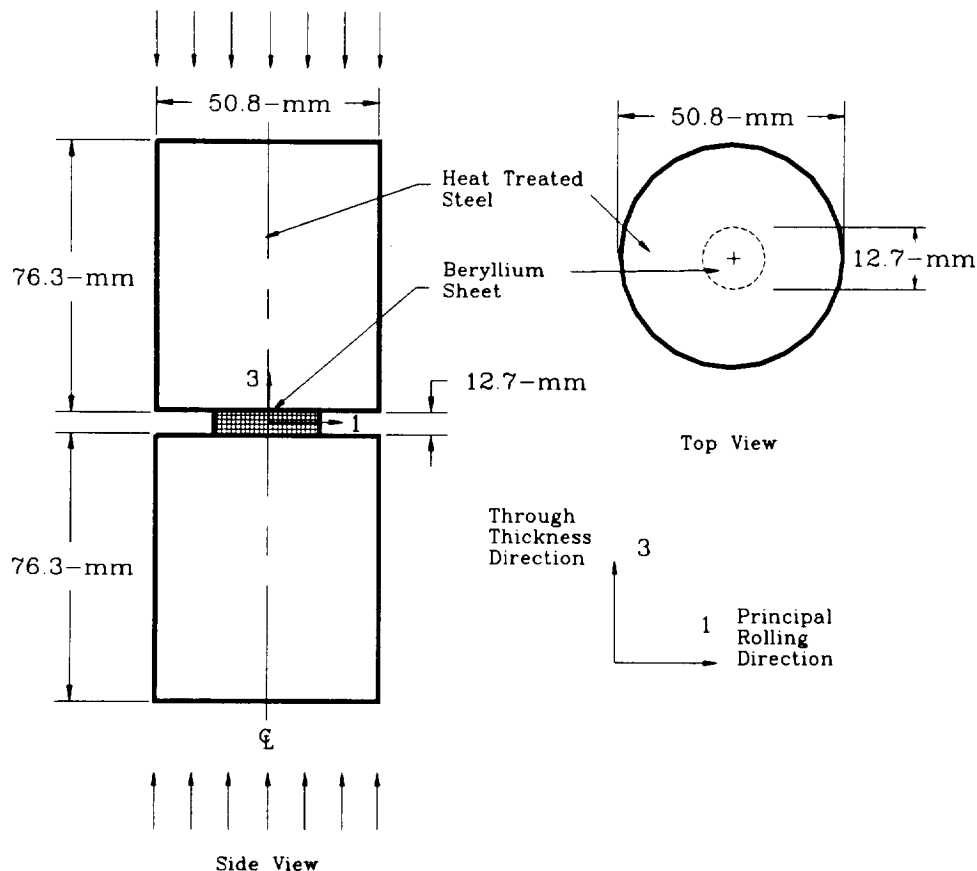


FIG. 112. Experimental Setup for Through-Thickness Compression Test

The experiment is carried out in displacement (stroke) control. The rate of motion of the top cross-head of the MTS machine is maintained at 4.2×10^{-2} mm/s (0.1 in./min). Prior to the actual experiment, compliance of the machine and the experimental assembly (except for the beryllium structure) is measured. This is done in such a manner that the true displacement of the beryllium specimen at failure can be obtained. Sensitivity of the MTS machine allows for reading displacement to within 3.9×10^{-6} mm (1.0×10^{-4} in.).

Initially, 12.7-mm \times 12.7-mm (0.5-in. \times 0.5-in.) square cross-rolled beryllium coupons were used for this experiment. It was observed, however, that due to stress concentrations at the edges, failure initiated at one or more of the four corners of the plate. To bypass this obstacle and to achieve a rather uniform stress distribution that is relatively free of stress concentrations, it was decided to test circular disks instead of square coupons. Results obtained from the square specimens were lower than the failure strength of the material obtained using circular disk specimens.

Due to geometrical limitations of the specimens no strain gages are attached. Load and deformation information is gathered for two specimens. Normal compressive stress in through-through direction is obtained by dividing the force of the MTS with the original,

undeformed surface area of the disk. Results of each compressive test and an average failure stress are shown in Table 18. Fig. 113 relates normal stress to through-thickness deformation for the entire range of loading. The through-thickness compressive strength is, approximately, two and one-half times larger than the in-plane compressive strength and three times larger than the in-plane tensile strength.

A magnified photograph one of the failed beryllium disks is shown in Fig. 114. Only a single, through-thickness crack develops prior to failure. Although the specimen is loaded in a smooth, continuous manner, it breaks suddenly and without warning. No strain hardening is observed. This is in contrast to the behavior exhibited during the in-plane compression tests (see section 5.2). During the compression tests non-linear behavior is observed, although the material fails catastrophically.

TABLE 18. Failure Strength for Through-Thickness Compression Specimens

Specimen Number	Failure Stress	
	MPa	(ksi)
(1)	(2)	(3)
1	1,718.2	(249.2)
2	1,729.9	(250.9)
Average	1,724.0	(250.0)

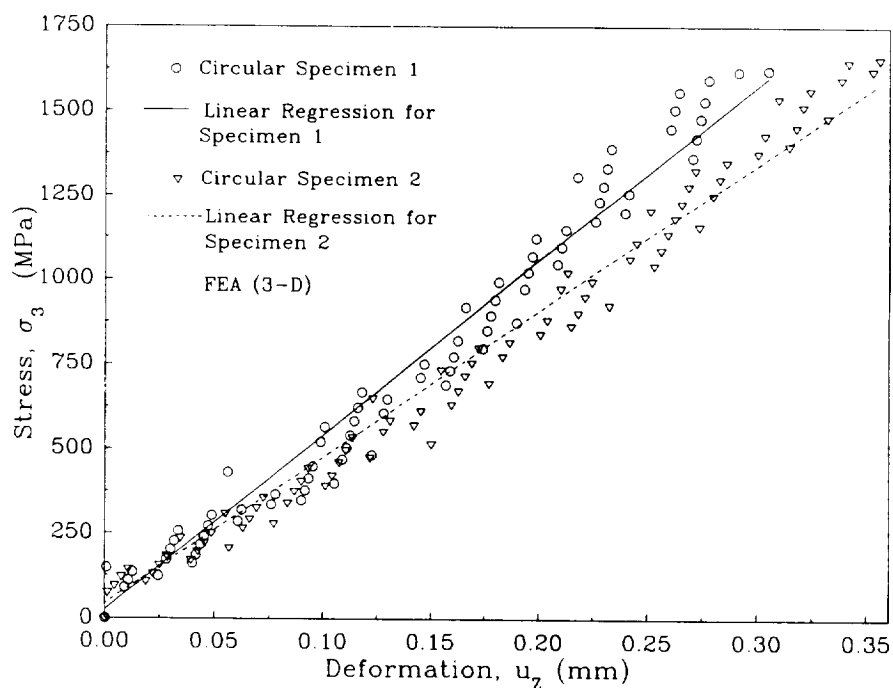


FIG. 113. Stress versus Deformation for Through-Thickness Compression

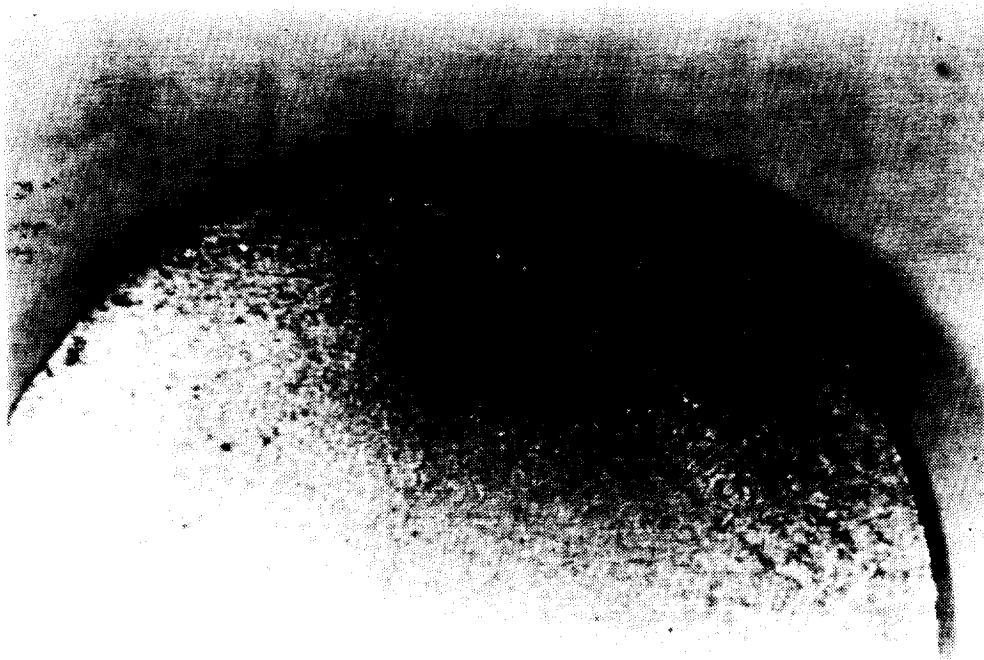


FIG. 114. Magnified Photograph of Failed Through-Thickness Compression Specimen

5.5.2 Numerical Simulation

Physical testing is numerically simulated using both two- and three-dimensional FEA models. For the two-dimensional model, five-hundred eight-noded isoparametric plane strain elements are used. Ten elements simulate behavior in the through-thickness direction. Non-linear geometry and inhomogeneous properties of the material are incorporated into the model. Figs. 115-117 show stress distributions for the through-thickness analysis. The load used is a prorated portion of the average of the experimentally obtained failure loads. As in the case of the through-thickness shear tests discussed earlier (section 5.4), this experiment is simulated with contact loading at the interfaces between the beryllium disk and the steel cylinders.

The three-dimensional model also considers inhomogeneous material properties and geometric nonlinearities. It consists of eight-hundred twenty-node hexahedral elements. Again, the plate is simulated using ten elements in the through-thickness direction. Symmetry of the structure is taken into consideration and, thus, only one-eighth of the plate is modeled. Results obtained are similar to those obtained from the two-dimensional model.

Finally, this problem is also simulated using axisymmetric elements. The axis of symmetry is the left vertical edge of Fig. 116. The beryllium plate consists of two-thousand finite elements. Two-hundred elements are used to simulate the cylinders. The advantage of using axisymmetric elements is that the amount of computational time is considerably decreased.

All three numerical simulations yield comparable results as far as the distribution of the normal through-thickness stress is concerned. An essentially uniform distribution of this stress is obtained throughout the disk for all three numerical simulations. Numerical and experimental results for stress at the center of the plate versus vertical stroke of the MTS machine are compared in Fig. 113. Agreement between FEM and the experimental data is within acceptable levels.

5.5.3 Determination of Failure Coefficients F_3 and F_{33}

Failure coefficients F_3 and F_{33} are determined using Eq. 35 and the average of the strengths listed in Table 18. An elementary calculation gives the following numerical values for the failure coefficients:

$$F_3 = 8.71 \times 10^{-4} \text{ MPa}^{-1} \quad (6.01 \times 10^{-3} \text{ ksi}^{-1}) \dots\dots\dots (223)$$

$$F_{33} = 8.41 \times 10^{-7} \text{ MPa}^{-2} \quad (1.38 \times 10^{-4} \text{ ksi}^{-2}) \dots\dots\dots (224)$$

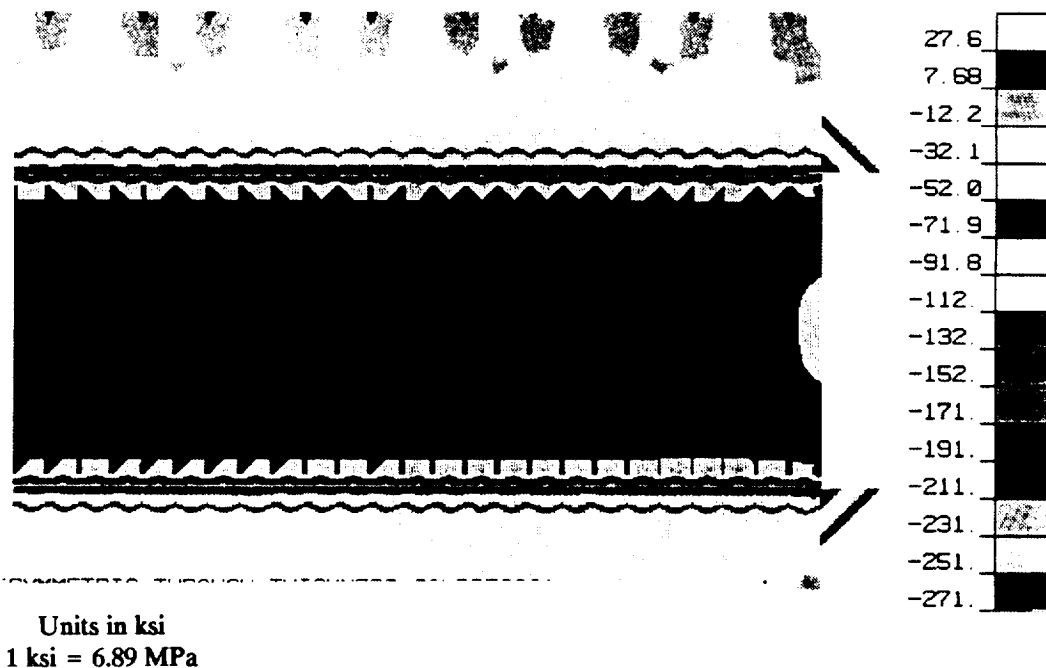


FIG. 115. Distribution of Through-Thickness Compressive Stress from 2-D Simulation

Units in ksi
1 ksi = 6.89 MPa

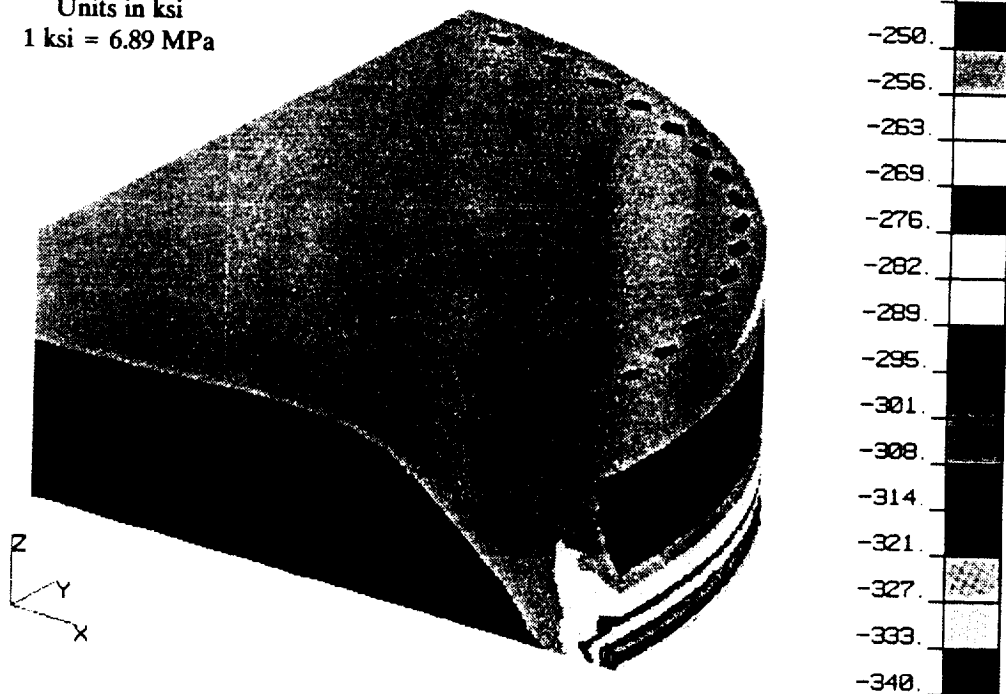


FIG. 116. Distribution of Through-Thickness Compressive Stress from 3-D Simulation

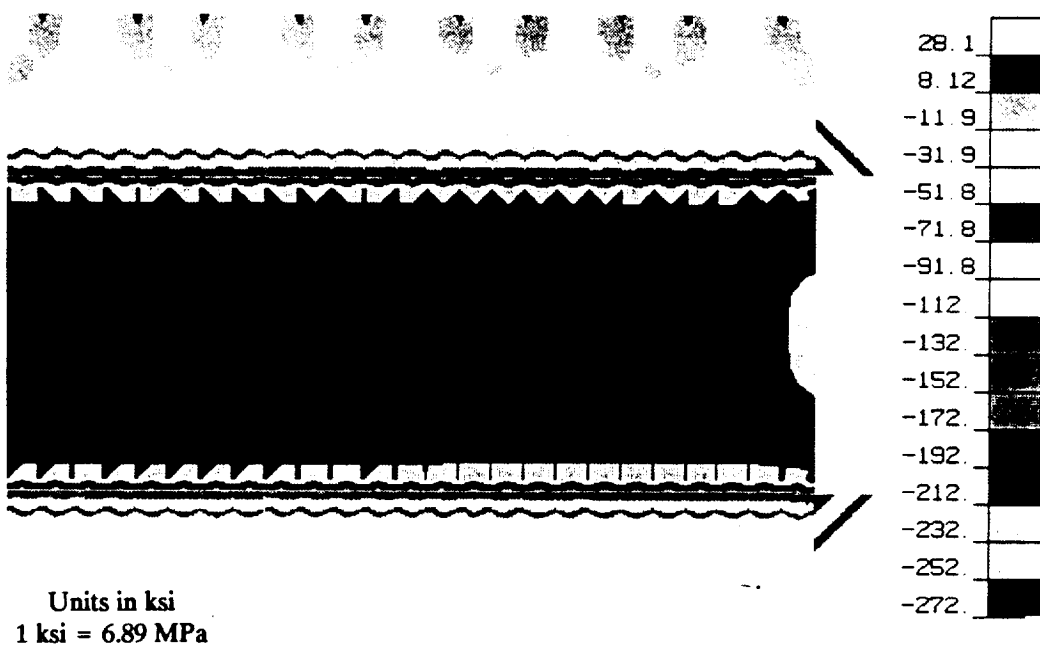


FIG. 117. Distribution of Axisymmetric Through-Thickness Compressive Stress

6. EXPERIMENTAL DETERMINATION OF INTERACTION FAILURE COEFFICIENTS

6.1 INTRODUCTION

A distinct feature of the new proposed criterion is that the failure surface is described by a relatively large number of interaction coefficients. As a consequence the number of experiments required to evaluate the coefficients increases considerably. For the case of cross-rolled beryllium sheet, which is treated as a specially orthotropic, three-dimensional material in this study, the number of necessary interaction coefficients is eighteen (Table 13). Of the eighteen coefficients, nine are due to interactions among normal stresses aligned with the direction of the material axes while the other nine are from interactions among shearing and normal stresses.

According to the new criterion, establishment of the interaction coefficients is divided into two parts: (1) determine the normal interaction coefficients subject to all constraints imposed by asymptotic equations from experiments involving only normal stress distributions, such as Eqs. 68-73, and (2) determine the shear-normal interaction coefficients from experiments that involve both shearing and normal stresses. A functional is established for each case. Minimization of these functionals yields two independent sets of simultaneous equations. The solution of each set of equations yields the interaction coefficients.

6.2 MULTIAXIAL STATE OF STRESS: σ_1 , σ_3 , AND σ_5

The fact that cross-rolled beryllium sheets are available only in thin plate form complicates the task of setting up experiments for establishing the coefficients. For this study, the procedure outlined in the previous paragraph is modified because it is virtually impossible to design a biaxial test with one of the loading axes normal to the plane of the material. As an alternative, a combined state of stress that includes both normal and shearing stresses that act in the plane of the normal stresses is proposed. This stress state is achieved by rotating one of the in-plane material axes with respect to the other two axes from the test described in section 5.5 (see Appendix VII). Five of these tests are carried out for each orientation of in-plane material axes. Results of the tests and complementary numerical simulations are described in sections 6.2.1 and 6.2.2, respectively.

6.2.1 Laboratory Experiments

Small, round beryllium disks that have a diameter of 12.7 mm (0.5 in.) are used for a set of experiments that cause failure under a combined state of stress. These specimens are identical with those used in the normal through-thickness compression test described in section 5.5. Directions of principal and secondary rolling are marked on each specimen by the manufacturer. To ensure correct orientation each specimen is examined through a low power microscope.

The experimental set-up consists of a series of A-2 tool steel rods that are cut at angles of 30°, 35°, 37°, 40°, and 45° with respect to the horizontal axis (see Fig. 118). Each rod is hardened to 60/62 on the Rockwell "C" scale. The original length the rod is 152.4 mm (6.0 in.). The beryllium specimen is centered with the load axis and placed parallel to the cut surfaces of the steel holders. All three parts (two holders and the beryllium disk) are enclosed in a 6.4-mm (0.25-in.) thick cylindrical steel collar. The collar itself is cut lengthwise (parallel to the loading direction). Its main purpose is to provide containment of the apparatus. Care is taken to avoid development of any reactional forces between the collar and the cylinders. The collar is confined in place by a steel 254.0-mm × 254.0-mm (10.0-in. × 10.0-in.) plate situated circumferentially at the center of the collar which, in turn, is supported by two 254.0-mm × 254.0-mm × 127.0-mm (10.0-in. × 10.0-in. × 5.0-in) steel blocks. The whole arrangement rests on a horizontal platform that is the lower crosshead of a 2.2×10^6 -N (5.0×10^5 -lb) MTS compression testing machine. Each specimen is loaded in stroke control at a rate of 0.09 mm/s (0.04 in./min). The direction of loading is aligned with the z-direction of the Cartesian coordinate axes (see Fig. 118).

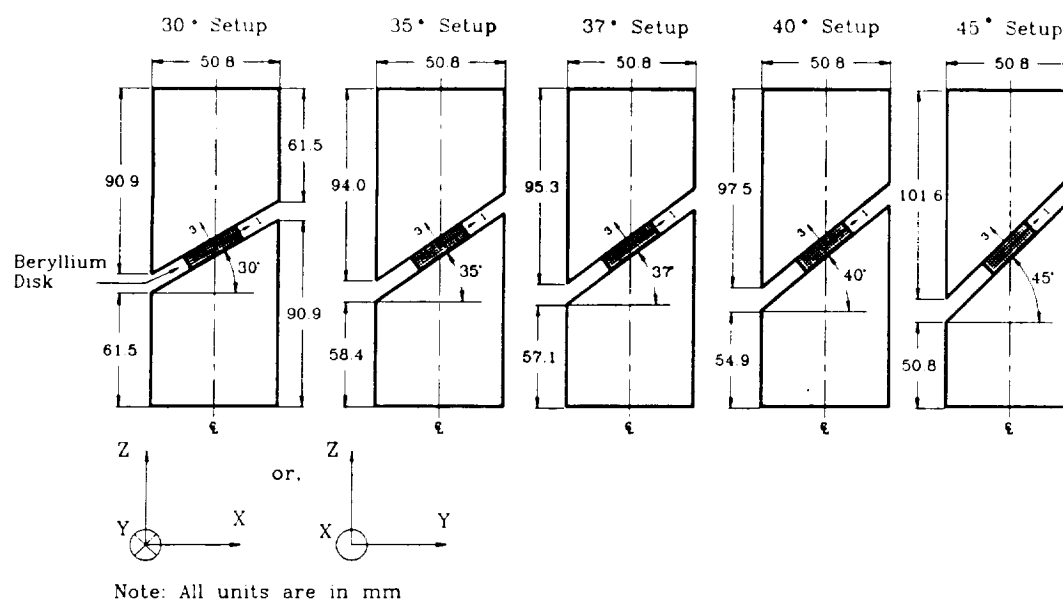


FIG. 118. Experimental Fixtures for Combined Normal and Shearing Stress Tests

Initially, each specimen is positioned between the cylinders such that the material axes are aligned with the three mutually perpendicular Cartesian coordinate axes (special orthotropic orientation). For this set of experiments the secondary direction of cross-rolling remains in alignment with the y -axis, while the principal rolling and the through-thickness directions are rotated through an angle equal to the cut angle of the holders, i.e., 30° , 35° , 37° , 40° , and 45° , respectively. Two specimens are tested for each holder configuration, for a total of ten specimens.

Collective results for failure stresses of all five experimental arrangements discussed in this section are shown in Table 19. Failure stresses computed from a simplified stress transformation are compared with those from FEA simulation. FEA stresses are taken from a point at the center of the beryllium disk. Initially, the normal stress acting on the steel loader in the direction of the Cartesian z -axis (Fig. 118) is computed by dividing the applied force with the cross-sectional area of the cylinder normal to the same axis. A uniform stress distribution is assumed to be acting on the projection of the beryllium disk in the direction of the applied load and in the vicinity of the specimen. The magnitude of this stress is calculated by dividing the load at failure by the projected area of the beryllium disk in the direction of the z -axis. Magnitudes of the component of failure stress at the center of the beryllium specimens are determined via a simple stress transformation with respect to the material axes (see section 6.4.1 and Appendix VII). Agreement between the simplified analysis and FEA is well within acceptable bounds. The maximum difference in predicted stress is 1.0%. In addition, Fig. 119 provides a synoptic output of load versus vertical displacement for the 30° , 35° , 37° , 40° , and 45° degree configurations. The 30° and 35° specimens exhibit a linear behavior prior to failure while the 37° , 40° , and 45° specimens show signs of non-linear behavior. This phenomenon is attributed to two possible causes: (a) through-thickness interlayer planes slip with respect to each other due to an increase of the shearing stress, and (b) non-uniform initial load application due to misalignment of the components of the experimental setup. Fig. 120 shows a histogram of the maximum compressive load corresponding to the total vertical deflection for each of the ten specimens.

All disk specimens failed suddenly, which is characteristic of brittle behavior. In addition, no definite yield point can be established for any of these test configurations. This leads to the assumption that the material behaves in an almost linearly elastic manner prior to failure. Careful examination of the failed specimens reveals that the 30° and 35° specimens exhibit a failure behavior similar to that of the through-thickness compression specimen, i.e., they form a single crack before failure. The 37° specimens show more than one crack in the through-thickness direction (Fig. 121); each crack is similar to those of the

30° specimens. Cracks observed in the 40° specimens are indicative of a mixed mode failure: shear and compression. A major inclined crack at an angle of, approximately, 45° occurs in the through-thickness direction. In addition, two perpendicular cracks, each penetrating approximately one-third of the through-thickness dimension, extend from each flat face of the specimen and intersect the major inclined crack (Fig. 122). For the 45° specimens the cracks in the through-thickness direction exhibit similar behavior to that of the 40° specimen. The number of cracks increases and new ones form at an angle of approximately -45° with respect to the major inclined crack. The latter propagate through the top and bottom one-third of the specimen in the through-thickness direction (Fig. 123).

TABLE 19. Failure Strengths for Disk Specimens with σ_1 , σ_3 , and σ_5 State of Stress

Specimen		Failure Stress from Simplified Analysis					
Angle of Inclination	Number	σ_1		σ_3		σ_5	
		MPa	(ksi)	MPa	(ksi)	MPa	(ksi)
(1)	(2)	(3)	(4)	(5)	(6)	(7)	(8)
30°	1	-529.4	(-76.8)	-1,588.1	(-230.3)	916.9	(133.0)
	2	-531.1	(-77.0)	-1,593.3	(-231.1)	919.9	(133.4)
35°	1	-711.6	(-103.2)	-1,451.4	(-210.5)	1,016.3	(147.4)
	2	-720.9	(-104.6)	-1,470.3	(-213.2)	1,029.5	(149.3)
37°	1	-805.0	(-116.8)	-1,417.7	(-205.6)	1,068.3	(155.0)
	2	-815.2	(-118.2)	-1,435.6	(-208.2)	1,081.8	(156.9)
40°	1	-934.4	(-135.5)	-1,327.0	(-192.5)	1,113.5	(161.5)
	2	-937.3	(-135.9)	-1,331.2	(-193.1)	1,117.0	(162.0)
45°	1	-1,190.4	(-172.7)	-1,190.4	(-172.7)	1,190.4	(172.7)
	2	-1,199.2	(-173.9)	-1,199.2	(-173.9)	1,199.2	(173.9)
Specimen		Failure Stress from FEA Simulation					
30°	1	-528.8	(-76.7)	-1,588.1	(-230.0)	920.5	(133.5)
	2	-530.2	(-76.9)	-1,591.4	(-230.8)	923.2	(133.9)
35°	1	-710.9	(-103.1)	-1,448.6	(-210.1)	1,015.6	(147.3)
	2	-719.8	(-104.4)	-1,467.3	(-212.8)	1,030.1	(149.4)
37°	1	-807.4	(-117.1)	-1,419.7	(-205.9)	1,066.0	(154.6)
	2	-817.8	(-118.6)	-1,437.6	(-208.5)	1,079.1	(156.5)
40°	1	-937.7	(-136.0)	-1,330.7	(-193.0)	1,114.2	(161.6)
	2	-940.5	(-136.4)	-1,334.9	(-193.6)	1,117.7	(162.1)
45°	1	-1,174.2	(-170.1)	-1,180.4	(-171.2)	1,192.8	(173.0)
	2	-1,181.1	(-171.3)	-1,188.0	(-172.3)	1,201.1	(174.2)

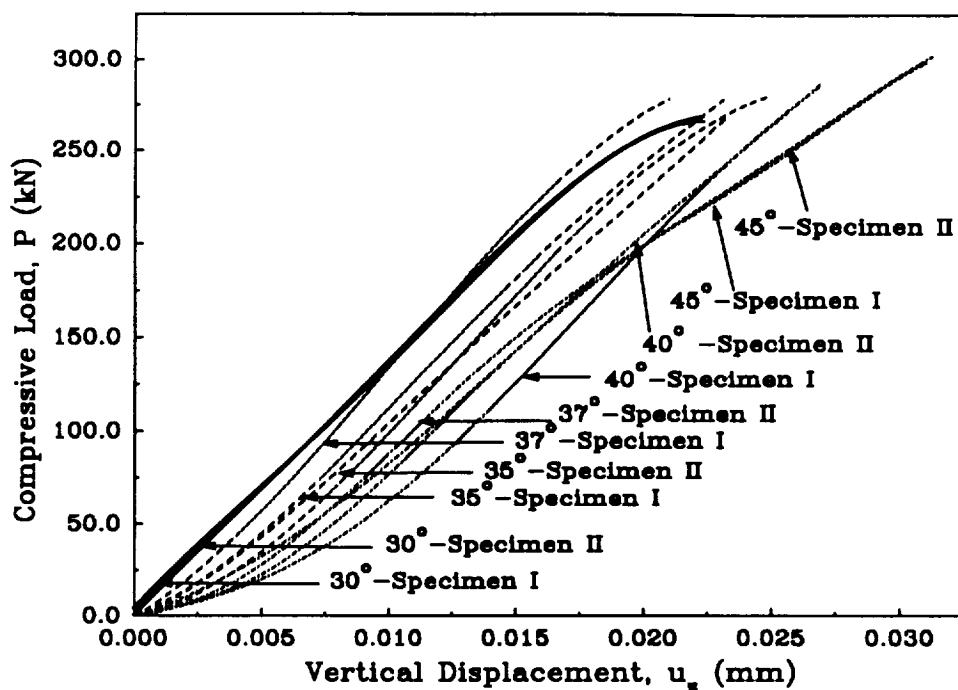


FIG. 119. Load versus Displacement for 30°, 35°, 37°, 40°, and 45° Planes of Inclination (σ_1 , σ_3 , and σ_5)

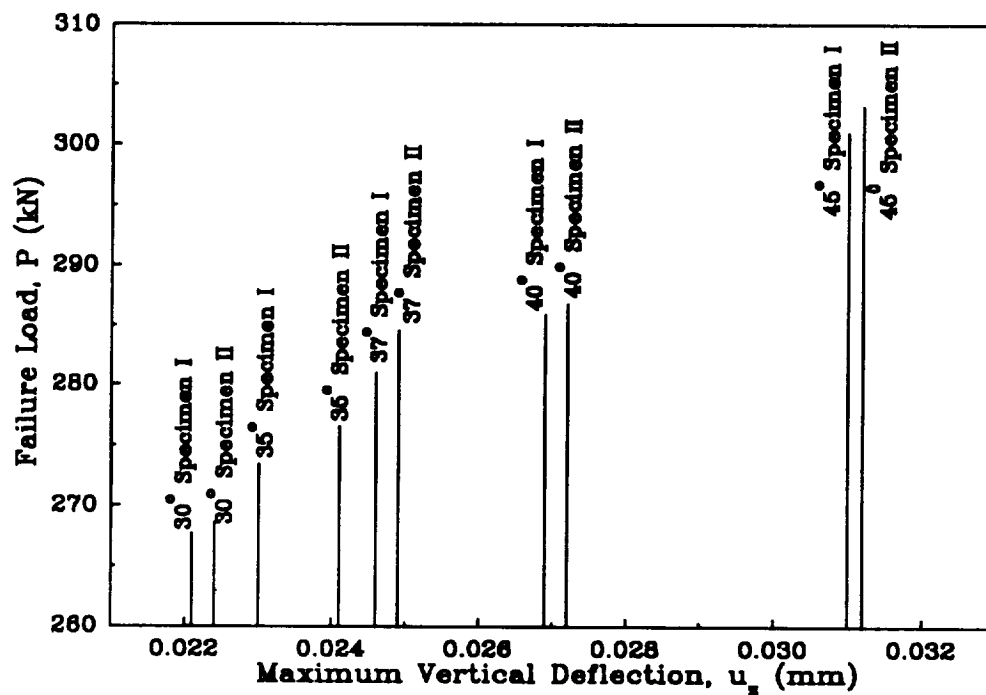


FIG. 120. Histogram of Maximum Compressive Load and Maximum Vertical Deflection for 30°, 35°, 37°, 40°, and 45° Planes of Inclination (σ_1 , σ_3 , and σ_5)



FIG. 121. Magnified Photograph of Failed Specimen that is Inclined 37°



FIG. 122. Magnified Photograph of Failed Specimen that is Inclined 40°



FIG. 123. Magnified Photograph of Failed Specimen that is Inclined 45°

6.2.2 Numerical Simulation

Several FEA models are used to simulate each test. Initially, two-dimensional models are constructed that are comprised of eight-noded, plane-strain isoparametric elements. Steel components are modeled as isotropic high-strength material that are physically connected to the beryllium disk. The results from these simulations do not agree well with the experimental output.

Subsequently, each experiment is simulated as a contact problem. Hertzian rigid surfaces are used for the non-beryllium components. The beryllium disk is simulated using either eight-noded, plane-strain elements for two-dimensional analysis or twenty-noded, solid, isoparametric finite elements for three-dimensional analysis. Each beryllium disk has two material axes that are rotated with respect to the third axis (see Fig. 118). Each three-dimensional model takes advantage of symmetry of the overall arrangement with respect to a plane passing through the x - z Cartesian axes. Thus, only one-half of the structure is discretized. The through-thickness dimension of the beryllium disk is approximated using ten elements for both the two- and three-dimensional simulations.

Selected output from two- and three-dimensional numerical simulation of various stress components at failure are shown in Figs. 124-127 for a 30° specimen rotated about an axis parallel with the secondary direction of rolling. Distribution of stress in the middle of

the 30° specimen compares well with the transformed experimental values presented in Table 19. It should be noted, however, that regions of stress concentration occur in the vicinity of the intersection of the flat and cylindrical surfaces of the specimens. FEA results are presented in Table 19 for comparison with results obtained from simple stress transformation.

The two- and three-dimensional simulations yield almost identical results. Thus, for simplicity, time, and computational savings all remaining beryllium disks are analyzed using two-dimensional simulation. Distributions of selected stress components are shown in Figs. 128 through 131. Patterns of stress distribution similar to those found for the 30° specimen appear in all inclined specimens. Moreover, the middle portion of each beryllium specimen exhibits a state of stress similar to that shown in Table 19.

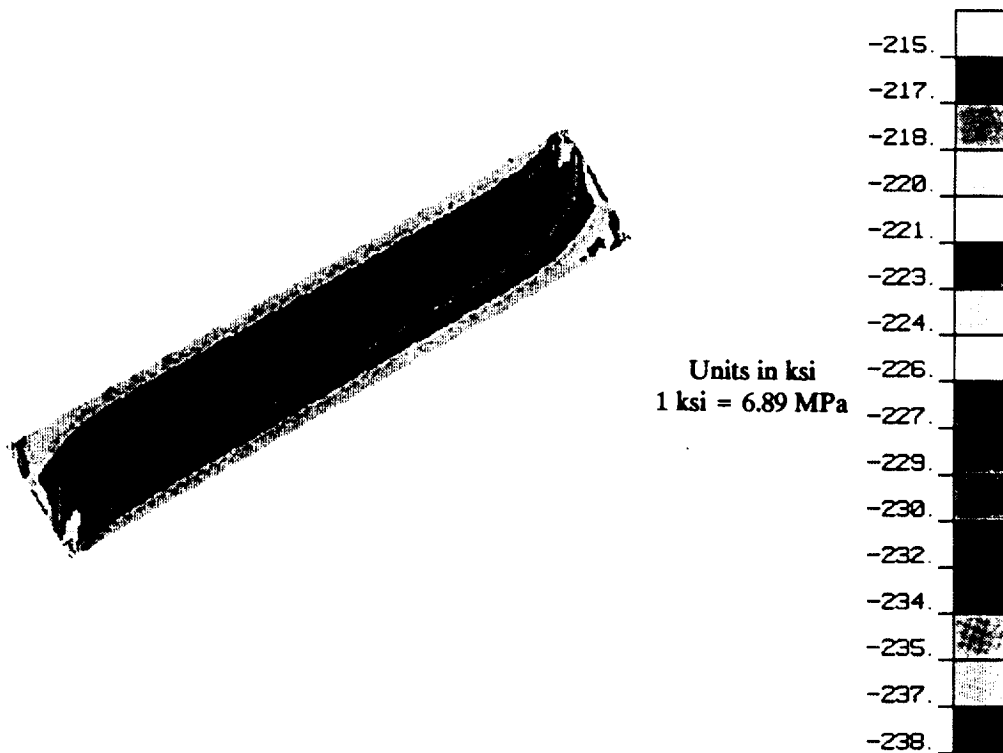


FIG. 124. Distribution of Through-Thickness Normal Stress from 2-D Simulation for 30° Specimen

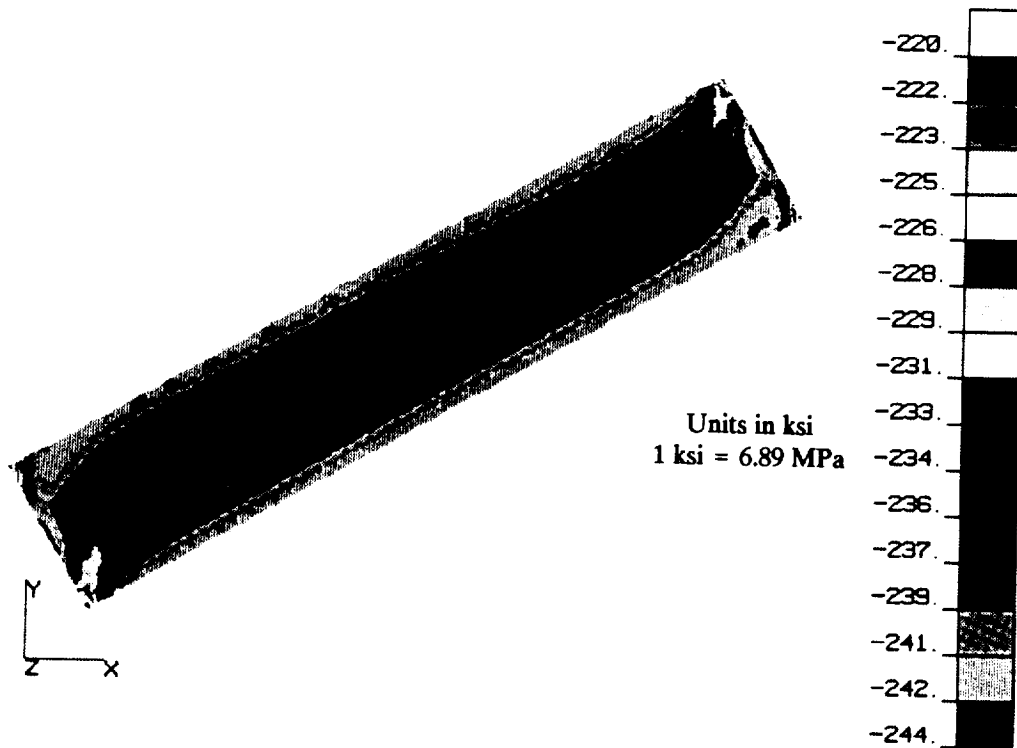


FIG. 125. Distribution of Through-Thickness Normal Stress from 3-D Simulation for 30° Specimen

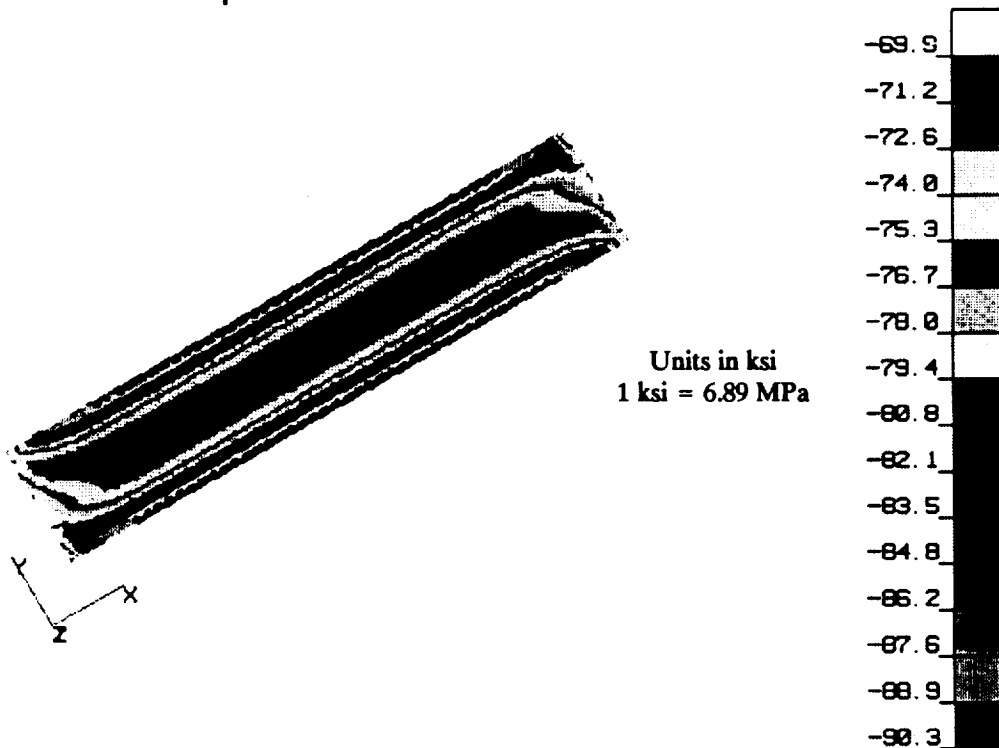


FIG. 126. Distribution of In-Plane Normal Stress from 2-D Simulation for 30° Specimen

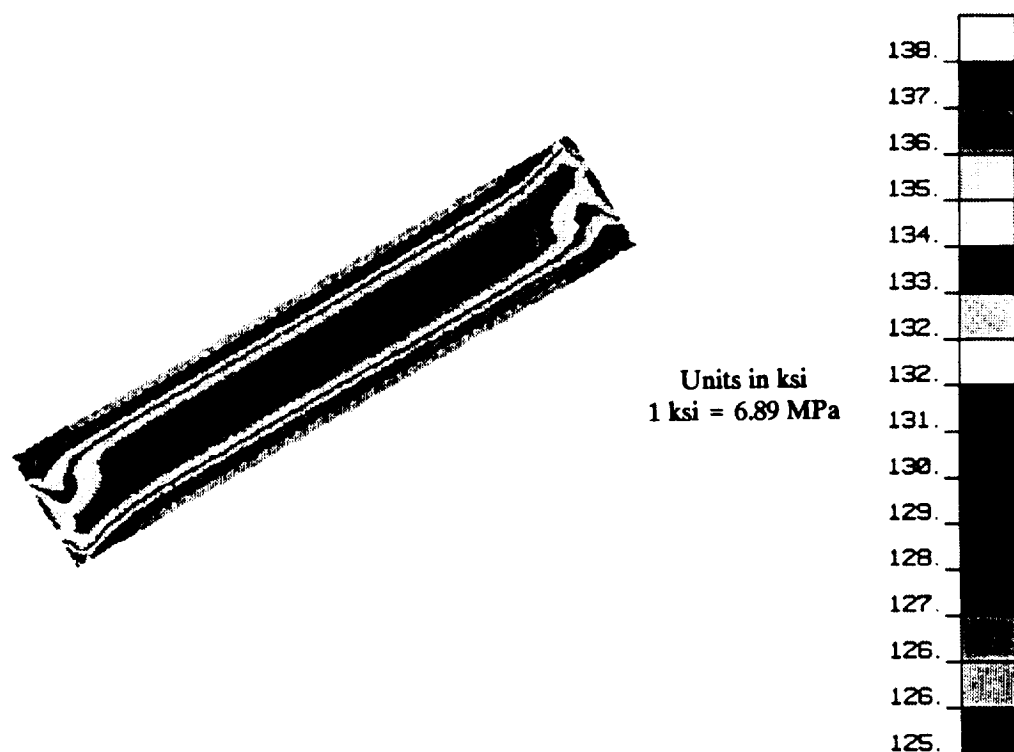


FIG. 127. Distribution of Shearing Stress from 2-D Simulation for 30° Specimen

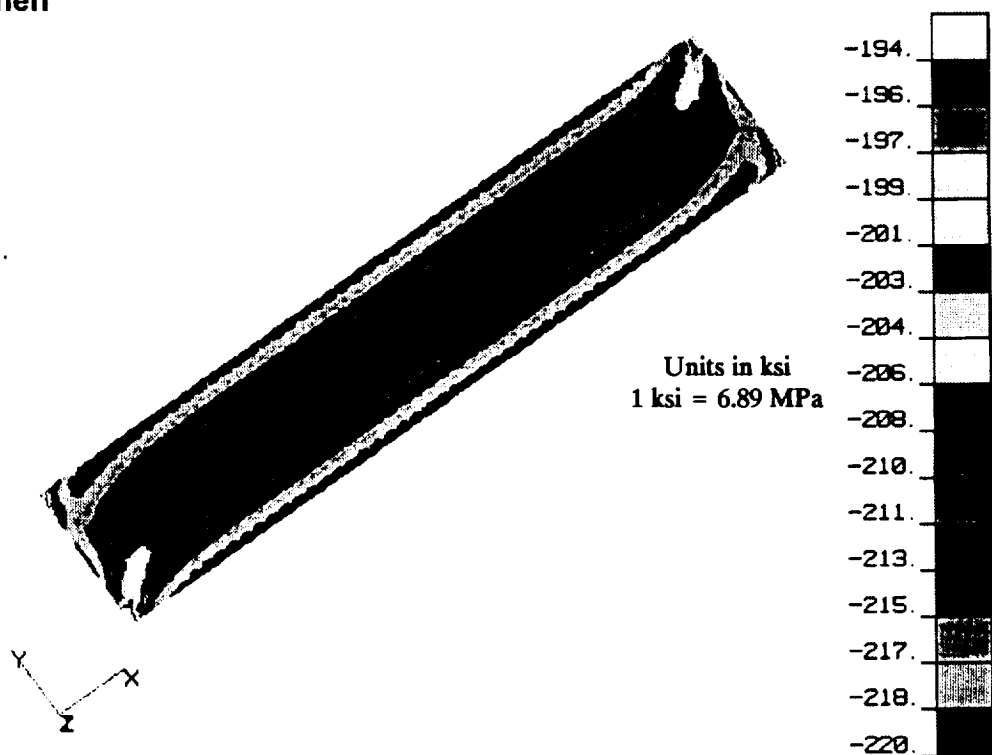


FIG. 128. Distribution of Through-Thickness Normal Stress from 2-D Simulation for 35° Specimen

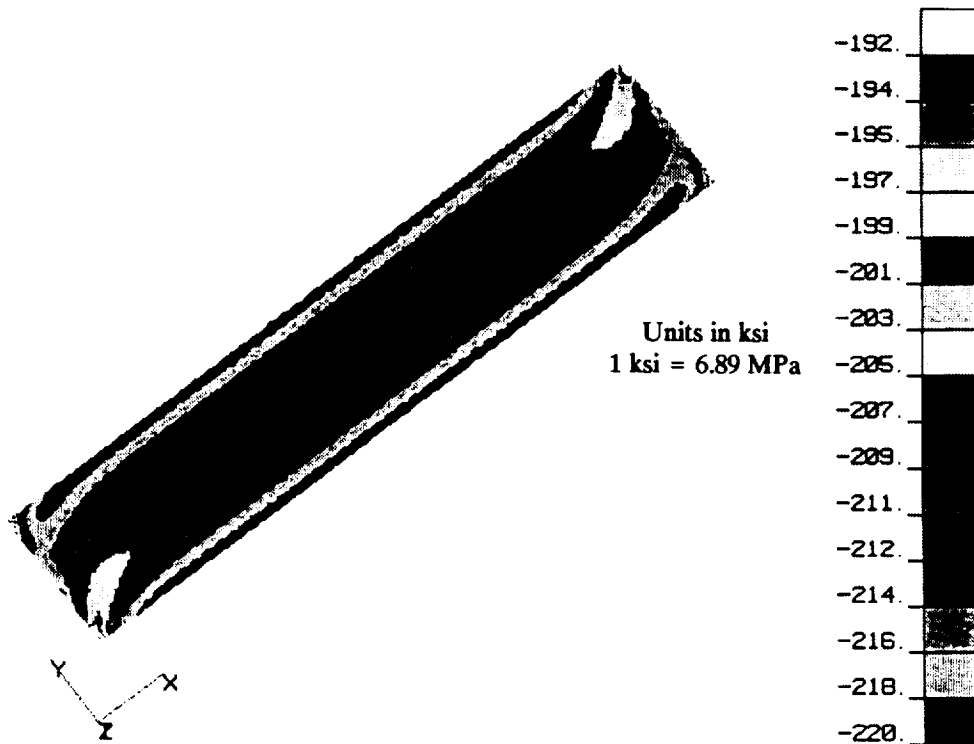


FIG. 129. Distribution of Through-Thickness Normal Stress from 2-D Simulation for 37° Specimen

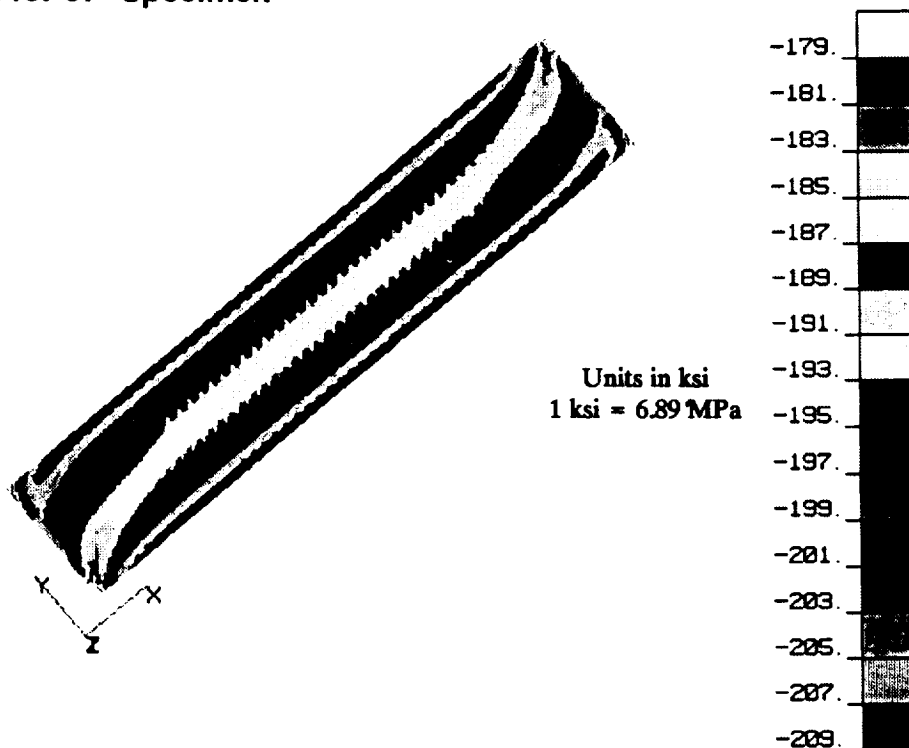


FIG. 130. Distribution of Through-Thickness Normal Stress from 2-D Simulation for 40° Specimen

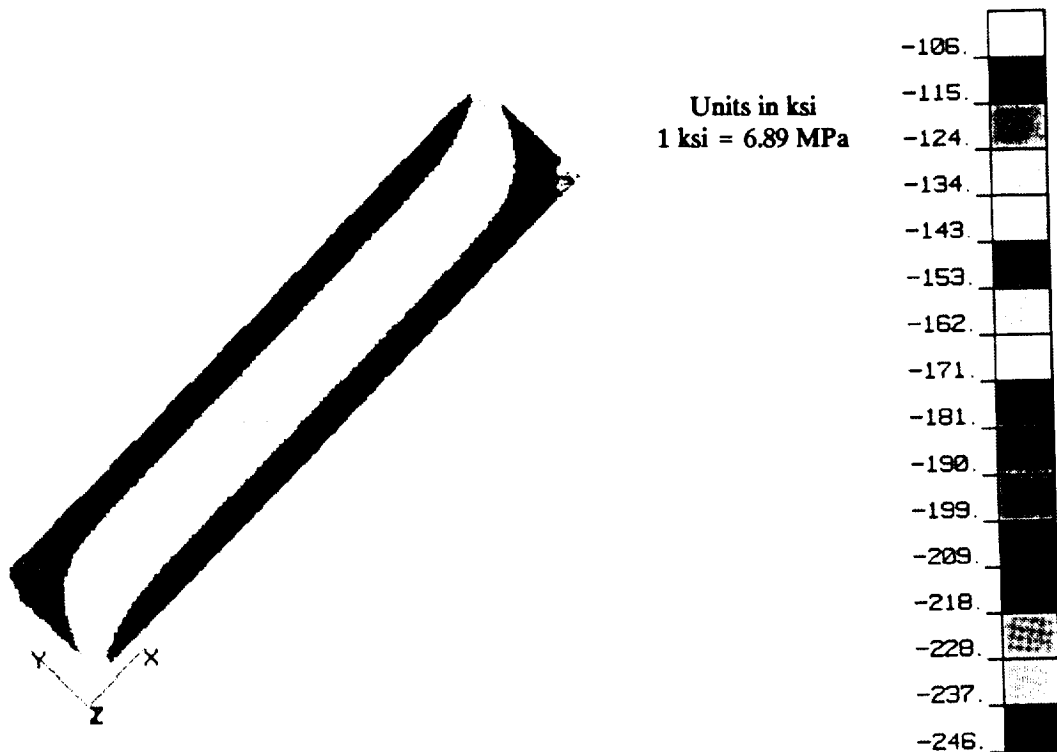


FIG. 131. Distribution of Through-Thickness Normal Stress from 2-D Simulation for 45° Specimen

6.3 MULTIAXIAL STATE OF STRESS: σ_2 , σ_3 , AND σ_4

6.3.1 Laboratory Experiments

Beryllium specimens that are identical in size to those used for the experiments described in the previous section and have a diameter of 12.7 mm (0.5 in.) are used for a similar set of compression-shear experiments. The directions of principal and secondary rolling are provided by the manufacturer. Once again, the rolling orientations of all specimens are verified through a low power microscope.

The experimental set-up is exactly the same as before except that the principal direction of cross-rolling is aligned with the y-axis (see Fig. 118). The secondary rolling and through-thickness directions are rotated clockwise about the y-axis through an angle equal to the cut angle of the holders, i.e., 30°, 35°, 37°, 40°, and 45°, respectively. The 2.2×10^6 -N (5.0×10^5 -lb) MTS compression testing machine is used to apply load. Two specimens are tested for each holder configuration for a total of ten disks. Each specimen is loaded in stroke control at a rate of 0.09 mm/s (0.04 in./min). The direction of loading coincides with the z-direction of the Cartesian coordinate axes (Fig. 118). No strain gages

or other transducers are attached to the specimens. Compliance of the test setup without a beryllium disk was determined (see section 5.5) so that deformation of the disk itself can be measured by subtracting the compliance from the stroke reading of the MTS machine.

Results for failure stress for all five experimental arrangements discussed in this section are shown in Table 20. These are obtained via the same transformation of stress from the loading to the material axes (Fig. 118) as described in section 6.2. A uniform stress distribution is assumed to be acting on the projection of the beryllium disk in the direction of the applied load and in the vicinity of the specimen. The magnitude of this stress is given by dividing the load at failure by the projected area of the beryllium disk. Magnitudes of the component of failure stress at the center of the beryllium specimens are determined via a simple stress transformation with respect to the material axes (see section 6.4.1 and Appendix VII). Good agreement is observed between the simplified analysis and FEA for the stress components at failure. The maximum difference in predicted stress components is approximately 3.5%. The histogram shown in Fig. 132 provides a synoptic output of the experimental results for the 30°, 35°, 37°, 40°, and 45° configurations. It displays the maximum compressive load and maximum vertical deflection for each specimen.

Each disk specimen fails suddenly which is characteristic of brittle behavior with no definite yield point. No ductile behavior and strain hardening effects are observed. Examination of the failed specimens reveals that the 30° and 35° orientations exhibit a failure behavior similar to that of the through-thickness compression specimen (see section 6.2.1): they form a single crack before failure. The 37° specimens show formation of more than one crack but each crack is similar to those of the 30° specimens. A mixed mode of failure, shear and compression, is observed for the 40° specimens. Cracks in the through-thickness direction for the 45° specimens exhibit similar behavior to that of the 40° specimen. The failed specimens exhibit similar distribution of crack formation as those shown in Figs. 121-123.

6.3.2 Numerical Simulation

Alignment of material properties for the two- and three-dimensional numerical models discussed in the previous section are changed to account for the differences in the material orientation of these specimens. Good agreement is observed between simplified transformed and numerical stresses at failure. No fringe plots are shown for these simulations. Omission of these figures is done to avoid repetitive presentation of results, since the patterns observed from these simulations are similar to those presented for the σ_1 , σ_3 , and σ_5 simulations.

TABLE 20. Failure Strengths of Disk Specimens with σ_2 , σ_3 , and σ_4 State of Stress

Specimen		Failure Stress from Simplified Analysis					
Angle of Inclination	Number	σ_1		σ_3		σ_5	
		MPa	(ksi)	MPa	(ksi)	MPa	(ksi)
(1)	(2)	(3)	(4)	(5)	(6)	(7)	(8)
30°	1	-449.5	(-72.5)	-1,498.5	(-217.3)	865.2	(125.5)
	2	-500.4	(-72.6)	-1,501.2	(-217.7)	866.7	(125.7)
35°	1	-659.6	(-95.7)	-1,345.4	(-195.1)	942.1	(136.6)
	2	-662.0	(-96.0)	-1,350.1	(-195.8)	945.4	(137.1)
37°	1	-741.5	(-107.5)	-1,305.7	(-189.4)	983.9	(142.7)
	2	-746.5	(-108.3)	-1,314.7	(-190.7)	990.7	(143.7)
40°	1	-873.4	(-126.7)	-1,240.5	(-179.9)	1,040.9	(151.0)
	2	-874.9	(-126.9)	-1,242.6	(-180.2)	1,042.6	(151.2)
45°	1	-1,076.3	(-156.1)	-1,076.3	(-156.1)	1,076.3	(156.1)
	2	-1,076.6	(-156.2)	-1,076.6	(-156.2)	1,076.6	(156.2)

Specimen		Failure Stress from FEA Simulation					
30°	1	-515.1	(-74.7)	-1,550.0	(-224.8)	865.2	(130.1)
	2	-516.4	(-74.9)	-1,552.8	(-225.2)	866.7	(130.3)
35°	1	-664.0	(-96.3)	-1,354.2	(-196.4)	942.1	(137.3)
	2	-666.1	(-96.6)	-1,358.3	(-197.0)	945.4	(137.8)
37°	1	-745.4	(-108.1)	-1,308.7	(-189.8)	983.9	(142.9)
	2	-750.9	(-108.9)	-1,324.5	(-192.1)	990.7	(144.0)
40°	1	-878.4	(-127.4)	-1,246.6	(-180.8)	1,040.9	(151.8)
	2	-879.8	(-127.6)	-1,248.7	(-181.1)	1,042.6	(151.9)
45°	1	-1,078.4	(-156.4)	-1,081.1	(-156.8)	1,081.8	(156.9)
	2	-1,079.8	(-156.6)	-1,081.8	(-156.9)	1,082.5	(157.0)

6.4 EVALUATION OF INTERACTION COEFFICIENTS

The two sets of experimental values of components of failure stress obtained from the inclined beryllium disks are listed in Tables 19 and 20. The triaxial state of stress (two normal and a shearing stress component) allows for the calculation of ten interaction coefficients, namely, F_{13} , F_{113} , F_{133} , F_{155} , and F_{355} from the first set (Table 19) and F_{23} , F_{223} , F_{233} , F_{244} , and F_{344} from the second set (Table 20). The stress transformation from the loading to the material axes and the scheme used for establishing these coefficients are found in sections 6.4.1-6.4.3 and Appendix VIII.

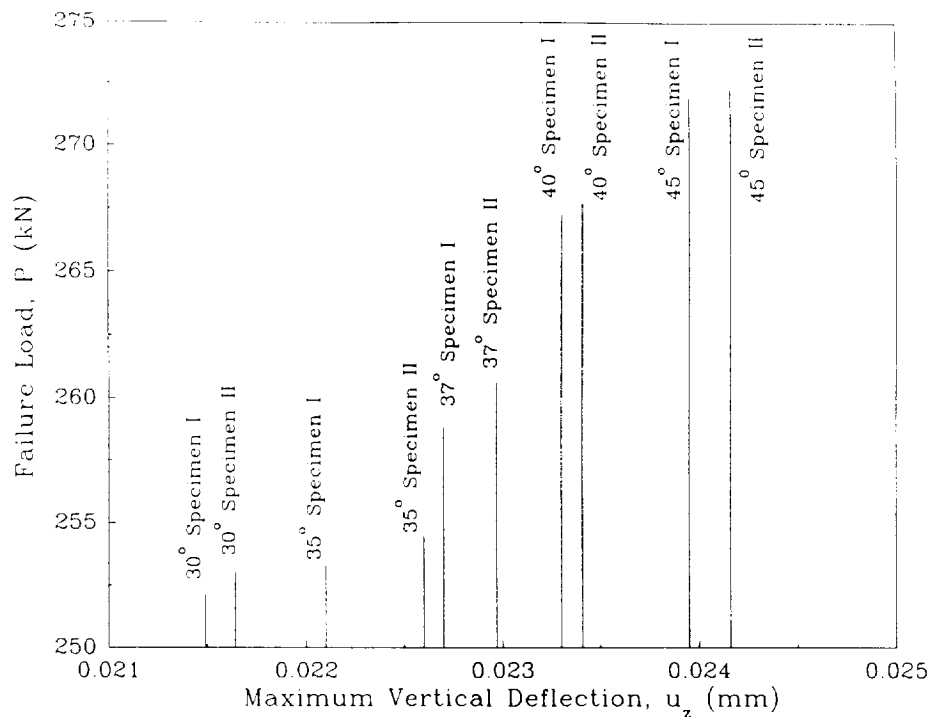


FIG. 132. Histogram of Maximum Compressive Load and Maximum Vertical Deflection for 30°, 35°, 37°, 40°, and 45° Planes of Inclination (σ_2 , σ_3 , and σ_4)

6.4.1 Theoretical Considerations

The general transformation of stress with respect to any orthogonal coordinate axes is given by the following tensorial relation (Sokolnikoff 1964):

$$\sigma_{ij} = \alpha_{in} \alpha_{jn} \sigma_{nn} \dots \dots \dots (225)$$

where α_{ki} and α_{lj} are direction cosines for a second-order tensor transformation.

A matrix form that is equivalent to Eq. 225 is as follows:

$$[\sigma_M] = [R]^T [\sigma_L] [R] \dots \dots \dots (226)$$

where $[R]$ is a matrix of direction cosines relating the coordinate and material axes, $[\sigma_M]$ is the transformed stress tensor, and $[\sigma_L]$ is the original stress tensor. As an example, consider the σ_1 , σ_3 , and σ_5 test described in section 6.2.1 with a 30° angle of inclination. In this case $[\sigma_L]$ and $[R]$ are as follows:

$$[\sigma_L] = \begin{bmatrix} 0 & 0 & 0 \\ 0 & 0 & 0 \\ 0 & 0 & -\sigma_x \end{bmatrix}; [R] = \begin{bmatrix} 0.866 & 0 & 0.500 \\ 0 & 0 & 0 \\ -0.500 & 0 & 0.866 \end{bmatrix} \dots \dots \dots (227)$$

Substituting the $[\sigma_L]$ and $[R]$ matrices into Eq. 226 leads to the following stress tensor:

$$[\sigma_M] = \sigma_x \begin{bmatrix} -0.250 & 0 & 0.433 \\ 0 & 0 & 0 \\ 0.433 & 0 & 0.750 \end{bmatrix} \dots\dots\dots (228)$$

It can be seen that this experimental arrangement provides the following combined state of stress:

$$\sigma_1 = -0.250\sigma_x \quad \sigma_3 = -0.750\sigma_x \quad \sigma_5 = 0.433\sigma_x \dots\dots\dots (229)$$

For this state of stress the generalized form of the failure surface given by Eq. 61 becomes:

$$F_1\sigma_1 + F_3\sigma_3 + F_{11}\sigma_1^2 + F_{33}\sigma_3^2 + F_{55}\sigma_5^2 + 2F_{13}\sigma_1\sigma_3 + 3F_{113}\sigma_1^2\sigma_3 + 3F_{133}\sigma_1\sigma_3^2 + 3F_{155}\sigma_1\sigma_5^2 + 3F_{355}\sigma_3\sigma_5^2 = 1 \dots\dots\dots (230)$$

Coefficients F_1 , F_3 , F_{11} , F_{33} , and F_{44} are known from chapter 5. Rearranging Eq. 230 so that the unknown coefficients are gathered on the left hand side, leads to the following equation:

$$2F_{13}\sigma_1\sigma_3 + 3F_{113}\sigma_1^2\sigma_3 + 3F_{133}\sigma_1\sigma_3^2 + 3F_{155}\sigma_1\sigma_5^2 + 3F_{355}\sigma_3\sigma_5^2 = 1 - (F_1\sigma_1 + F_3\sigma_3 + F_{11}\sigma_1^2 + F_{33}\sigma_3^2 + F_{55}\sigma_5^2) \dots\dots\dots (231)$$

6.4.2 Determination of F_{13} , F_{113} , F_{133} , F_{155} , and F_{355}

Since five sets of experimental output (see Table 19) are available for each orientation of the disk, least squares can be employed to evaluate the failure coefficients F_{13} , F_{113} , F_{133} , F_{155} , and F_{355} (see Appendix VII). These coefficients are required to meet the two conditions discussed in section 3. Usually, all conditions are satisfied and closure, convexity, and non-singularity are achieved. In some cases, however, these conditions are not met and the same step-by-step procedures described in section 3.1 (or section 3.2 if hydrostatic failure is considered) need to be employed.

The failure coefficients obtained in the case of cross-rolled beryllium sheet are as follows:

$$F_{13} = 4.48 \times 10^{-6} \text{ MPa}^{-2} \quad (2.13 \times 10^{-4} \text{ ksi}^{-2}) \dots\dots\dots (232)$$

$$F_{113} = 1.81 \times 10^{-9} \text{ MPa}^{-2} \quad (5.92 \times 10^{-7} \text{ ksi}^{-3}) \dots\dots\dots (233)$$

$$F_{133} = 1.96 \times 10^{-9} \text{ MPa}^{-3} \quad (6.41 \times 10^{-7} \text{ ksi}^{-3}) \dots\dots\dots (234)$$

$$F_{155} = -1.29 \times 10^{-13} \text{ MPa}^{-3} \quad (-4.21 \times 10^{-11} \text{ ksi}^{-3}) \dots\dots\dots (235)$$

$$F_{355} = 3.30 \times 10^{-14} \text{ MPa} \quad (1.08 \times 10^{-11} \text{ ksi}^{-3}) \dots\dots\dots (236)$$

6.4.3 Interaction Coefficients F_{23} , F_{223} , F_{233} , F_{244} , and F_{344}

In a similar fashion, results from experimental strength tests with the secondary rolling direction oriented in the direction of the inclined plane (Table 20) may be employed to obtain the failure coefficients F_{23} , F_{223} , F_{233} , F_{244} , and F_{344} . Following the steps described in section 6.4.1 leads to the following specialized form of the failure criterion:

$$F_2\sigma_2 + F_3\sigma_3 + F_{22}\sigma_2^2 + F_{33}\sigma_3^2 + F_{44}\sigma_4^2 + 2F_{23}\sigma_2\sigma_3 + 3F_{223}\sigma_2^2\sigma_3 + 3F_{233}\sigma_2\sigma_3^2 + 3F_{244}\sigma_2\sigma_4^2 + 3F_{344}\sigma_3\sigma_4^2 = 1 \quad (237)$$

Subsequently, Eq. 237 is modified by collecting terms that include unknown coefficients. The new equation is as follows:

$$2F_{23}\sigma_2\sigma_3 + 3F_{223}\sigma_2^2\sigma_3 + 3F_{233}\sigma_2\sigma_3^2 + 3F_{244}\sigma_2\sigma_4^2 + 3F_{344}\sigma_3\sigma_4^2 = 1 - (F_2\sigma_2 + F_3\sigma_3 + F_{22}\sigma_2^2 + F_{33}\sigma_3^2 + F_{44}\sigma_4^2) \quad (238)$$

Application of a standard least squares technique (Devore 1987) to the five sets of test data listed in Table 20 leads to the following coefficients:

$$F_{23} = 2.29 \times 10^{-6} \text{ MPa}^{-2} \quad (1.09 \times 10^{-4} \text{ ksi}^{-2}) \quad (239)$$

$$F_{223} = 1.55 \times 10^{-9} \text{ MPa}^{-3} \quad (5.08 \times 10^{-7} \text{ ksi}^{-3}) \quad (240)$$

$$F_{233} = 1.08 \times 10^{-9} \text{ MPa}^{-3} \quad (3.53 \times 10^{-7} \text{ ksi}^{-3}) \quad (241)$$

$$F_{244} = -2.81 \times 10^{-10} \text{ MPa}^{-3} \quad (-9.22 \times 10^{-8} \text{ ksi}^{-3}) \quad (242)$$

$$F_{344} = 2.04 \times 10^{-10} \text{ MPa}^{-3} \quad (6.70 \times 10^{-8} \text{ ksi}^{-3}) \quad (243)$$

The ten interaction coefficients determined in sections 6.4.2 and 6.4.3 yield failure surfaces that do not meet all necessary conditions outlined in section 3.1. Thus, implementation of constraining equations is necessary. These calculations are described in detail in chapter 8.

6.4.4 Determination of F_{12} , F_{112} , F_{122} , F_{166} , and F_{266} , and F_{144} , F_{255} , and F_{366}

Data from tests that apply in-plane tension, compression, and a combined state of stress (provided by the 45° off-axis specimen described in section 4.2.2) contribute to determination of the F_{12} , F_{112} , F_{122} , F_{166} , and F_{266} failure coefficients. The format

outlined in section 3 is followed. From the first condition, normal interaction coefficients F_{12} , F_{112} , and F_{122} are computed from a standard least-squares scheme (Devore 1987). The second condition defines a functional which, in turn, yields a system of nonlinear equations. The solution of this system of equations determines the remaining two failure coefficients: F_{166} and F_{266} . This is accomplished via the mathematical package MACSYMA (MIT Publications 1982). The normal interaction coefficients are:

$$F_{12} = -1.29 \times 10^{-6} \text{ MPa}^{-2} \quad (-6.11 \times 10^{-5} \text{ ksi}^{-2}) \dots\dots\dots (244)$$

$$F_{112} = -6.90 \times 10^{-10} \text{ MPa}^{-3} \quad (-2.26 \times 10^{-7} \text{ ksi}^{-3}) \dots\dots\dots (245)$$

$$F_{122} = -2.18 \times 10^{-10} \text{ MPa} \quad (-7.14 \times 10^{-8} \text{ ksi}^{-3}) \dots\dots\dots (246)$$

The normal-shear interaction coefficients are:

$$\begin{aligned} F_{166} &= -9.64 \times 10^{-10} \text{ MPa}^{-3} \quad (-3.16 \times 10^{-7} \text{ ksi}^{-3}) \\ F_{266} &= -9.64 \times 10^{-10} \text{ MPa}^{-3} \quad (-3.16 \times 10^{-7} \text{ ksi}^{-3}) \dots\dots\dots (247) \end{aligned}$$

Data from tests on three different specimens that apply a combination of all six components of stress (see Fig. 14) via double (in-plane and out-of-plane) rotations each at 45° are used to calculate the normal-shear interaction coefficients F_{144} , F_{255} , and F_{366} . It should be noted that these coefficients are the only unknown parameters at this point. Thus, a least-squares scheme is used to provide the best fit values for F_{144} , F_{255} , and F_{366} . These are as follows:

$$\begin{aligned} F_{144} &= -8.91 \times 10^{-10} \text{ MPa} \quad (2.92 \times 10^{-7} \text{ ksi}^{-3}) \\ F_{255} &= -9.82 \times 10^{-11} \text{ MPa} \quad (-3.22 \times 10^{-8} \text{ ksi}^{-3}) \dots\dots\dots (248) \\ F_{366} &= 0 \end{aligned}$$

Details concerning the formulation and extraction of these coefficients are given in Appendix VII.

6.5 STATE OF STRESS WITH IN-PLANE COMPRESSION AND OUT-OF-PLANE SHEAR

6.5.1 Experimental Investigation

Cross-rolled beryllium coupons that are rectangular in shape are used to induce a combined state of in-plane compression and out-of-plane shearing stress. The geometry of the specimens themselves is identical to those used for the compression test in section 5.2 (see Figs. 58 and 59). Loading is achieved with the aid of a 89.0-kN (20-kip) and 113.0-N-

m (1000-(in.-lb)) capacity biaxial machine (tension/compression-torsion) manufactured by Material Testing System (MTS).

Two different specimen orientations are considered: one has the direction of compressive loading parallel with the principal material axis (principal axis of rolling) and the other has its direction of compressive loading perpendicular to the principal material axis. Two specimens are tested for each orientation (a total of four plates). Each specimen has two, type FCA, 1.0-mm (3.8×10^{-2} in.) rosette gages (0° - 90° arrangement), one at the center of each side. The specimens are loaded by the same fixtures used for the in-plane compression test (Fig. 60). For each plate 9.53 mm (0.38 in.) of each end is secured into the fixtures. This permits a clear span length of 19.05 mm (0.75 in.) that is subjected to the combined compression and shearing loading. Each specimen is loaded in torsion at a twist rate of $0.19^\circ/\text{s}$. In each case, the beryllium specimen is compressed in the axial direction to 275.8 MPa (40.0 ksi) which is well within the linear elastic range of the material. The compressive stress is maintained throughout the experiment. Subsequently, the specimens are loaded in torsion to failure. It is assumed that the middle portion of the plate between the fixtures is acted upon by uniform compressive stress and torsional moment.

A summary of the test results is presented in Table 21. The compressive stress at failure is computed by dividing the axial force by the cross-sectional area of each specimen. Calculations for the torsional shearing stress at failure are described in section 6.5.2. Fig. 133 shows one of the specimens after failure. The specimens did not fail suddenly. However, examination of the failed specimen indicates development of brittle surfaces. A typical graph of torsional moment versus angle of twist is shown in Fig. 134. It can be seen that the material's ultimate torsional capacity occurs at yield which can be recognized after an angle of twist of approximately 3° . Beyond yield the specimens are still intact although major cracks appear throughout the middle one-third of the plate. This is due to the compressive stress that allows the material to achieve considerable torsional twist and concomitantly to maintain the torsional moment capacity at yield as well. It should be noted, however, that after yield the torsional moment is slightly reduced and then a modest hardening effect is observed. The material slips continuously after it yields.

6.5.2 Theoretical Considerations

It is assumed that the compression-torsion specimen acquires its maximum strength capacity while being loaded within the elastic range. In this case the state of stress imposed on the specimen can be resolved into two components: in-plane compression and out-of-plane shear. Moreover, the effect of each component is treated independently. Superposition of results yields the overall effect of the combined stresses. Since section

5.2.3 discusses theoretical studies for compressive components of stress, the focus of this section is limited to determination of the shearing stress.

TABLE 21. Failure Strength for Compression-Torsion Specimens

Specimen Orientation	Compression		Torsional Shear			
			σ_4		σ_5	
	MPa (2)	(ksi) (3)	MPa (4)	(ksi) (5)	MPa (6)	(ksi) (7)
(1)						
Parallel	275.8	(40.0)	368.2	(53.4)	279.2	(40.5)
Parallel	275.8	(40.0)	368.9	(53.5)	279.9	(40.6)
Perpendicular	275.8	(40.0)	285.4	(41.4)	376.4	(54.6)
Perpendicular	275.8	(40.0)	286.8	(41.6)	377.8	(54.8)

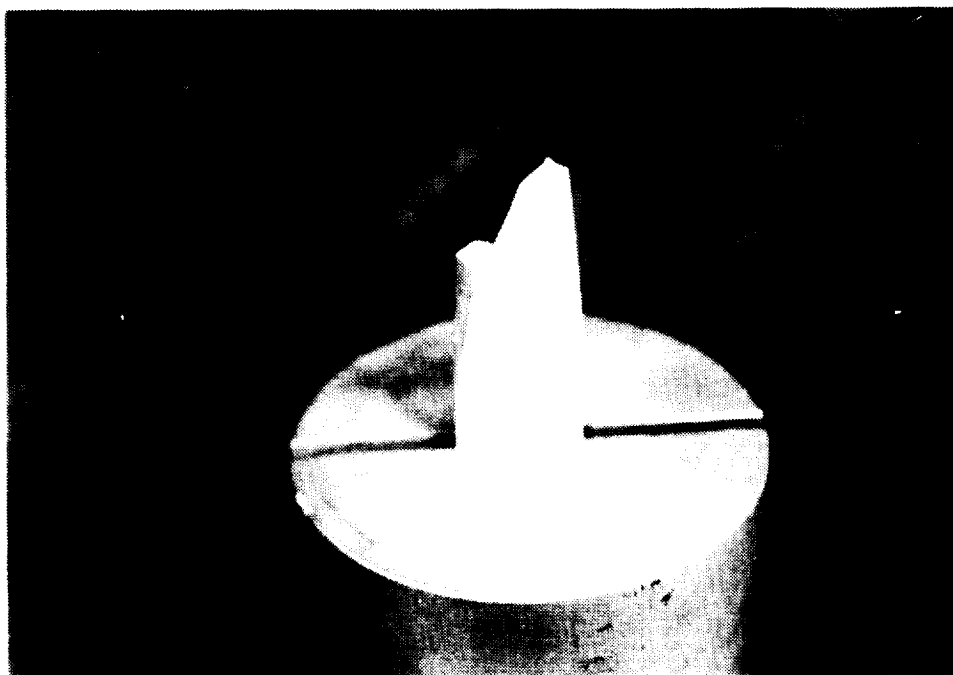


FIG. 133. Failed Compression-Torsion Specimen

Fig. 135 shows graphs of torsional moment versus normal strain measured along the principal and secondary directions of cross-rolling for the first specimen that is tested in each orientation. Strain gages are referenced using a capital letter and a number: the letter accounts for the alignment of the gage with respect to the material axis (A = parallel to longitudinal axis; B = perpendicular to longitudinal axis); the number refers to the specimen number (two specimens were tested per orientation).

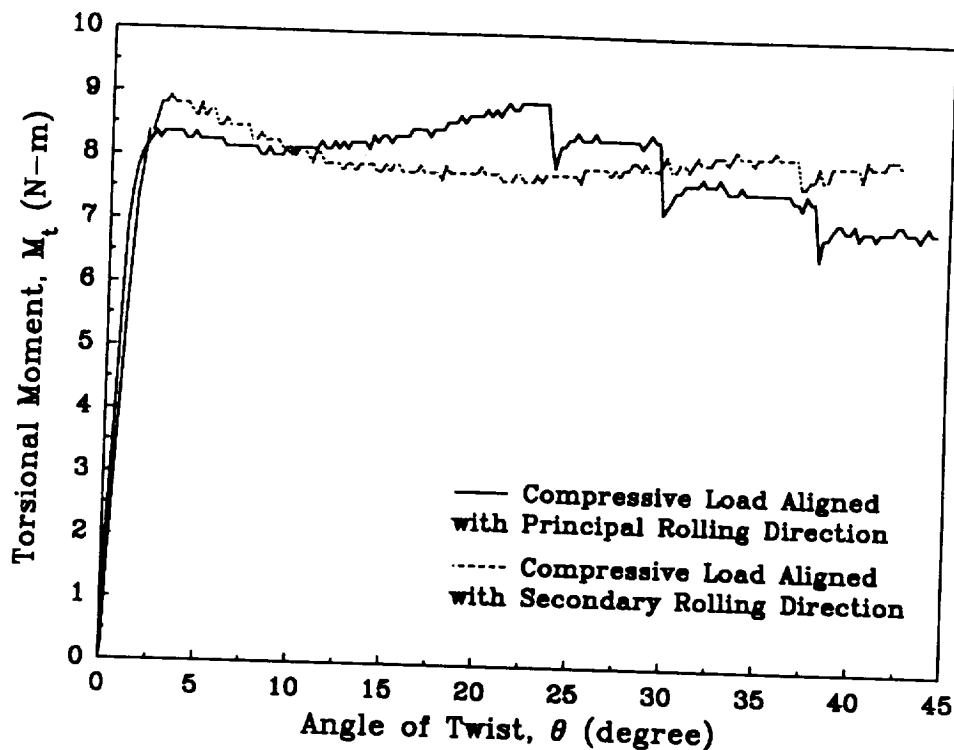


FIG. 134. Torsional Moment versus Angle of Twist

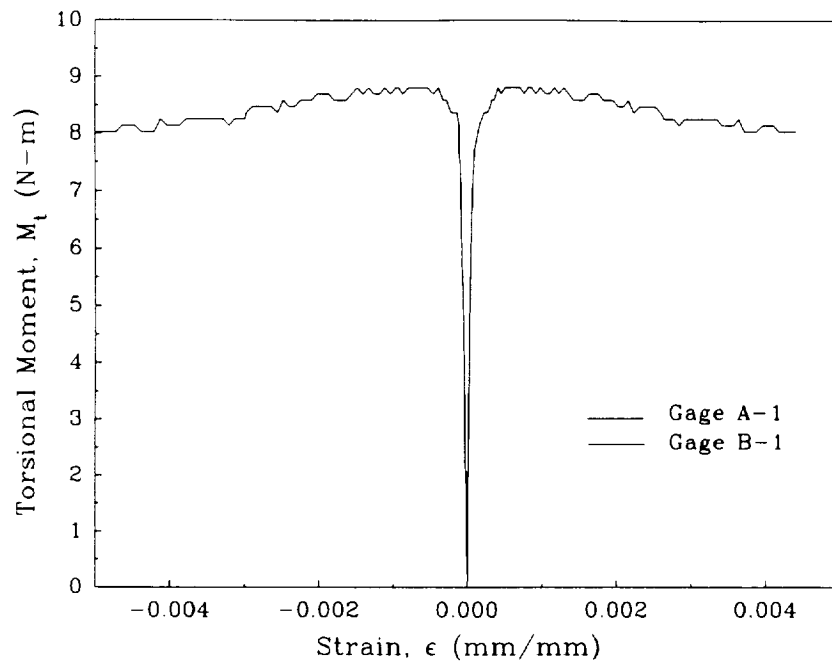
Consider a long homogeneous orthotropic bar of rectangular section with sides of length a and b . The orthotropic directions are parallel to the coordinate axes as shown in Fig. 136. The principal shear moduli associated with sides a and b are G_1 and G_2 , respectively. A torsional moment, M_t , is applied to the bar. Assuming small deformations and rotations the differential equation governing this problem is as follows (Lekhnitskii 1981):

$$g \frac{\partial^2 \psi}{\partial x^2} + \frac{\partial^2 \psi}{\partial y^2} = -\frac{8hG_2}{\pi} \sum_{m=1,3,\dots}^{\infty} \frac{1}{m} \sin \frac{m\pi x}{a} \dots \dots \dots (249)$$

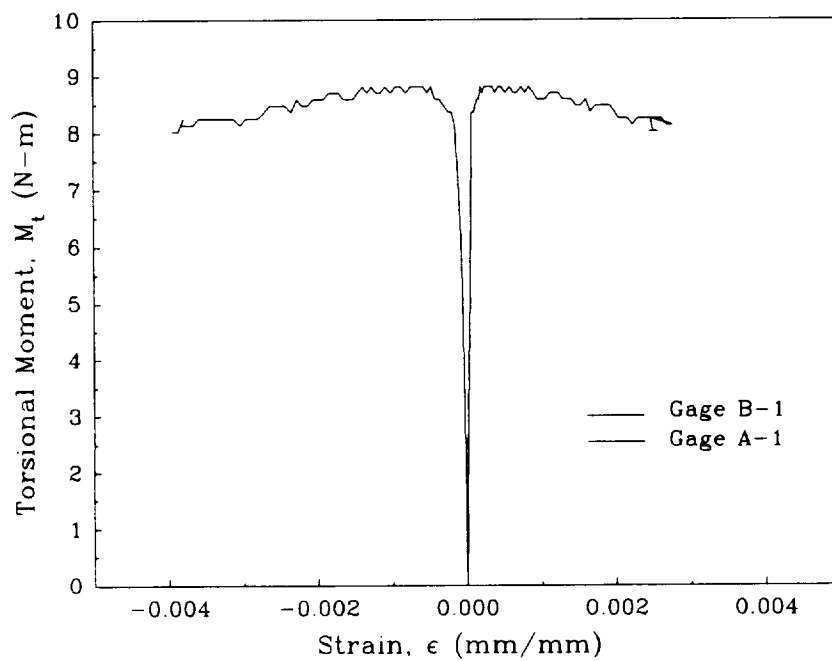
where ψ is a stress function that vanishes at all four sides of the cross-section ($x = 0, a$ and $y = 0, \pm b/2$), g is G_2/G_1 , and θ is the angle of twist. The general solution of Eq. 249 is (Lekhnitskii 1981):

$$\psi = Y_m(y) \sin \frac{m\pi x}{a} \dots \dots \dots (250)$$

$$Y_m = A_m \cosh \frac{m\pi\mu}{a} y + B_m \sinh \frac{m\pi\mu}{a} y + \frac{8\theta G_1 a^2}{m^3 \pi^3} \dots \dots \dots (251)$$



(a)



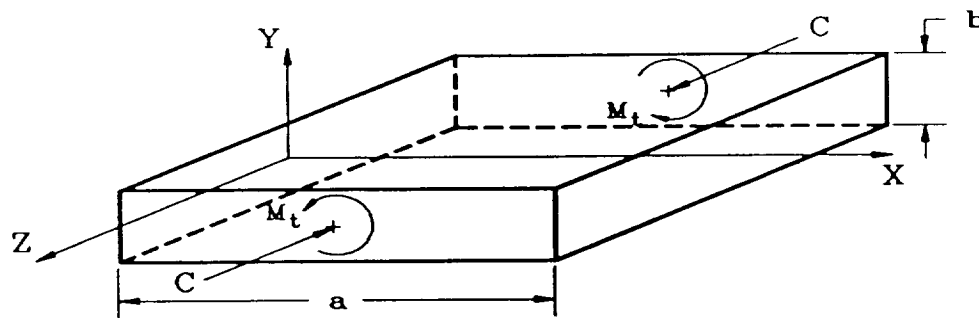
(b)

FIG. 135. Torsional Moment versus Normal and Transverse Strain for Specimen with (a) Principal and (b) Secondary Material Axes Aligned with Loading Orientation

where $\mu = \sqrt{g}$, and A_m and B_m are constants determined from the boundary conditions at $y = \pm b/2$. The solution assumes that the bar obeys Hooke's law. Thus, the stress function ψ becomes:

$$\psi = \frac{8\theta G_I a^2}{\pi^3} \sum_{m=1,3,\dots}^{\infty} \frac{1}{m^3} \left(1 - \frac{\cosh \frac{m\pi\mu y}{a}}{\cosh \frac{m\pi\mu}{2c}} \right) \sin \frac{m\pi x}{a} \dots\dots\dots (252)$$

where c is the ratio a/b .



M_t Torsional Moment
 C Compression

FIG. 136. Free Body Diagram of Compression-Torsion Specimen

The six stress components that are applied to the rectangular beryllium bar in section 6.5.1 are as follows (Lekhnitskii 1981):

$$\sigma_1 = \sigma_2 = \sigma_3 = \sigma_6 = 0, \quad \sigma_4 = \frac{\partial \psi}{\partial y}, \quad \text{and} \quad \sigma_5 = -\frac{\partial \psi}{\partial x} \dots\dots\dots (253)$$

Therefore, with the aid of Eq. 252 stresses σ_4 and σ_5 can be rewritten as follows:

$$\sigma_4 = \frac{8\theta G_I a^2}{\pi^2} \sum_{m=1,3,\dots}^{\infty} \frac{1}{m^3} \left(1 - \frac{\sinh \frac{m\pi\mu y}{a}}{\cosh \frac{m\pi\mu}{2c}} \right) \sin \frac{m\pi x}{a} \dots\dots\dots (254)$$

$$\sigma_s = \frac{8\theta G_1 a^2}{\pi^2} \sum_{m=1,3,\dots} \frac{1}{m^3} \left(1 - \frac{\cosh \frac{m\pi\mu y}{a}}{\cosh \frac{m\pi\mu}{2c}} \right) \cos \frac{m\pi x}{a} \dots\dots\dots (255)$$

To simplify these two equations, the following four additional parameters are defined:

$$d = \frac{c}{\mu} = \frac{c}{\sqrt{g}} \dots\dots\dots (256)$$

$$\beta = \frac{32d^2}{\pi^2} \sum_{m=1,3,\dots} \frac{1}{m^3} \left(1 - \frac{2d}{m\pi} \tanh \frac{m\pi}{2d} \right) \dots\dots\dots (257)$$

$$\kappa_1 = \frac{8d}{\pi^2 \beta} \sum_{m=1,3,\dots} \left(\frac{(-1)^{\frac{m-1}{2}}}{m^2} \tanh \frac{m\pi}{2d} \right) \dots\dots\dots (258)$$

$$\kappa_2 = \frac{d}{\beta} \left(1 - \frac{8d}{\pi^2} \sum_{m=1,3,\dots} \frac{1}{m^2 \cosh \frac{m\pi}{2d}} \right) \dots\dots\dots (259)$$

The torsional rigidity C, twist, and maximum shearing stresses are determined by the formulae (Lekhnitskii 1981):

$$C = G_2 ab^3 \beta \dots\dots\dots (260)$$

$$d = \frac{M_t}{C} = \frac{M_t}{G_2 ab^3 \beta} \dots\dots\dots (261)$$

$$MAX\sigma_4 = \frac{M_t \kappa_1}{ab^3} \dots\dots\dots (262)$$

$$MAX\sigma_5 = \frac{M_t \kappa_2}{ab^2 \mu} \dots\dots\dots (263)$$

For an orthotropic material the locations of maximum shearing stress correspond to the middle of either the longer or of the shorter side, depending on d. Application of Eqs. 260 through 263 to the beryllium specimens is carried out by means of a computer program written in the C language that appears in Appendix IX. The results are shown in Table 21.

Equations 260-263 only take into consideration the torsional state of stress for the experiment described in section 6.5.1. Assuming the specimen is within its elastic range the compressive stress is added to the torsional shearing stresses by superposition.

6.5.3 Interaction Coefficients F_{155} and F_{244}

Two interaction failure coefficients can be obtained from this experimental set-up. Using Eq. 66 and the uniform compression, and also assuming that the only components of stress at failure are obtained from an out-of-plane shearing force, the following specialized equation is derived:

$$F_1\sigma_1 + F_{11}\sigma_1^2 + F_{55}\sigma_5^2 + 3F_{155}\sigma_1\sigma_5^2 = 1 \dots\dots\dots (264)$$

This form assumes that the principal material axis is aligned with the direction of application of the compressive stress. Solving for F_{155} , the only unknown in the above equation, gives

$$F_{155} = \frac{1 - (F_1\sigma_1 + F_{11}\sigma_1^2 + F_{55}\sigma_5^2)}{3\sigma_1\sigma_5^2} \dots\dots\dots (265)$$

Similarly, for the case in which the direction of the principal material axis is perpendicular to the application of compressive stress, the governing strength equation is:

$$F_2\sigma_2 + F_{22}\sigma_2^2 + F_{44}\sigma_4^2 + 3F_{244}\sigma_2\sigma_4^2 = 1 \dots\dots\dots (266)$$

Solving for F_{244} :

$$F_{244} = \frac{1 - (F_2\sigma_2 + F_{22}\sigma_2^2 + F_{44}\sigma_4^2)}{3\sigma_2\sigma_4^2} \dots\dots\dots (267)$$

Direct substitution of the experimental strengths reported in Table 21 into Eqs. 265 and 267 yields the following coefficients:

$$F_{155} = -9.40 \times 10^{-9} \text{ MPa}^{-3} \quad (-3.09 \times 10^{-6} \text{ ksi}^{-3}) \dots\dots\dots (268)$$

$$F_{244} = -9.63 \times 10^{-9} \text{ MPa}^{-3} \quad (-3.16 \times 10^{-6} \text{ ksi}^{-3}) \dots\dots\dots (269)$$

It should be noted that the above values of F_{155} and F_{244} are dramatically different from those obtained in sections 6.4.2 and 6.4.3.

7. NON-DESTRUCTIVE EVALUATION TESTS

7.1 INTRODUCTION

Two types of non-destructive evaluation tests are used to evaluate or verify strength and other material parameters for cross-rolled beryllium sheet: (a) hardness, and (b) ultrasonic techniques. The hardness test is used to determine tensile strength of beryllium in the three orthogonal material directions and compare with results obtained from destructive tests (see section 6). The ultrasonic test supplies an estimate of the modulus of elasticity in the through-thickness direction. The main advantage of these techniques is that they are easy to use and save time. However, they may not provide the accuracy needed to properly evaluate material characteristics.

7.2 HARDNESS TEST

Hardness tests are used primarily as a basis for comparison of materials, especially with regard to specifications for manufacturing and heat treatment, quality control, and correlation with other properties and behavior (Davis et al. 1982). The physics of hardness is not yet fully understood, although the general concept, which has to do with solidity and firmness of matter, is easily comprehended. Hence, there is not a unique definition of hardness. Some arbitrary definitions associated with hardness are based mainly on the nature of the tests. For example, some tests measure resistance to permanent indentation under static or dynamic loading, energy absorption under impact loads, resistance to scraping, resistance to abrasion, resistance to cutting or drilling, etc. These definitions have developed with the necessity for expressing quantitative performance requirements under different conditions of service.

The concept that hardness is resistance to indentation or penetration of a surface forms the basis for a number of commercially available instruments. A variety of hardness tests has been devised. The most commonly used, however, are the Rockwell and Brinell tests (Asceland 1989; Davis et al. 1982). The Rockwell test is used in this study. Its principle of operation includes exerting a static load on an indenter which, in turn, deforms the specimen. The hardness measured is parallel to the direction of movement of the indenter. The measured hardness number is a function of the degree of indentation of the test specimen.

The operation and specific procedures for the Rockwell hardness tests have been standardized by ASTM (ASTM E 18). Some essential provisions as outlined by the standards include:

(1) The test surface should be flat and free from scale, oxide film, pits, and foreign material that may affect the results. A pitted surface can yield erratic readings owing to some indentation being near the edge of a depression which results in free flowing of metal around the indenter and, consequently, a low reading. Avoiding oiled surfaces is recommended since such a condition reduces friction under the indenter and results in a lower hardness reading.

(2) The bottom surface should be free from scale, dirt, or other foreign material that may crush or flow under the test pressure, thus, affecting the outcome.

(3) The thickness of the piece tested should be such that no bulge or other marking appears on the surface opposite the indenter. For hard material, such as cross-rolled beryllium sheet, the thickness may be as little as 0.25 mm (0.01 in.). Charts are available in ASTM E 18 for selecting proper scales for use with thin sheets.

(4) All hardness tests should be performed on a single thickness of the material under consideration. Stacking of two or more pieces of the same material to provide adequate thickness does not yield the same result as for a solid piece of the composite thickness due to relative movement between the various pieces.

(5) The hardness number of a curved surface determined using the Rockwell hardness test is likely in error because of the shape of the surface. A small area should be flattened prior to performing the test. For certain size specimens corrections can be made for curvature (see ASTM E 18).

The Rockwell hardness tester applies load via weights and levers. The indenter is either a steel ball or a braille (a diamond cone). The hardness number is read from a graduated dial indicator and, subsequently, converted into tensile strength with the aid of charts provided by the vendor. Fig. 137 shows such a device.

Initially, the Rockwell tester is calibrated with the use of special test blocks provided by the manufacturer. Prior to use with beryllium, the tester is calibrated for both the Rockwell "B" and "C" scales. The "B" scale uses a 1.5-mm (0.16-in.) diameter steel ball for a penetrator. A minor load mass of 10 kg (22.1 lb) and a major load mass of 100 kg (221.0 lb) is used for testing medium hard to very hard metals such as beryllium. The calibration yields an error of ± 0.5 hardness numbers. This is well within the acceptable limits set by the ASTM E 18 standard of ± 2.0 . The Rockwell "C" scale, which uses the diamond braille, a minor load mass of 10 kg (22.1 lb), and a major load mass of 150 kg

(331.0 lb) is used to test very hard metals. Calibration for this scale is also acceptable since an error of ± 0.8 hardness numbers is obtained.

Initially, a 12.7-mm \times 12.7-mm \times 2.54-mm (0.5-in. \times 0.5-in. \times 0.1-in.) cross-rolled beryllium specimen is used in conjunction with a Rockwell hardness machine to determine tensile strength in the three orthogonal directions of the material. A second specimen, a 12.7-mm (0.5-in.) diameter disk that is 2.54-mm (0.1-in.) thick, is used only for through-thickness hardness evaluation tests.

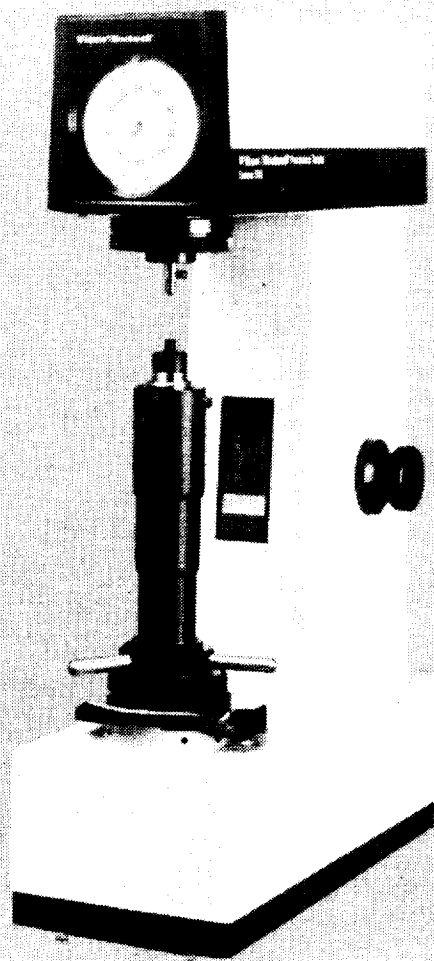


FIG. 137. Hardness Testing Machine

Figs. 138 and 139 show magnified pictures of indentations produced by the penetrator for the through-thickness and longitudinal directions, respectively. Indentations similar to those shown in the longitudinal direction are also observed in the transverse direction, although they are not shown. For all three directions, the Rockwell "B" scale is used. Testing of the square specimen in the longitudinal and transverse directions of

principal rolling yields results very close to those obtained from uniaxial tensile testing in the corresponding direction. Average tensile strengths of 518.2 MPa (75.2 ksi) and 547.4 MPa (79.4 ksi) are computed for the principal and secondary in-plane material axes, respectively. These values compare well with the experimentally determined strengths shown in Table 5.

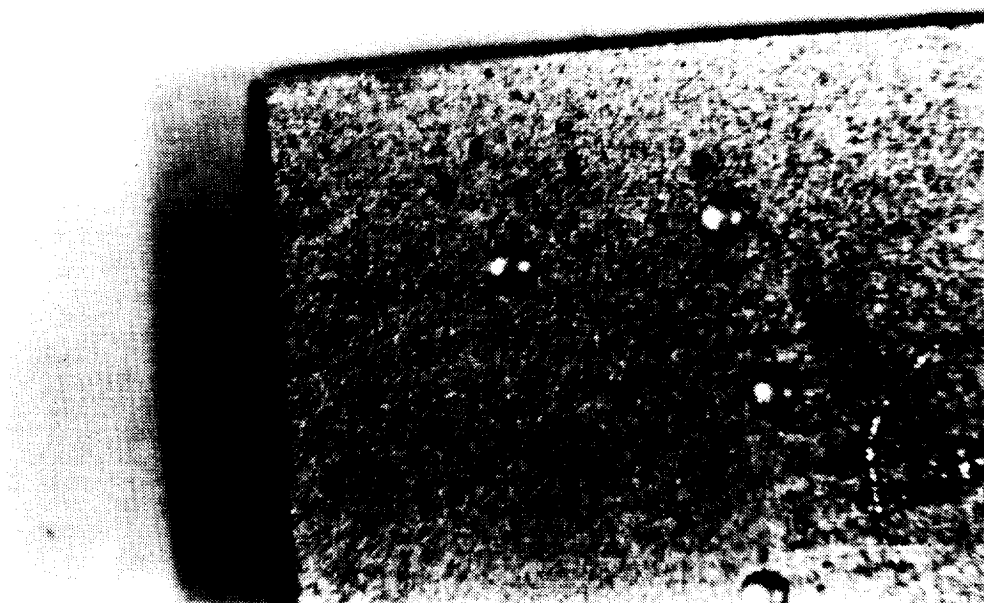


FIG. 138. Indentations from Through-Thickness Hardness Test



FIG. 139. Hardness Test Indentations in SR-200 Beryllium Used to Determine σ_1

Potentially significant results are obtained when the square and disk specimens are tested for hardness in the through-thickness direction. The Rockwell "B" scale is employed for most tests, although the Rockwell "C" scale is also used. This is due to the fact that the indications of the former scale fall in the upper part of the range of the scale and validation of the results is achieved by employing the latter scale. Results from the Rockwell "C" test fall in the lower end of the range and are consistent with the hardness outcomes reported by the Rockwell "B" scale. Data obtained from both the square and disk specimens indicate an average through-thickness tensile strength of 765.3 MPa (111.0 ksi) in this direction which is 3.8 times as large as the one reported by Lockheed (Fenn et al. 1967).

Based on lack of agreement of the hardness tests results with those reported by Lockheed, a third specimen similar to the first one (square in plan view) is tested. The results obtained are consistent with tests on the two previous specimens. Tensile strengths obtained using the Rockwell "B" scale for the square and disk specimens are reported in Table 22 for all three principal directions of orthotropy.

Although, hardness tests are not regarded as totally reliable, they do provide a good indication of the material's tensile strength behavior in the direction under consideration. A large discrepancy exists between the tensile strength of SR-200 beryllium sheet in the through-thickness direction reported by Lockheed and results from the hardness test. The more conservative of the two values, which is the tensile strength reported by Lockheed, is used for determination of the principal coefficients F_3 and F_{33} (see section 5).

7.3 ULTRASONIC TEST

7.3.1 Background

A relatively simple and rapid way to establish material modulus in the through-thickness direction is to use an ultrasonic technique. Here, this method is applied to cross-rolled beryllium sheets. In order to verify whether or not the material exhibits significant variation of elastic properties in the through-thickness direction, five reduced-thickness disks are tested ultrasonically. The thickness of the disks varies from 2.54 mm (0.1 in.) to 0.60 mm (0.02 in.) in increments of 0.60 mm (0.02 in.). The thinnest specimen is obtained from the middle of a 2.54-mm (0.1-in.) disk by a chemical etching technique performed by the material supplier (Electrofusion Corp.). Each successively thicker disk is obtained by etching less material from a 2.54-mm (0.1-in.) disk. It is assumed that the chemical process does not affect the material properties.

TABLE 22. Tensile Strengths from Hardness Testing for Principal Material Axes

Specimen		Rockwell "B"	Equivalent Tensile Strength	
Shape (1)	Orientation (2)	Dial Reading (3)	MPa (4)	(ksi) (5)
Square	Longitudinal			
	1	80.8	508.8	(73.8)
	2	81.0	510.2	(74.0)
	3	81.0	510.2	(74.0)
	4	82.0	530.9	(77.0)
	5	82.0	530.9	(77.0)
	Average	81.4	518.2	(75.2)
	Transverse			
	1	82.0	530.9	(77.0)
	2	82.5	544.7	(79.0)
	3	82.5	544.7	(79.0)
	4	83.0	558.5	(81.0)
	5	83.0	558.5	(81.0)
	Average	82.6	547.4	(79.4)
	Short Transverse			
	1	99.0	772.2	(112.0)
	2	99.0	772.2	(112.0)
	3	99.0	772.2	(112.0)
	Average	99.0	772.2	(112.0)
Disk	Short Transverse			
	1	98.0	758.4	(110.0)
	2	98.0	758.4	(110.0)
	3	99.5	686.0	(113.0)
	Average	98.5	765.3	(111.0)

Normal incidence pulse-echo and through-transmission techniques are employed for each specimen (Bray and Stanley 1989). A schematic of the experimental setup is shown in Fig. 140. Piezoelectric sources of variable frequencies of excitation are used. Two conditions are necessary for the success of the test: knowledge of the distance of travel of the pulse and absence of internal flaws. Time required for the excitation wave to either travel through the material or be reflected is measured from the wave pattern that is shown on an oscilloscope. Results obtained from the two methods are consistent with each other.

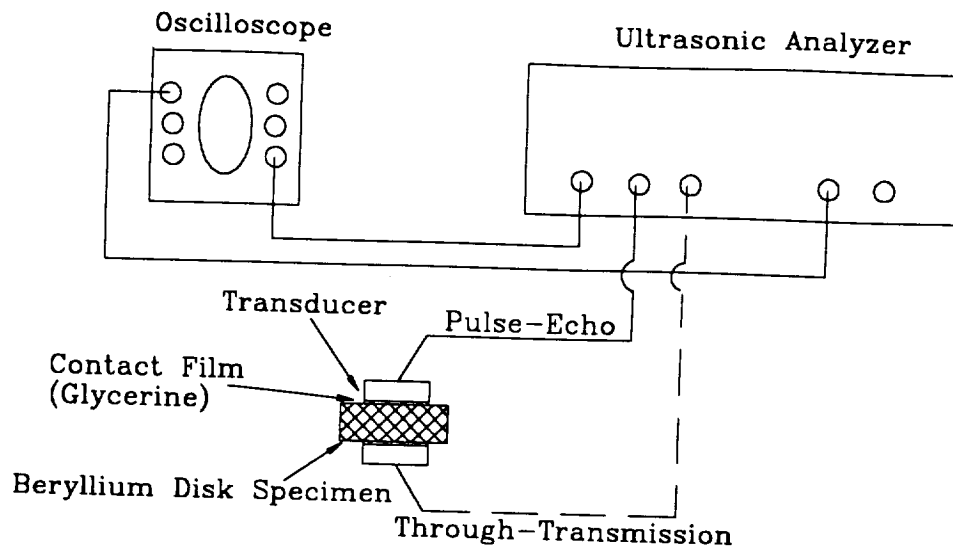


FIG. 140. Experimental Setup for Ultrasonic Testing

The average elastic modulus and Poisson's ratio for each specimen can be calculated using the following equations:

$$E_a = \rho c_2^2 \frac{[3(c_1^2 - 4c_2^2)]}{c_1^2 - c_2^2} \dots \dots \dots (270)$$

$$\mu_a = \frac{(c_1^2 - 2c_2^2)}{2(c_1^2 - c_2^2)} \dots \dots \dots (271)$$

where E_a is the modulus in the through-thickness direction; μ_a is the average of the Poisson's ratios; c_1 is the velocity of the longitudinal wave; c_2 is the velocity of the shear wave; and ρ is the density of the material (Bray and Stanley 1986). It should be emphasized that these estimates are average quantities of the modulus and Poisson's ratios for the entire specimen subjected to ultrasonic testing.

Overall goal of these tests is to obtain a distribution of these parameters from a series of sections with variable thickness. As described earlier, these sections are centered about the neutral plane of the plate.

7.3.2. Determination of Elastic Constants for Each Layer

For this study five sections of SR-200 beryllium are tested using an NDE technique. Each section is symmetric about the middle plane as shown in Fig. 141. Section 1 has a thickness of 0.51 mm (0.02 in.) while section 5 has a thickness of 2.54 mm (0.10 in.). Intermediate sections, 2, 3, and 4 increase by 0.51 mm (0.02 in.) in thickness. Sections 2, 3,

4, and 5 are considered to be composed of 4, 6, 8, and 10 different layers, respectively, that are 0.25 mm (0.01 in.) thick (see Fig. 141).

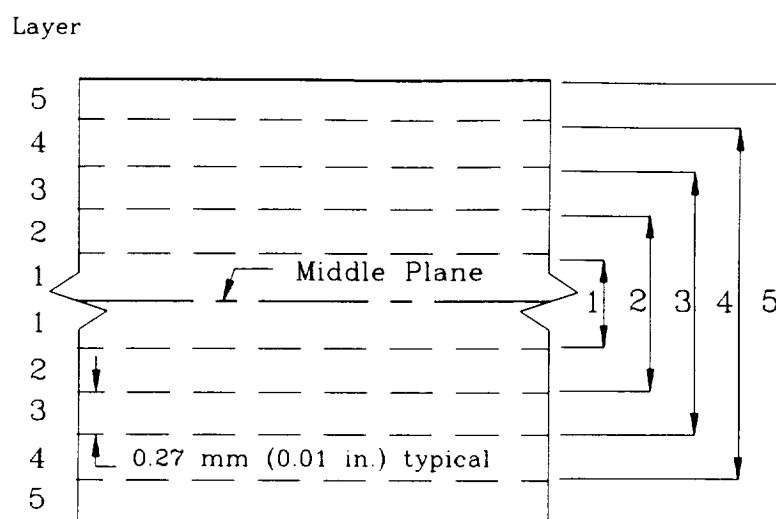


FIG. 141. Location and Dimension of Through-Thickness Layers

The goal of this sequence of experiments is to obtain the through-thickness moduli, E_3 , and Poisson's ratios, ν_{13} and ν_{23} , for each of the ten layers. It is assumed that all other material properties are known. In addition, average E_3 , ν_{13} , and ν_{23} values for each section can be established indirectly from the average of three NDE tests per section by using Eqs. 270 and 271. Results of these calculations are shown in Table 23.

TABLE 23. Elastic Constants for Specimens from NDE Measurements

Specimen	Thickness (mm)	c_1^a (m/s)	c_2^a (m/s)	Layers	Material Properties			
					E_3		ν_{13}	ν_{23}
					GPa	(ksi)		
(1)	(2)	(3)	(4)	(5)	(6)	(7)	(8)	(9)
	0.508	12,774	8,574	1	296.5	(43,000)	0.089	0.091
	1.016	12,774	8,574	1,2	296.5	(43,000)	0.089	0.091
	1.524	12,947	8,731	1,2,3	305.5	(44,300)	0.085	0.086
	2.032	13,389	9,070	1,2,3,4	327.5	(47,000)	0.083	0.085
	2.540	13,855	9,429	1,2,3,4,5	351.0	(51,000)	0.081	0.083

^aAverage of three measurements

Different schemes, such as the average and equivalent through-thickness modulus rule of mixtures, can be employed for calculating E_3 , ν_{13} , and ν_{23} for each layer, depending on the orientation of the layers of material (Asceland 1989). These models suggest

representation of the through-thickness and in-plane moduli in terms of equivalent spring stiffnesses. Limitations arise, however, especially for the calculation of Poisson's ratios, if coupling between the equivalent springs is employed. This gives rise to a system of indeterminate equations. Thus, for a solution to be obtained additional assumptions are imposed, such as requiring that the total in-plane strain of the material is equal to the mean in-plane strain of all layers comprising the medium.

7.3.3. Numerical Simulation

In order to avoid these simplifying assumptions, evaluation of the through-thickness modulus and Poisson's ratios for each layer are obtained using numerical simulation. The method described in what follows is based on a recursive procedure that allows for the determination of E_3 , ν_{13} , and ν_{23} , of each layer. That is, once the elastic properties of i^{th} layer are known, the properties of the $i+1^{\text{th}}$ layer can be determined.

For section 1, which is comprised of two layers having the same elastic properties, constants E_3 , ν_{13} , and ν_{23} are determined from experimental measurements of the wave velocities, c_1 and c_2 , and Eqs. 270 and 271. Velocity measurements for section 2, which has four layers and two different sets of material properties, are used to determine an estimate of E_3 , ν_{13} , and ν_{23} for the overall section by employing Eqs. 270 and 271.

Consider a small section taken from a thin plate that extends infinitely far in all directions from the point in question. In the event that a uniform stress in the through-thickness direction is applied to the top surface of section 2, and provided that the layers 1 and 2 are not physically connected, then the deformation experienced by the two sets of layers is similar to that shown in Fig. 142. Only one-eighth of the arrangement is shown, i.e., planes x - y , y - z , and x - z are planes of symmetry.

If the material is made up of the same two sets of layers but this time there is a physical connection or bonding between them (Fig. 143), then for a load situation similar to that of Fig. 142 the deformed structure is analogous to what is shown in Fig. 144. Planes 1, 2, and 3 are planes of symmetry and, thus, only one-eighth of the structure is shown. In addition, it is assumed that the body deforms in such a manner that the normal displacements in the two in-plane orthogonal directions of layer 1 are the same as those of layer 2.

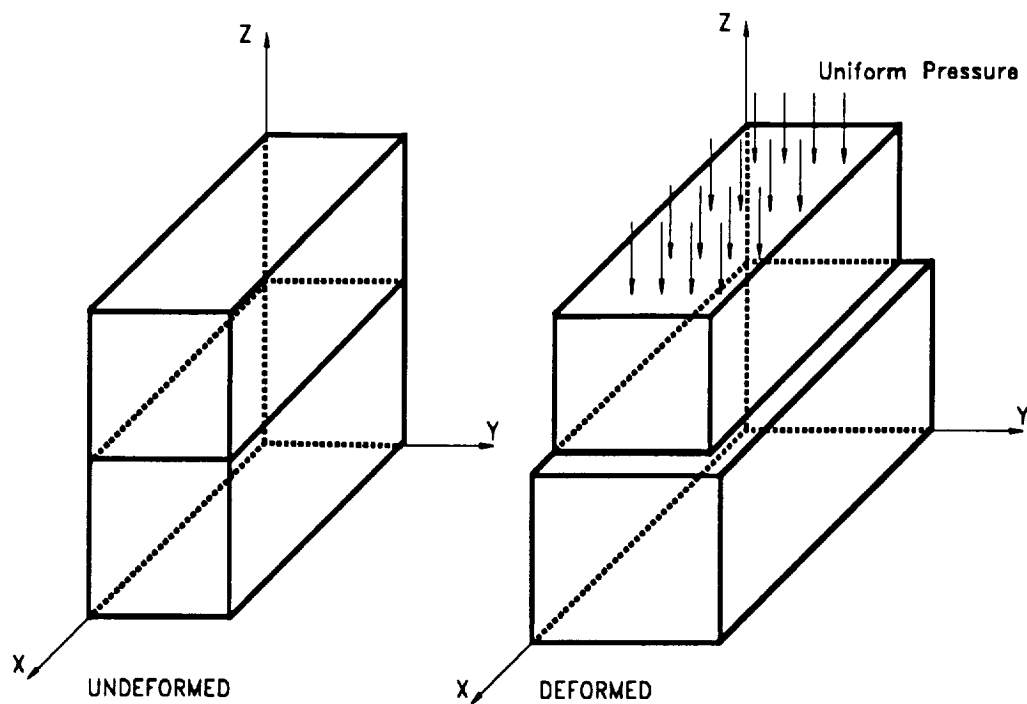


FIG. 142. Two Independent Layers with Different Elastic Properties E_3 , ν_{13} , and ν_{23} in Undeformed and Deformed Configurations

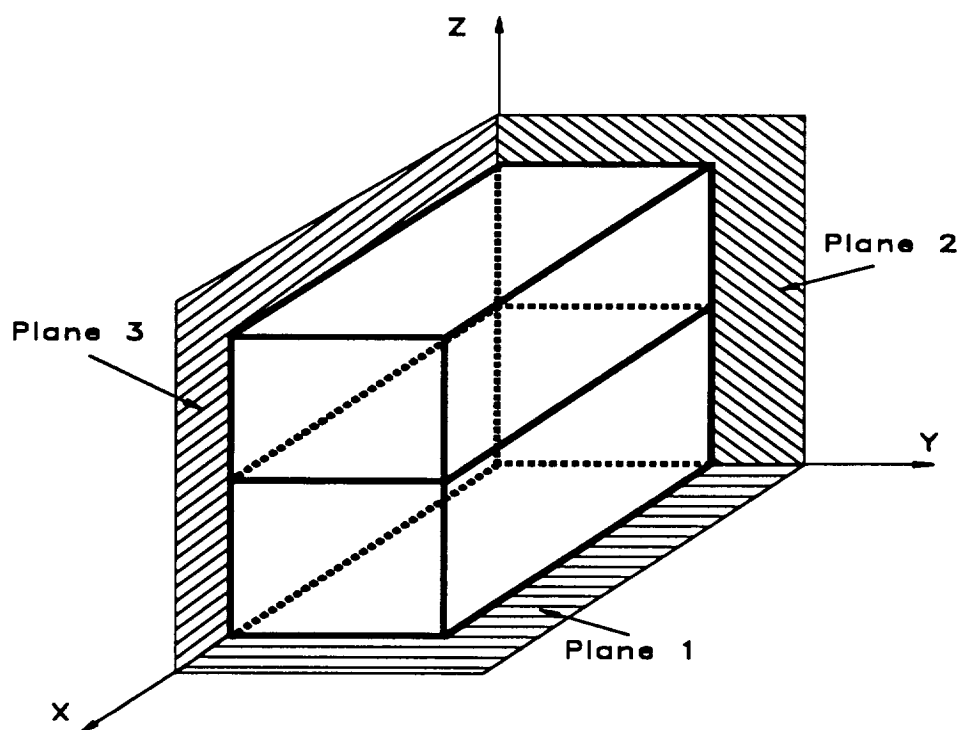


FIG. 143. Undeformed Medium of Two Connected Layers with Different E_3 , ν_{13} , and ν_{23}

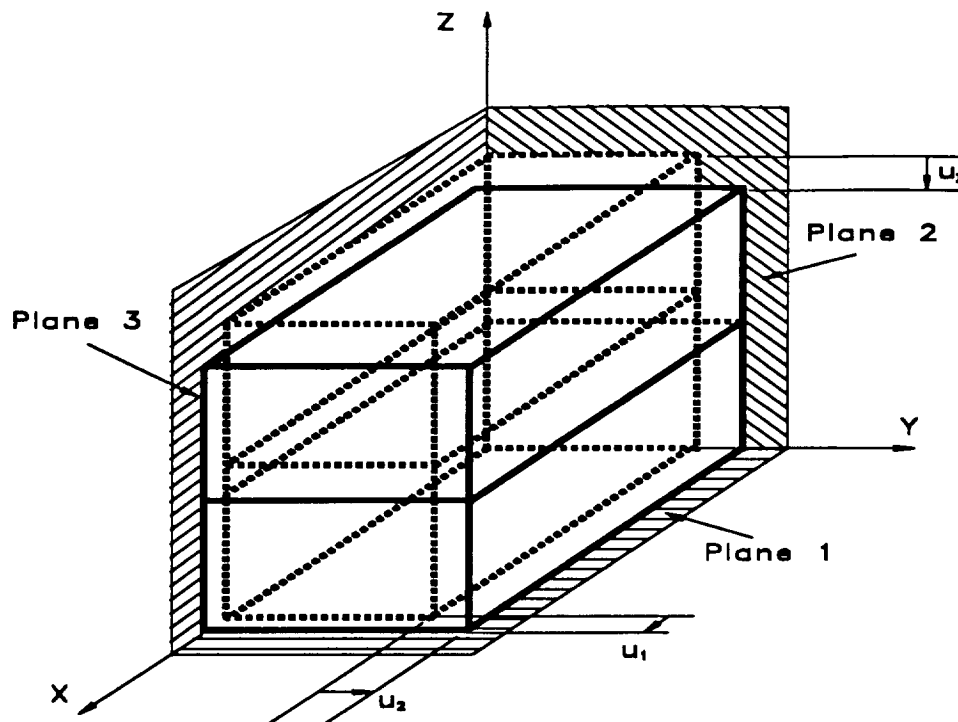


FIG. 144. Deformed Medium of Two Connected Layers with Different E_3 , ν_{13} , and ν_{23}

Material properties are known for the inner layer, but not for the topmost layer. To establish E_3 , ν_{13} , and ν_{23} for the top layer a numerical model is constructed. For the first analysis both layers are given the overall material properties of the entire section as determined from Eqs. 270 and 271 and listed in Table 23. The Poisson's ratios ν_{31} and ν_{32} are assumed to be identical. A uniform load is applied as shown in Fig. 142 that induces linear elastic displacements, strains, and stresses. The deformation in each of the two in-plane directions is kept the same for both layers via multi-point constraining (MPC) equations. Magnitudes of displacements in the three mutually perpendicular directions are noted.

The second stage for the solution of the unknown material properties involves a trial and error process with multiple analyses. A series of simple FEA simulations is carried out in order to establish E_3 , ν_{13} , and ν_{23} of the top layer. The numerical model used is geometrically identical to the model used with the composite section (Fig. 143). The material properties E_3 , ν_{13} , and ν_{23} , however, of each layer are different. The bottom layer is given the material properties established experimentally or from a previous series of analyses. The top layer is, initially, given the material properties of the entire section from Table 23. Displacements in the three orthogonal directions that result from the FEA

analysis are noted. In the event that these displacements do not match the components of displacement obtained from the composite model, the elastic constants E_3 , ν_{13} , and ν_{23} are adjusted by a factor. The magnitude of this factor is determined from the ratio of the displacement of the overall section to that of the independent layer simulation. The same adjustment procedure is repeated for the uppermost layer until the assigned material coefficients yield displacement components that are identical to those of the overall section in the first analysis.

Once material properties are known for all layers in a given section, the next thicker section is considered in a similar manner. That is, the properties of the outermost layer are determined by a numerical trial and error procedure that results in deformations in the three orthogonal directions that are the same as those resulting from the average properties determined by the NDE tests. By repetition of this procedure E_3 , ν_{13} , and ν_{23} are determined for all remaining layers. Approximately 20 simple analyses are required for each section. Table 24 lists the material properties for each layer of cross-rolled beryllium sheet. Fig. 145 shows graphical distribution of E_3 obtained from the numerical simulation. Only the properties of five of these layers are shown since symmetry about the middle plane is assumed. The results show a significant variation of the through-thickness modulus, E_3 . The outermost layer has an E_3 which is 180% larger than the corresponding E_3 of the innermost layer. The Poisson's ratios of the outer layers, on the other hand, decrease by as much as 18% compared to the Poisson's ratios of the inner layers.

TABLE 24. Elastic Constants for Layers from NDE Measurements

Layer	Thickness		Material Properties			
	t		E_3		ν_{13}	ν_{23}
	mm	(in.)	GPa	(ksi)		
(1)	(2)	(3)	(4)	(5)	(6)	(7)
1	0.254	(0.010)	296.5	(43,000)	0.089	0.091
2	0.254	(0.010)	296.5	(43,000)	0.089	0.091
3	0.254	(0.010)	325.9	(47,100)	0.077	0.077
4	0.254	(0.010)	396.4	(57,500)	0.075	0.077
5	0.254	(0.010)	533.7	(77,400)	0.076	0.077

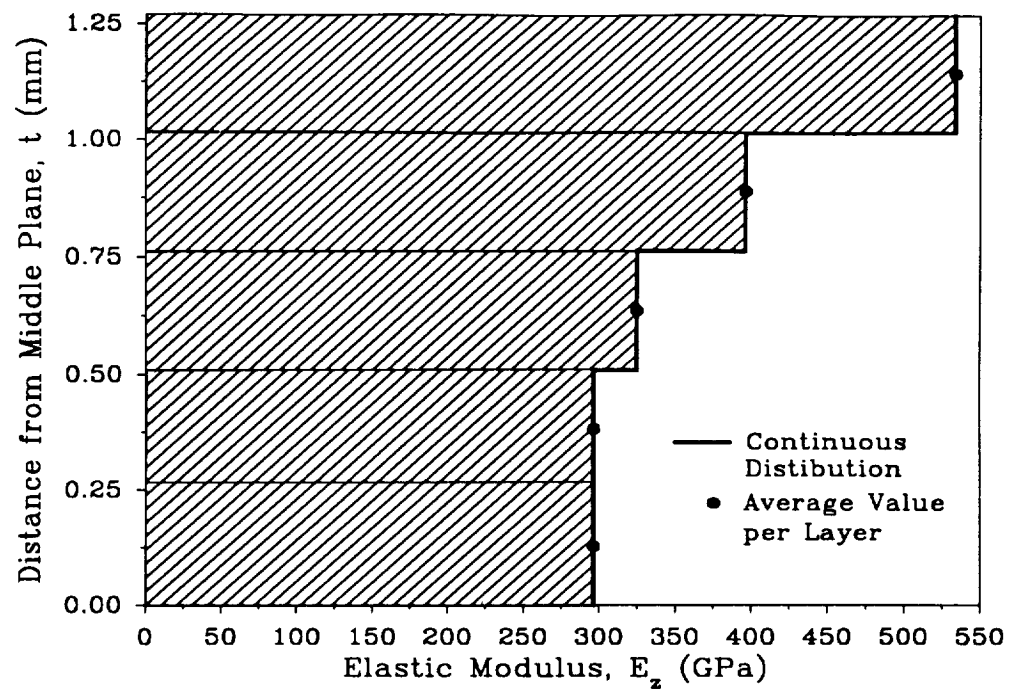


FIG. 145. Variation of Through-Thickness Modulus with Distance from Middle Plane

8. FAILURE SURFACES FOR SR-200 BERYLLIUM SHEET STRUCTURES

8.1 CLOSURE AND CONVEXITY OF FAILURE SURFACES

The new criterion for failure prediction described in chapter 3 requires that both conditions of closure and convexity are met. This chapter describes the process used to check and modify the coefficients of the failure criterion so that the failure surface satisfies these conditions for SR-200 beryllium. A number of failure surfaces which describe failure envelopes are shown for illustration purposes.

8.1.1 Closure of a Failure Surface

In-plane interaction coefficients F_{12} , F_{112} , F_{122} , F_{166} , and F_{266} that are determined in chapter 6 for beryllium sheet material using least-squares interpolation satisfy all conditions set by the new criterion in section 3.2 and, thus, no modification of their magnitude is necessary. On the other hand, interaction coefficients F_{13} , F_{113} , F_{133} , F_{144} , and F_{244} do not satisfy the closure conditions found in the same section. This is done using a FORTRAN code, named CHECK, that examines all conditions of closure. Coefficients F_{23} , F_{223} , F_{233} , F_{255} , and F_{355} also violate closure conditions. A scheme is needed that establishes functionals which yield an appropriate set of coefficients that satisfies all conditions of closure.

As an example, consider the set of coefficients F_{13} , F_{113} , F_{133} , F_{144} , and F_{244} . The failure criterion first calls for an estimate of the normal interaction coefficients. These coefficients are only functions of the normal stresses at failure excluding uniaxial stress situations. Using the experimental data from chapter 6 and employing a least-squares fit, preliminary coefficients of Eqs. 232-236 are determined. Subsequently, the magnitude of these coefficients is altered using CHECK that tests for satisfaction of all necessary closure conditions defined in sections 3.1 and 3.2. The program initially reads ultimate stress data for each set of coefficients and prepares matrices in a format suitable for LISP that are, subsequently, employed by the mathematical package MACSYMA for determination of the unknown coefficients using least-squares. It should be noted that data for the coefficients from section 6.3 involve both normal and normal-shear interaction coefficients. Initially, however, the criterion for closure requires estimation of the normal interaction coefficients. Thus, partitioning of each data matrix is employed to accomplish this task. If the new set of normal interaction coefficients does not satisfy the necessary conditions the same technique is repeated in an iterative manner until all conditions are met.

Once the normal interaction coefficients have been determined, a second functional, corresponding to Eq. 199, is defined that yields a set of non-linear polynomial equations. These equations are solved simultaneously using MACSYMA to determine the final normal-shear interaction coefficients. CHECK prepares the matrices necessary to establish the remaining coefficients in a manner similar to that described for the normal interaction coefficients. Subsequently, these coefficients are checked for closure. In the event that closure is not obtained, the program alerts the user as to which coefficient and what condition of closure is violated. In this case, necessary conditions for closure are appended to the functional in the form of Lagrange constraints. Minimization of the new functional yields a number of equations that are solved simultaneously. Thus, a new set of normal-interaction coefficients is established. Closure conditions are checked and in the event that not all conditions are satisfied the functional is modified again so as to accommodate the necessary conditions for closure. This procedure is repeated until closure is accomplished for all normal-shear interaction coefficients.

As an example, consider the case of closure for the normal interaction coefficients F_{13} , F_{113} , F_{133} . The magnitudes of these coefficients are given by Eqs. 239-241 of chapter 6. They are presented in a matrix form as follows

$$\begin{bmatrix} F_{13} \\ F_{113} \\ F_{133} \end{bmatrix} = \begin{bmatrix} 4.48 \times 10^{-6} \text{ MPa}^{-2} \\ 1.81 \times 10^{-9} \text{ MPa}^{-3} \\ 1.96 \times 10^{-9} \text{ MPa}^{-3} \end{bmatrix} \dots\dots\dots (279)$$

Since these coefficients do not satisfy the conditions of closure, the magnitude of each coefficient is modified via CHECK in order to meet all necessary conditions. For this case, eight iterations are needed to accomplish the task. The final result yields the following coefficients:

$$\begin{bmatrix} F_{13} \\ F_{113} \\ F_{133} \end{bmatrix} = \begin{bmatrix} -2.15 \times 10^{-7} \text{ MPa}^{-2} \\ 2.55 \times 10^{-10} \text{ MPa}^{-3} \\ 1.74 \times 10^{-10} \text{ MPa}^{-3} \end{bmatrix} \dots\dots\dots (280)$$

8.1.2 Convexity of a Failure Surface

Although all normal and interaction coefficients satisfy requirements for closure as defined in sections 3.1 and 3.2, convexity of the generalized failure surface may not be satisfied. To ensure that convexity is satisfied, all coefficients, interaction and normal, need to satisfy certain relations. For a surface to be convex the equation of the surface must be either positive definite or positive semi-definite (Thorpe 1979). For this condition to be

satisfied, it is sufficient to show that the determinant of the failure surface function is greater than or equal to zero. Due to the fact that the failure surface incorporates second, fourth, and sixth-order tensors it is required that the determinant of each individual tensor is greater than or equal to zero:

$$Det[F_i] \geq 0 \dots\dots\dots (281)$$

$$Det[F_{ij}] \geq 0 \dots\dots\dots (282)$$

$$Det[F_{ijk}] \geq 0 \dots\dots\dots (283)$$

where $i, j, k = 1, 2, \dots, 6$. It is stressed that the convexity conditions of the polynomial can be checked in either the uncontracted or contracted configuration. The contracted configuration is chosen for this discussion.

The determinant of each tensor polynomial is as follows (Wu and Scheublein 1974; Bradley 1975):

$$Det[F_i] = \begin{bmatrix} F_1 & 0 & 0 & 0 & 0 & 0 \\ 0 & F_2 & 0 & 0 & 0 & 0 \\ 0 & 0 & F_3 & 0 & 0 & 0 \\ 0 & 0 & 0 & F_4 & 0 & 0 \\ 0 & 0 & 0 & 0 & F_5 & 0 \\ 0 & 0 & 0 & 0 & 0 & F_6 \end{bmatrix} \dots\dots\dots (284)$$

$$Det[F_{ij}] = \begin{bmatrix} F_{11} & F_{12} & F_{13} & 0 & 0 & 0 \\ F_{12} & F_{22} & F_{23} & 0 & 0 & 0 \\ F_{13} & F_{23} & F_{33} & 0 & 0 & 0 \\ 0 & 0 & 0 & F_{44} & 0 & 0 \\ 0 & 0 & 0 & 0 & F_{55} & 0 \\ 0 & 0 & 0 & 0 & 0 & F_{66} \end{bmatrix} \dots\dots\dots (285)$$

$$Det[F_{ijk}] = Det[F_{1jk}]Det[F_{2jk}]Det[F_{3jk}]Det[F_{4jk}]Det[F_{5jk}]Det[F_{6jk}] \dots\dots\dots (286)$$

It should be noted that Eq. 284 is automatically satisfied since F_4 , F_5 , and F_6 are zero for orthotropic material. The determinants of all sub-matrices of Eq. 284 should also satisfy Eq. 281. This is achieved if all non-zero components of the contracted second-order tensor in Eq. 284 are positive:

$$F_i \geq 0 \quad \text{For } i = 1, 2, 3 \dots\dots\dots (287)$$

From Eq. 285 the following conditions cause the failure surface to become convex (Tsai and Wu 1974; Karr et al. 1983; and Bradley 1975):

$$F_{ii} \geq 0 \quad \text{For } i = 1, 2, \dots, 6 \dots\dots\dots (288)$$

$$F_{ii}F_{jj} - F_{ij}^2 \geq 0 \quad \text{For } i, j = 1, 2, 3, \dots, 6; j \neq i \dots\dots\dots (289)$$

$$\text{Det}[F_{ij}] = \sum (-1)^{\sigma(\pi)} F_{i_1} F_{2_j} \dots F_{6_n} \geq 0 \quad \text{For } i, j, \dots, n = 1, 2, 3, \dots, 6 \dots\dots\dots (290)$$

where $\sigma(\pi)$ is an index which takes the value of 1 for even permutations, the value of -1 for odd permutations of the numbers 1 through 6, and there is no summation of repeated indices (Bradley 1975).

For convexity to be satisfied at all levels, that is, for a surface to be convex for any combination of stress components, it is necessary and sufficient that the cubic-order tensor determinants satisfy Eq. 286 for the overall determinant, $\text{Det}[F_{ijk}]$, as well as for any combination of product of the sub-determinants (Thorpe 1979). For example, if a state of stress is imposed on a structure in such a manner that only σ_1 , σ_2 , σ_3 , and σ_4 are present, then both the matrix and sub-matrices should satisfy Eq. 286. The determinant of F_{ijk} automatically satisfies this condition since $\text{Det}[F_{5jk}]$ and $\text{Det}[F_{6jk}]$ are zero (Wu and Scheublein 1974). Sub-matrix determinants should satisfy the relations

$$\text{Det}[F_{1jk}] \text{Det}[F_{2jk}] \text{Det}[F_{3jk}] \text{Det}[F_{4jk}] \geq 0 \dots\dots\dots (291)$$

$$\text{Det}[F_{1jk}] \text{Det}[F_{2jk}] \text{Det}[F_{3jk}] \geq 0 \dots\dots\dots (292)$$

$$\text{Det}[F_{1jk}] \text{Det}[F_{2jk}] \text{Det}[F_{4jk}] \geq 0 \dots\dots\dots (293)$$

$$\text{Det}[F_{1jk}] \text{Det}[F_{3jk}] \text{Det}[F_{4jk}] \geq 0 \dots\dots\dots (294)$$

$$\text{Det}[F_{2jk}] \text{Det}[F_{3jk}] \text{Det}[F_{4jk}] \geq 0 \dots\dots\dots (295)$$

$$\text{Det}[F_{1jk}] \text{Det}[F_{2jk}] \geq 0 \dots\dots\dots (296)$$

$$\text{Det}[F_{1jk}] \text{Det}[F_{3jk}] \geq 0 \dots\dots\dots (297)$$

$$\text{Det}[F_{1jk}] \text{Det}[F_{4jk}] \geq 0 \dots\dots\dots (298)$$

$$\text{Det}[F_{2jk}] \text{Det}[F_{3jk}] \geq 0 \dots\dots\dots (299)$$

$$\text{Det}[F_{2jk}] \text{Det}[F_{4jk}] \geq 0 \dots\dots\dots (300)$$

$$Det[F_{3jk}]Det[F_{4jk}] \geq 0 \dots\dots\dots (301)$$

These equations are satisfied when each sub-determinant is either positive or zero. For the case of cross-rolled beryllium sheet, an orthotropic material, determinants of the cubic-order coefficients are as follows:

$$Det[F_{1jk}] = \begin{bmatrix} 0 & F_{112} & F_{113} & 0 & 0 & 0 \\ F_{112} & F_{122} & 0 & 0 & 0 & 0 \\ F_{113} & 0 & F_{133} & 0 & 0 & 0 \\ 0 & 0 & 0 & F_{144} & 0 & 0 \\ 0 & 0 & 0 & 0 & F_{155} & 0 \\ 0 & 0 & 0 & 0 & 0 & F_{166} \end{bmatrix} \dots\dots\dots (302)$$

$$Det[F_{2jk}] = \begin{bmatrix} F_{112} & F_{122} & 0 & 0 & 0 & 0 \\ F_{122} & 0 & F_{223} & 0 & 0 & 0 \\ 0 & F_{223} & F_{233} & 0 & 0 & 0 \\ 0 & 0 & 0 & F_{244} & 0 & 0 \\ 0 & 0 & 0 & 0 & F_{255} & 0 \\ 0 & 0 & 0 & 0 & 0 & F_{266} \end{bmatrix} \dots\dots\dots (303)$$

$$Det[F_{3jk}] = \begin{bmatrix} F_{113} & 0 & F_{133} & 0 & 0 & 0 \\ 0 & F_{223} & F_{233} & 0 & 0 & 0 \\ F_{133} & F_{233} & 0 & 0 & 0 & 0 \\ 0 & 0 & 0 & F_{344} & 0 & 0 \\ 0 & 0 & 0 & 0 & F_{355} & 0 \\ 0 & 0 & 0 & 0 & 0 & F_{366} \end{bmatrix} \dots\dots\dots (304)$$

$$Det[F_{4jk}] = \begin{bmatrix} 0 & 0 & 0 & F_{144} & 0 & 0 \\ 0 & 0 & 0 & F_{244} & 0 & 0 \\ 0 & 0 & 0 & F_{344} & 0 & 0 \\ 0 & 0 & 0 & F_{344} & 0 & 0 \\ F_{144} & F_{244} & F_{344} & 0 & 0 & 0 \\ 0 & 0 & 0 & 0 & 0 & 0 \end{bmatrix} \dots\dots\dots (305)$$

$$Det[F_{5jk}] = \begin{bmatrix} 0 & 0 & 0 & F_{155} & 0 & 0 \\ 0 & 0 & 0 & F_{255} & 0 & 0 \\ 0 & 0 & 0 & F_{355} & 0 & 0 \\ 0 & 0 & 0 & 0 & 0 & 0 \\ F_{155} & F_{255} & F_{355} & 0 & 0 & 0 \\ 0 & 0 & 0 & 0 & 0 & 0 \end{bmatrix} \dots\dots\dots (306)$$

$$Det[F_{6jk}] = \begin{bmatrix} 0 & 0 & 0 & 0 & 0 & F_{166} \\ 0 & 0 & 0 & 0 & 0 & F_{266} \\ 0 & 0 & 0 & 0 & 0 & F_{366} \\ 0 & 0 & 0 & 0 & 0 & 0 \\ 0 & 0 & 0 & 0 & 0 & 0 \\ F_{166} & F_{266} & F_{366} & 0 & 0 & 0 \end{bmatrix} \dots\dots\dots (307)$$

Determinants of F_{4jk} , F_{5jk} , and F_{6jk} are equal to zero. Consequently, the determinant of the global tensorial matrix (Eq. 283) is positive semi-definite since it is equal to zero. The requirement that determinants of F_{1jk} , F_{2jk} , and F_{3jk} be positive semi-definite introduces conditions of convexity. These conditions are expressed by the following equations:

$$-(F_{133}F_{112}^2 + F_{122}F_{113}^2)F_{144}F_{155}F_{166} \geq 0 \dots\dots\dots (308)$$

$$-(F_{112}F_{223}^2 + F_{233}F_{122}^2)F_{244}F_{255}F_{266} \geq 0 \dots\dots\dots (309)$$

$$-(F_{223}F_{133}^2 + F_{113}F_{233}^2)F_{344}F_{355}F_{366} \geq 0 \dots\dots\dots (310)$$

Program CHECK warns the user of possible conflicts that may be associated with the convexity conditions and indicates which coefficients need to be modified.

8.2 Failure Surfaces

Combining the results obtained from chapters 5, 6, and 7 and assuming that hydrostatic pressure does not cause failure, it is now possible to define the failure surface criterion for cross-rolled beryllium sheet, SR-200 specification. This is obtained by numerical substitution of the principal and interaction coefficients into Eq. 61 and results in the following equation:

$$\begin{aligned} & (2.44\sigma_1 + 2.31\sigma_2 + 29.33\sigma_3) \times 10^{-3} (ksi^{-1}) + [1.35\sigma_1^2 + 1.25\sigma_2^2 + 1.33\sigma_3^2 + 1.67\sigma_4^2 \\ & + 1.39\sigma_5^2 + 5.17\sigma_6^2 - 2(0.61\sigma_1\sigma_2 + 0.10\sigma_1\sigma_3 + 0.62\sigma_2\sigma_3)] \times 10^{-4} (ksi^{-2}) \\ & + 3(-2.26\sigma_1^2\sigma_2 + 0.84\sigma_1^2\sigma_3 - 0.71\sigma_1\sigma_2^2 - 0.56\sigma_2^2\sigma_3 - 0.55\sigma_1\sigma_3^2 - 0.49\sigma_2\sigma_3^2 \\ & + 0.19\sigma_1\sigma_4^2 - 1.10\sigma_2\sigma_4^2 + 0.45\sigma_3\sigma_4^2 - 1.42\sigma_1\sigma_5^2 - 0.21\sigma_2\sigma_5^2 - 2.19\sigma_3\sigma_5^2 \\ & - 3.16\sigma_1\sigma_6^2 - 3.16\sigma_2\sigma_6^2 + 0.00\sigma_3\sigma_6^2) \times 10^{-7} (ksi^{-3}) = 1 \end{aligned} \quad (311)$$

Although the failure surface for beryllium sheet is a function of six stress components, three normal and three shearing stresses mutually perpendicular to each other, the graphical representation is limited to a maximum of three components of stress at a time. For the purpose of this study, graphical representations of a maximum of, at most,

three components of stress are presented. Moreover, a total of twenty $[6!/(2 \times 3 \times 3!)]$ possible combinations can be obtained. However, some of these combinations are unlikely to occur. For example, a beryllium plate structure is unlikely to be designed to withstand out-of-plane shear and in-plane normal stresses such as $(\sigma_1, \sigma_4, \sigma_5)$, or $(\sigma_2, \sigma_4, \sigma_5)$, or $(\sigma_3, \sigma_4, \sigma_6)$.

For illustration purposes, a number of failure surfaces are presented that involve various combinations of stress components. A total of six failure surfaces are plotted. These surfaces are shown by means of gray-scale fringe plots and contour plots in Figs. 146 through 151. The failure surface for any other combination of stress components can be plotted provided that the appropriate equation is extracted from the generalized Eq. 311. This is done by setting equal to zero the components of stress that are not considered. As stated earlier, for plotting purposes only three components of stress can be considered at a time in order to form the appropriate failure surface.

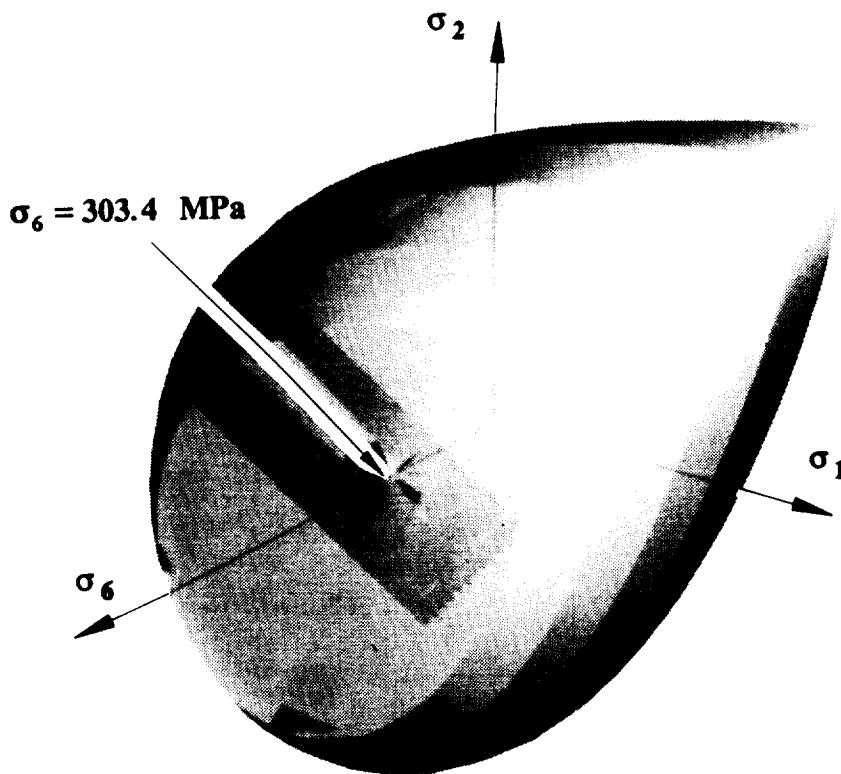


FIG. 146 Failure Surface for $\sigma_1, \sigma_2, \sigma_6$

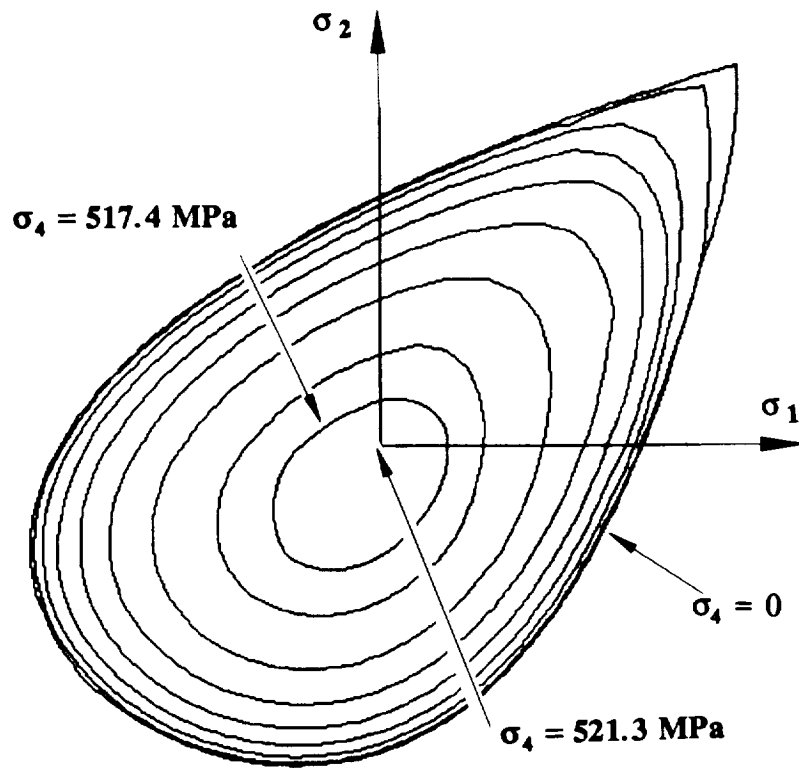


FIG. 147 Contours of Failure Surface for σ_1 , σ_2 , σ_4

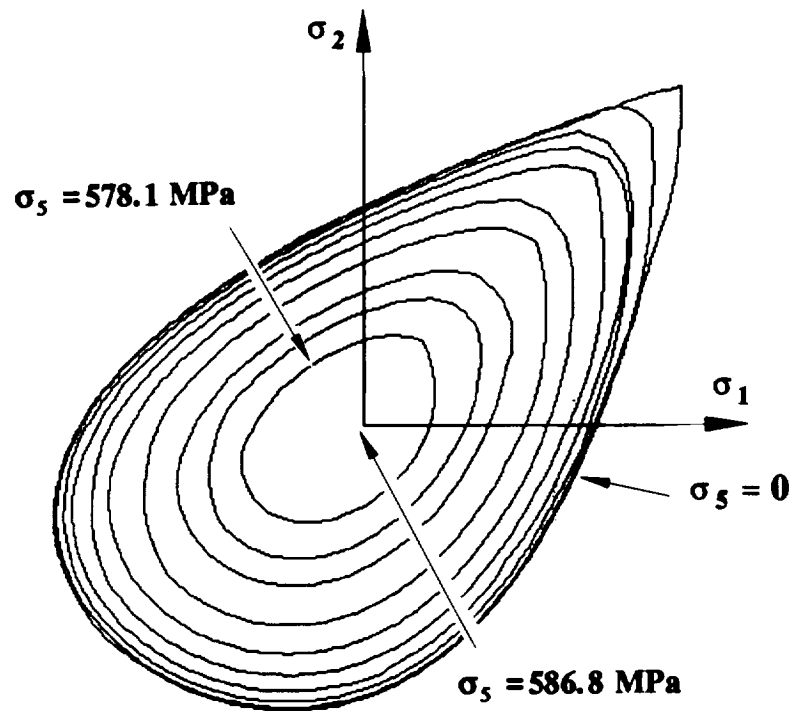


FIG. 148 Contours of Failure Surface for σ_1 , σ_2 , σ_5

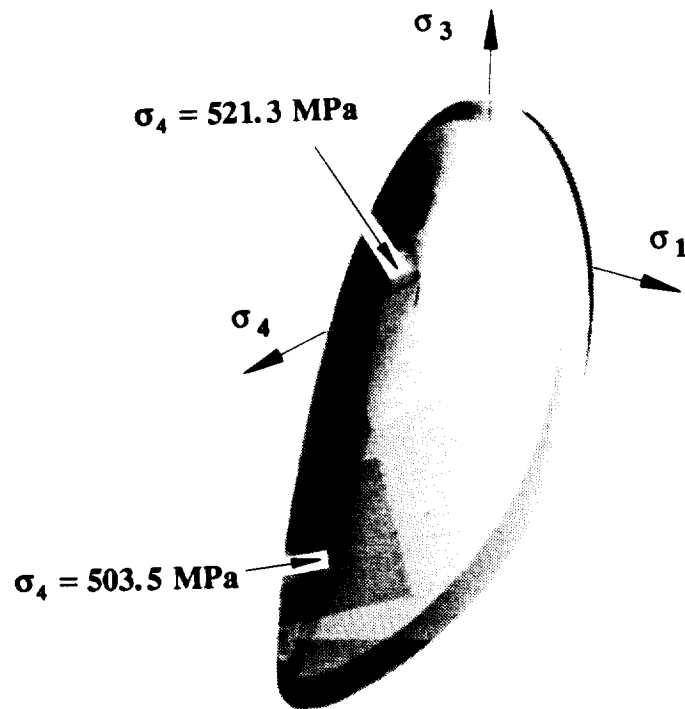


FIG. 149 Failure Surface for σ_1 , σ_3 , σ_4

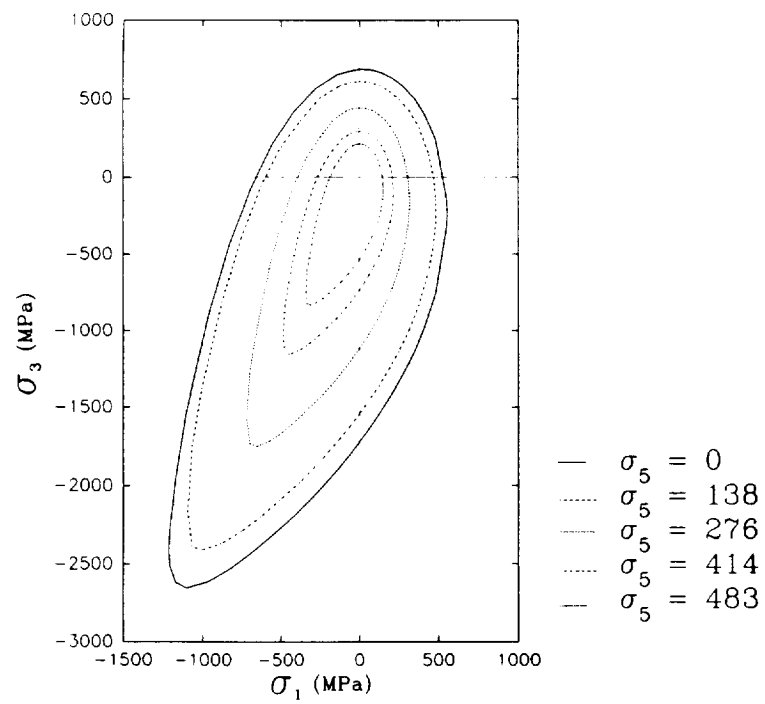


FIG 150 Failure Surface for σ_1 , σ_3 , σ_5

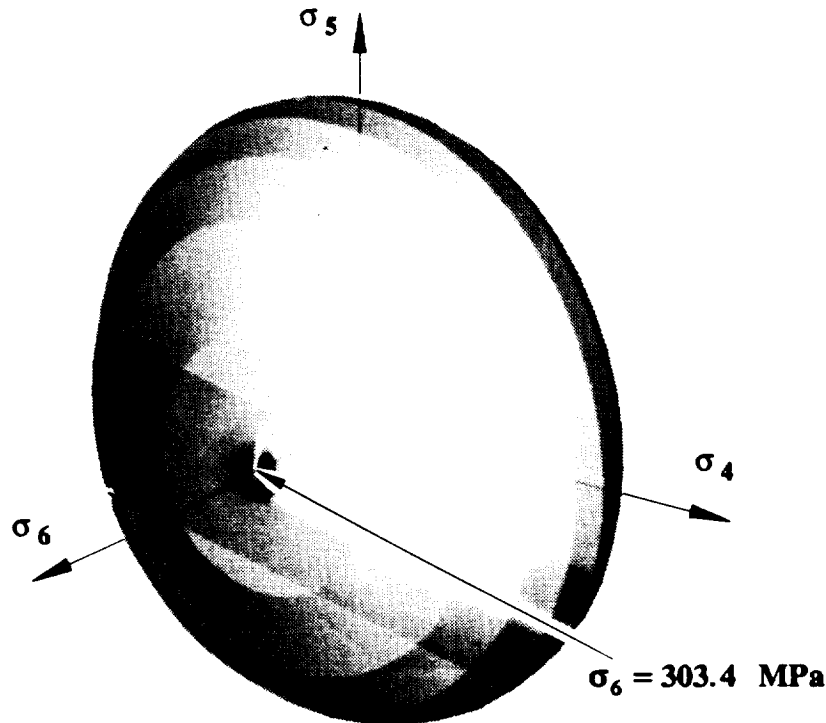


FIG. 151 Failure Surface for σ_4 , σ_5 , σ_6

8.2.1 In-Plane State of Stress (σ_1 , σ_2 , and σ_6)

The failure surface shown in Fig. 146 is valid for in-plane normal and shearing stresses σ_1 , σ_2 , and σ_6 , respectively. It is defined by the relation

$$\begin{aligned} & (2.44\sigma_1 + 2.31\sigma_2) \times 10^{-3} (\text{ksi}^{-1}) + [1.35\sigma_1^2 + 1.25\sigma_2^2 + 5.17\sigma_6^2 \\ & - 2(0.61\sigma_1\sigma_2)] \times 10^{-4} (\text{ksi}^{-2}) \\ & + 3(-2.26\sigma_1^2\sigma_2 - 0.71\sigma_1\sigma_2^2 - 3.16\sigma_1\sigma_6^2 - 3.16\sigma_2\sigma_6^2) \times 10^{-7} (\text{ksi}^{-3}) = 1 \end{aligned} \quad (312)$$

The surface is symmetric about the σ_1 - σ_2 plane. This is due to the orthotropic nature of beryllium, i.e., positive and negative shearing strengths (σ_6) have the same absolute value. It should be noted from Fig. 146 that this failure surface is nearly symmetric with respect to the plane defined by the relation

$$\sigma_1 - \sigma_2 = 0 \quad (313)$$

Moreover, the major interaction zone of the normal stresses σ_1 and σ_2 occurs in the positive quadrant of the failure surface, i.e., the tension-tension region.

8.2.2 Combinations of In-Plane Normal Stresses (σ_1, σ_2) and Out-of-Plane Shearing Stress (σ_4 or σ_5)

The two failure surfaces shown in Figs. 147 and 148 are those associated with two in-plane normal stresses and an out-of-plane shearing component of stress σ_4 and σ_5 , respectively. The equations of these surfaces are

$$\begin{aligned} & (2.44\sigma_1 + 2.31\sigma_2) \times 10^{-3} (ksi^{-1}) \\ & + [1.35\sigma_1^2 + 1.25\sigma_2^2 + 1.67\sigma_4^2 - 2(0.61\sigma_1\sigma_2)] \times 10^{-4} ksi^{-2} \dots\dots\dots (314) \\ & + 3(-2.26\sigma_1^2\sigma_2 - 0.71\sigma_1\sigma_2^2 + 0.19\sigma_1\sigma_4^2 - 1.10\sigma_2\sigma_4^2) \times 10^{-7} (ksi^{-3}) = 1 \end{aligned}$$

$$\begin{aligned} & (2.44\sigma_1 + 2.31\sigma_2) \times 10^{-3} (ksi^{-1}) + [1.35\sigma_1^2 + 1.25\sigma_2^2 + 1.39\sigma_5^2 - 2(0.61\sigma_1\sigma_2)] \\ & \times 10^{-4} (ksi^{-2}) + 3(-2.26\sigma_1^2\sigma_2 - 0.71\sigma_1\sigma_2^2 - 1.42\sigma_1\sigma_5^2 - 0.21\sigma_2\sigma_5^2) \\ & \times 10^{-7} (ksi^{-3}) = 1 \dots\dots\dots (315) \end{aligned}$$

As in the case of Eq. 312, the shapes defined by these curves are nearly symmetric with respect to the σ_1 - σ_2 plane and the interaction of terms is largely due to the relationship between the normal stresses in the tensile region of the failure envelope.

8.2.3 Combination of Normal Stresses σ_1, σ_3 and Planar Shearing Stress σ_4

Failure surfaces presented by recent theories deal mainly with in-plane stress or strain failure. Experimental work for cross-rolled beryllium sheet described in chapters 4, 5, 6, and 7 permits the determination of failure surfaces that incorporate the through-thickness normal and shearing stress effects. One such surface involves stress components $\sigma_1, \sigma_3, \sigma_4$, where σ_1 and σ_3 are normal stresses and σ_4 is the shearing stress associated with the (1-3) plane. Thus, Eq. 311 becomes

$$\begin{aligned} & (2.44\sigma_1 + 29.33\sigma_3) \times 10^{-3} (ksi^{-1}) + [1.35\sigma_1^2 + 1.33\sigma_3^2 + 1.67\sigma_4^2 - 2(0.10)\sigma_1\sigma_3] \\ & \times 10^{-4} (ksi^{-2}) + 3(0.84\sigma_1^2\sigma_3 - 0.55\sigma_1\sigma_3^2 + 0.19\sigma_1\sigma_4^2 + 0.45\sigma_3\sigma_4^2) \times 10^{-7} (ksi^{-3}) = 1 \dots\dots\dots (316) \end{aligned}$$

As is the case for Eq. 311, the shape defined by the surface is nearly symmetrical with respect to the σ_1 - σ_3 plane. However, the interaction of stress components shifts to the compression-compression quadrant of the failure surface (Fig. 149). From the failure surface it can be deduced that the material withstands much higher compressive loadings in the through-thickness direction and directions associated with in-plane axes (1-3) compared to tensile loadings for the same orientations.

8.2.4 Combination of Normal Stresses σ_2 , σ_3 and Planar Shearing Stress σ_5

Another combination that considers an out-of-plane component of shearing stress in conjunction with in-plane components of normal stress is given by

$$\begin{aligned} & (2.31\sigma_2 + 29.33\sigma_3) \times 10^{-3} (\text{ksi}^{-1}) + [1.25\sigma_2^2 + 1.33\sigma_3^2 + 1.39\sigma_5^2 - 2(0.62\sigma_2\sigma_3)] \\ & \times 10^{-4} (\text{ksi}) + 3(0.84\sigma_1^2\sigma_3 - 0.55\sigma_1\sigma_3^2 - 1.42\sigma_1\sigma_5^2) \times 10^{-7} (\text{ksi}^{-3}) = 1 \end{aligned} \quad \dots (317)$$

This stress combination is similar to the one described in section 8.1.3 in that it considers two normal stress components (σ_2 and σ_3) and the shearing stress associated with the (2-3) plane, σ_5 . Again, the interaction of stress components shifts to the compression-compression quadrant of the failure surface and the material appears to be able to withstand higher compressive than tensile stress conditions (see Fig. 150).

Failure in the tension-tension zone is limited due to the fact that the tensile strength of the material in the out-of-plane direction is considerably lower than the respective tensile strength in the same direction. In addition, considerable interaction of the normal and shearing stress components is not evident in this region.

8.2.5 Combination of Shearing Stresses σ_4 , σ_5 , and σ_6

Although, it is very unlikely for a stress combination that involves only the three mutually perpendicular shearing stress components to occur, the failure surface defined from such a state of stress is presented for the sake of illustration. The equation required to graph the failure surface for shearing components is given by the relation:

$$(1.67\sigma_4^2 + 1.39\sigma_5^2 + 5.17\sigma_6^2) \times 10^{-4} (\text{ksi}^{-2}) = 1 \quad \dots (318)$$

The surface described by this equation is that of an ellipsoid (Fig. 151). It should be noted that the shearing stress failure equation does not involve any interaction coefficients among the three components of shearing stresses, i.e., it is assumed that for an orthotropic material such as cross-rolled beryllium sheet the shearing stresses act independently.

9. NUMERICAL MODELING AND FAILURE PREDICTION FOR SR-200 BERYLLIUM STRUCTURES

9.1 INTRODUCTION

The current study of cross-rolled beryllium sheets incorporates numerical simulation of the experimental set-ups for establishing the failure criterion. Numerical simulation is also used to predict the state of stress for structures subjected to a variety of loadings. This simulation is done mainly for three reasons: (a) to optimize the geometrical configuration of the experimental specimens such that a minimum amount of material is used and, thus, to reduce manufacturing costs; (b) to check the validity of the desired state of stress for each experiment, especially in cases where two or more stress components are involved; and (c) to analyze cross-rolled beryllium structures under either a simple or complex static state of stress, and predict ultimate loads and stresses that the structure can withstand.

Discussion in this chapter focuses on details of the different types of finite elements incorporated in the numerical models and the failure prediction scheme used for SR-200 beryllium structures. Comparison of numerical simulation and experimental results for several structures demonstrates accuracy of the failure criterion.

9.2 NUMERICAL MODEL SPECIFICATION

All finite element models are prepared using an engineering graphics package, PATRAN-II (1991). Pre-processing involves generation of the physical dimensions of the structure under consideration, finite element meshing with elements chosen from an element library available in the package, implementing necessary and essential (displacement and load) boundary conditions, optimizing the model and reducing central processing unit (CPU) time using techniques such as the root-mean-square bandwidth, and translating the model into an input file that can be used with a finite element commercial code for the actual analysis.

The FEA package used to analyze all numerical models for cross-rolled beryllium sheet structures is ABAQUS, a non-linear, general-purpose implicit FEA code. It allows for incorporation of user subroutines for pre-processing, analysis, or post-processing modifications. ABAQUS provides a very wide library of elements for use in structural analysis as well as specialized elements, such as interface elements, for analyzing contact problems or linking solid and plate elements.

A variety of elements is used for the numerical analysis of beryllium structures. The choice of elements for each structure is based primarily on the state of stress, geometry of the structure, and accuracy required. Fig. 152 shows each type of element that is used and the corresponding nomenclature of ABAQUS. In addition, for the sake of completeness the degrees-of-freedom are listed for each element.

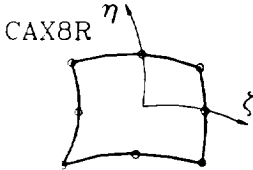
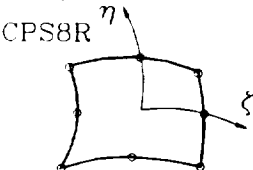
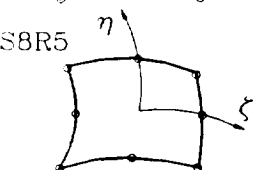
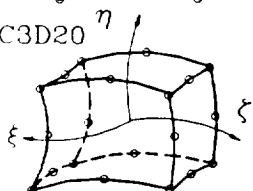
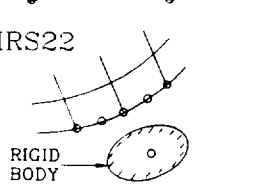
ELEMENT TYPE	ELEMENT DESCRIPTION	DEGREES OF FREEDOM
 CAX8R	AXISYMMETRIC ELEMENT 8 NODE QUADRATIC REDUCED INTEGRATION	u_r, u_θ
 CPS8R	PLANE STRESS ELEMENT 8 NODE QUADRATIC REDUCED INTEGRATION	u_x, u_y
 S8R5	GENERAL SHELL ELEMENT 8 NODE QUADRATIC REDUCED INTEGRATION	u_x, u_y, u_z Φ_x, Φ_y
 C3D20	3-D CONTINUUM ELEMENT 20 NODE QUADRATIC BRICK	u_x, u_y, u_z
 IRS22 RIGID BODY	INTERFACE ELEMENT (NODE AND RIGID BODY) 2 NODE LINEAR	u_x, u_y, u_z Φ_x, Φ_y, Φ_z

FIG. 152. Finite Elements Used for Numerical Simulation

The material properties for cross-rolled beryllium sheet used in all analyses are those discussed in chapters 4 and 7. It should be noted that initially the material properties incorporated in the numerical models were those reported by Fenn et al. (1967). Although these properties adequately describe the behavior of this material for relatively simple states of stress, i.e., uniaxial and true biaxial, they fail to yield satisfactory results for a cross-rolled

beryllium structure subjected to a complex state of stress, e.g., normal through-thickness stress with in-plane tension and shearing stresses acting simultaneously.

9.3 AUTOMATION OF NUMERICAL SIMULATION

Closed-form solutions for nonlinear orthotropic plate problems are rare and extremely limited in generality. Also, for structures under complex loading conditions, closed-form solutions are usually untenable. For these reasons finite element analysis (FEA) is employed in this study to predict stresses and, thereby, failure loads. This method of analysis offers the generality needed to model structures with complex geometries, as well as the flexibility to simulate non-homogeneous orthotropic material and behavior into the range of nonlinear geometry.

ABAQUS yields stress levels at all salient locations within a continuum. This numerical data is used in conjunction with the high-order criterion to predict failure. The general procedure is to iteratively adjust the load. Each nodal point in the structure is checked after each analysis for exceeding limits of the failure criterion (see Fig. 153). If stresses at all locations in the structure due to a given load render the left side of Eq. 311 less than unity, it is predicted that the component does not fail. In this case the load is increased and the finite element analysis is repeated. If the state of stress at one or more nodal points renders the right side of Eq. 311 greater than unity, it is predicted that the stresses in the component exceed failure stresses. In this case the load is decreased and the analysis is repeated. The failure criterion is satisfied when the left side of Eq. 311 is within a specified tolerance of unity, at one or more points. Thus, failure of the structure is predicted to occur and the analysis is terminated.

To begin the process, the user is requested to supply the name of the ABAQUS input file. The magnitude of load for this first analysis is usually chosen to induce stresses that are well within the linear elastic range of the material. After the first analysis, the program updates the load levels of the input file in the following manner: It first checks, using Eq. 311, the value of the stress envelope at each node, $f(\sigma_j)$; each component of load is then increased or decreased by the factor

$$df = \frac{1 - f(\sigma_j)}{f(\sigma_j)} \dots \dots \dots (319)$$

Note that this equation assumes a linear relationship between the load and stresses and does not correct for non-linear behavior. The process is repeated until the term $1 - f(\sigma_j)$ is within $\pm 1\%$ for one or more nodes, and stresses at the remaining nodes are within the failure

envelope. This load level is predicted to cause failure. For example, consider a structure that has a concentrated load of 4.45 kN (1.0 kip) and a uniform through-thickness pressure of 689.5 MPa (100 psi). Suppose that the initial analysis check yields a factor $f(\sigma_j)$ of 0.84. In this case the updated load levels are 5.30 kN (1.19 kip) and 820.8 MPa (119.0 psi) for the concentrated force and uniform pressure, respectively. For loads at multiple nodes, the magnitude of each load is prorated according to the last incremental load state. If more or less precision is desired the tolerance for the term $1-f(\sigma_j)$ can be easily modified to accommodate the new requirement.

This procedure is implemented on a CRAY/YMP 2/116 running UNICOS 6.0. A batch file obtains user input and controls two programs: ABAQUS version 4.9 and a special purpose FORTRAN program. Fig. 153 illustrates the control that is applied by a custom command procedure, also known as a script file. The procedure first obtains the necessary user input data for ABAQUS, such as the name of the FEA model and starts the analysis by ABAQUS. After the analysis is complete the FORTRAN program checks for stresses that exceed failure, and either terminates the job or restarts ABAQUS at a new load level depending on the existence of a file named "fail.dat" that is conditionally created by the FORTRAN code.

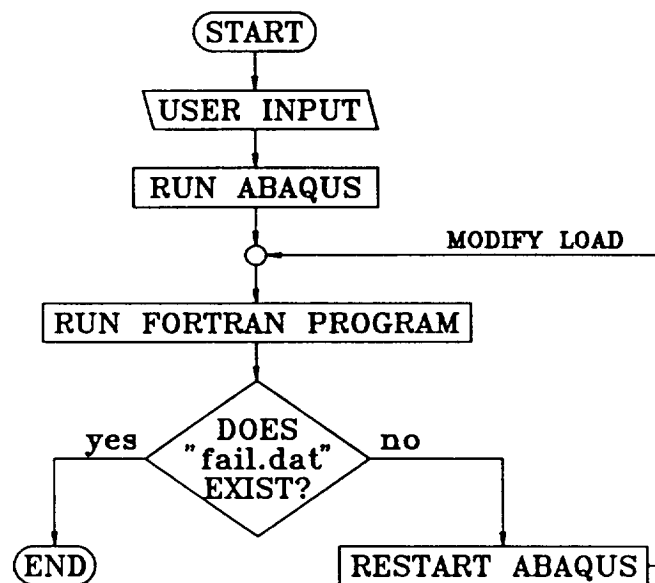


FIG. 153. Flow Chart for Batch Submission

The FORTRAN program, "cb.exe," accomplishes four functions. It reads stresses from the output file of ABAQUS, checks these stresses for exceedence of the limits of the failure criterion, reads the ABAQUS input file, and generates a revised version of the

ABAQUS input file. The flow chart in Fig. 154 illustrates the order in which the program performs each function. The FORTRAN code reads the ABAQUS output file node by node, substitutes the state of stress at each FEA node into Eq. 311, and determines whether or not the stress at any point within the body exceeds the failure criterion. It should be noted that this code can be modified such that it reads the stresses at the integration points (Gauss quadrature points) instead at the nodes. If failure has occurred the program writes a list of one or more failed nodes and their corresponding magnitude from evaluation by the failure criterion to a file named "fail.dat." If failure is not predicted the program reads the current FEA input file, modifies the magnitude of the load according to Eq. 319, and generates a new FEA input file.

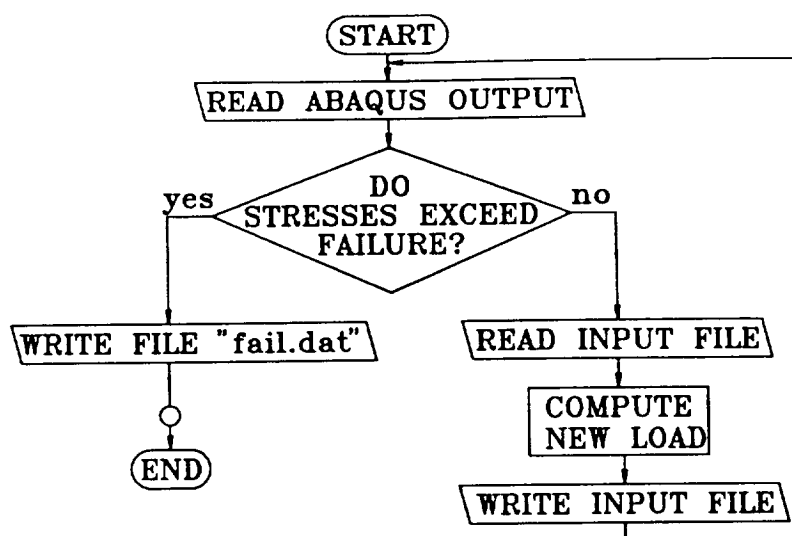


FIG. 154. Flow Chart for FORTRAN Program

An example of all computer files used in the procedure is shown in Fig. 155. This figure displays the general flow and relationship of each file. Initially, "abapp," the batch file, calls for ABAQUS to analyze the structure that is defined by the input file "example.inp." ABAQUS performs the analysis and returns three files: "example.fil," which contains displacements, strains, and stresses as well as the model's material and geometric properties in ASCII format; "example.dat," which is a text file listing model and output results; and "example.res," which is a restart file. A failure prediction check is performed by "cb.exe." If the structure fails then the conditional file "fail.dat" that lists failed nodes is created. If the structure does not fail "cb.exe" creates the restart file "res.inp" which contains an updated load history that ABAQUS uses for further analysis. The same procedure is repeated until the structure fails, i.e., for each adjusted loading case the files

"example.fil," "example.res," and "example.dat" are created and "cb.exe" checks output of the analysis for failed nodes.

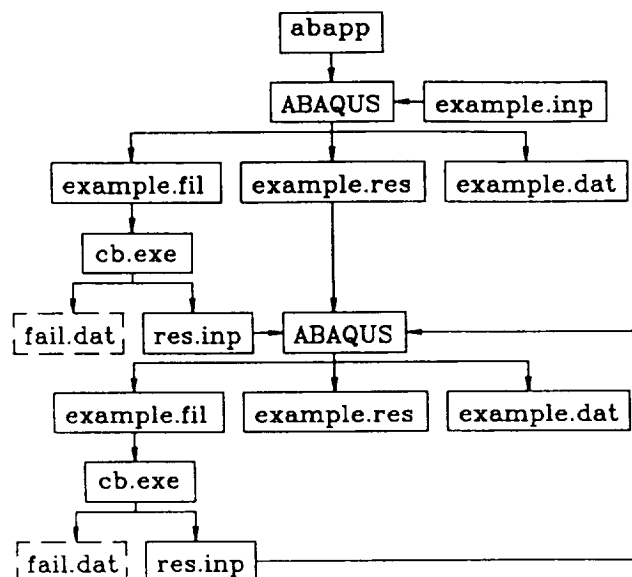


FIG. 155. Hierarchical File Sequence of Failure Prediction Scheme

Execution times vary according to the model size and the number of increments needed. For linear analysis of two-dimensional models comprised of eight-noded, quadrilateral, isoparametric elements the execution time is approximately equal to the number of increments times the time it takes for a single linear analysis. For example, if the analysis for each load increment uses two minutes of central processing units (CPU) time and it takes ten increments to predict failure, then the failure analysis takes approximately twenty minutes. For failure analysis using nonlinear geometrical simulation the program takes approximately twice as much CPU time as that required for a single linear analysis. The same pattern is observed for execution times of three-dimensional models.

9.4 VERIFICATION OF FAILURE PREDICTION

9.4.1 Plate-Plug Experiment

9.4.1.1 Description of Laboratory Experiment

In an effort to predict brittle failure of anisotropic cross-rolled beryllium sheets, a special experiment was designed to induce a complex state of stress (Papados 1991). A 38.1-mm × 38.1-mm × 2.54-mm (1.5-in. × 1.5-in. × 0.1-in.) cross-rolled beryllium SR-200 sheet was brazed to a beryllium block plug using silver foil BAg-19 brazing (see Fig. 156).

Table 11 (chapter 5) summarizes the chemical composition of the cross-rolled beryllium plate and plug. The plug was also brazed to a SS-44M-7-4 pressure fitting which, in turn, was connected to a 137.9-MPa (20.0-ksi) MTS hydraulic pressure actuator via SS-483-A-24 pressure tubing. The MTS hydraulic pressure actuator was calibrated for pressure loadings of up to 34.5 MPa (5.0 ksi) as shown in Fig. 157. To ensure safety and confine flow of hydraulic oil, the plate-plug specimen was enclosed in non-transparent tubing with Plexiglas sealing each end.

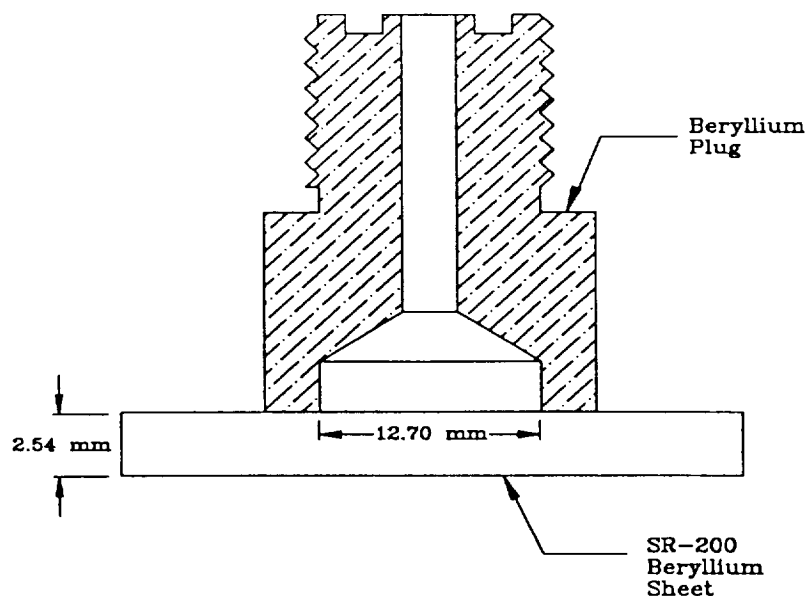


FIG. 156. Plug-Plate Arrangement

Six Micro-Measurement EA-06-031CE-350 strain gages were mounted on the cross-rolled beryllium sheet: five on the surface of the side opposite the plug and one on the plug side of the plate. Fig. 158 illustrates positions of the strain gages on the specimen. Strain gages were selected to match thermal coefficient recommendations for beryllium experiments. Moreover, this type of gage was selected due to its relatively short length and self-compensating temperature characteristics at room temperature. Gages were mounted onto the beryllium surface following procedures recommended by the gage manufacturer. Nominal resistance of the strain gage was chosen to be 350 ohms due to data acquisition requirements. LabTech Notebook, version 5 (LabTech 1987), and an interface board provide real-time data acquisition. It should be noted that eight strain gages were originally mounted on the bottom surface, but gages 1 and 8 were damaged during preliminary trial

loadings and, thus, only six were functioning at the time the structure was loaded to ultimate failure.

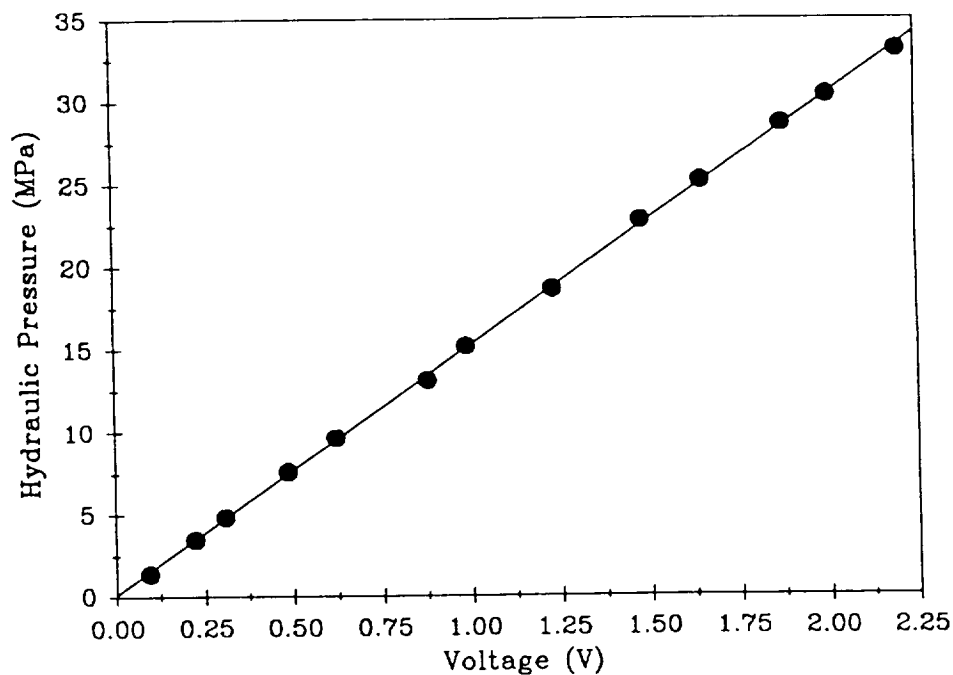


FIG. 157. Pressure Calibration of Hydraulic Actuator

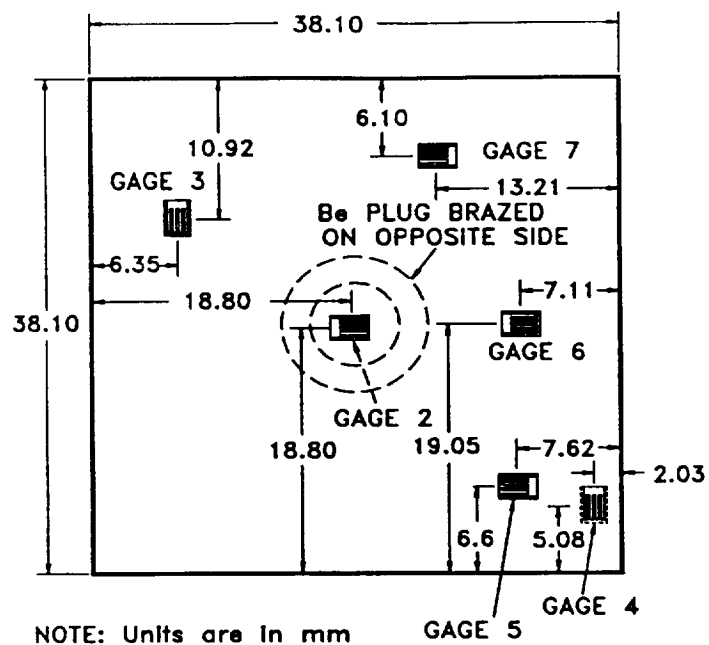


FIG. 158. Location of Strain Gages on Plate-Plug Specimen

Load was applied to the structure by increasing pressure in the hydraulic cavity at a rate of 344.8 kPa/s (50.0 psi/sec). Graphs of strain versus pressure distribution are presented in Figs. 159-161 for functioning strain gages. Normal strain in the center of the beryllium plate (Gage 2) was linear with increasing hydraulic pressure and reached a maximum of 465 microstrain. Gages 3 and 6 exhibited a linear relationship with load but had absolute strains that were much less than at the center of the plate. A nonlinear behavior was evident for gages 4, 5, and 7. The structure failed at a hydraulic pressure of 32.5 MPa (4,710 psi).

9.4.1.2 Numerical Simulation

A three-dimensional finite element model, shown in Fig. 162, was generated for simulation of the laboratory experiment. The analytical model exploits symmetric geometrical properties of the specimen and, thus, only one-quarter of the actual structure is modeled by finite elements and appropriate boundary conditions. Six-hundred and twelve, twenty-noded hexahedral finite elements subdivide the plate-plug fixture.

Nonhomogeneous material properties model the through-thickness variations of the elastic moduli (see section 7.3.3). Effects of nonlinear geometry are also taken into account since preliminary numerical simulation manifests its importance. The flat plate is approximated by ten layers of hexahedral solid elements in the through-thickness direction. Special attention in the design of the mesh is given to the region of the plate-plug interface due to concern that the silver foil brazing might be a critical area.

The plate-plug structure is given an initial load of 17.8 MPa (2,500 psi). A total of four FEA analyses provide convergence to the predicted loading to within $\pm 1\%$. Three nodes located at the plate-plug interface satisfy the condition of failure. This occurs at a load level of 34.5 MPa (5,000 psi). The percent difference with respect to unity for the satisfaction of Eq. 311 is 0.92%.

Graphical representation of numerically predicted through-thickness displacement and axial stress for the load case of 34.5 MPa (5,000 ksi) are shown in the gray fringe plots of Figs. 163-164. Maximum through-thickness displacement of 7.77×10^{-3} mm (3.04×10^{-4} in.) occurs at a distance of 1.2 mm (0.05 in.) from the center of the plate. The maximum tensile normal stress of 142.5 MPa (20.6 ksi) occurs at the plate-plug interface. The bottom surface directly below the center of the plate experiences a tensile stress of 127.6 MPa (18.5 ksi). The magnitude of the normal stress component in the global x-direction is considerably reduced in regions outside the plate-plug cavity.

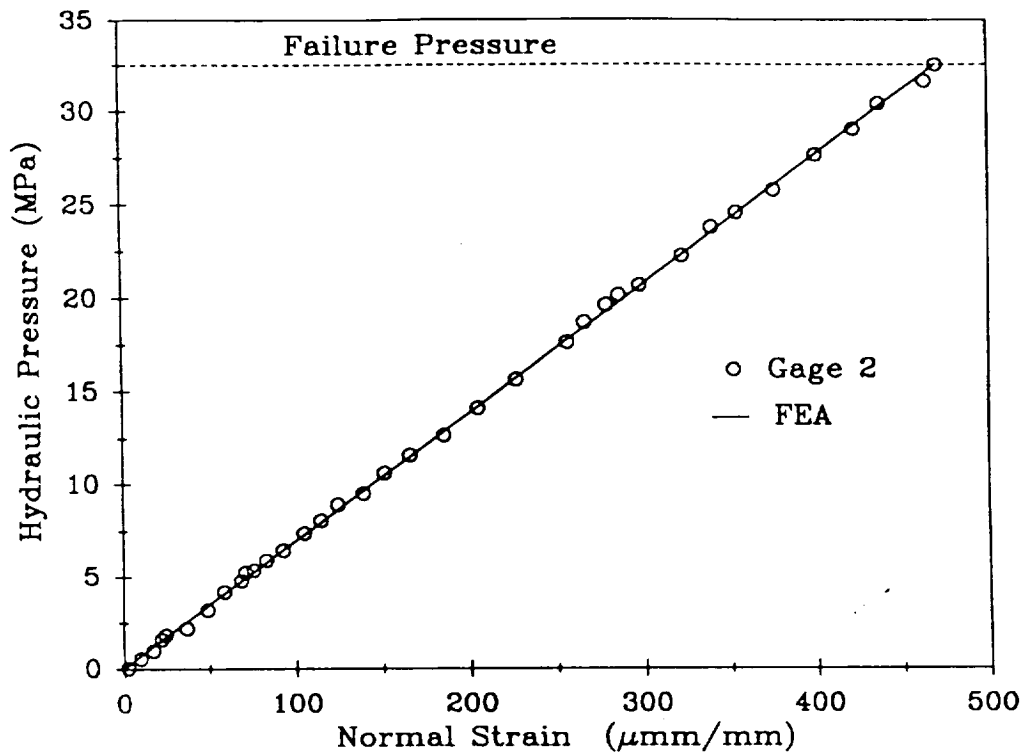


FIG. 159. Hydraulic Pressure versus Normal Strain for Gage 2

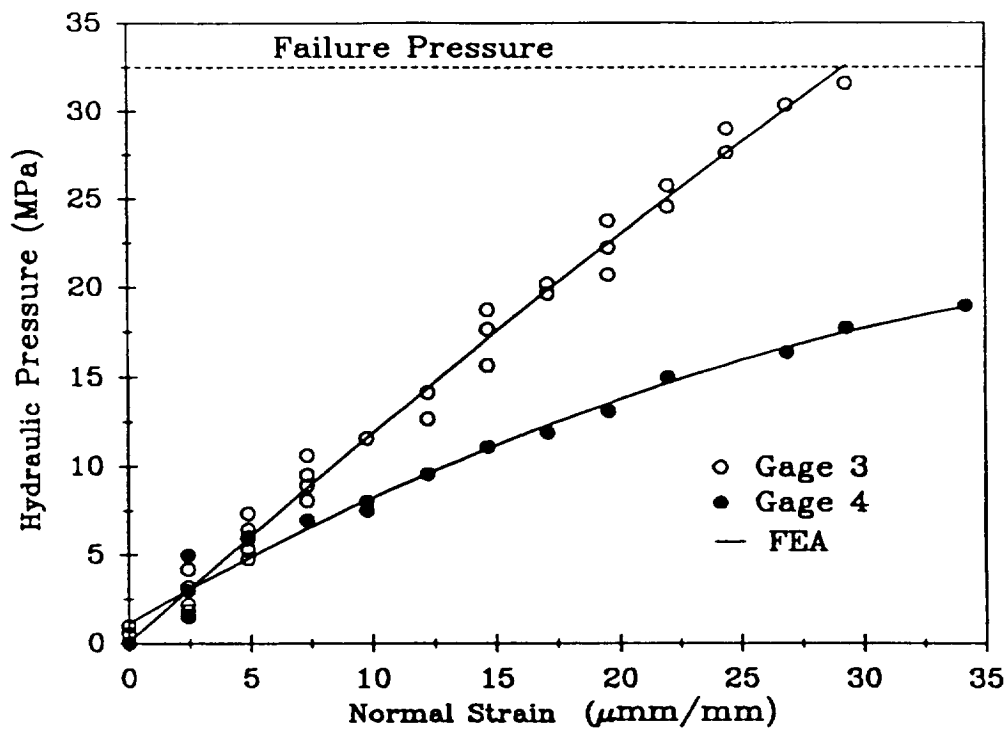


FIG. 160. Hydraulic Pressure versus Normal Strain for Gages 3 and 4

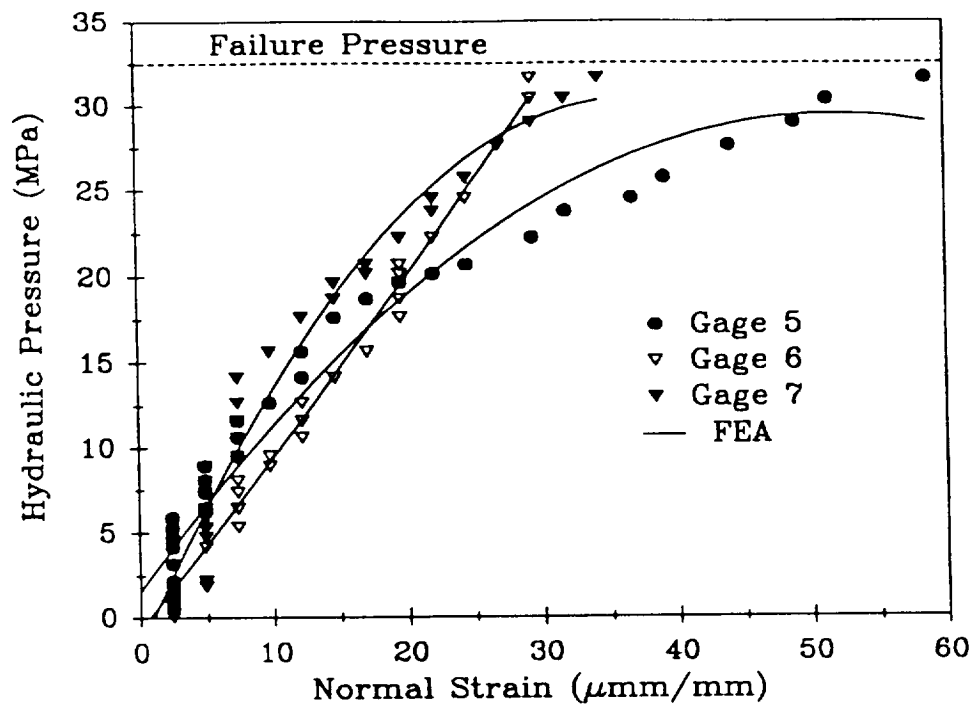


FIG. 161. Hydraulic Pressure versus Normal Strain for Gages 5, 6, and 7

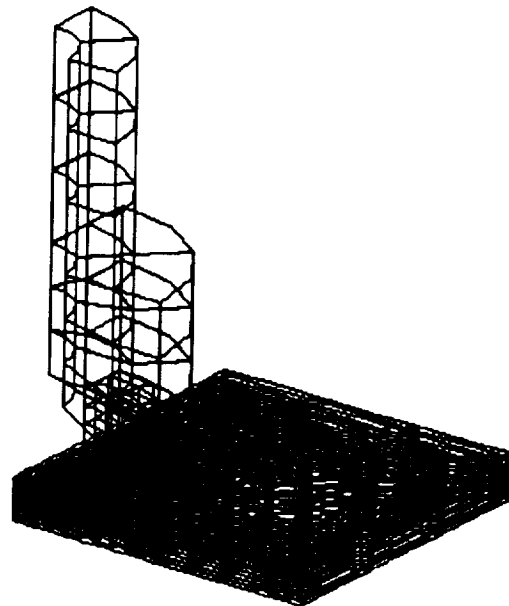


FIG. 162. Finite Element Mesh for Plate-Plug Structure

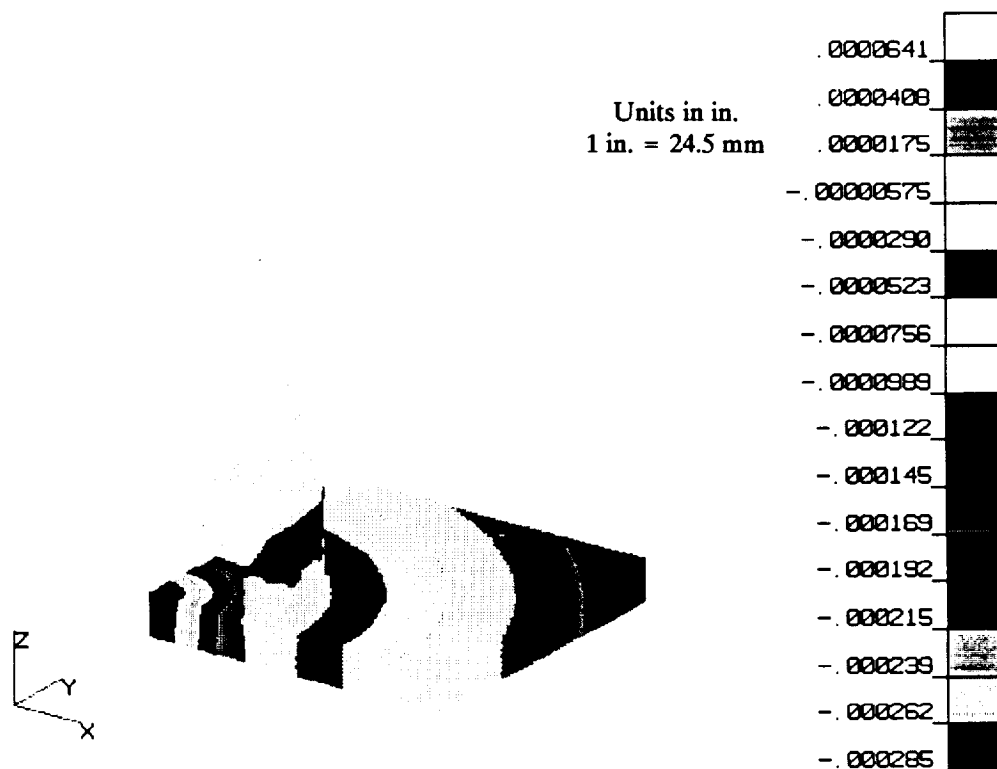


FIG. 163. Distribution of Through-Thickness Displacement, u_z

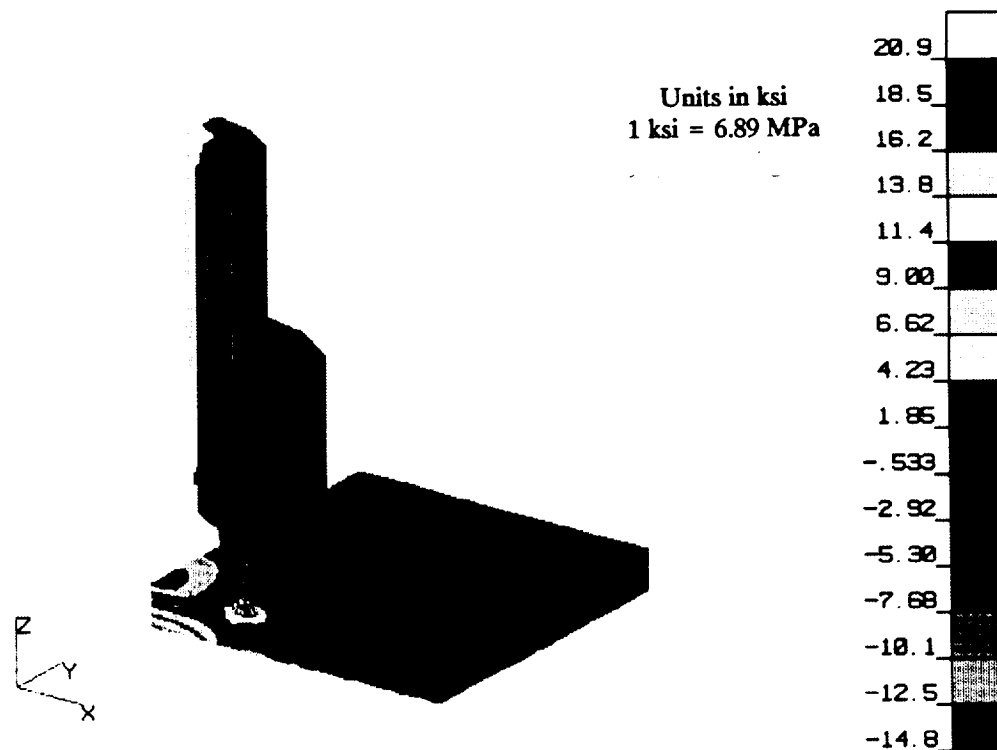


FIG. 164. Distribution of Normal Stress in Global x-Direction

9.4.1.3 Observations

The plate itself did not fail catastrophically as expected, but rather a combination of failures of the silver foil brazing and the beryllium plate surface caused the plate and plug to separate. This is verified both by the thin layer of beryllium residue remaining attached to the plug and by a series of photographs made by a scanning electron microscope (SEM) of the plate-plug interface after failure. Two SEM photographs are shown in Figs. 165 and 166. The first photograph shows the matrix of the material prior to the experiment. A uniform metal matrix that is free of cracks can be seen. The second SEM photograph is taken from the failed specimen. Microcracks appear in the matrix of the beryllium structure. Remnants of ruptured parts of the brazing medium which still adhere to the beryllium surface are also visible.

Results from the numerical simulation indicate that in-plane stress components are predominant in the center regions of the plate within the plate-plug cavity. A complex state of stress is observed at the plate-plug interface which includes radial, shear, and through-thickness normal components.

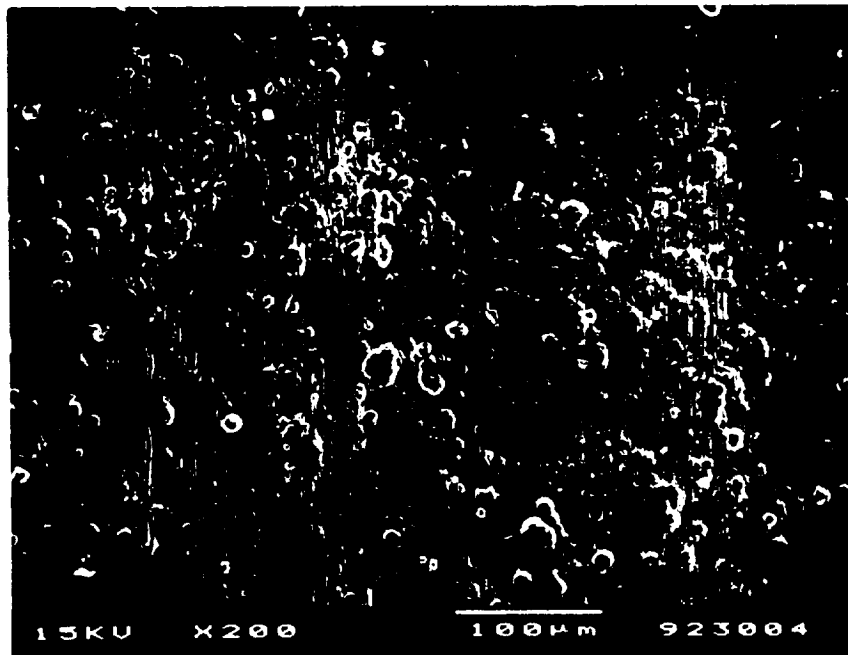


FIG. 165. Scanning Electron Microscope Photograph 1

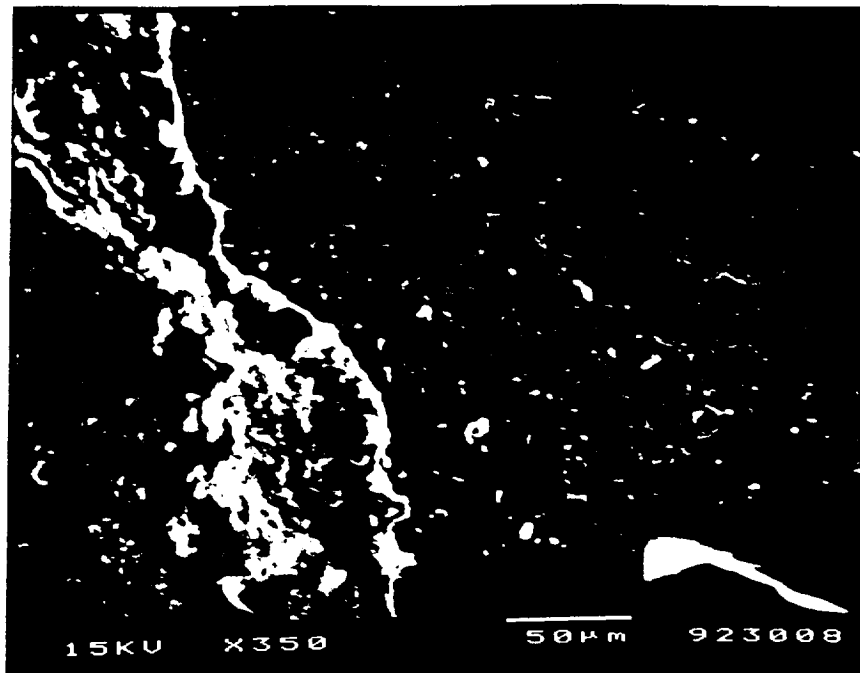


FIG. 166. Scanning Electron Microscope Photograph 2

Agreement of analytical and experimental results is acceptable for all strain gage locations. Failure prediction for this structure indicates a failure pressure of 34.5 MPa (5,000 psi) while the structure failed at a pressure of 32.5 MPa (4,710 psi). It is believed that the difference between the experimental and numerical results is due primarily to the premature failure of the brazing interface.

9.4.2 Clamped Plates under Influence of Concentrated Load

Experimental results for tests carried out on a series of clamped beryllium plates loaded by a central concentrated load are reported by Mascorro (1991). Numerical failure prediction is reported that uses a Tsai-Wu failure criterion with linear elastic analysis. The numerical models use eight-noded shell elements and homogeneous, orthotropic material properties. Results from two of these tests and complementary FEA simulations are used in the current study to verify the failure prediction capabilities of the high-order criterion.

Clear span dimensions of cross-rolled beryllium plates used in the current study are (a) 101.6 mm × 50.8 mm (4.0 in. × 2.0 in.) and (b) 50.8 mm × 25.4 mm (2.0 in. × 1.0 in.). Each plate is clamped along all four edges and loaded to failure by a concentrated load at the center of the structure. This is accomplished using a punching-point loader that is tapered to a 6.35-mm (0.25-in.) diameter ball-like end (see Fig. 167).

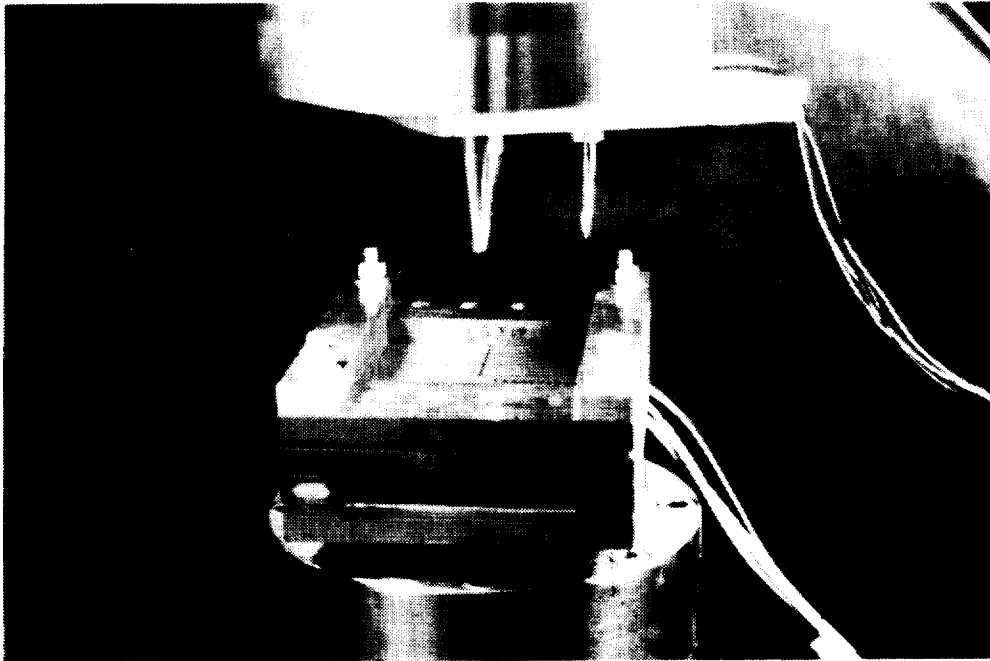


FIG. 167. Clamped Plate with Load Applicator

In the current study, a three-dimensional numerical model is constructed for each test. Twenty-noded hexahedral elements simulate each plate with ten elements in the through-thickness direction. Only one-fourth of each structure is modeled due to conditions of symmetry. Material properties are described in chapters 4 and 7. The concentrated load at the center of the plate is simulated using a decaying two-dimensional exponential distribution of the actual load (Fig. 168). This load extends twice as far as the actual radius of the mechanical loader. It should be noted that 70% of the load is applied within a radial distance of 1.33 mm (0.08 in.) from the center of the plate. A decaying distributed load is used due to the fact that the loader does not actually apply a concentrated load, in a strict sense, but rather a distributed load. The highest intensity of this distribution of load is directly below the tip of the loader. The magnitude decreases with the radial distance from the center of the plate. However, the influence of the loader is restricted to a distance that is two to three times the radius of the tip from the center of the plate (Timoshenko 1970).

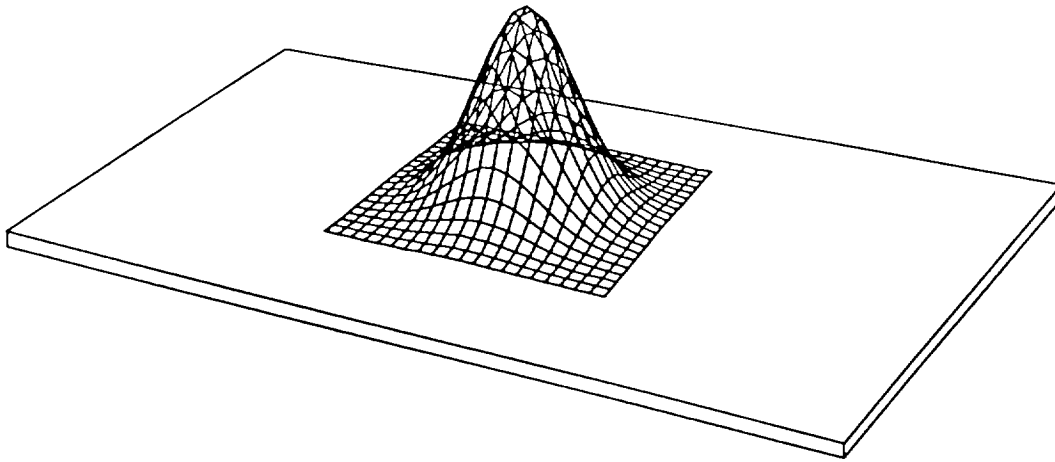


FIG. 168. Load Distribution for 101.6-mm × 50.8-mm (4.0-in. × 2.0-in.) Plate

Output stresses from FEA are averaged at the nodes of each element. Magnitude of these stresses is used by the failure prediction scheme to modify the level of the load for the next iteration until the failure load is estimated as described in section 9.3.

9.4.2.1 101.6-mm × 50.8-mm (4.0-in. × 2.0-in.) Plate

The current attempt at failure prediction with the higher-order criterion uses a total of three-thousand twenty-noded hexahedral elements each having twenty-seven integration points to model the 101.6-mm × 50.8-mm (4.0-in. × 2.0-in.) plate. A special mesh refinement is applied in the vicinity of the distributed load. The pressure load extends three times the radius of the tip of the loader in a radial direction from the center of the plate.

The distributed load used in the initial FEA analysis has an equivalent force of a 1.56 kN (0.35 kip). The failure load is predicted after six FEA iterations to be 2.51 kN (0.56 kip). Eighty-two minutes of cumulative CPU time on the CRAY is required for the analysis. The final iteration yields six nodes that have a state of stress that lies outside the failure surface of Eq. 311. All of these nodes are located on the bottom surface near the center of the plate. The minimum percent difference from satisfaction of Eq. 311 is -0.4% which occurs at the predicted load of 2.51 kN (0.56 kip). Fig. 169 illustrates the distribution of the normal stress in the global x-direction that occurs at this load.

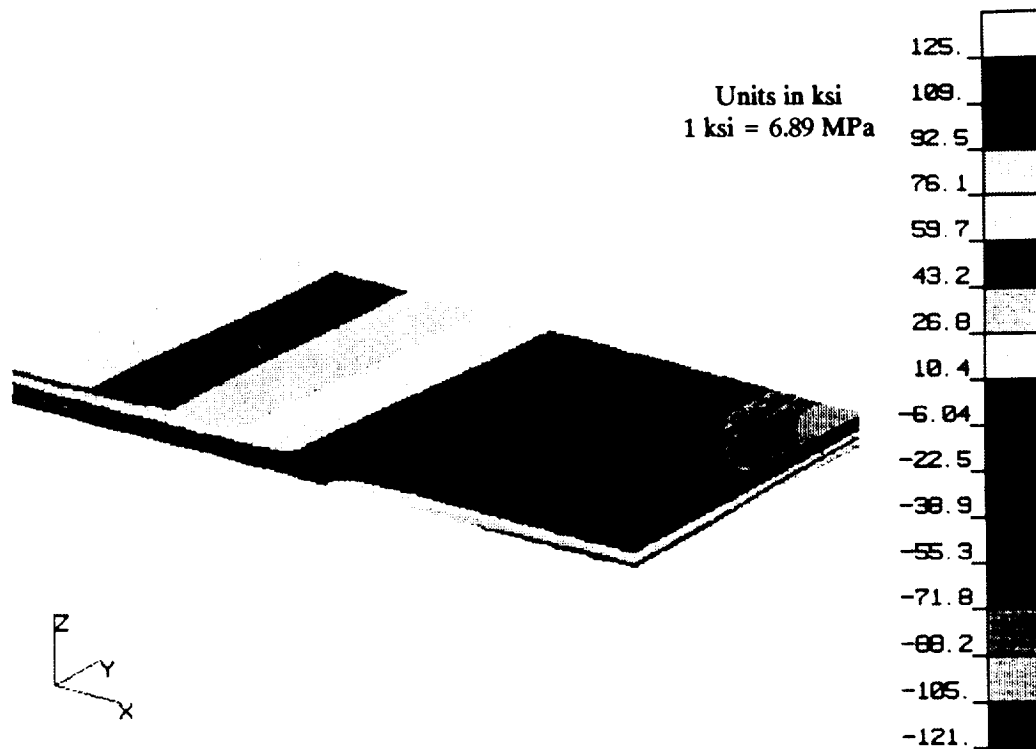


FIG. 169. Distribution of Normal Stress along Principal Material Axis for 101.6-mm × 50.8-mm (4.0-in. × 2.0-in.) Plate

Results obtained from this simulation are in very good agreement with the experimental data reported by Mascorro (1991). The failure load reported from the experiment is 2.53 kN (0.57 kip). There is less than a 1% error between the predicted and experimental failure load.

In addition, there is an improvement (approximately 3%) in comparison with the numerical results from the two-dimensional formulation reported by Mascorro (1991) that incorporates the Tsai-Wu failure envelope. This improvement is attributed to a number of factors: (a) the current analysis incorporates a higher-order criterion that takes into consideration interaction of stress components that the Tsai-Wu criterion neglects; the new criterion considers components of stress in the through-thickness direction unlike the Tsai-Wu criterion that only involves in-plane components of stress; (b) due to the inhomogeneity of the material properties in the through-thickness direction, the three-dimensional mesh includes a more precise material characterization of cross-rolled beryllium sheet material compared to the two-dimensional model; (c) a more refined mesh is used for the numerical model; and (d) a discontinuous and less refined distribution of pressure that applies two levels of stress is used by Mascorro (1991) to emulate the loading of the indenter. This approach is too coarse to adequately simulate the actual distribution of load. In the current approach a continuous decaying function more precisely approximates the load.

9.4.2.2 50.8-mm × 25.4-mm (2.0-in. × 1.0-in.) Plate

A second beryllium plate (Mascorro 1991) is used to verify the high-order criterion. It has a clear span of 50.8 mm × 25.4 mm (2.0 in. × 1.0 in.) and is clamped on all four edges (see Fig. 167).

The experiment is simulated using a total of two-thousand seven-hundred and fifty, twenty-noded hexahedral elements, each having twenty-seven integration points. The results obtained from this numerical simulation, in conjunction with the failure prediction scheme from the higher-order cubic criterion, are in good agreement with the experimental data reported by Mascorro (1991). The failure load induced by the indenter is reported to be 2.45 kN (0.55 kip). Numerical simulation estimates the failure load to be 2.49 kN (0.56 kip). The error between the numerical and experimental results is 1.5%. This is a definite improvement compared to an error of 13.5% due to the failure prediction results from the Tsai-Wu criterion (Mascorro 1991).

The initial distributed load used in the analysis corresponds to a 1.56-kN (0.35-kip) concentrated load. The failure load is predicted after six FEA iterations. A cumulative of 78 minutes of CPU time is required for the analysis. The final iteration yields eleven nodes that fail. All failed nodes are located on the bottom surface near the center of the beryllium plate. The minimum percent difference from unity is -1.29% for the failure load of 2.49 kN (0.56 kip).

Fig. 170 illustrates the final distribution of normal stress in the global x-direction of the structure for the numerically induced failure load of 2.49 kN (0.56 kip).

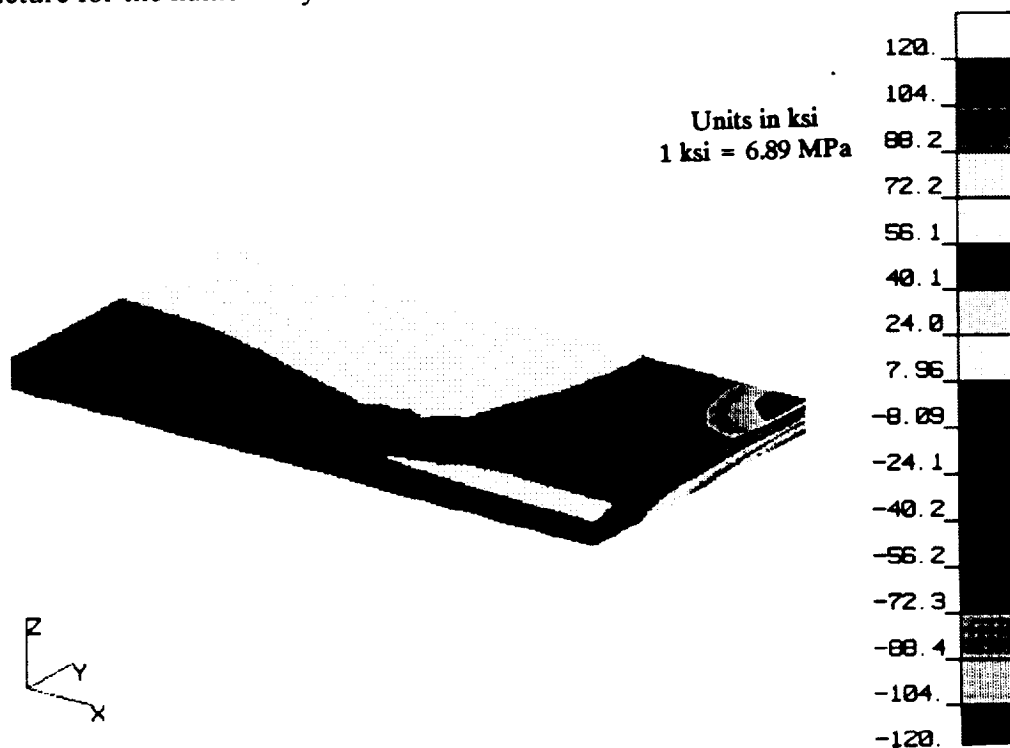


FIG. 170. Distribution of Normal Stress along Principal Material Axis for 50.8-mm x 25.4-mm (2.0-in. x 1.0-in.) Plate

10. CONCLUSION

10.1 SUMMARY

A macroscopic failure criterion that incorporates a cubic-order tensor polynomial has been developed. The new criterion is multi-dimensional and actively involves all six components of stress, i.e., in-plane and through-thickness components of stress are considered. Application of the criterion is made for failure prediction of 2.54-mm (0.1-in) thick SR-200 beryllium, and orthotropic material known to fail catastrophically in a brittle manner, especially when deformed by out-of-plane loadings. However, in its most general form the mathematical approach can be used to predict failure of other types of anisotropic material using the same general conditions of closure (chapter 3). On the other hand, the criterion can be simplified to predict failure of orthotropic material for in-plane stress situations. In this case the equations simplify to the criterion proposed by Jiang and Tennyson (1989). In the most simplified case, the higher-order criterion can be used for failure prediction of isotropic material.

The failure prediction model is applied to cross-rolled beryllium SR-200 sheet material using data from tensile and compressive tests that have significant stresses in all three mutually perpendicular directions, experiments on two circular plates, and combinations of off-axis experiments that involve three components of stress. Results of these tests provide the required strength parameters for the cubic criterion as described in sections 6 and 7. The strength parameters for beryllium vary considerably for different material orientations and states of stress. For example, normal in-plane tensile and compressive strengths are 537.8 MPa (79 ksi) and 658.8 MPa (95.6 ksi), respectively. On the other hand, the through-thickness normal compressive strength is 1,724 MPa (250 ksi) while the tensile strength in the same direction is 200 MPa (29 ksi). Moreover, the in-plane biaxial strength is estimated to be 827.4 (120 ksi) which is approximately one and one-half times greater than the in-plane uniaxial tensile strength in each direction of principal rolling.

The majority of laboratory experiments used to determine the strength magnitudes for establishing the failure coefficients are simulated using finite elements. A variety of elements is used for the analysis depending on the geometry and the load distribution. These include eight-noded axisymmetric, in-plane, and shell elements, as well as twenty-noded hexahedral elements. Two-node interface elements are used for contact problems. The numerical analyses yield distribution of stress for various experimental setups. Displacement, strain, and stress levels for selected output are shown via fringe plots for a

number of simulations. In general, the FEA results are in good agreement with experimentally measured quantities.

Material properties for cross-rolled beryllium sheet are reported by Fenn et al. (1967). In-plane moduli are verified by experiments conducted recently by Henkener et al. (1991) and Roschke et al. (1991). Furthermore, NDE techniques and an iterative FEA procedure described in section 7.3 establish that the through-thickness modulus and Poisson's ratio vary with respect to distance from the neutral axis of the plate. The through-thickness modulus shows a variation from 296.5 GPa (43,000 ksi) at the middle plane to 533.7 GPa (77,400 ksi) at the outer layer (see Fig. 136) for an increase of 80%. On the other hand, Poisson's ratios ν_{13} and ν_{23} vary from 0.089 and 0.091 at the center of the plate to 0.076 and 0.077, respectively, at the outer layer for a decrease of approximately 16% in each case. The newly determined material properties in the through-thickness direction are used in conjunction with all three-dimensional simulations for 2.54-mm (0.1-in.) thick beryllium sheet.

The resulting failure criterion for SR-200 beryllium is given by Eq. 311. Select failure surfaces involving three active components of stress are presented in section 8 for the sake of illustration. Any other combination of three normal and shearing components of stress can be extracted from Eq. 311 and plotted in standard Cartesian coordinates.

The criterion is incorporated into a system of custom-designed routines that make use of a general-purpose finite element analysis code, ABAQUS. Numerical simulation applies modified load histories to a structural component that is being analyzed and checks the stress level at each nodal point in the finite element mesh. If the component does not meet the criterion set by Eq. 311 to within $\pm 1\%$, the load is adjusted according to Eq. 319 and the analysis is repeated. The same recursion scheme is followed until Eq. 311 is satisfied to within $\pm 1\%$, at which point the component is considered to have failed and the analysis is terminated. Non-linear geometrical analysis is used for each simulation.

Verification of the cubic criterion is accomplished by failure prediction of three structures: (a) a plate-plug arrangement subjected to a complex state of stress via a hydraulic loading; (b) a 101.6-mm \times 50.8-mm (4.0-in. \times 2.0-in.) clamped plate with a concentrated load at its center; and (c) a 50.8-mm \times 25.4-mm (2.0-in. \times 1.0-in.) clamped plate with a concentrated load at the center. Experimental and numerical results of the latter two experiments are reported as well as failure prediction results based on the Tsai-Wu model (Mascorro 1991). A three-dimensional FEA mesh is used to model each structure. Symmetry conditions are exploited to reduce CPU time. Using the newly developed failure criterion, new material characterization, and finite element code, the failure load for each structure is predicted to within one percent. For the two plate

structures this is an improvement over the accuracy reported by using the Tsai-Wu model (Mascorro 1991).

The main advantage of this criterion compared to those presented in the past is that it actively involves all six components of stress and, thus, failures due primarily to through-thickness normal and shearing stresses can be predicted. Most of the earlier criteria are concerned only with in-plane states of stress. In addition, all possible interaction coefficients that relate normal and shearing stresses are present in the cubic-order polynomial failure surface. This is in contrast to other criteria that include either no or limited interaction coefficients. Moreover, the cubic-order polynomial provides a more accurate approximation of the failure surfaces compared to the second-order polynomials employed by other criteria (Tsai and Wu 1971; Priddy 1974).

Disadvantages that arise from the higher-order criterion are mainly due to: (a) mathematical complexity of the criterion including simultaneous solution of non-linear equations in order to obtain the normal and shear interaction coefficients (see section 3.3); (b) three-dimensional numerical simulations are required to actively involve all six components of stress used by the failure scheme described in section 9, thus, increasing the CPU time for each FEA analysis considerably; and (c) the criterion calls for a large number of experiments. For the case of orthotropic material, such as cross-rolled beryllium sheet, the minimum number of experiments necessary for establishing a failure criterion is fifteen (see Table 12). Twenty-four independent experiments are used in the current effort. It should be noted that the accuracy of the high-order criterion is enhanced by incorporating data obtained from more than the minimum number of experiments that are necessary.

The higher-order criterion failure criterion is shown to be a viable approach for estimating failure of cross-rolled beryllium structures that are statically loaded. The iterative computer method presented is well-suited for design and research environments. Accuracy of the failure prediction scheme can be easily altered to accommodate more relaxed or stricter tolerance requirements for design and evaluation of beryllium components.

10.2 RECOMMENDATIONS AND FUTURE WORK

Cross-rolled SR-200 beryllium sheet structures loaded statically to failure under either simple or complex states of stress can be adequately analyzed and the failure loads can be accurately predicted using a combination of material properties (including through-thickness variation of elastic moduli) and a new failure prediction criterion that incorporates closure of a cubic-order polynomial tensor. However, it is recommended that more refined work be carried out to establish an even more precise distribution of the material properties. Special care should be given to variation of the normal modulus E_3 and Poisson's ratios ν_{13}

and ν_{23} , in the through-thickness direction. Either destructive or non-destructive evaluation or a combination of both methods is recommended. This will enhance accuracy of the failure prediction model used for cross-rolled beryllium sheets, SR-200 specification.

True in-plane biaxial tests need to be performed to ensure validity of the in-plane normal interaction coefficients. This test should be carried out in accordance to the guidelines suggested by Ferron et al. (1988) with the exception of thinning out the middle portion of the specimen and drilling holes. The thicker section required for the supports of the biaxial specimen can be accomplished by appending aluminum pads on each support area of the structure.

Another parameter that requires further investigation is the through-thickness tensile strength of cross-rolled beryllium. Test results reported by Fenn et al. (1967) do not agree with the hardness testing performed on the material and reported in chapter 7. A new experimental setup needs to be devised in order to accurately determine the value of this parameter.

In addition, testing of beryllium structures need to be carried out at both higher and lower temperature ranges since this material is often used in aerospace applications where temperature gradients and ranges can impose considerable stresses.

Dynamic and vibrational testing of beryllium sheet structures should be considered in order to account for the actual states of stress experienced by beryllium sheet components primarily during launching of the space shuttle. The new criterion can be modified to include variations of stress (or strain) that compensate for the dynamic loadings encountered by structures in flight. Physical testing to establish rate-dependent failure coefficients of stress may be strenuous especially for determination of interaction coefficients of stress rates. As a first approximation, it is suggested that only normal rate interaction coefficients be included in the criterion.

Structural components in aerospace applications are often introduced to short duration cyclic loadings. This can lead to fatigue failures. Hot-pressed beryllium shows high resistance to fatigue cracking and endurance strength level (Brush Wellman 1986). Fatigue studies, however, for SR-200 beryllium sheet are not complete. Thus, strength versus number of cycles to failure (S-N) curves need to be developed for this grade of beryllium at room and elevated temperatures. Subsequently, stress (or strain) dependent dynamic failure coefficients can be adjusted to account for fatigue loadings. This is done by comparing dynamic and fatigue failure strengths at different frequency levels common for both loading situations. The more conservative of the two failure strengths is maintained for calculating the failure coefficients and thus, establishing a complete failure criterion for SR-200 beryllium structures.

REFERENCES

- ABAQUS, Version 4.8 (1990). *User's manual*, Hibbitt, Karlsson & Sorensen, Inc., Providence, RI.
- ABAQUS, Version 4.8 (1990). *Theory manual*, Hibbitt, Karlsson & Sorensen, Inc., Providence, RI.
- Asceland, D. R. (1989). *The science and engineering of materials*. PWS-KENT Publishing Company, Boston, MA.
- Ashkenazi, E. K. (1965). "Problem of the anisotropy of strength." *Mechanica Polimerov*, 1(2), 79-92.
- Bradley, G. L. (1975). *A primer of linear algebra*, New Jersey, Prentice-Hall, Inc.
- Brush Wellman (1986). "Designing with beryllium." *Brush Wellman Inc.*, Cleveland, OH.
- Cooke, F. W., Damiano, V. V., London, G. J., Conrad, H., and Banerjee, B. R. F. (1971). "Structure property relations in beryllium sheet." *Journal of Materials*, 6(2), 403-421.
- Davis, H. E., Troxell, G. E., and Hauck, G. F. W. (1982). *The testing of engineering materials*. McGraw-Hill Book Company, New York, NY.
- Devore, J. L. (1987). *Probability and statistics for engineering and the sciences*, (second edition). Brooks/Cole Publishing Co., Monterey, CA.
- Fenn, R. W. Jr., Cooks, D. D., Kinder, W. C., and Lempiere, B. M. (1967). "Test methods for mechanical properties of anisotropic materials (beryllium sheet)." *Technical Report AFML-TR-67-212*, Lockheed Missiles and Space Company, Houston, TX.
- Ferron, G., and Makinde, A. (1988). "Design and development of a biaxial strength testing device." *J. Testing and Evaluation*, 16(3), 253-256.
- Grant, L. A. (1983). "Successful application of beryllium sheet materials to satellite structures." *Presented at 24th Annual AIAA SDM Conference*, Lake Tahoe, NV.
- Grant, L. A., Hardesty, R. E., and Jarmin, R. A. (1985). "Fabrication of complex beryllium assemblies using "photon-fusion" technology." *26th Annual AIAA Conference*, Orlando, FL.
- Gol'denblat, I. I., and Kopnov, V. A. (1965). "Strength of glass-reinforced plastics in the complex stress state." *Mekhanica Polimerov*, 1(2), 70-78.
- Henkener, J. A., Spiker, I. K., and Castner, W. L. (1991). "The mechanical behavior of cross-rolled beryllium sheet." *NASA Technical Memorandum*, The Johnson Space Center, Houston, TX.
- Hill, R. (1948). "A theory of the yielding and plastic flow of anisotropic metals." *Proc., Royal Society A*, 193, 281.
- Hill, R. (1950). *The mathematical theory of plasticity*, Oxford, The Clarendon Press.

- Hoffman, O. (1967). "The brittle strength of material." *J. Composites and Materials*, 1, 200-206.
- Jiang, Z., and Tennyson, R. C. (1989). "Closure of the cubic tensor polynomial failure surface." *J. Composites and Material*, 23, 208-231.
- Karr, D. G., and Das, S. C. (1983). "Ice strength in brittle and ductile failure modes." *Structural Engineering*, 109(12), 2802-2811.
- Kojola, K. L. (1961). "The brittleness problem in beryllium." *SAE Aeronautics and Space Engineering and Manufacturing Meeting*, Los Angeles, CA.
- Lekhnitskii, S. G. (1981). *Theory of elasticity of an anisotropic body*, (third edition), Mir Publishers, New York, NY.
- Lekhnitskii, S. G. (1968). *Anisotropic plates*, (second edition), Gordon and Breach Science Publishers, New York, NY.
- Mallick, K. P. (1950). *Fiber-Reinforced Composites*, New York, Marcel Dekker, Inc.
- Malmeister, A. K. (1966). "Geometry of theories of strength." *Mechanica Polimerov*, 2(4), 519-534.
- Marder, J. M. (1986). "Beryllium in stress-critical environments." *American Society of Metals*, 8(1), 17-26.
- Mascorro, E., Roschke, P. N., and Papados, P. P. (1991). "Failure prediction of thin beryllium structures." *Proc., ASCE Structural Congress*, Indianapolis, IN.
- MIT Publications (1988). *MACSYMA: User's guide*, Symbolics, Inc., Boston, MA.
- Monch, E., Galster, D., (1963). "A method of producing a defined uniform biaxial tensile stress field." *British Journal of Applied Physics*, 14, 810-812.
- Papados, P. P., and Roschke, P. N. (1991). "High order criterion for failure prediction of thin beryllium sheets." *Proc., International RILEM/ESIS Conference*, Noordwijk, The Netherlands, 673-682.
- PATRAN, A Division of PDA Engineering, Release 2.3 (1988). *PATRAN Plus user manual Vol. I & II*, PDA Engineering, Costa Mesa, CA.
- Pollock, T. C. (1977). "The fracture of beryllium single crystals." Dissertation presented to the University of Virginia, at Richmondville, Virginia, in partial fulfillment of the requirements for the degree of Doctor of Philosophy.
- Priddy, T. G. (1974). "A fracture theory for brittle anisotropic materials." *J. Engineering Materials and Technology*, Transactions of the ASME, 91-96.
- Roschke, P. R., and Papados, P. P. (1989). "Failure prediction of thin beryllium sheets used in spacecraft structures." *Annual Report*, NASA Grant Number: NAG 9-280.

- Roschke, P. N., Papados, P. P., and Mascorro, E. (1990). "Failure prediction of thin beryllium sheets used in spacecraft structures." *Annual Report*, NASA Grant Number: NAG 9-280.
- Sokolnikoff, I. S. (1964). *Tensor analysis - theory and application to geometry and mechanics of continua*, second edition, John Wiley and Sons Inc., New York, NY.
- Tennyson, R. C., and Elliot, W. G. (1983). "Failure analysis of composite laminates including biaxial compression." *NASA CR 172192*.
- Tennyson, R. C., Nanyaro, A. P. and Wharram, G. E. (1980). "Application of the cubic order polynomial strength criterion to the failure analysis of composite materials." *J. Composite Materials*, 14, 28-41.
- Thorpe, J. A. (1979). *Elementary topics in differential geometry*, New York, Springer-Verlog.
- Tsai, S. W., and Wu, E. M. (1971). "A general theory of strength for anisotropic material." *J. Composite Materials*, 5, 58-80.
- Webster, D. W., and London, G. J. (1979). *Beryllium science and technology: Vol. I & II*, New York, Plenum Press.
- Wu, E. M. (1974). "Optimal Experimental Measurements of anisotropic failure tensors." *J. Composite Materials*, 6, 472-489.
- Wu, E. M., and Scheublein, J. K. (1974). "Laminate strength - a direct procedure." *Composites Materials: Testing and Design (Third Conference)*, ASTM STP 546, 188-206.

APPENDIX I.

FAILURE COEFFICIENTS FOR TSAI AND WU'S CRITERION

For an anisotropic material in three-dimensional space the contracted form of the second- and fourth-order failure strength tensors are as follows (Tsai and Wu 1971):

$$F_i = \begin{bmatrix} F_1 \\ F_2 \\ F_3 \\ F_4 \\ F_5 \\ F_6 \end{bmatrix} \dots\dots\dots (320)$$

$$F_{ij} = \begin{bmatrix} F_{11} & F_{12} & F_{13} & F_{14} & F_{15} & F_{16} \\ & F_{22} & F_{23} & F_{24} & F_{25} & F_{26} \\ & & F_{33} & F_{34} & F_{35} & F_{36} \\ & & & F_{44} & F_{45} & F_{46} \\ & & & & F_{55} & F_{56} \\ & & & & & F_{66} \end{bmatrix} \dots\dots\dots (321)$$

In their uncontracted form symmetry is exhibited by both sets of strength coefficients. Thus, the number of independent strength coefficients for the contracted form of F_i and F_{ij} is six and twenty-one, respectively.

For an orthotropic material the number of independent strength components for F_i and F_{ij} further reduces to three and nine, respectively, due to uncoupling between the normal and shearing strengths and the assumed neutral effect of the sign of the shearing stress on the failure strength. Thus, Eqs. 320 and 321 become:

$$F_i = \begin{bmatrix} F_1 \\ F_2 \\ 0 \\ 0 \\ 0 \\ F_6 \end{bmatrix} \dots\dots\dots (322)$$

$$F_{ij} \begin{bmatrix} F_{11} & F_{12} & F_{13} & 0 & 0 & 0 \\ & F_{22} & F_{23} & 0 & 0 & 0 \\ & & F_{33} & 0 & 0 & 0 \\ & & & F_{44} & 0 & 0 \\ & & & & F_{55} & 0 \\ & & & & & F_{66} \end{bmatrix} \dots\dots\dots (323)$$

In addition, when a triclinic material only undergoes a state of plane stress Eqs. 320 and 321 are further simplified to

$$F_i = \begin{bmatrix} F_1 \\ F_2 \\ F_6 \end{bmatrix} \dots\dots\dots (324)$$

$$F_{ij} = \begin{bmatrix} F_{11} & F_{12} & F_{16} \\ & F_{22} & F_{26} \\ & & F_{66} \end{bmatrix} \dots\dots\dots (325)$$

Furthermore, for the case of a specially orthotropic material, such as graphite-epoxy composites (Tsai and Wu 1971), the coefficients F_6 , F_{16} , and F_{26} can be set equal to zero.

APPENDIX II.

OVERVIEW OF JIANG AND TENNYSON'S CRITERION

Expansion of terms in Eq. 37 and application of plane stress assumptions as well as orthotropic material behavior leads to the following equation:

$$F_1\sigma_1 + F_2\sigma_2 + F_{11}\sigma_1^2 + F_{22}\sigma_2^2 + F_{66}\sigma_6^2 + 2F_{12}\sigma_1\sigma_2 + 3F_{112}\sigma_1^2\sigma_2 + 3F_{122}\sigma_1\sigma_2^2 + 3F_{166}\sigma_1\sigma_6^2 + 3F_{266}\sigma_2\sigma_6^2 = 1 \quad (326)$$

Eq. 326 can be rearranged as follows:

$$(3F_{166}\sigma_1 + 3F_{266}\sigma_2 + F_{66})\sigma_6^2 = -(F_1\sigma_1 + F_2\sigma_2 + F_{11}\sigma_1^2 + F_{22}\sigma_2^2 + 2F_{12}\sigma_1\sigma_2 + 3F_{112}\sigma_1^2\sigma_2 + 3F_{122}\sigma_1\sigma_2^2 - 1) \quad (327)$$

Closure is accomplished by imposing the following conditions (Jiang and Tennyson 1989):

(a) Ensure that the cubic equation describing the intersecting $(\sigma_1 - \sigma_2)$ plane is closed.

(b) Real values of σ_6 must exist for any given values of σ_1 and σ_2 . Thus, the asymptotic plane defined by

$$3F_{166}\sigma_1 + 3F_{266}\sigma_2 + F_{66} = 0 \quad (328)$$

should not intersect the cubic surface described by condition (a). Implications of these conditions are described in the following sections.

INVESTIGATION OF NECESSARY CONDITIONS

From Eq. 326 the image of the failure surface on the $(\sigma_1 - \sigma_2)$ plane when $\sigma_6 = 0$ becomes,

$$F_1\sigma_1 + F_2\sigma_2 + F_{11}\sigma_1^2 + F_{22}\sigma_2^2 + 2F_{12}\sigma_1\sigma_2 + 3F_{112}\sigma_1^2\sigma_2 + 3F_{122}\sigma_1\sigma_2^2 = 1 \quad (329)$$

The asymptotes correlating the interaction coefficients are obtained by rewriting Eq. 329 as a quadratic in terms of either σ_1 or σ_2 and by minimizing Eq. 329 with respect to σ_1 or σ_2 . Setting the coefficients of these terms equal to zero leads to:

$$F_{11} + 3F_{112}\sigma_2 = 0 \quad (330)$$

$$F_{22} + 3F_{122}\sigma_1 = 0 \quad (331)$$

$$2F_{12} + 6F_{112}\sigma_1 + 6F_{122}\sigma_2 = 0 \quad (332)$$

Eqs. 330, 331, and 332 are multiplied by F_{122}^2 , F_{112}^2 , and $-F_{112}F_{122}$, respectively, added, and rearranged to yield the following expression:

$$3F_{112}^2 F_{122} \sigma_1 + 3F_{112} F_{122}^2 \sigma_2 = F_{11}^2 F_{122} + F_{22}^2 F_{112} - 2F_{12} F_{112} F_{122} \dots\dots\dots (333)$$

which replaces Eq. 332 as the third asymptotic equation.

For closure to be ensured the asymptotes given by Eqs. 330 through 332 should not intersect the surface represented by Eq. 329. Two conditions that guarantee closure are derived from Eq. 331 by substitution of the tensile and compressive strength values associated with the longitudinal material direction. These conditions are shown by Eq. 334 and 335. Similarly, Eq. 330 and 332 yield two and four additional independent conditions, respectively; one condition per independent variable of each equation. Thus, the following conditions are established:

$$\frac{-F_{22}}{3F_{122}} \leq -X' \quad \text{for} \quad F_{122} > 0 \dots\dots\dots (334)$$

$$\frac{-F_{22}}{3F_{122}} \geq X \quad \text{for} \quad F_{122} < 0 \dots\dots\dots (335)$$

$$\frac{-F_{11}}{3F_{112}} \leq -Y' \quad \text{for} \quad F_{112} > 0 \dots\dots\dots (336)$$

$$\frac{-F_{11}}{3F_{112}} \geq Y \quad \text{for} \quad F_{112} < 0 \dots\dots\dots (337)$$

$$\frac{-T}{3F_{112}} \leq -X' \quad \text{for} \quad \frac{-T}{F_{112}} < 0 \dots\dots\dots (338)$$

$$\frac{-T}{3F_{112}} \geq X \quad \text{for} \quad \frac{-T}{F_{112}} > 0 \dots\dots\dots (339)$$

$$\frac{-T}{3F_{122}} \leq -Y' \quad \text{for} \quad \frac{-T}{F_{122}} < 0 \dots\dots\dots (340)$$

$$\frac{-T}{3F_{122}} \geq Y \quad \text{for} \quad \frac{-T}{F_{122}} > 0 \dots\dots\dots (341)$$

where,

$$T = \frac{F_{11}^2 F_{122} + F_{22}^2 F_{112} - 2F_{12} F_{112} F_{122}}{3F_{112} F_{122}} \dots\dots\dots (342)$$

EVALUATION OF F_{12} AND F_{112} AND F_{122}

Assuming that there are data from n sets of biaxial load tests that correspond to $(\sigma_{1i}, \sigma_{2i})$ ($i = 1, 2, \dots, n$), it is possible to evaluate the interaction coefficients by a least-square fit of the cubic Eq. 329. If closure, as specified by Eqs. 334-341, is not accomplished, one or more of the constraints that intersect the failure surface are shifted in space (i.e. their coefficients are modified) in such a manner that all constraints are satisfied and the surface is closed (Jiang and Tennyson 1989).

As an example, suppose that the asymptote,

$$F_{22} + 3F_{122}\sigma_1 = 0 \dots\dots\dots (343)$$

intersects the failure surface between $(-X', 0, 0)$ and the origin. Closure is accomplished by shifting the asymptote to the left of the line $\sigma_1 + X' = 0$. Eq. 343 becomes an asymptote to the failure surface if it is allowed to pass through point $(-X', 0, 0)$. Then the cubic curve of Eq. 229 can be simplified into a quadratic and linear curves. This is accomplished by collecting quadratic, linear, and constant terms with respect to the independent variable, σ_2 .

$$(-3F_{122}X' + F_{22})\sigma_2^2 + (3F_{112}X'^2 - 2F_{12}X' + F_2)\sigma_2 + (F_{11}X'^2 - F_1X' - I) = 0 \dots\dots\dots (344)$$

For an infinity of roots for σ_2 to exist it must follow that:

$$-3F_{122}X' + F_{22} = 0 \dots\dots\dots (345)$$

$$3F_{112}X'^2 - 2F_{12}X' + F_2 = 0 \dots\dots\dots (346)$$

$$F_{11}X'^2 - F_1X' - I = 0 \dots\dots\dots (347)$$

Eq. 347 can also be obtained by substituting $\sigma_1 = -X'$ into the cubic criterion of Eq. 37. Application of Lagrange multipliers allows incorporation of Eqs. 345 and 346 as constraint conditions to Eq. 329. In this manner the following functional is obtained for calculation of the interaction parameters:

$$\Phi = \sum_{i=1}^n (F_1\sigma_{1i} + F_2\sigma_{2i} + F_{11}\sigma_{1i}^2 + F_{22}\sigma_{2i}^2 + 2F_{12}\sigma_{1i}\sigma_{2i} + 3F_{112}\sigma_{1i}^2\sigma_{2i} + 3F_{122}\sigma_{1i}\sigma_{2i}^2 - I)^2 \dots\dots\dots (348)$$

$$+ \lambda_1(-3F_{122}X' + F_{22}) + \lambda_2(3F_{112}X'^2 - 2F_{12}X' + F_2)$$

where λ_1 and λ_2 represent Lagrange multipliers.

Minimizing the functional Φ with respect to F_{12} , F_{112} , F_{122} , λ_1 , and λ_2 yields five equations with an identical number of unknowns. Coefficients F_i and F_{ii} ($i = 1, 2$) are obtained via uniaxial tests that supply strength parameters as described in section 4. The five equations are as follows:

$$\frac{\partial \Phi}{\partial F_{12}} = -2\lambda_2 X' + 4 \sum_{i=1}^{nI} \sigma_{li} \sigma_{2i} (F_1 \sigma_{li} + F_2 \sigma_{2i} + F_{11} \sigma_{li}^2 + F_{22} \sigma_{2i}^2 + 2F_{12} \sigma_{li} \sigma_{2i} + 3F_{112} \sigma_{li}^2 \sigma_{2i} + 3F_{122} \sigma_{2i}^2 \sigma_{li} - 1) = 0 \quad (349)$$

$$\frac{\partial \Phi}{\partial F_{112}} = 3\lambda_2 X'^2 + 6 \sum_{i=1}^{nI} \sigma_{li}^2 \sigma_{2i} (F_1 \sigma_{li} + F_2 \sigma_{2i} + F_{11} \sigma_{li}^2 + F_{22} \sigma_{2i}^2 + 2F_{12} \sigma_{li} \sigma_{2i} + 3F_{112} \sigma_{li}^2 \sigma_{2i} + 3F_{122} \sigma_{2i}^2 \sigma_{li} - 1) = 0 \quad (350)$$

$$\frac{\partial \Phi}{\partial F_{122}} - 3\lambda_1 X' + 6 \sum_{i=1}^{nI} \sigma_{2i}^2 \sigma_{li} (F_1 \sigma_{li} + F_2 \sigma_{2i} + F_{11} \sigma_{li}^2 + F_{22} \sigma_{2i}^2 + 2F_{12} \sigma_{li} \sigma_{2i} + 3F_{112} \sigma_{li}^2 \sigma_{2i} + 3F_{122} \sigma_{2i}^2 \sigma_{li} - 1) = 0 \quad (351)$$

$$\frac{\partial \Phi}{\partial \lambda_1} = -3F_{122} X' + F_{22} = 0 \quad (352)$$

$$\frac{\partial \Phi}{\partial \lambda_2} = 3F_{112} X'^2 - 2F_{12} X' + F_2 = 0 \quad (353)$$

EVALUATION OF F_{166} AND F_{266}

For closure condition (b) to be met the following asymptote, which does not intersect the curve of condition (a), must exist (Jiang and Tennyson 1989):

$$3F_{166} \sigma_1 + 3F_{266} \sigma_2 + F_{66} = 0 \quad (354)$$

For this condition to be satisfied Eq. 354 should not intersect the failure surface defined by Eq. 329. This condition occurs only if the line given by Eq. 354 is, at most, tangent to Eq. 329. Solving Eq. 354 for σ_2 (see Eq. 355):

$$\sigma_2 = -\frac{(3F_{166} \sigma_1 + F_{66})}{3F_{266}} \quad (355)$$

and substituting the result into Eq. 329 yields the following equation for determination of the coordinates of the point of intersection of the two curves:

$$A\sigma_1^3 + B\sigma_1^2 + C\sigma_1 + D = 0 \quad (356)$$

where A , B , C , and D are constants that are functions of F_i , F_{ij} , and F_{i66} for $i = 1, 2$.

$$A = 27(F_{122}F_{166}^2 - F_{112}F_{166}F_{266}) \quad (357)$$

$$B = 9(F_{266}^2F_{11} + F_{166}^2F_{22} - 2F_{266}F_{166}F_{12} - 2F_{112}F_{166}F_{66} + 2F_{122}F_{166}F_{66}) \quad (358)$$

$$C = 3(F_{266}^2 F_1 - 3F_2 F_{166} F_{266} + 2F_{22} F_{66} F_{166} - 2F_{12} F_{66} F_{266} + F_{66}^2 F_{122}) \dots (359)$$

$$D = F_{66}^2 F_{22} - 3F_{266} F_{66} F_2 - 9F_{266}^2 \dots (360)$$

The points of tangency are given by the repeating σ_2 roots of Eq. 356. The closed-form solution of the cubic Eq. 356 yields the following condition of constraint:

$$27A^2 D^2 - 18ABCD + 4AD - B^2 C^2 + 4B^3 D = 0 \dots (361)$$

A functional, Ψ , is defined from a least-squares fit of nl failure data, $(\sigma_{1i}, \sigma_{2i}, \sigma_{6i})$ for $i = 1, 2, \dots, nl$, and the constraint condition of Eq. 361 that is included by means of Lagrange multipliers:

$$\begin{aligned} \Psi = & \sum_{i=1}^{nl} (F_1 \sigma_{1i} + F_2 \sigma_{2i} + F_{11} \sigma_{1i}^2 + F_{22} \sigma_{2i}^2 + F_{66} \sigma_{6i}^2 + 2F_{12} \sigma_{1i} \sigma_{2i} + 3F_{112} \sigma_{1i}^2 \sigma_{2i} \\ & + 3F_{122} \sigma_{1i} \sigma_{2i}^2 + 3F_{166} \sigma_{1i} \sigma_{6i}^2 + 3F_{266} \sigma_{2i} \sigma_{6i}^2 - 1)^2 \\ & + \mu_1 (27A^2 D^2 - 18ABCD + 4AD - B^2 C^2 + 4B^3 D) \end{aligned} \dots (362)$$

where μ_1 is a Lagrange multiplier.

Minimizing the functional, Ψ , with respect to F_{166} , F_{266} , and μ_1 leads to a set of three nonlinear simultaneous equations:

$$\frac{\partial \Psi}{\partial F_{166}} = 0, \quad \frac{\partial \Psi}{\partial F_{266}} = 0, \quad \frac{\partial \Psi}{\partial \mu_1} = 0 \dots (363)$$

Simultaneous solution of Eq. 363 (MIT Publications 1988) gives F_{166} , F_{266} , and μ_1 .

APPENDIX III. DERIVATION OF EQUATIONS 74, 75, AND 76

The asymptotic equations required for the satisfaction of condition (a) (see section 3.3), that are the same as Eqs. 68 through 73, are given by the following expressions:

$$F_{11} + 3F_{112}\sigma_2 + 3F_{113}\sigma_3 = 0 \dots\dots\dots (364)$$

$$F_{22} + 3F_{122}\sigma_1 + 3F_{223}\sigma_3 = 0 \dots\dots\dots (365)$$

$$F_{33} + 3F_{133}\sigma_1 + 3F_{233}\sigma_2 = 0 \dots\dots\dots (366)$$

$$2F_{12} + 3F_{112}\sigma_1 + 3F_{122}\sigma_2 + 3F_{123}\sigma_3 = 0 \dots\dots\dots (367)$$

$$2F_{13} + 3F_{113}\sigma_1 + 3F_{133}\sigma_3 + 3F_{123}\sigma_2 = 0 \dots\dots\dots (368)$$

$$2F_{23} + 3F_{223}\sigma_2 + 3F_{233}\sigma_3 + 3F_{123}\sigma_1 = 0 \dots\dots\dots (369)$$

Addition of Eqs. 365 and 366 and solution for σ_1 yields the expression:

$$\sigma_1 = -\frac{F_{22} + F_{33} + 3F_{223}\sigma_3 + 3F_{233}\sigma_2}{3(F_{122} + F_{133})} \dots\dots\dots (370)$$

Likewise, expressions for σ_2 , and σ_3 are obtained from the combination of Eqs. 364 and 366, and Eq. 364 and 365, respectively:

$$\sigma_2 = -\frac{F_{11} + F_{33} + 3F_{113}\sigma_3 + 3F_{133}\sigma_1}{3(F_{112} + F_{233})} \dots\dots\dots (371)$$

$$\sigma_3 = -\frac{F_{11} + F_{22} + 3F_{122}\sigma_1 + 3F_{112}\sigma_2}{3(F_{113} + F_{223})} \dots\dots\dots (372)$$

Substituting Eqs. 372, 371, and 370 into Eqs. 367, 368, and 369, respectively, and rearranging gives the following equations:

$$(3F_{112}F_{113} + 3F_{112}F_{223} - 6F_{122}F_{123})\sigma_1 + (3F_{122}F_{113} + 3F_{122}F_{223} - 6F_{112}F_{123})\sigma_2 \dots\dots\dots (373)$$

$$= 2F_{11}F_{123} + 2F_{22}F_{123} - 2F_{12}F_{113} - 2F_{12}F_{223}$$

$$(3F_{113}F_{112} + 3F_{113}F_{233} - 6F_{133}F_{123})\sigma_1 + (3F_{133}F_{112} + 3F_{133}F_{233} - 6F_{113}F_{123})\sigma_3 \dots\dots\dots (374)$$

$$= 2F_{11}F_{123} + 2F_{33}F_{123} - 2F_{13}F_{112} - 2F_{13}F_{233}$$

$$(3F_{223}F_{122} + 3F_{223}F_{133} - 6F_{233}F_{123})\sigma_2 + (3F_{233}F_{122} + 3F_{233}F_{133} - 6F_{223}F_{123})\sigma_3 \dots\dots\dots (375)$$

$$= 2F_{22}F_{123} + 2F_{33}F_{123} - 2F_{23}F_{122} - 2F_{23}F_{133}$$

Eqs. 373 through 375 are the same as Eqs. 74 through 76, respectively. It should be noted that Eqs. 367 to 369 are three-variable dependent equations, i.e., each is a functions of σ_1 , σ_2 , and σ_3 . Eqs. 373-375, however, are two-variable dependent expressions and, thus, simpler to manipulate mathematically.

APPENDIX IV. DERIVATION OF EQUATIONS 115 THROUGH 118

The asymptotic equations required for satisfaction of condition (a) are given by Eqs. 376 and 377:

$$F_{11} + 3F_{112}\sigma_2 + 3F_{113}\sigma_3 = 0 \dots\dots\dots(376)$$

$$F_{33} + 3F_{133}\sigma_1 + 3F_{233}\sigma_2 = 0 \dots\dots\dots(377)$$

The goal in what follows is to extract the asymptotic equations associated with the planes described by Eqs. 376 and 377.

Suppose that the asymptotic plane given by Eq. 376 is parallel with the σ_1 axis and intersects the open-ended failure surface as shown in Fig. 4. Adjustment in the F_{112} and F_{113} terms orients this plane with respect to the σ_1 axis. Closure is accomplished by requiring that the plane of Eq. 376 pass through the line $(\sigma_1, -Y', -Z')$, where $-Y'$ and $-Z'$ are uniaxial compressive strengths along the σ_2 and σ_3 axes, respectively. Thus, Eq. 376 can be modified to become an asymptotic plane for the failure surface (see Fig. 5).

Substituting $\sigma_2 = -Y'$ and $\sigma_3 = -Z'$ into Eq. 67 and rearranging the result leads to the following relation:

$$\begin{aligned} &(-3F_{112}Y' - 3F_{113}Z' + F_{11})\sigma_1^2 + (3F_{122}Y'^2 + 3F_{133}Z'^2 - 3F_{12}Y' - 3F_{23}Z' + F_1)\sigma_1 \\ &+ (-3F_{233}Z'^2 Y' - 3F_{223}Y'^2 Z' + 2F_{23}Y'Z' + F_{22}Y'^2 + F_{33}Z'^2 - F_3Z' - F_2Y' - I) = 0 \dots\dots\dots(378) \end{aligned}$$

For an infinity of σ_1 roots to exist the following conditions from Eq. 378 need to be satisfied:

$$-3F_{112}Y' - 3F_{113}Z' + F_{11} = 0 \dots\dots\dots(379)$$

$$3F_{122}Y'^2 + 3F_{133}Z'^2 - 3F_{12}Y' - 3F_{23}Z' + F_1 = 0 \dots\dots\dots(380)$$

$$-3F_{233}Z'^2 Y' - 3F_{223}Y'^2 Z' + 2F_{23}Y'Z' + F_{22}Y'^2 + F_{33}Z'^2 - F_3Z' - F_2Y' - I = 0 \dots\dots\dots(381)$$

Eq. 381 has the same form that results if $\sigma_2 = -Y'$ and $\sigma_3 = -Z'$ are substituted into the original failure criterion (Eq. 61) and, therefore, it can not be considered as a limiting (asymptotic) equation. Thus, only Eqs. 379 and 380 are retained and Eq. 381 is no longer considered.

Similarly, suppose that the asymptotic plane given by Eq. 377 is parallel with the σ_3 axis and intersects the open-ended failure surface as shown in Fig. 4. Adjustment in the F_{133} and F_{233} terms orients this plane with respect to the σ_3 axis. Closure is accomplished by requiring that the plane represented by Eq. 377 passes through the line $(-X', -Y', \sigma_3)$,

where $-X'$ and $-Y'$ are uniaxial compressive strengths along the σ_1 and σ_2 axes, respectively. Thus, Eq. 377 can be modified to become an asymptotic plane for the failure surface (see Fig. 5).

Substituting $\sigma_1 = -X'$ and $\sigma_2 = -Y'$ into Eq. 67 and rearranging the result leads to the following relation:

$$\begin{aligned} & (-3F_{133}X' - 3F_{233}Y' + F_{33})\sigma_3^2 + (3F_{113}X'^2 + 3F_{223}Y'^2 - 3F_{13}X' - 3F_{23}Y' + F_3)\sigma_3 \\ & + (-3F_{112}X'^2 Y' - 3F_{122}Y'^2 X' + 2F_{12}X'Y' + F_{11}X'^2 + F_{22}Y'^2 - F_1X' - F_2Y' - I) = 0 \end{aligned} \quad (382)$$

Similarly, for an infinity of σ_3 roots to exist the following conditions from Eq. 382 need to be satisfied:

$$-3F_{133}X' - 3F_{233}Y' + F_{33} = 0 \quad (383)$$

$$3F_{113}X'^2 + 3F_{223}Y'^2 - 3F_{13}X' - 3F_{23}Y' + F_3 = 0 \quad (384)$$

$$-3F_{112}X'^2 Y' - 3F_{122}Y'^2 X' + 2F_{12}X'Y' + F_{11}X'^2 + F_{22}Y'^2 - F_1X' - F_2Y' - I = 0 \quad (385)$$

Eq. 385 has the same form that results if $\sigma_1 = -X'$ and $\sigma_2 = -Y'$ are substituted into the original failure criterion (Eq. 61) and, therefore, it can not be considered as a limiting (asymptotic) equation. Thus, only Eqs. 383 and 384 are retained and Eq. 385 is no longer considered.

Eqs. 379, 380, 383 and 384 are identical to Eqs. 115 through 118.

APPENDIX V.

THEORETICAL DETERMINATION OF NORMAL-SHEAR INTERACTION COEFFICIENTS

The following asymptotic expressions, originally given by Eqs. 130 and 131, will be shown to provide the normal-shear interaction coefficients F_{144} , F_{244} , F_{344} , F_{155} , F_{255} , and F_{355} :

$$3F_{144}\sigma_1 + 3F_{244}\sigma_2 + 3F_{344}\sigma_3 + F_{44} = 0 \quad \dots\dots\dots (386)$$

$$3F_{155}\sigma_1 + 3F_{255}\sigma_2 + 3F_{355}\sigma_3 + F_{55} = 0 \quad \dots\dots\dots (387)$$

Coefficients of each equation are determined in a separate subsection.

DERIVATION OF STRENGTH COEFFICIENTS F_{144} , F_{244} , AND F_{344}

One way of rewriting Eq. 386 is as follows:

$$\sigma_2 = -\frac{3F_{144}\sigma_1 + 3F_{344}\sigma_3 + F_{44}}{3F_{244}} \quad \dots\dots\dots (388)$$

Substituting σ_2 from Eq. 388 into Eq. 67 and rearranging, leads to the following convenient form:

$$\begin{aligned} & (A_{14}\sigma_1^3 + A_{24}\sigma_1^2 + A_{34}\sigma_1 + A_{44}) + (B_{14}\sigma_3^3 + B_{24}\sigma_3^2 + B_{34}\sigma_3 + B_{44}) \\ & + (C_{14}\sigma_1^2\sigma_3 + C_{24}\sigma_1\sigma_3^2 + C_{34}\sigma_1\sigma_3) = 0 \quad \dots\dots\dots (389) \end{aligned}$$

where,

$$\begin{aligned} A_{14} &= 27(F_{144}^2 F_{122} - F_{244} F_{144} F_{112}) \\ A_{24} &= 9(F_{244}^2 F_{11} + 2F_{144} F_{44} F_{122} - F_{244} F_{44} F_{112} - 2F_{144} F_{244} F_{12} + F_{144}^2 F_{22}) \\ A_{34} &= 3(F_{44}^2 F_{122} + 2F_{144} F_{44} F_{22} - 3F_{144} F_{244} F_2 - 2F_{244} F_{44} F_{12} + 3F_{244}^2 F_1) \\ A_{44} &= 0.5(F_{44}^2 F_{22} - 3F_{244} F_{44} F_2 - 9F_{244}^2) \\ B_{14} &= 27(F_{344}^2 F_{223} - F_{244} F_{344} F_{233}) \\ B_{24} &= 9(F_{344}^2 F_{22} + 2F_{344} F_{44} F_{223} - F_{244} F_{44} F_{233} - 2F_{244} F_{344} F_{23} + F_{244}^2 F_{33}) \quad \dots\dots\dots (390) \\ B_{34} &= 3(F_{44}^2 F_{223} + 2F_{344} F_{44} F_{22} - 3F_{244} F_{344} F_2 - 2F_{244} F_{44} F_{32} + 3F_{244}^2 F_3) \\ B_{44} &= 0.5(F_{44}^2 F_{22} - 3F_{244} F_{44} F_2 - 9F_{244}^2) \end{aligned}$$

$$C_{14} = 27(F_{244}^2 F_{113} + 2F_{144} F_{344} F_{122} - F_{244} F_{344} F_{112} + F_{144}^2 F_{223} - 2F_{144} F_{244} F_{123})$$

$$C_{24} = 27(F_{344}^2 F_{122} + 2F_{344} F_{144} F_{223} - F_{144} F_{244} F_{233} + F_{244}^2 F_{133} - 2F_{244} F_{344} F_{123})$$

$$C_{34} = 18(F_{122} F_{344} F_{44} + F_{144} F_{22} F_{344} + F_{144} F_{44} F_{223} - F_{244} F_{344} F_{12} - F_{144} F_{244} F_{23} + F_{244}^2 F_{13} - F_{44} F_{244} F_{123})$$

The closed-form solution of the bicubic Eq. 389 yields repeating, real roots for σ_1 and σ_3 at points of tangency of Eq. 388 with respect to Eq. 389. Some side conditions are necessary to ensure solution of Eq. 389. The repeating roots and side conditions are given by the relations:

$$27 A_{14}^2 A_{44} A_{44}^2 - 18 A_{14} A_{24} A_{34} A_{44} + 4 A_{14} A_{34}^3 - A_{24}^2 A_{34}^2 + A_{24}^3 A_{44} = 0 \dots\dots\dots (391)$$

$$27 B_{14}^2 B_{44}^2 - 18 B_{14} B_{24} B_{34} B_{44} + 4 B_{14} B_{34}^3 - B_{24}^2 B_{34}^2 + B_{24}^3 B_{44} = 0 \dots\dots\dots (392)$$

$$C_{14} = 27(F_{244}^2 F_{113} + 2F_{144} F_{344} F_{122} - F_{244} F_{344} F_{112} + F_{144}^2 F_{223} - 2F_{144} F_{244} F_{123}) = 0 \dots\dots\dots (393)$$

$$C_{24} = 27(F_{344}^2 F_{122} + 2F_{344} F_{144} F_{223} - F_{144} F_{244} F_{233} + F_{244}^2 F_{133} - 2F_{244} F_{344} F_{123}) = 0 \dots\dots\dots (394)$$

$$C_{34} = 18(F_{122} F_{344} F_{44} + F_{144} F_{22} F_{344} + F_{144} F_{44} F_{223} - F_{244} F_{344} F_{12} - F_{144} F_{244} F_{23} + F_{244}^2 F_{13} - F_{44} F_{244} F_{123}) = 0 \dots\dots\dots (395)$$

The following least squares functional can be set up by assuming that there are $n2$ sets of data, $(\sigma_{2i}, \sigma_{3i}, \sigma_{4i})$ for $(j = 1, 2, \dots, n2)$, and by using Eq. 67 and Eqs. 391-395:

$$\begin{aligned} \Omega = & \sum_{i=1}^{n2} (F_2 \sigma_{2i} + F_3 \sigma_{3i} + F_{22} \sigma_{2i}^2 + F_{33} \sigma_{3i}^2 + F_{44} \sigma_{4i}^2 + 2F_{23} \sigma_{2i} \sigma_{3i} + 3F_{223} \sigma_{2i}^2 \sigma_{3i} \\ & + 3F_{233} \sigma_{3i}^2 \sigma_{2i} + 3F_{244} \sigma_{2i} \sigma_{4i}^2 + 3F_{344} \sigma_{3i} \sigma_{4i}^2 + 3F_{244} \sigma_{2i} \sigma_{4i}^2 - 1)^2 \\ & + v_1 (27 A_{14}^2 A_{44}^2 - 18 A_{14} A_{24} A_{34} A_{44} + 4 A_{14} A_{34}^3 - A_{24}^2 A_{34}^2 + A_{24}^3 A_{44}) \dots\dots\dots (396) \\ & + v_2 (27 B_{14}^2 B_{44}^2 - 18 B_{14} B_{24} B_{34} B_{44} + 4 B_{14} B_{34}^3 - B_{24}^2 B_{34}^2 + B_{24}^3 B_{44}) \\ & + v_3 C_{14} + v_4 C_{24} + v_5 C_{34} = 0 \end{aligned}$$

where v_1 through v_5 are Lagrange multipliers. The functional, Ω , reaches an extreme value (maximum or minimum) when the following conditions are imposed:

$$\begin{aligned} \frac{\partial \Omega}{\partial F_{144}} = 0, \quad \frac{\partial \Omega}{\partial F_{244}} = 0, \quad \frac{\partial \Omega}{\partial F_{344}} = 0, \quad \frac{\partial \Omega}{\partial v_1} = 0, \\ \frac{\partial \Omega}{\partial v_2} = 0, \quad \frac{\partial \Omega}{\partial v_3} = 0, \quad \frac{\partial \Omega}{\partial v_4} = 0, \quad \frac{\partial \Omega}{\partial v_5} = 0, \dots\dots\dots (397) \end{aligned}$$

Thus, a set of eight non-linear simultaneous equations is obtained. A mathematical package such as MACSYMA (MIT Publications 1988) is employed to solve for the coefficients F_{144} , F_{244} , and F_{344} from Eq. 397. From experiments described in sections 6.4.2 and 6.5.3 values of F_{144} , F_{244} , and F_{344} for SR-200 beryllium are -1.29×10^{-13}

MPa⁻³ (-4.21×10^{-11} ksi⁻³), -9.63×10^{-9} MPa⁻³ (-3.16×10^{-6} ksi⁻³), and 3.30×10^{-14} MPa⁻³ (1.08×10^{-11} ksi⁻³), respectively.

DERIVATION OF STRENGTH COEFFICIENTS F_{155} , F_{255} , AND F_{355}

One way of rewriting Eq. 387 as follows:

$$\sigma_1 = -\frac{3F_{255}\sigma_2 + 3F_{355}\sigma_3 + F_{55}}{3F_{155}} \dots\dots\dots (398)$$

Substituting σ_1 from Eq. 398 into Eq. 67 and rearranging leads to the following convenient form:

$$(A_{15}\sigma_2^3 + A_{25}\sigma_2^2 + A_{35}\sigma_2 + A_{45}) + (B_{15}\sigma_3^3 + B_{25}\sigma_3^2 + B_{35}\sigma_3 + B_{45}) \dots\dots\dots (399) \\ + (C_{15}\sigma_2^2\sigma_3 + C_{25}\sigma_2\sigma_3 + C_{35}\sigma_2\sigma_3) = 0$$

where,

$$\begin{aligned} A_{15} &= 27(F_{255}^2 F_{112} - F_{255} F_{155} F_{122}) \\ A_{25} &= 9(F_{255}^2 F_{11} + 2F_{255} F_{55} F_{112} - F_{155} F_{55} F_{122} - 2F_{155} F_{255} F_{21} + F_{155}^2 F_{22}) \\ A_{35} &= 3(F_{55}^2 F_{112} + 2F_{255} F_{55} F_{11} - 3F_{155} F_{255} F_{11} - 2F_{155} F_{55} F_{21} + 3F_{155}^2 F_{22}) \\ A_{45} &= 0.5(F_{55}^2 F_{11} - 3F_{155} F_{55} F_{11} - 9F_{155}^2) \\ B_{15} &= 27(F_{355}^2 F_{113} - F_{155} F_{355} F_{133}) \\ B_{25} &= 9(F_{355}^2 F_{11} + 2F_{355} F_{55} F_{113} - F_{155} F_{55} F_{133} - 2F_{155} F_{355} F_{31} + F_{155}^2 F_{33}) \dots\dots\dots (400) \\ B_{35} &= 3(F_{55}^2 F_{113} + 2F_{355} F_{55} F_{11} - 3F_{155} F_{355} F_{11} - 2F_{155} F_{55} F_{31} + 3F_{155}^2 F_{33}) \\ B_{45} &= 0.5(F_{55}^2 F_{11} - 3F_{155} F_{55} F_{11} - 9F_{155}^2) \\ C_{15} &= 27(F_{255}^2 F_{113} + 2F_{255} F_{355} F_{112} - F_{155} F_{355} F_{122} + F_{155}^2 F_{223} - 2F_{155} F_{255} F_{123}) \\ C_{25} &= 27(F_{355}^2 F_{112} + 2F_{355} F_{255} F_{113} - F_{155} F_{255} F_{133} + F_{155}^2 F_{233} - 2F_{155} F_{355} F_{123}) \\ C_{35} &= 18(F_{255} F_{355} F_{11} + F_{255} F_{55} F_{113} + F_{355} F_{55} F_{112} - F_{255} F_{155} F_{13} - F_{355} F_{155} F_{12} \\ &\quad + F_{155}^2 F_{23} - F_{55} F_{155} F_{123}) \end{aligned}$$

The closed-form solution of the cubic Eq. 399 yields repeating, real roots for σ_2 and σ_3 at points of tangency of Eq. 398 with respect to 399. Some side conditions are necessary to ensure solution of Eq. 399. The repeating roots and side conditions are given by the relations:

$$27 A_{15}^2 A_{45}^2 - 18 A_{15} A_{25} A_{35} A_{45} + 4 A_{15} A_{35}^3 - A_{25}^2 A_{35}^2 + A_{25}^3 A_{45} = 0 \dots\dots\dots (401)$$

$$27 B_{15}^2 B_{45}^2 - 18 B_{15} B_{25} B_{35} B_{45} + 4 B_{15} B_{35}^3 - B_{25}^2 B_{35}^2 + B_{25}^3 B_{45} = 0 \dots\dots\dots (402)$$

$$C_{15} = 27(F_{255}^2 F_{113} + 2F_{255}F_{355}F_{112} - F_{155}F_{355}F_{122} + F_{155}^2 F_{223} - 2F_{155}F_{255}F_{123} = 0 \dots\dots\dots(403)$$

$$C_{25} = 27(F_{355}^2 F_{112} + 2F_{355}F_{255}F_{113} - F_{155}F_{255}F_{133} - 2F_{155}F_{355}F_{223} + F_{155}^2 F_{233} - 2F_{155}F_{355}F_{123}) = 0 \dots\dots\dots(404)$$

$$C_{35} = 18(F_{255}F_{355}F_{11} + F_{255}F_{55}F_{113} + F_{355}F_{55}F_{112} - F_{255}F_{155}F_{13} - F_{355}F_{155}F_{12} + F_{155}^2 F_{23} - F_{55}F_{155}F_{123}) = 0 \dots\dots\dots(405)$$

The following least squares functional can be set up by assuming that there are $n3$ sets of data, $(\sigma_{2i}, \sigma_{3i}, \sigma_{5i})$ for $(j = 1, 2, \dots, n3)$, and by using Eq. 401-405:

$$\begin{aligned} \Pi = & \sum_{i=1}^{n3} (F_2 \sigma_{2i}^2 + F_3 \sigma_{3i}^2 + F_{22} \sigma_{2i}^4 + F_{33} \sigma_{3i}^4 + F_{55} \sigma_{5i}^2 + 2F_{23} \sigma_{2i}^2 \sigma_{3i}^2 + 3F_{223} \sigma_{2i}^2 \sigma_{3i}^2 \\ & + 3F_{233} \sigma_{3i}^2 \sigma_{2i}^2 + 3F_{255} \sigma_{2i}^2 \sigma_{5i}^2 + 3F_{355} \sigma_{3i}^2 \sigma_{5i}^2 + 3F_{255} \sigma_{2i}^2 \sigma_{5i}^2 - 1)^2 \\ & + \xi_1 (27 A_{15}^2 A_{55}^2 - 18 A_{15} A_{25} A_{35} A_{55} + 4 A_{15} A_{35}^3 - A_{25}^2 A_{35}^2 + A_{25}^3 A_{55}) \dots\dots\dots(406) \\ & + \xi_2 (27 B_{15}^2 B_{55}^2 - 18 B_{15} B_{25} B_{35} B_{55} + 4 B_{15} B_{35}^3 - B_{25}^2 B_{35}^2 + B_{25}^3 B_{55}) \\ & + \xi_3 C_{15} + \xi_4 C_{25} + \xi_5 C_{35} \end{aligned}$$

where ξ_1 through ξ_5 are Lagrange multipliers. The functional, Π , reaches an extreme value (maximum or minimum) when the following conditions are imposed:

$$\begin{aligned} \frac{\partial \Pi}{\partial F_{155}} = 0, \quad \frac{\partial \Pi}{\partial F_{255}} = 0, \quad \frac{\partial \Pi}{\partial F_{355}} = 0, \quad \frac{\partial \Pi}{\partial \xi_1} = 0, \\ \frac{\partial \Pi}{\partial \xi_2} = 0, \quad \frac{\partial \Pi}{\partial \xi_3} = 0, \quad \frac{\partial \Pi}{\partial \xi_4} = 0, \quad \frac{\partial \Pi}{\partial \xi_5} = 0, \dots\dots\dots(407) \end{aligned}$$

Thus, a set of eight non-linear simultaneous equations is obtained. MACSYMA (MIT Publications 1988) is employed to solve for the coefficients F_{155} , F_{255} , and F_{355} from Eq. 407. From experiments described in sections 6.4.3 and 6.5.3 values of F_{155} , F_{255} , and F_{355} for SR-200 beryllium are -9.40×10^{-9} MPa⁻³ (-3.09×10^{-6} ksi⁻³), -2.81×10^{-10} MPa⁻³ (-9.22×10^{-8} ksi⁻³), and 2.04×10^{-10} MPa⁻³ (6.70×10^{-8} ksi⁻³), respectively.

APPENDIX VI.

45° IN-PLANE STRESS TRANSFORMATION

General transformation of second-order stress tensors is as follows (Sokolnikoff 1964):

$$\sigma_{ij} = \alpha_{ki} \alpha_{lj} \sigma_{kl} \dots\dots\dots (408)$$

where α_{ki} and α_{li} are direction cosines for a second-order tensor transformation and σ_{kl} and σ_{ij} are the original and transformed stress tensors, respectively (Lekhnitskii 1987). In matrix form Eq. 408 becomes:

$$[\sigma_M] = [R]^T [\sigma_L] [R] \dots\dots\dots (409)$$

where $[R]$ is a matrix of direction cosines relating the coordinate and material axes, and $[\sigma_M]$ and $[\sigma_L]$ are the stress tensors with respect to the material and loading axes, respectively (see Fig. 171). For an in-plane uniaxial tensile test on a specimen whose material axes are oriented 45° with respect to the loading axes, $[\sigma_L]$ and $[R]$ are as follows:

$$[\sigma_L] = \begin{bmatrix} \sigma_x & 0 & 0 \\ 0 & 0 & 0 \\ 0 & 0 & 0 \end{bmatrix}; \quad [R] = \begin{bmatrix} 0.707 & 0.707 & 0 \\ -0.707 & 0.707 & 0 \\ 0 & 0 & 1 \end{bmatrix} \dots\dots\dots (410)$$

Substituting $[\sigma_L]$ and $[R]$ into Eq. 409 leads to the following material stress tensor:

$$[\sigma_M] = \sigma_x \begin{bmatrix} \frac{1}{2} & \frac{1}{2} & 0 \\ \frac{1}{2} & \frac{1}{2} & 0 \\ 0 & 0 & 0 \end{bmatrix} \dots\dots\dots (411)$$

Thus, the non-zero components of stress of $[\sigma_M]$ are:

$$\sigma_1 = \sigma_2 = \sigma_6 = 0.5\sigma_x \dots\dots\dots (412)$$

where σ_1 , σ_2 , and σ_6 are the in-plane normal and shearing components of the $[\sigma_M]$ stress matrix, and σ_x is the axial component of stress of the $[\sigma_L]$ matrix. It should be noted that the out-of-plane components of stress σ_3 , σ_4 , and σ_5 are zero.

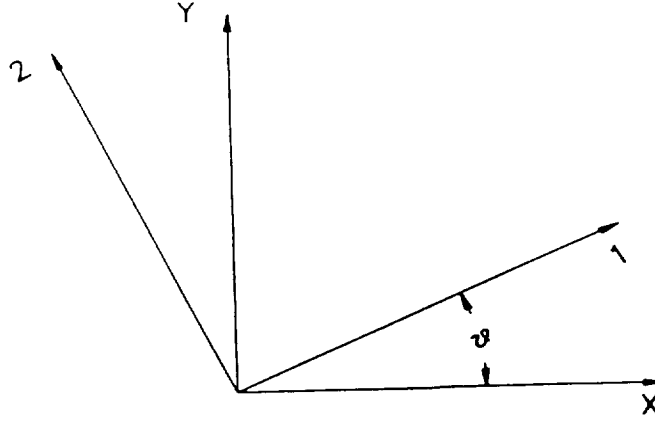


FIG. 171. Rotation of In-Plane Axes

ELASTIC PROPERTIES WITH RESPECT TO MATERIAL AXES

The constitutive equations for linear orthotropic material are as follows (Sokolnikoff 1964):

$$\varepsilon_1 = \frac{\sigma_1}{E_1} - \nu_{12} \frac{\sigma_2}{E_2} - \nu_{13} \frac{\sigma_3}{E_3} \dots\dots\dots (413)$$

$$\varepsilon_2 = \frac{\sigma_2}{E_2} - \nu_{21} \frac{\sigma_1}{E_1} - \nu_{23} \frac{\sigma_3}{E_3} \dots\dots\dots (414)$$

$$\varepsilon_3 = \frac{\sigma_3}{E_3} - \nu_{31} \frac{\sigma_1}{E_1} - \nu_{32} \frac{\sigma_2}{E_2} \dots\dots\dots (415)$$

$$\gamma_6 = \frac{\sigma_6}{G_{12}} \dots\dots\dots (416)$$

where σ_i are the six components of stress with respect to the material axes, ε_i are components of strain with respect to the principal material axes, γ_6 is the in-plane shearing component of strain, E_i are the three principal moduli of elasticity, ν_{ij} are the Poisson's ratios, and G_{12} is the in-plane shear modulus. Substitution of Eq. 412 into Eqs. 413-416 leads to the following stress-strain relations:

$$\varepsilon_1 = \sigma_1 \left[\frac{1}{2E_1} - \frac{\nu_{12}}{2E_2} \right] \dots\dots\dots (417)$$

$$\varepsilon_2 = \sigma_1 \left[\frac{1}{2E_2} - \frac{\nu_{21}}{2E_1} \right] \dots\dots\dots (418)$$

$$\varepsilon_3 = -\sigma_1 \left[\frac{\nu_{31}}{2E_1} + \frac{\nu_{32}}{2E_2} \right] \dots\dots\dots (419)$$

$$\varepsilon_6 = \frac{\sigma_1}{2G_{12}} \dots\dots\dots (420)$$

Moreover, stiffness coefficients (Lekhnitskii 1987) are defined as follows:

$$S_{1x} = \frac{\sigma_x}{\varepsilon_1} = \frac{2E_1E_2}{E_2 - \nu_{12}E_1} \dots\dots\dots (421)$$

$$S_{2x} = \frac{\sigma_x}{\varepsilon_2} = \frac{2E_1E_2}{E_1 - \nu_{21}E_2} \dots\dots\dots (422)$$

$$S_{3x} = \frac{\sigma_x}{\varepsilon_3} = -\frac{2E_1E_2}{\nu_{31}E_2 + \nu_{32}E_1} \dots\dots\dots (423)$$

By substituting strength values and Poisson's ratios that are obtained from the 45° tensile test (see section 4.2.2) and an earlier report (Fenn et al. 1967), the following coefficients of the stiffness matrix are obtained for cross-rolled beryllium sheet material:

$$\begin{aligned} S_{1x} &= 646.7 \text{ GPa} (93.8 \times 10^6 \text{ psi}) \\ S_{2x} &= 635.0 \text{ GPa} (92.1 \times 10^6 \text{ psi}) \dots\dots\dots (424) \\ S_{3x} &= 17.9 \text{ GPa} (2.6 \times 10^6 \text{ psi}) \end{aligned}$$

ELASTIC PROPERTIES WITH RESPECT TO LOADING AXES

In a manner that is analogous to the stress transformation of Eq. 409, the strain tensor can be transformed from material to loading axes as follows (Lekhnitskii 1987):

$$[\varepsilon_M] = [R]^T [\varepsilon_L] [R] \dots\dots\dots (425)$$

where [R] is a matrix of direction cosines that relate the coordinate and material axes, and $[\varepsilon_M]$ and $[\varepsilon_L]$ are strain tensors with respect to the material and loading axes, respectively.

When the material axes are oriented 45° with respect to the loading axis, the relations obtained from such a transformation are:

$$\epsilon_x = 0.5(\epsilon_1 + \epsilon_2 + 2\epsilon_6) \dots\dots\dots (426)$$

$$\epsilon_y = 0.5(\epsilon_1 + \epsilon_2 - 2\epsilon_6) \dots\dots\dots (427)$$

where ϵ_x , ϵ_y are components of strain with respect to the loading axis, and ϵ_1 , ϵ_2 , and ϵ_3 , are components of strain obtained from Eqs. 417-420. Therefore, the modulus of elasticity, E_x , and the stiffness coefficient, S_{yx} , for the loading axes are calculated for beryllium sheet material as follows (see section 4.2.2):

$$E_x = \frac{\sigma_x}{\epsilon_x} = 295.2 \text{ GPa} (42.8 \times 10^6 \text{ psi}) \dots\dots\dots (428)$$

$$S_{yx} = \frac{\sigma_x}{\epsilon_y} = -3,753.5 \text{ GPa} (-544.4 \times 10^6 \text{ psi}) \dots\dots\dots (429)$$

where ϵ_x and ϵ_y are obtained from strain gage measurements (Gardner 1990) at 0° and 90° with respect to the load axis, respectively, for a loading stress σ_x .

APPENDIX VII.

STRESS TRANSFORMATION FOR ROTATION OF IN-PLANE MATERIAL AXES

General transformation of stress tensors is as follows (Sokolnikoff 1964):

$$\sigma_{ij} = \alpha_{ki} \alpha_{lj} \sigma_{kl} \dots\dots\dots (430)$$

where α_{ki} and α_{li} are direction cosines for a second-order tensor transformation and σ_{ij} and σ_{kl} are the transformed and original stress tensors, respectively. In matrix form Eq. 430 becomes:

$$[\sigma_M] = [R]^T [\sigma_L] [R] \dots\dots\dots (431)$$

where $[R]$ is a matrix of direction cosines relating the coordinate and material axes, and $[\sigma_M]$ and $[\sigma_L]$ are the material and load stress tensors, respectively. Suppose that two of the principal material axes, Y and Z are rotated through an angle θ about a normal that is parallel with the other material direction, X , (see Fig. 172).

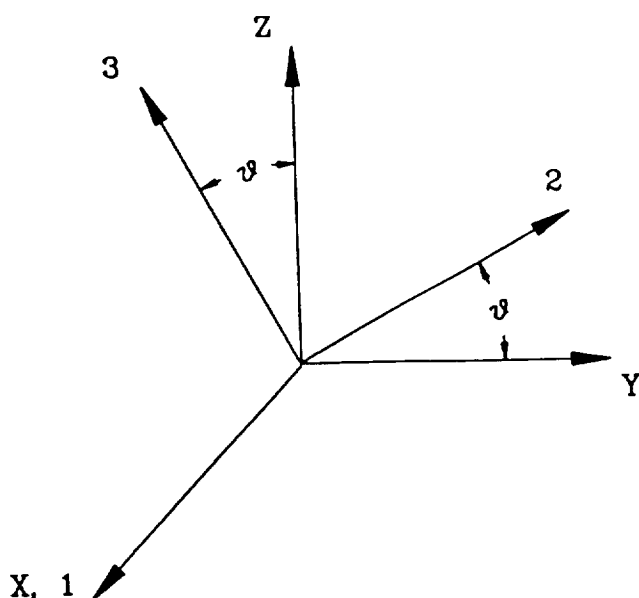


FIG. 172. Rotation of an In-Plane Axis

The stress transformation of Eq. 431 for a compressive load in the z -direction, $-\sigma_z$, requires the following $[\sigma_L]$ and $[R]$ matrices:

$$[\sigma_L] = \begin{bmatrix} 0 & 0 & 0 \\ 0 & 0 & 0 \\ 0 & 0 & -\sigma_z \end{bmatrix}; \quad [R] = \begin{bmatrix} 1 & 0 & 0 \\ 0 & \cos \theta & \sin \theta \\ 0 & -\sin \theta & \cos \theta \end{bmatrix} \dots\dots\dots (432)$$

Substituting $[\sigma_L]$ and $[R]$ from Eq. 432 into Eq. 431 leads to the following material stress tensor:

$$[\sigma_M] = \sigma_z \begin{bmatrix} 0 & 0 & 0 \\ 0 & -\sin^2 \theta & \frac{\sin(2\theta)}{2} \\ 0 & \frac{\sin(2\theta)}{2} & -\cos^2 \theta \end{bmatrix} \dots\dots\dots (433)$$

For the case in which the axes are rotated through an angle of 45° Eq. 433 becomes:

$$[\sigma_M] = \sigma_z \begin{bmatrix} 0 & 0 & 0 \\ 0 & \frac{-1}{2} & \frac{1}{2} \\ 0 & \frac{1}{2} & \frac{-1}{2} \end{bmatrix} \dots\dots\dots (434)$$

Thus, the non-zero components of stress of $[\sigma_M]$ are:

$$\sigma_2 = \sigma_3 = -\sigma_4 = -0.5\sigma_z \dots\dots\dots (435)$$

where σ_i for $i = 1, 2, \dots, 6$ are components of the symmetric stress tensor, σ_{ij} .

APPENDIX VIII.

LEAST SQUARES SCHEME FOR EVALUATION OF UNKNOWN COEFFICIENTS

The least squares scheme required for evaluation of the interaction strength coefficients calls for a polynomial regression technique that involves more than one variable. The purpose of this appendix is to summarize the method of least squares used for determination of the principal and normal-shear interaction coefficients used in the failure criterion for SR-200 beryllium.

Here, it is assumed that a best fit is required for a function that depends on multiple variables. The experimental data associated with this function yield $n, k+1$ tuples $(x_{11}, x_{21}, x_{31}, \dots, x_{k1}, y_1), (x_{12}, x_{22}, x_{32}, \dots, x_{k2}, y_2), \dots, (x_{1n}, x_{2n}, x_{3n}, \dots, x_{kn}, y_n)$. The least squares fit equation is (Devore 1987)

$$\begin{aligned}
 & f(a_0, a_1, \dots, a_n, a_0, b_1, \dots, b_n, c_1, \dots, c_n, h_1, \dots, h_n) \\
 &= \sum_{i=1}^n [y_i - (a_0 + a_1 x_{1i} + a_2 x_{2i} + \dots + a_k x_{ki}) \\
 &\quad - (b_1 x_{1i}^2 + b_2 x_{2i}^2 + \dots + b_k x_{ki}^2) - (c_1 x_{1i} x_{2i} + \dots + c_1 x_{(k-1)i} x_{ki}) \dots \\
 &\quad - (h_1 x_{1i}^m + \dots + h_k x_{ki}^m)]^2 \dots \dots \dots (436)
 \end{aligned}$$

where x_{ij} is the value of the i^{th} variable associated with the j^{th} observation, y_i is the computed value of the best-fit function for the i^{th} observation, l is $k(k-1)/2$ so that all quadratic interactions of the n variables are accounted for, and m is the order of the best-fit polynomial. It should be noted that in Eq. 436 only quadratic interactions are shown. However, the method may be used to include higher-order interaction terms. The assumption for using this technique of data fit is that the experimental data obtained for each observation are independent with respect to each other (Devore 1987).

The least squares estimates are those values of the coefficients that minimize the function f . Upon taking partial derivatives of f with respect to each coefficient and equating the partials to zero, a system of linear equations is obtained since the polynomial f is a quadratic function of the coefficients. The matrix representation of this system is given by the following equation,

$$\{y\} = [X]\{a\} \dots \dots \dots (437)$$

where $\{a\}$ represents the unknown coefficients in a vector form, $\{y\}$ is a vector containing the estimated values of the polynomial f for each observation, and $[X]$ is the matrix

containing the powered terms of f . For example, the matrices corresponding to Eq. 437 are:

$$\{y\} = \{y_1, y_2, \dots, y_k\}^T \dots\dots\dots (438)$$

$$\{a\} = \{a_0, a_1, \dots, a_k, b_1, b_2, \dots, b_k, c_1, c_2, \dots, c_l, \dots, h_1, h_2, \dots, h_k\}^T \dots\dots\dots (439)$$

$$[X] = \begin{bmatrix} 1 & x_{11}x_{21}\dots x_{k1}x_{11}^2x_{21}^2\dots x_{k1}^2x_{11}x_{21}\dots x_{(k-1)1}x_{k1}\dots x_{11}^m\dots x_{k1}^m \\ 1 & x_{12}x_{22}\dots x_{k2}x_{12}^2x_{22}^2\dots x_{k2}^2x_{12}x_{22}\dots x_{(k-1)2}x_{k2}\dots x_{12}^m\dots x_{k2}^m \\ 1 & x_{13}x_{23}\dots x_{k3}x_{13}^2x_{23}^2\dots x_{k3}^2x_{13}x_{23}\dots x_{(k-1)3}x_{k3}\dots x_{13}^m\dots x_{k3}^m \\ & \dots \\ 1 & x_{1n}x_{2n}\dots x_{kn}x_{1n}^2x_{2n}^2\dots x_{kn}^2x_{1n}x_{2n}\dots x_{(k-1)n}x_{kn}\dots x_{1n}^m\dots x_{kn}^m \end{bmatrix} \dots\dots\dots (440)$$

The unknown variables of the $\{a\}$ vector are solved using the following method:

- (1) Both sides of Eq. 437 are multiplied by $[X]$ transpose.

$$[X]^T \{y\} = [X]^T [X] \{a\} \dots\dots\dots (441)$$

For n independent observations the products $[X]^T [X]$ and $[X]^T \{y\}$ yield an $n \times n$ matrix and an $n \times 1$ matrix, respectively.

- (2) The inverse of $([X]^T [X])$ is then found using standard matrix operation techniques.

- (3) The $\{a\}$ vector can be computed by multiplying the inverse of $([X]^T [X])$ with $[X]^T \{y\}$ as follows:

$$([X]^T [X])^{-1} [X]^T \{y\} = ([X]^T [X])^{-1} ([X]^T [X]) \{a\} \dots\dots\dots (442)$$

or,

$$\{a\} = ([X]^T [X])^{-1} [X]^T \{y\} \dots\dots\dots (443)$$

It should be noted that if only some of the coefficients found in vector $\{a\}$ are unknown, the same method can be employed to establish the remaining coefficients. This is accomplished by modifying the $\{a\}$ vector such that it includes only the unknown coefficients, the $[X]$ matrix such that it does not include terms associated with the known coefficients, and $\{y\}$ by recomputing the vector to include the known coefficient terms. For the same example presented earlier suppose that all a_i , b_i , and h_i coefficients are known a priori. Then Eqs. 438, 439, and 440 are modified to become:

$$\{y\} = \{y_1', y_2', \dots, y_k'\}^T \dots\dots\dots (444)$$

$$\{a\} = \{c_1, c_2, \dots, c_l\}^T \dots\dots\dots (445)$$

$$[X] = \begin{bmatrix} x_{11}x_{21}\dots x_{(k-1)1}x_{k1} \\ x_{12}x_{22}\dots x_{(k-1)2}x_{k2} \\ x_{13}x_{23}\dots x_{(k-1)3}x_{k3} \\ \dots \\ x_{1i}x_{2i}\dots x_{(k-1)i}x_{ki} \end{bmatrix} \dots\dots\dots (446)$$

APPENDIX IX.

LISTING OF C-PROGRAM TO COMPUTE MAXIMUM SHEARING STRESS

```

/* torcon.c */
#include <stdio.h>
#include <math.h>
#ifdef PI
#define PI 3.1415926536
main() /* a program to compute torsional constants for orthotropic
material */
{
    float beta, kappal, kappa2, mu, theta;
    float betas, kappals, kappa2s;
    float a, b, c, d, g, g1, g2, mt, cl, cn;
    float tn, pi4, clon, conls, mii, maxshr;
    float c2on, con2s, shr4, shr5, inmjsq;
    int m, n, nj, ms, mi, mj;

    printf(" This is a Program to Compute Torsional Constants\n");
    printf(" Maximum Shearing Stresses for Orthotropic Material\n");
    printf(" \n");
    printf(" written by Photios P. Papados at Texas A&M University\n");
    printf(" \n");
    printf(" \n");
    printf(" Enter the Principal and Secondary Shearing Moduli (psi):\n");
    scanf("%f, %f", &g1, &g2); /* getting g1 and g2 */
    printf(" \n");
    printf(" Enter Cross-Sectional Geometry of Rectangular Bar or
Plate:\n");
    printf("(`a' being the large and `b' being the short dimension
(in.))\n");
    scanf("%f, %f", &a, &b); /* getting a and b */
    printf(" \n");
    printf(" Enter the Maximum Torsional Moment for this Section (lb-
in):\n");
    scanf("%f", &mt);
    c = a / b;
    g = g2 / g1;
    mu = sqrt(g);
    d = c / mu;

    ms = 0;
    betas = 0.0;
    kappals = 0.0;
    kappa2s = 0.0;
    pi4 = PI*PI*PI*PI;
    while (m < 75)
    {
        mi = (m+1)*(m+1);
        mii = mi;

```

```

ms = ms + mi;
mj = m+1;
inmjsq = 1/mii;

tn = tanh(mj*PI/2/d);
beta = 32*d*d/pi4/mj/mj/mj/mj*(1-2*d/mj/PI*tn);
betas +=beta;

cn = cosh(mj*PI/2/d);
c2on = inmjsq/cn;
con2s += c2on;

clon = (-1)*cos((mj+1)/2*PI)*tn/mii;
conls += clon;

m = m + 2;
}

printf("total beta = %.4f\n", betas);
printf("\n\n");
kappal = 8*d*conls/PI/PI/betas;
printf("total kappal = %.4f\n", kappal);
printf("\n\n");
kappa2 = d/betas*(1-8/PI/PI*con2s);
printf("total kappa2 = %.4f\n", kappa2);
printf("\n\n");

c1 = g2*a*b*b*b*betas;
theta = mt/g2/a/b/b/b/betas;
shr4 = mt*kappal/a/b/b/1000;
shr5 = mt*kappa2/a/mu/b/b/1000;
if (shr4 > shr5)
    maxshr = shr4;
else
    maxshr = shr5;

printf("For a %.2f x %.2f Section with a Torsional Moment = %.2f (lb-
in),\n \
    G1 = %.2f (ksi), and G2 = %.2f (ksi)\n",
a,b,mt,g1/1000,g2/1000);
printf("\n");
printf("The Torsional Rigidity of the Plate is %.2f lb-in*in\n", c1);
printf("\n");
printf("The Maximum Twist of the Plate is %.2f\n", theta);
printf("\n");
printf("The Shearing Stresses are: Shear1 = %.2f ksi, Shear2 = %.2f
ksi\n",
    shr4, shr5);
printf(" \n");
printf("The Maximum Shearing Stress is %.2f (ksi)\n", maxshr);
#endif
}

```

APPENDIX X. SAMPLE INPUT ABAQUS MODEL

```

*HEADING
3D NEW SHEAR MODEL - 1991 (JULY). See Sections 8.2 and 8.3.
** NEUTRAL FILE GENERATED ON: 24-JUL-91 16:05:15 PATABA VERSION: 3.1
**
**  NODE DEFINITIONS
**
*DATA CHECK
*RESTART,WRITE,FREQUENCY=10
*PREPRINT, MODEL=NO,HISTORY=NO,ECHO=NO
*NODE
    1,  0.7500000000E+00,  0.0000000000E+00,  0.0000000000E+00
    2,  0.7500000000E+00,  0.5000000007E-01,  0.0000000000E+00
    3,  0.7500000000E+00,  0.1000000001E+00,  0.0000000000E+00
    4,  0.7500000000E+00,  0.1500000006E+00,  0.0000000000E+00
    5,  0.7500000000E+00,  0.2000000003E+00,  0.0000000000E+00

...

    10355,  0.206294227E+01,  0.599870265E+00,  0.5000000045E-01
    10356,  0.206807685E+01,  0.601766884E+00,  0.5000000045E-01
    10357,  0.207834601E+01,  0.605560124E+00,  0.5000000045E-01
    10358,  0.208348083E+01,  0.607456744E+00,  0.5000000045E-01
    10359,  0.208861542E+01,  0.609353364E+00,  0.5000000045E-01
**
**  NODE SETS FROM MATERIALS
**
*NSET, NSET=MID1
 2290 2291 2292 2293 2294 2295 2296 2297 2298 2299 2300 2301 2302 2303
2304 2305
 2306 2307 2308 2309 2310 2311 2312 2313 2314 2315 2316 2317 2318 2319
2320 2321
 2322 2323 2324 2325 2326 2327 2328 2329 2330 2331 2332 2333 2334 2335
2336 2337
 2338 2339 2340 2341 2342 2343 2344 2345 2346 2347 2348 2349 2350 2351
2352 2353

...

*NSET, NSET=MID2
 1639 1640 1641 1642 1643 1644 1645 1646 1647 1648 1649 1650 1651 1652
1653 1654
 1655 1656 1657 1658 1659 1660 1661 1662 1663 1664 1665 1666 1667 1668
1669 1670
 1671 1672 1673 1674 1675 1676 1677 1678 1679 1680 1681 1682 1683 1684
1685 1686

...

*NSET, NSET=MID3

```

```

  988  989  990  991  992  993  994  995  996  997  998  999 1000 1001
1002 1003
  1004 1005 1006 1007 1008 1009 1010 1011 1012 1013 1014 1015 1016 1017
1018 1019
  1020 1021 1022 1023 1024 1025 1026 1027 1028 1029 1030 1031 1032 1033
1034 1035

```

...

```
*NSET, NSET=MID4
```

```

   1   2   3   4   5   6   7   8   9  10  11  12  13  14
15  16
   17  18  19  20  21  22  23  24  25  26  27  28  29  30
31  32
   33  34  35  36  37  38  39  40  41  42  43  44  45  46
47  48
   49  50  51  52  53  54  55  56  57  58  59  60  61  62
63  64

```

...

**

** ELEMENT DEFINITIONS

**

```
*ELEMENT, TYPE=C3D8, ELSET=PID1
```

```

  301,  22,  23,  39,  38,  988,  989, 1005, 1004
  302,  23,  24,  40,  39,  989,  990, 1006, 1005

```

...

```

  894,  965,  966,  981,  980, 1616, 1617, 1632, 1631
  900,  971,  972,  987,  986, 1622, 1623, 1638, 1637
*ELEMENT, TYPE=C3D8, ELSET=PID8
   1,   1, 358, 373,   2,  37,  673,  688,   53
   2, 358, 359, 374, 373,  673,  674,  689,  688

```

...

```

  5131, 9087, 9328, 9330, 9089, 9107, 9348, 9350, 9109
  5132, 9328, 9329, 9331, 9330, 9348, 9349, 9351, 9350
*ELEMENT, TYPE=C3D8, ELSET=PID9
   901,  988,  989, 1005, 1004, 1639, 1640, 1656, 1655
   902,  989,  990, 1006, 1005, 1640, 1641, 1657, 1656

```

...

```

  5151, 9107, 9348, 9350, 9109, 9127, 9368, 9370, 9129
  5152, 9348, 9349, 9351, 9350, 9368, 9369, 9371, 9370
*ELEMENT, TYPE=C3D8, ELSET=PID10
  1501, 1639, 1640, 1656, 1655, 2290, 2291, 2307, 2306
  1502, 1640, 1641, 1657, 1656, 2291, 2292, 2308, 2307

```

...

5171, 9127, 9368, 9370, 9129, 9147, 9388, 9390, 9149
5172, 9368, 9369, 9371, 9370, 9388, 9389, 9391, 9390
*ELEMENT, TYPE=C3D8 , ELSET=PID11
2101, 2290, 2291, 2307, 2306, 2941, 2942, 2958, 2957
2102, 2291, 2292, 2308, 2307, 2942, 2943, 2959, 2958

...

5191, 9147, 9388, 9390, 9149, 9167, 9408, 9410, 9169
5192, 9388, 9389, 9391, 9390, 9408, 9409, 9411, 9410
*ELEMENT, TYPE=C3D20 , ELSET=PID3
3001 4607 4609 4623 4621 4694 4696 4710 4708 4608 4617 4622 4616 4695
4704 4709 4703 4669 4670 4675 4674
3002 4609 4611 4625 4623 4696 4698 4712 4710 4610 4618 4624 4617 4697
4705 4711 4704 4670 4671 4676 4675

...

3527 7180 7182 7195 7193 7254 7256 7269 7267 7181 7188 7194 7187 7255
7262 7268 7261 7210 7211 7216 7215
3528 7182 7184 7197 7195 7256 7258 7271 7269 7183 7189 7196 7188 7257
7263 7270 7262 7211 7212 7217 7216
*ELEMENT, TYPE=C3D20 , ELSET=PID4
3017 4694 4696 4710 4708 3938 3940 3954 3952 4695 4704 4709 4703 3939
3948 3953 3947 4756 4757 4762 4761
3018 4696 4698 4712 4710 3940 3942 3956 3954 4697 4705 4711 4704 3941
3949 3955 3948 4757 4758 4763 4762

...

3543 7254 7256 7269 7267 7328 7330 7343 7341 7255 7262 7268 7261 7329
7336 7342 7335 7284 7285 7290 7289
3544 7256 7258 7271 7269 7330 7332 7345 7343 7257 7263 7270 7262 7331
7337 7344 7336 7285 7286 7291 7290
*ELEMENT, TYPE=C3D20 , ELSET=PID6
3081 4013 4969 4979 4027 4072 5030 5040 4074 4968 4975 4978 4018 5029
5036 5039 4073 4067 5014 5017 4068
3082 4969 4971 4981 4979 5030 5032 5042 5040 4970 4976 4980 4975 5031
5037 5041 5036 5014 5015 5018 5017

...

3575 7402 7404 7417 7415 7476 7478 7491 7489 7403 7410 7416 7409 7477
7484 7490 7483 7432 7433 7438 7437
3576 7404 7406 7419 7417 7478 7480 7493 7491 7405 7411 7418 7410 7479
7485 7492 7484 7433 7434 7439 7438
*ELEMENT, TYPE=C3D20 , ELSET=PID7
3097 4072 5030 5040 4074 4085 5091 5101 4087 5029 5036 5039 4073 5090
5097 5100 4086 4080 5075 5078 4081
3098 5030 5032 5042 5040 5091 5093 5103 5101 5031 5037 5041 5036 5092
5098 5102 5097 5075 5076 5079 5078

...

3591 7476 7478 7491 7489 7550 7552 7565 7563 7477 7484 7490 7483 7551
 7558 7564 7557 7506 7507 7512 7511
 3592 7478 7480 7493 7491 7552 7554 7567 7565 7479 7485 7492 7484 7553
 7559 7566 7558 7507 7508 7513 7512
 *ELEMENT, TYPE=C3D20 , ELSET=PID12
 5193 3765 9413 9423 4231 3777 9487 9497 4242 9412 9418 9422 4230 9486
 9492 9496 4241 4237 9466 9470 4238
 5194 9413 9190 9425 9423 9487 3916 9499 9497 9414 9419 9424 9418 9488
 9493 9498 9492 9466 9467 9471 9470

...

5287 9867 9869 9880 3926 9929 9931 9942 3928 9868 9874 9879 9873 9930
 9936 9941 9935 9891 9892 9896 9895
 5288 9869 9871 3927 9880 9931 9933 3929 9942 9870 9875 9881 9874 9932
 9937 9943 9936 9892 9893 9897 9896
 *ELEMENT, TYPE=C3D20 , ELSET=PID13
 5209 3777 9487 9497 4242 3789 9561 9571 4253 9486 9492 9496 4241 9560
 9566 9570 4252 4248 9540 9544 4249
 5210 9487 3916 9499 9497 9561 3918 9573 9571 9488 9493 9498 9492 9562
 9567 9572 9566 9540 9541 9545 9544

...

5303 9929 9931 9942 3928 9991 999310004 3930 9930 9936 9941 9935 9992
 999810003 9997 9953 9954 9958 9957
 5304 9931 9933 3929 9942 9993 9995 393110004 9932 9937 9943 9936 9994
 999910005 9998 9954 9955 9959 9958
 *ELEMENT, TYPE=C3D20 , ELSET=PID14
 5225 3789 9561 9571 4253 3801 9635 9645 4264 9560 9566 9570 4252 9634
 9640 9644 4263 4259 9614 9618 4260
 5226 9561 3918 9573 9571 9635 3920 9647 9645 9562 9567 9572 9566 9636
 9641 9646 9640 9614 9615 9619 9618

...

*ELEMENT, TYPE=C3D20 , ELSET=PID15
 3065 3946 4908 4918 3960 4013 4969 4979 4027 4907 4914 4917 3951 4968
 4975 4978 4018 4000 4953 4956 4001
 3066 4908 4910 4920 4918 4969 4971 4981 4979 4909 4915 4919 4914 4970
 4976 4980 4975 4953 4954 4957 4956

...

*ELEMENT, TYPE=C3D20 , ELSET=PID16
 5241 3801 9635 9645 4264 3813 9709 9719 4275 9634 9640 9644 4263 9708
 9714 9718 4274 4270 9688 9692 4271
 5242 9635 3920 9647 9645 9709 3922 9721 9719 9636 9641 9646 9640 9710
 9715 9720 9714 9688 9689 9693 9692

...

*ELEMENT, TYPE=C3D20 , ELSET=PID17

```

5257 3813 9709 9719 4275 3825 9783 9793 4286 9708 9714 9718 4274 9782
9788 9792 4285 4281 9762 9766 4282
5258 9709 3922 9721 9719 9783 3924 9795 9793 9710 9715 9720 9714 9784
9789 9794 9788 9762 9763 9767 9766

```

```

...

```

```

**
** ELEMENT PROPERTIES
**
**
**SOLID SECTION, ELSET=PID1, MATERIAL=MID4
**
**SOLID SECTION, ELSET=PID3, MATERIAL=MID4
**
**SOLID SECTION, ELSET=PID4, MATERIAL=MID4
**
**SOLID SECTION, ELSET=PID6, MATERIAL=MID2
**
**SOLID SECTION, ELSET=PID7, MATERIAL=MID1
**
**SOLID SECTION, ELSET=PID8, MATERIAL=MID4

```

```

...

```

```

**
**
** MATERIAL DEFINITIONS
**
**
**E1,E2,E3,V12,V13,V23,G12,G13
**G23
** 0 - .02 INCHES FROM CENTER OF PLATE
**MATERIAL, NAME=MID1
**ELASTIC, TYPE=ENGINEERING CONSTANTS
43.32E+03,42.58E+03,43E+3,.077,.089,.091,19.85E+03,19.04E+03
19.04E+03
**EXPANSION, TYPE=ISO , ZERO=0.0000E+00
**
** .02 - .03 INCHES FROM CENTER OF PLATE
**MATERIAL, NAME=MID2
**ELASTIC, TYPE=ENGINEERING CONSTANTS
43.32E+03,42.58E+03,47.1E+3,.077,.077,.077,19.85E+03,19.04E+03
19.04E+03
**EXPANSION, TYPE=ISO , ZERO=0.0000E+00
**
** .03 - .04 INCHES FROM CENTER OF PLATE
**MATERIAL, NAME=MID3
**ELASTIC, TYPE=ENGINEERING CONSTANTS
43.32E+03,42.58E+03,57.5E+3,.077,.075,.077,19.85E+03,19.04E+03
19.04E+03
**EXPANSION, TYPE=ISO , ZERO=0.0000E+00
**
** .04 - .05 INCHES FROM CENTER OF PLATE

```



```

*MATERIAL, NAME=MID4
*ELASTIC, TYPE=ENGINEERING CONSTANTS
43.32E+03,42.58E+03,77.4E+3,.077,.076,.077,19.85E+03,19.04E+03
19.04E+03
*EXPANSION, TYPE=ISO , ZERO=0.0000E+00
**
**  LOAD CASE    100
**
*STEP, NLGEOM, AMP=RAMP, CYCLE=20
**
LOAD CASE    100
*STATIC, PTOL= 1.000      ,MTOL= 10.00
**
*DLOAD, OP=NEW
      301, P6,  -7.75000000
      316, P6,  -7.75000000
      331, P6,  -7.75000000

...

      2956, P6,  -7.75000000
      2971, P6,  -7.75000000
      2986, P6,  -7.75000000
**
**
**
*BOUNDARY, OP=NEW
**
      1,  3,,   0.0
      2,  3,,   0.0
      3,  3,,   0.0

...

      9823,  2,,   0.0
      9827,  2,,   0.0
      9835,  2,,   0.0
*EL FILE, POSITION=AVERAGED AT NODES
S
E
*EL PRINT, POSITION=AVERAGED AT NODES
S
E
*NODE FILE, GLOBAL=YES
U
*NODE PRINT, GLOBAL=YES
U
*FILE FORMAT, ASCII
*END STEP

```

APPENDIX XI.

SELECTIVE LISTING OF FORTRAN PROGRAM CHECK

```

program main
.....

      write(*,1)
1      format ('      This is a Least-Squares Program',/)
      write(*,2)
2      format ('      written by Photios P. Papados',/)
      write(*,3)
3      format (' ***Each matrix is limited to 200 by 200***',/)
      write(*,*) ' '
      write(*,*) ' The program has the following general scheme:'
      write(*,*) ' '
c
      write(*,*) ' i.e.  $A x = y$  '
      write(*,4)
4      format (' It computes the x and y matrices',/)
      write(*,*) '  $x^T A x = x^T y$  '
      write(*,*) '  $[x^T x]^{-1} * [x^T A x] = [x^T x]^{-1} x^T y$  '
      write(*,*) '  $A = [x^T x]^{-1} x^T y$  '
      write(*,*) ' '
      write(*,*) 'Please Follow all Steps Carefully'
      write(*,*) ' '
c      determination of x-matrix
c
      idum=0
      xdum=0.0
      write(*,*) ' '
      write(*,*) ' Determination of the x- and y-matrices'
      write(*,*) ' Enter the number of experiments performed'
      read(*,*) nl
      write(*,*) ' Enter number of available stress components'
      read(*,*) nx
      write(*,*) ' Enter the number of unknown coefficients'

.....

      write(*,*) 'Is this the first or second least-squares fit ?'
      write(*,*) 'Enter 1 for first or 2 for second'
      read(*,*) ichose
      if (ichose.eq.1) goto 7
      if (ichose.eq.2) goto 8
c      endif
c
8      continue
      write(*,*) ' Enter the three normal interaction coefficients'
      write(*,*) ' From which stress combinations, i.e. (s1, s2)'
      write(*,*) ' Enter 1 for s1, 2 for s2, 3 for s3'
      write(*,*) ' NOTE: You can enter only one stress combination'

```

```

.....

      y(i)=1-(b1(i)+b2(i)+b3(i)+b4(i)+b5(i))
10    continue
      write(*,*) 'Print the y matrix'
      call wtmat(y,n1,1,1,m1)
      write(*,*) ' '
.....

      write(*,*) 'Print the x-matrix'
      m1=n1
      write(*,*) ' '
c
      write(*,30)
30    format(' Enter name of output file:      ', $)
      read(*,40) nfile
40    format(a)
      open(unit=1, file=nfile, status='new')
.....

      write(*,*) 'The program is computing the y-matrix'
.....
.....

      write(*,*) 'The program is computing the x-matrix'
.....
.....

220  format(' Do you want the x-matrix saved?
2    Please answer with Y=yes, N=no: ' $)
      read(*,221)iichose
221  format(a)
      if(iichose.eq.'N'.or.iichose.eq.'n') then
         goto 260
      elseif(iichose.eq.'Y'.or.iichose.eq.'y') then
         write(*,230)
230  format(' Enter name of output file:      ', $)
      read(*,240) nfile

260  continue
      write(*,*) 'First Read the x-matrix'
      write(*,*) ' '
      write(*,*) 'Enter the dimensions of the x-matrix: rows, columns'
      read (*,*) nr, nc
      n1=nr
      n2=nc
      isys=0

```

```

c      m1=n1
c      m2=n2
      call rdmatrix(x,n1,n2,sys,m1)

c
c      compute x transpose
c
      call tran(x,xt,n1,n2,m1)
      write(*,*) 'This is the xt-matrix'
      call wrmat(xt,n2,n1,1,m1)
c      call move(xt,t,n2,n1,1,m1)
      m2=n1
      m3=n2
      call mults(xt,x,xtx,n2,n1,n2,m1,m2,m3)
      write(*,*) ' '
      write(*,*) 'This is the xt*x matrix'
      m1=nc
      n2=nc
      call wrmat(xtx,n2,n2,1,m1)
      call wrmat(xtx,n2,n2,1,m1)
      call move(xtx,t1,n2,n2,m1,m1)
      call INVERT(N2,N2,N2,T1,T,AUGM,VY1)
      call move(t,xtxin,n2,n2,m1,m1)
      write(*,*) 'This is the inverse xt*x-matrix'
      call wrmat(xtxin,n2,n2,1,m1)
      write(*,*) ' '
      write(*,*) ' This is to check the matrices xtx and xtxin'
      call mults(xtxin,xtx,a,n2,n2,n2,n2,n2,n2)
      write(*,*) 'This is the I-matrix'
      call wrmat(a,n2,n2,1,n2)
      write(*,*) 'Now Read the y-matrix'
      write(*,*) 'Enter the dimensions of the y-matrix: rows, columns'
      read (*,*) nry, ncy
      n1=nry
      n2=ncy
      sys=0
      m1=n1
      m2=n2
      call rdmatrix(y,n1,n2,sys,m1)
      call wrmat(y,n1,n2,1,m1)
      m1=n2
c      m2=n1
c      m3=n2
      WRITE(*,*) ' '
      WRITE(*,*) 'N2=',N2, 'N1=', N1
      write(*,*) 'This is the xt-matrix'
      call wrmat(XT,n2,n1,1,N1)
      call mults(xt,y,xtyn,n2,n1,n2,N1,N1,N2)
      WRITE(*,*) ' '
      write(*,*) 'This is the xt*y-matrix'
      call wrmat(xty,n2,n2,1,N2)
      m2=n2
      call nullr(a,n2,1,N2)
      call mults(xtxin,xty,a,n2,n2,n2,n2,N2,N2)
      write(*,*) 'This is the A-matrix of Least-Squares Coefficients'

```

```

      call wrmat(a,n2,n22,1,m1)
c      write(*,*) 'The A-matrix of coefficients is stored'
c      write(*,*) 'in the file "acoeff.dat"'
      call wtmat(a,n2,n22,1,N2)
1000  continue
      write(*,*) ' '
      write(*,1010)
1010  format('Would you like to continue with new data analysis?
      2 Please answer with Y=yes, N=no: '$)
      read(*,1011)iichose
1011  format(a)
      if(iichose.eq.'N'.or.iichose.eq.'n') then
         goto 1012
      elseif(iichose.eq.'Y'.or.iichose.eq.'y') then
         goto 1020
      endif
1012  continue
      end

c      Subroutine Package
.....

      end

```

APPENDIX XII.

NOTATION

A, B, C, D	=	constants which are functions of F_i , F_{ij} , and F_{ijk} (Jiang and Tennyson)
a, b	=	sides of section undergoing torsion
a_i, b_i, c_i	=	material coefficients for Priddy's criterion
d_i, e_i, f	=	unknown coefficients for least-squares
a_i, b_i, c_i, h_i	=	constants which are functions of F_i , F_{ij} , and F_{ijk}
A_{ij}, B_{ij}, C_{ij}	=	matrix similar to the elastic compliance used in Priddy's criterion
$[A], a_{ij}$	=	least squares unknown coefficients in vector form
$\{a\}$	=	torsional rigidity
C	=	aspect ratio a/b .
c	=	material constants for Hoffman's criterion
C_1-C_9	=	longitudinal and shear wave velocities, respectively
c_1, c_2	=	parameters used with torsional problem
$d, \beta, \kappa_1, \kappa_2$	=	average through-thickness modulus for thickness t
E_a	=	elastic moduli for long, transverse, and through-thickness material directions, respectively
E_1, E_2, E_3	=	
$F, G, H,$	=	material constants for Hill's criterion
L, M, N	=	orthonormal, uniaxial, compressive strengths
F_{cx}, F_{cy}, F_{cz}	=	pure shear strengths
F_{sy}, F_{sz}, F_{sxy}	=	orthonormal, uniaxial, tensile strengths for Hoffman's criterion
F_{tx}, F_{ty}, F_{tz}	=	contracted equivalents of the second, fourth, and sixth-order strength tensors
F_i, F_{ij}, F_{ijk}	=	
$F_{ij}, F_{ijkl},$	=	second, fourth, and sixth-order strength tensors
F_{ijklmn}	=	shear strength parameters for Priddy's criterion
$F_{ij} (i \neq j)$	=	tensile and compressive strengths, respectively
F_{ti}, F_{ci}	=	yield surface function
f_y	=	fit function for least-squares
$f(a_i, b_i, c_i, h_i)$	=	failure surface function
$f(\sigma_k)$	=	
g	=	G_2/G_1
G_1, G_2	=	shear moduli associated with sides a and b
G_{12}, G_6	=	in-plane shear moduli
G_{13}, G_5	=	shear moduli for (1-3) plane
G_{23}, G_4	=	shear moduli for (2-3) plane
I	=	intensity
I, I', II, III	=	stress invariants of Priddy's criterion
II, III	=	second and third stress invariants
J_1, J_2, J_3	=	invariants of the stress tensor σ_{ij}
J_1', J_2', J_3'	=	invariants of the deviatoric stress tensor σ_{ij}'
$K1, L1, M1,$		
$K2, L2, M2,$		
$K3, L3, M3,$		
$K1', L1', M1',$		

$K2', L2', M2',$ $K3', L3', M3', T$	=	constants which are functions of F_{ij} and F_{ijk}
M_t	=	torsional moment
R, S, T	=	principal shear yield stresses (Hill, Hoffman)
$R, S, T,$ R', S', T'	=	principal positive and negative shear failure stresses
$[R]$	=	rotational matrix
S_{yx}	=	measured stiffness in y-direction due to stress in the x-direction
S_{1x}, S_{2x}, S_{3x}	=	stiffnesses in the long, transverse, and through-thickness direction due to an applied stress in the x-direction
W	=	equivalent form of strain energy density
X, Y, Z	=	principal tensile yield stresses (Hill, Hoffman)
$X, Y, Z,$ X', Y', Z'	=	principal tensile and compressive failure stresses
x_c, y_c, z_c	=	center(s) of ellipsoidal surface from Hoffman's criterion
x_{ij}	=	value of the i^{th} variable associated with the j^{th} observation
$[X]$	=	matrix containing the powered terms of $f(a_i, b_i, c_i, h_i)$
y_i	=	computed value of the best-fit function for the i^{th} observation
$Y_m(y)$	=	amplitude of stress function, ψ
$\{y\}$	=	vector form of estimated values of $f(a_{i-1}, b_i, c_i, h_i)$
α	=	angle of rolling with respect to first principal material axis
α_{ki}, α_{lj}	=	direction cosines for transformation of stress tensor
δ_{ij}	=	Kronecker delta
$\epsilon_1, \epsilon_2, \epsilon_3$	=	strain in the long, transverse, and through-thickness material directions, respectively
$\epsilon_{12}, \epsilon_6$	=	in-plane shear strain
$\epsilon_{13}, \epsilon_5$	=	shear strain on the (1-3) plane
$\epsilon_{23}, \epsilon_4$	=	shear strain on the (2-3) plane
$[\epsilon_L]$	=	strain matrix with respect to load axes
$[\epsilon_M]$	=	strain matrix with respect to material axes
$\lambda_i, \mu_i, \nu_i, \xi_i$	=	Lagrange multipliers
μ	=	$!g$
μ_a	=	average through-thickness Poisson's ratio for thickness t
$-\mu/\rho$	=	mass absorption coefficient
$\nu_{12}, \nu_{21}, \nu_{13}$	=	Poisson's ratios
$\nu_{31}, \nu_{23}, \nu_{32}$	=	Poisson's ratios
ρ	=	density
σ_{ij}	=	second-order stress tensor

σ_{ij}'	=	deviatoric stress tensor
σ_1^0	=	octahedral shear stress at yield
σ_x	=	stress parallel to the direction of the load
$\sigma_x, \sigma_y, \sigma_z,$ $\sigma_{xy}, \sigma_{yz}, \sigma_{xz}$	=	stress components for Hill's and Hoffman's criteria
$\sigma_{xx}, \sigma_{yy}, \sigma_{zz},$ $\sigma_{xy}, \sigma_{xz}, \sigma_{yz}$	=	components of $[\sigma]$
$\sigma_x', \sigma_y', \sigma_z',$ $\tau_{xy}', \tau_{xz}', \tau_{yz}'$	=	components of the deviatoric stress
$\sigma_1, \sigma_2, \sigma_3$	=	principal stresses of second-order stress tensor used to define $J_1, J_2,$ and J_3
$\sigma_1, \sigma_2, \sigma_3$	=	stress in the long, transverse, and through-thickness material directions, respectively
$\sigma_1, \sigma_2, \sigma_3,$ $\sigma_4, \sigma_5, \sigma_6$	=	components of $[\sigma_i]$ and $\{\sigma_i\}$
$\sigma_1', \sigma_2', \sigma_3'$	=	principal stresses of deviatoric stress tensor
$[\sigma]$	=	second-order stress tensor in matrix form
$[\sigma_i]$	=	contracted equivalent of $[\sigma]$ in matrix form
$[\sigma_L]$	=	load orientation stress matrix
$[\sigma_M]$	=	material orientation stress matrix
$\{\sigma\}$	=	vector form of stress tensor
$\{\sigma_i\}$	=	contracted equivalent of $[\sigma]$ in vector form
Φ, Ψ, Ω, Π	=	functionals from new criterion
x	=	thickness of the material
ψ	=	stress function for torsion
x		

